Dissertation

Oxygen Stoichiometry Changes in $SrTiO_3$ under UV Illumination

ausgeführt zum Zwecke der Erlangung des akademischen Grades eines
Doktors der technischen Wissenschaften
unter der Leitung von

Univ. Prof. Dipl.-Phys. Dr.rer.nat. Jürgen Fleig
E164
Institut für Chemische Technologien und Analytik

eingereicht an der Technischen Universität Wien
Institut für Chemische Technologien und Analytik
von

Alexander Viernstein
Mat.Nr.: 01125305

Wien, August 2021 Alexander Viernstein

Abstract

$SrTiO_3$ is a promising material for high temperature photovoltaic cells, which might be used for powering small off-grid devices such as sensors. However, questions arose regarding the stability of $SrTiO_3$ under UV irradiation and properties of $SrTiO_3$ thin films, possibly usable in such solar cells. The main aim of this thesis was to investigate the impact of UV irradiation on the defect chemistry of $SrTiO_3$ single crystals and thin films at elevated temperatures. Moreover, the pseudo-intrinsic behavior of $SrTiO_3$ thin films was examined.

In Fe-doped $SrTiO_3$, UV irradiation results in an enhanced oxygen incorporation rate which leads to a filling of oxygen vacancies and to an oxidation of Fe^{3+} to Fe^{4+}. The corresponding change in the oxygen stoichiometry causes a color change of the samples (darkening), which was found to be irreversible at room temperature. The original transparent/brownish color can only be restored after annealing at 700 °C in air. The time dependence of these changes was monitored by UV/Vis spectroscopy which allowed determination of an oxygen chemical diffusion coefficient. In addition, to this high temperature photochromic effect, UV irradiation results in a significant increase of the in-plane bulk conductivity measured by impedance spectroscopy and van der Paw experiments. An enhancement by more than a factor of five was revealed, due to an increased electron hole concentration under UV illumination in air. The corresponding shift of the oxygen chemical potential was estimated, yielding an equivalent p_{O_2} of 10^4 bar.

The increase of in-plane conductivity of undoped $SrTiO_3$ single crystals was even more pronounced, with increases by several orders of magnitude upon UV irradiation between 280 and 450 °C. After UV illumination the X-ray absorption spectrum of the Ti $L_{2,3}$-edge was shifted by +0.1 eV, again suggesting an oxidation due to UV light. In a next step, the p_{O_2} was drastically reduced, and $SrTiO_3$ became an n-type semiconductor. In dry H_2 at 350 °C the bulk in-plane conductivity dropped to 40 % of the initial (dark) value after UV irradiation. Oxygen was still incorporated under UV irradiation, thus increasing the oxygen chemical potential. This reduces the electron (now main electronic charge carrier) concentration and thus the conductivity. Here, however, H_2O rather than O_2 was photocatalytically split. Interestingly, after UV irradiation different characteristics could be identified in two regions of the $SrTiO_3$ single crystals. One region was located near the surface, where the UV light was absorbed,

and electron-hole pairs led to a strongly increased photoconductivity. The conductivity of the second much thicker layer beneath the absorption zone was lowered due to the chemical potential shift.

$SrTiO_3$ thin films were investigated as well and at first, the mass gain during UV exposure due to the oxygen incorporation was probed by $GaPO_4$ microbalances. A measurement set-up was built and verified by gas exchange experiments. Thereby the atmosphere was changed back and forth from O_2 to N_2 and the mass changes of $La_{0.6}Sr_{0.4}CoO_3$, undoped and Fe-doped $SrTiO_3$ specimens were monitored. The measured changes were in the ng range and in good accordance with oxygen vacancy concentration changes obtained from defect chemical calculations and literature data.

Finally, ultra-low (pseudo-intrinsic) conductivities of undoped and metal doped (Al, Ni, Fe) $SrTiO_3$ thin films were investigated by impedance spectroscopy between approx. 300-750 °C in air. They were epitaxially grown, by pulsed laser deposition from stochiometric targets. Positron annihilation lifetime spectroscopy, reciprocal space maps, and inductively-coupled plasma optical emission spectroscopy revealed Sr vacancies as predominant point defects. Fe-doped $SrTiO_3$ was used as model compound and further investigated by X-ray absorption spectroscopy and X-ray standing wave measurements. Fe was found to be located on both the A- and the B-site. Thus, the dopant seems to act as donor or acceptor depending on the site occupation. The pseudo-intrinsic behavior was explained by a model suggesting that the Fermi level is pinned to the band gap center by the interplay of Sr vacancies and Ti antisite defects both caused by a lack of Sr in the thin films.

Kurzfassung

In den kommenden Jahren wird der Bedarf an kleinen, vom Stromnetz entkoppelten Geräten als Teil des “Internet of Things“ stetig zunehmen. Die Bereitstellung von elektrischer Energie für diese Geräte ist eine große Herausforderung. Unter extremen Bedingungen könnten hier hochtemperatur-photovoltaische Zellen von Nutzen sein. Für solche Zellen ist $SrTiO_3$ ein vielversprechendes Absorbermaterial. Allerdings ergeben sich damit auch viele Fragen z.B. bezüglich der Stabilität und der Beleuchtung und der Eigenschaft von möglicherweise einsetzbaren Dünnfilmen. Daher war das Ziel der vorliegenden Arbeit, die Auswirkungen des UV-Lichtes auf die Defektchemie von $SrTiO_3$ Einkristallen und Dünnfilmen unter erhöhter Temperatur zu untersuchen. Darüber hinaus wurde das pseudo-intrinsische Verhalten von $SrTiO_3$ Dünnfilmen untersucht.

In Fe dotiertem $SrTiO_3$ führte die Beleuchtung mit UV-Licht zu einem beschleunigten Sauerstoffeinbau. Dadurch wurden Sauerstoffleerstellen gefüllt und Fe^{3+} zu Fe^{4+} oxidiert. Dies führte zu einer Farbänderung von bräunlich-transparent zu schwarz. Die Schwärzung war bei Raumtemperatur irreversibel und die ursprüngliche Färbung konnte erst mit Hilfe einer Auslagerung bei 700 °C an Luft wieder erreicht werden. Die beschriebenen Veränderungen wurden mit UV/Vis-Spektroskopie zeitabhängig verfolgt. Dies ermöglichte die Bestimmung von Diffusionskoeffizienten. Zusätzlich zu diesem hochtemperatur-photochromen Effekt führte das Beleuchten der Proben mit UV-Licht zu einer signifikanten Zunahme der in-plane Leitfähigkeit, welche mittels Impedanzspektroskopie und van der Pauw Messungen bestimmt wurde. Eine Verbesserung der Leitfähigkeit an Luft um mehr als das Fünffache konnte auf eine entsprechende Erhöhung der Lochkonzentration zurückgeführt werden. Die entsprechende Verschiebung des chemischen Potentials des Sauerstoffes entsprach einem Sauerstoffpartial-druck von 10^4 bar im Material.

In undotierten $SrTiO_3$ Einkristallen kam es durch die UV-Beleuchtung an Luft zwischen 280 und 450 °C sogar zu einer Verbesserung der in-plane Leitfähigkeit um mehrere Größenordnungen. Zusätzlich führte solch eine Beleuchtung zu einer Verschiebung im Röntgenabsorptions-spektrum der Ti $L_{2,3}$-Kante um +0.1 eV. Dies spricht für eine Oxidation unter UV-Licht. Im nächsten Schritt wurde der Sauerstoffpartialdruck drastisch abgesenkt, sodass $SrTiO_3$ von einem p- zu einem n-Halbleiter wurde. In trockener

Wasserstoffatmosphäre und bei 350 °C reduzierte sich die Leitfähigkeit von $SrTiO_3$ Einkristallen nach einer Beleuchtung mit UV-Licht um über 50 %. Die entsprechende Verringerung der Elektronenkonzentration war verursacht durch Sauerstoffeinbau aufgrund von photokatalytischer Wasserspaltung. Während der UV-Beleuchtung konnten zwei Regionen mit unterschiedlichen Eigenschaften identifiziert werden. In einer sehr dünnen direkt an der Oberfläche gelegenen Zone wurde das UV-Licht absorbiert und Elektron-Loch-Paare gebildet; dadurch stieg die Photo-Leitfähigkeit stark an. In der viel dickeren darunter befindlichen Schicht nahm die Leitfähigkeit durch den Sauerstoffeinbau jedoch ab.

In einem nächsten Schritt wurden $SrTiO_3$ Dünnfilme untersucht, indem die Massezunahme durch den Einbau von Sauerstoff mit Hilfe von $GaPO_4$ Mikrowaagen bestimmt bzw. nachgewiesen wurde. Ein neuer Messstand wurde zu diesem Zweck in der Arbeitsgruppe gebaut und mittels Gasaustauschexperimenten getestet. Dabei wurde zwischen O_2 und N_2 Atmosphären gewechselt und die Masseänderungen von $La_{0.6}Sr_{0.4}CoO_3$, undotierten und Fe dotierten $SrTiO_3$ Dünnfilmen gemessen. Die Veränderungen lagen allesamt im ng-Bereich und wurden mittels Literaturwerten bzw. durch defektchemische Rechnungen plausibilisiert.

Schließlich wurde mit Impedanzspektroskopie die pseudo-intrinsische Leitfähigkeit von undotierten und mit unterschiedlichen Metallen (Al, Ni, Fe) dotierten $SrTiO_3$ Dünnfilmen untersucht. Diese Messungen wurden an Luft bei Temperaturen zwischen ca. 300 °C und 700 °C durchgeführt. Alle Schichten wurden mittels Laserablation hergestellt und wuchsen epitaktisch auf $SrTiO_3$ oder Nb dotierten $SrTiO_3$ Einkristallen. Die Abscheidung selbst erfolgte von stöchiometrischen, polykristallinen Pellets. Die Proben wurden einer ausgedehnten Analyse unterzogen; so wurde „Positron annihilation lifetime“ Spektroskopie, „reciprocal space maps“, und induktiv gekoppelte Plasmaemissionsspektroskopie durchgeführt und Sr Leerstellen als vorherrschende Punktdefekte identifiziert. Im weiteren Verlauf diente Fe dotiertes $SrTiO_3$ als Beispielverbindung. Fe konnte sowohl am A- als auch am B-Platz mit Hilfe von Röntgenabsorptionsspektroskopie und „X-ray standing wave“ Messungen nachgewiesen werden. Somit wirkt dieses Dotierelement sowohl als Akzeptor- als auch Donordotierung. Zusätzlich wurde ein Modell entwickelt, mit welchem das pseudo-intrinsische Verhalten der erwähnten Schichten durch eine Fixierung des Fermi-Niveaus in die Mitte der Bandlücke erklärt wird. Verantwortlich hierfür ist das Zusammenspiel von Sr Leerstellen und Ti Substitutionsatomen auf einem Sr Gitterplatz.

Contents

1 Introduction

$SrTiO_3$ is one of the best investigated electroceramic materials and exhibits a cubic perovskite structure (ABO_3) above approx. 105 K.[1-3] It serves as a model perovskite[4, 5] with an indirect band gap energy of approx. 3.2 eV[6-8] and a direct band gap of 3.75 eV at room temperature.[8] It has an extremely wide range of applications, and is used e.g. as high-k dielectric for grain boundary barrier layer capacitors,[9, 10] as oxygen sensor,[11, 12] and as substrate for superconductors.[13] Additionally, it is capable to establish a highly conductive two-dimension electron gas at the $SrTiO_3/LaAlO_3$ interface,[14-17] is a promising material in the field of resistive switching[18-23] and can be used as mixed conductor for fuel cell electrodes[24] or as anode in Li-ion batteries.[25] Recently, also photovoltaic applications have been discussed, mainly at elevated temperatures of 300-500 °C.[26] This might become relevant also in the context of miniaturized autonomous wireless devices as parts of the internet of things

The conductivity of $SrTiO_3$ can either be mainly electronic or ionic.[1, 12, 27-31] Thus, the main charge carrier may change from electron or electron holes to oxygen vacancies. The type of conductivity is, among others, defined by p_{O_2}, temperature, doping, and applied voltages.[1, 5, 12, 27, 31-34] Consequently, many studies can be found dealing with the impact of these parameters on the $SrTiO_3$ properties and the underlying defect chemistry. For example, at 850 °C and a doping concentration of 1 mol% Fe, $SrTiO_3$ exhibits electronic n-type conductivity below a p_{O_2} of 10^{-12} bar. Between 10^{-12} and 10^{-7} bar it becomes an ionic conductor and above 10^{-7} bar a p-type conductive semiconductor.[27]

In Fe-doped $SrTiO_3$, Fe with a valency of 2+ to 5+ was found depending on sample type, of temperature and p_{O_2}.[35-43] Strong absorption bands at about 440 and 590 nm generally are attributed to the presence of Fe^{4+} under oxidizing conditions.[38, 44-46] However, the determination of the exact oxidation state of Fe is far from trivial, due to the partly covalent bond with oxygen and partly also due to the low Fe concentrations in the used single crystals. Nevertheless, trapped electron holes are referred to as Fe^{4+}, following the common nomenclature.

In the case of Fe-doped $SrTiO_3$, changes in the absorbance make it possible to track the changes in the Fe^{4+} concentration. These changes are directly connected to the oxygen

vacancy concentration due to defect chemical reasons.[1, 47] Thus, kinetic parameters of oxygen incorporation, release, or diffusion into, out, or through Fe-doped $SrTiO_3$ can be determined by monitoring absorbance changes after p_{O_2} jumps. [47, 48] Another approach for investigating the defect chemistry is based on the analysis of the electrical conductivity. For example, with the help of conductivity relaxation techniques, changes in the oxygen stoichiometry can be tracked and described.[49-51]

As mentioned above, not only temperature, p_{O_2} or doping influence the individual defect concentrations, but also the application of voltages can strongly modify the defect chemistry of $SrTiO_3$.[32-34, 52, 53] Such voltage driven processes can be utilized for memristive applications. [32, 54, 55] Thereby a redistribution of oxygen vacancies leads to resistive switching under a high electric field.[32] Moreover, applying high voltages onto Fe-doped $SrTiO_3$ also causes local color changes due to stoichiometric changes.[34, 56] A similar "electrocoloration" or "electrochemical blackening" was found in other oxides e.g. yttria stabilized zirconia as well.[57, 58]

Besides the discussed parameters influencing the oxygen bulk stoichiometry, also irradiation with above band gap light (UV light) can affect the bulk oxygen vacancy concentrations.[26] After UV illumination the oxygen chemical potential was increased and a battery-type voltage was thus obtained from an electrochemical cell composed of a $SrTiO_3$ electrode and an yttria stabilized zirconia (YSZ) electrolyte at 360 °C in air.[26] Moreover, it was shown that UV illumination accelerates the incorporation of oxygen into Fe-doped $SrTiO_3$.[45] On the other hand, during pulsed laser deposition the UV radiation of the plasma plume seems to enhance the oxygen vacancy concentration at 800 °C and a p_{O_2} of 10^{-8} bar.[59]

However, the defect chemical understanding of the UV induced effects on the (bulk) stoichiometry is still in its infancy. Improving this knowledge was a main goal of this thesis. A first approach was based on the analysis of optical properties. Considering voltage induced electrocoloration as the consequence of a changed oxygen vacancy concentration, above band gap irradiation should in principle also lead to an analogue photochromic effect in Fe-doped $SrTiO_3$ at elevated temperatures. Some metal oxides are known for their photochromic effects ($SrTiO_3$, TiO_2, etc.)[46, 60-67] but, those are not caused by oxygen stoichiometry changes of the bulk. Most of them are based on the activation or deactivation of color centers by light and take place at or far below room temperature. Here, the impact of the UV illumination on the bulk oxygen vacancy concentration, defect chemistry, and the

mechanism of color changes of Fe-doped $SrTiO_3$ single crystals were investigated at elevated temperatures and the results are summarized in chapter 2.

Not only color (i.e. absorption) may change by UV-induced bulk effects, also the conductivity is expected to change. Indeed, drastic changes were found in Fe-doped $SrTiO_3$ (chapter 2) and especially in undoped $SrTiO_3$ in air (chapter 3). Much smaller changes were found in H_2 but still allow far-reaching conclusions since UV irradiation led to a rare decrease of the conductivity (chapter 4).

In view of a possible use of $SrTiO_3$ thin films in photovoltaic cells the study was extended to properties of such films under UV illumination (chapter 5). Weight gains and losses due to the change of the oxygen vacancy concentrations under UV exposure were monitored. Since such changes are in the ng range simple thermogravimetry techniques[68, 69] do not suffice. Thus, $GaPO_4$ microbalances[70-73] were used. In a more general approach the reasons behind the ultralow conductivity of different $SrTiO_3$ films deposited by pulsed laser deposition was studied as well (chapter 6).[74] In a final review-like chapter the photocatalytic properties of $SrTiO_3$ are summarized (chapter 7).

2 High-temperature photochromism of Fe-doped $SrTiO_3$ caused by UV-induced bulk stoichiometry changes

The following chapter largely corresponds to the article: “High-Temperature Photochromism of Fe-Doped $SrTiO_3$ Caused by UV-Induced Bulk Stoichiometry Changes” published in Advanced Functional Materials. [75]

2.1 Introduction

In this chapter the changes in color and conductivity after UV irradiation of Fe-doped $SrTiO_3$ at elevated temperatures are discussed by means of UV/Vis absorption spectroscopy, *van der Pauw* measurements and in-plane electrochemical impedance spectroscopy (EIS). The predominant electronic charge carrier in the present measurement conditions were holes. Strong photochromic effects were found, with a UV induced color change from transparent/brownish to black. The results are discussed in terms of the standard defect model of Fe-doped $SrTiO_3$,[29] i.e. based on the defect chemical reactions for trapping/detrapping of holes (Equation 1) oxygen incorporation and –release (Equation 2) and electron-hole generation/recombination (Equation 3):

$$Fe_{Ti}^{x} \rightleftharpoons Fe_{Ti}' + h^{\bullet} \quad (1)$$

$$\frac{1}{2} O_2 + V_O^{\bullet\bullet} \rightleftharpoons O_O^{x} + 2\,h^{\bullet} \quad (2)$$

$$nil \rightleftharpoons e' + h^{\bullet} \quad (3)$$

Here, $h^{\bullet}$ denotes mobile electron holes while Fe_{Ti}^{x} represents the nominal Fe^{4+} state with a trapped hole, irrespective of the exact atomistic localization of this trapped hole (see above). From the thermodynamic data of the defect chemical reactions the chemical potential change in the bulk of Fe-doped $SrTiO_3$ induced by UV light can be estimated.[29] This photochromic effect is not only attractive from a basic science point of view and for self-

regulating optical transmittance of oxides, its fundamental mechanistic aspects may also be of high interest regarding applications in the field of light driven CO_2 or H_2O splitting or photo-charging of batteries.[76]

2.2 Experimental

Optical and electrochemical measurements were carried out on Fe-doped $SrTiO_3$ single crystals (5×5×0.5 mm^3/10×10×0.5 mm^3, (001) oriented) from Alineason Materials Technology GmbH, Germany. Laser Ablation-Inductively Coupled Plasma-Mass Spectrometry (LA-ICP-MS)[77, 78] revealed a Fe concentration of 0.016 ± 0.002 mol% based on the Ti content (ca. 2.7×10^{18} Fe cm^{-3}), which is lower than the nominal value (0.16 mol%). ICP-MS measurements also showed that Fe is the predominant aliovalent cation. In a first step, all specimens were annealed for 720 min at 1000 °C in air and then cooled with 5 °C min^{-1} to eliminate potential surface defects and inhomogeneities. After the procedure a smooth surface with no precipitations at the surface as sometimes reported, expected to be Sr-rich according to literature, was received.[79] In ToF-SIMS measurements a homogeneous cation composition after the typical transient response there in the first few nanometers underneath surfaces was observed.

For characterizing the light-induced changes, the following tools were employed. UV/Vis absorption experiments were carried out on a measurement setup consisting of a heating stage, and a UV/Vis system, in which a deuterium and a tungsten lamp (Edmund Optics Inc., Germany) were used as light sources and an Ocean Optics QE6500 (Halma plc, Great Britain) as spectrometer. A schematic of the setup is given in Figure 5a. The surface temperature of the Fe-doped $SrTiO_3$ crystal was determined on a reference sample with a sputtered thin film thermocouple. UV irradiation was performed by means of a UV-LED (365 nm, 3 W radial output) from Led Engin Inc., USA. and a quartz rod, acting as optical guide for the UV light. For in-situ absorbance experiments, this quartz rod was part of the UV/Vis setup (see Figure 5a), for ex-situ studies, the sample was positioned in a tube furnace with the quartz rod directing light onto the sample. Additionally, various UV irradiation experiments were carried out, with parts of the sample covered by a shadow mask and oxygen diffusion profiles were calculated using the finite element method in COMSOL Multiphysics© software (COMSOL AB, Sweden).

Van der Pauw experiments were used to monitor changes of the conductivity caused by a preceding illumination step (ex-situ, by the UV-LED described above). Four Pt-thin film electrodes (200 nm thickness) were sputter deposited in Ar (2×10^{-2} mbar) onto the edges of 5×5×0.5 mm^3 specimens using a DC magnetron sputtering system (BAL-TEC MED 020 Coating system, BalTec, Switzerland) and a shadow mask. For the actual conductivity measurements two Keithley 2000 multimeter and a 2410 1100 V Source Meter (Keithley Instruments, USA) were used, with the samples being positioned in a tube furnace.

In-situ observation of conductivity changes was performed by electrochemical impedance spectroscopy (EIS) on a 10×10×0.5 mm^3 single crystal with sputtered Pt-stripe electrodes on two edges with a distance of 5.8 mm in between (see Figure *12*Figure *11*). The sample was positioned in a tube furnace with UV-LED light exposure by means of a quartz rod at 350 °C and 400 °C. UV illumination and oxygen incorporation took place at the free Fe-doped $SrTiO_3$ surface and caused a conductivity increase and a coloration of the single crystal. The impedance of the sample was measured before, during and after UV exposure by means of a Novocontrol Alpha-A high performance Frequency Analyzer with an Electrochemical Test Station POT/GAL 30 V/2 A or a Novocontrol Alpha-A High Performance Frequency Analyzer, respectively (both Novocontrol Technologies GmbH & Co. KG, Germany).

2.3 Results and discussion of optical absorbance measurements

2.3.1 Ex-situ absorbance measurements

Figure 1 displays a sketch of the photochromic effects and the (defect) chemical processes in Fe-doped $SrTiO_3$ single crystals investigated in this study. UV irradiation at 350-440 °C causes oxygen incorporation by filling oxygen vacancies and is associated with a change of the color; annealing at 700 °C recoveres the color and defect state. For the optical characterization of the photochromic effects, two approaches (ex-situ and in-situ measurements) were employed. In the first approach (ex-situ), specimens were blackened by UV exposure at 440 °C in a tube furnace and the absorbance was measured subsequently at 200 °C surface temperature in an UV/Vis setup with heating stage. Four absorption spectra are shown in Figure *2*. First, the pristine Fe-doped $SrTiO_3$ single crystal with a brownish tint was measured after exposure to 700 °C for 180 min in air and quenching to room temperature in less than five minutes to preserve the vacancy concentration established at 700 °C. Second, the sample was investigated after UV illumination at 440 °C for 210 min. The third spectrum was

taken after another 930 min under UV light at 440 °C on the now black single crystal. At room temperature this blackened state was frozen-in and did not change.

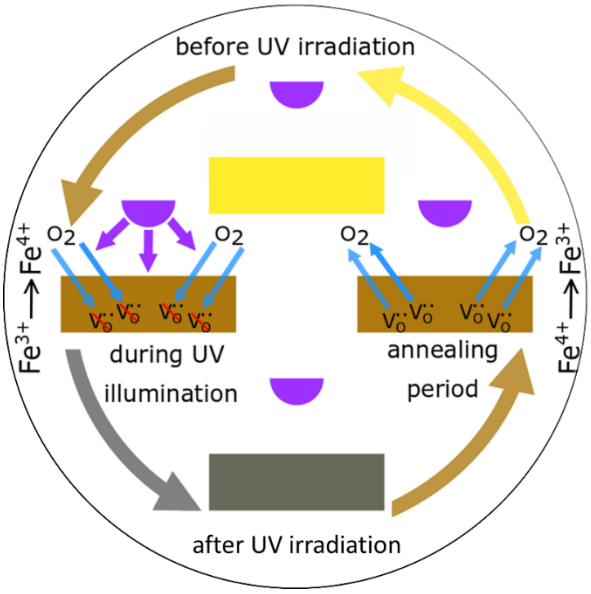

Figure 1: Basic concept of the coloration experiment: During UV illumination oxygen is incorporated into Fe-doped $SrTiO_3$, simultaneously Fe^{3+} is oxidized and the color of the single crystal changes from transparent/brownish to dark brown/black. After annelaing at 700 °C for 720 min in air, their original composition/color is restored.

However, the initial state can be re-established by annealing at 700 °C in air (>720 min), see fourth spectrum. Photographs of a Fe-doped $SrTiO_3$ sample in Figure *3*a show the drastic photochromic effect. Moreover, the diffusive nature of this effect was revealed by irradiating only a part of a Fe-doped $SrTiO_3$ crystal at 440 °C (Figure 3b). Also, the parts of the sample covered during UV exposure change their color with a clear in-plane coloration profile. In an optical microscope the diffusion front appears homogeneous to the µm-level, consequently the curvature of the blackened zone in Figure 3b is ascribed to the shape of the waveguide. Hence, existence of the strong in-plane profile indicates that a bulk diffusion process plays an important role in the coloration. As detailed in the following, it comes from the incorporation of oxygen, which diffuses through the specimen, fills the oxygen vacancies, and changes the properties of the whole Fe-doped $SrTiO_3$ single crystal Effects of dislocations which are sometimes discussed as possible line-shaped fast diffusion paths [80]or oxygen reduced zones[81, 82] were not observed.

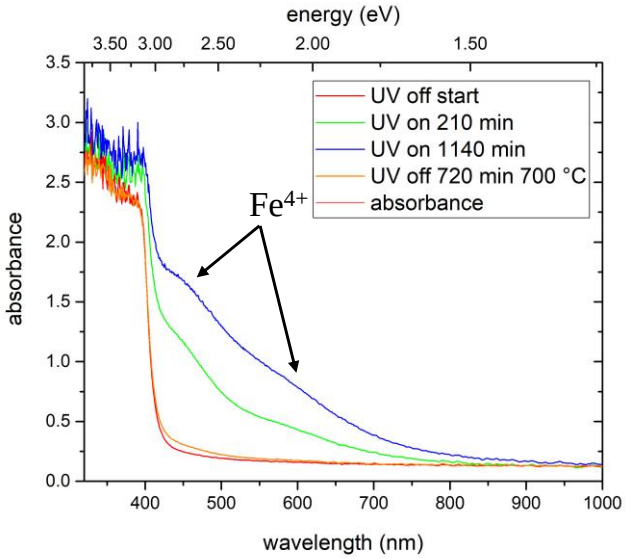

Figure 2: UV/Vis spectra of the ex-situ measurements, all obtained at 200 °C surface temperature - starting with a single crystal after 700 °C (180 min) annealing (red line). Due to UV illumination at 440 °C in air, the absorbance increased to the green line (UV on for 210 min) and finally to the blue line (UV on for 1140 min): Two broad Fe^{4+} absorption bands appeared at about 450 and 600 nm. After 720 min at 700 °C without irradiation, the absorbance nearly reached the initial state (orange line).

After UV irradiation, not only the average absorbance was increased over the whole spectral width, but particularly two broad absorption bands appeared around 450 nm and 600 nm in the UV/Vis absorption spectra measured at 200 °C. The already strong absorbance after 210 min upon UV was further increased by longer exposure. This becomes even better visible when subtracting the absorbance of an undoped $SrTiO_3$ single crystal (Crystec, Germany) (Figure 4a). The two broad absorption bands in Fe-doped $SrTiO_3$ are commonly attributed to Fe^{4+}, while Fe^{3+} exhibits almost no absorption in the visible regime.[35, 39, 44, 45, 83] The enhanced absorbance and the two Fe^{4+} bands disappeared after an annealing step at 700 °C. This strongly suggests an oxidation of the Fe-doped $SrTiO_3$ samples upon UV, i.e. an oxygen uptake with a Fe^{3+} to Fe^{4+} transition and a decrease of the oxygen vacancy concentration,[44, 45] in accordance with the defect chemical model of Fe-doped $SrTiO_3$.[29]

Hence, experimental evidence that the defect chemical state of the entire Fe-doped $SrTiO_3$ crystal can be changed by UV exposure was obtained. This is very different from reported photochromic effects in transition metal oxides occurring at room temperature or below, see Introduction. In those experiments, UV light modifies electron occupation of defect related color centers, and elevated temperatures quickly annihilate the photochromism. In

the experiments presented the absorbance effects are due to compositional changes (oxygen vacancy annihilation) at elevated temperatures.

A closer look at Figure 4 reveals, that the single crystals probably contain a small amount of Fe^{4+} already before UV irradiation at ambient p_{O_2}. This was visible as brownish tint and led to a small peak in the UV/Vis spectra at 405 nm (measured at 200 °C) or 430 nm (measured at 440 °C), though no absorption band could be found in the region of 590/600 nm. During UV illumination the Fe^{4+} related peak became much stronger and its maximum or plateau shifted to slightly higher wavelengths (420-430 nm at 200 °C and 440 nm at 440 °C). Additionally, a second absorption band appeared at around 600 nm. In literature, an additional charge transfer from Fe^{4+} to Fe^{5+} was reported for photochromic absorption experiments far below room temperature, with bands at 623 nm and 490 nm. However, those bands were never observed here.[38]

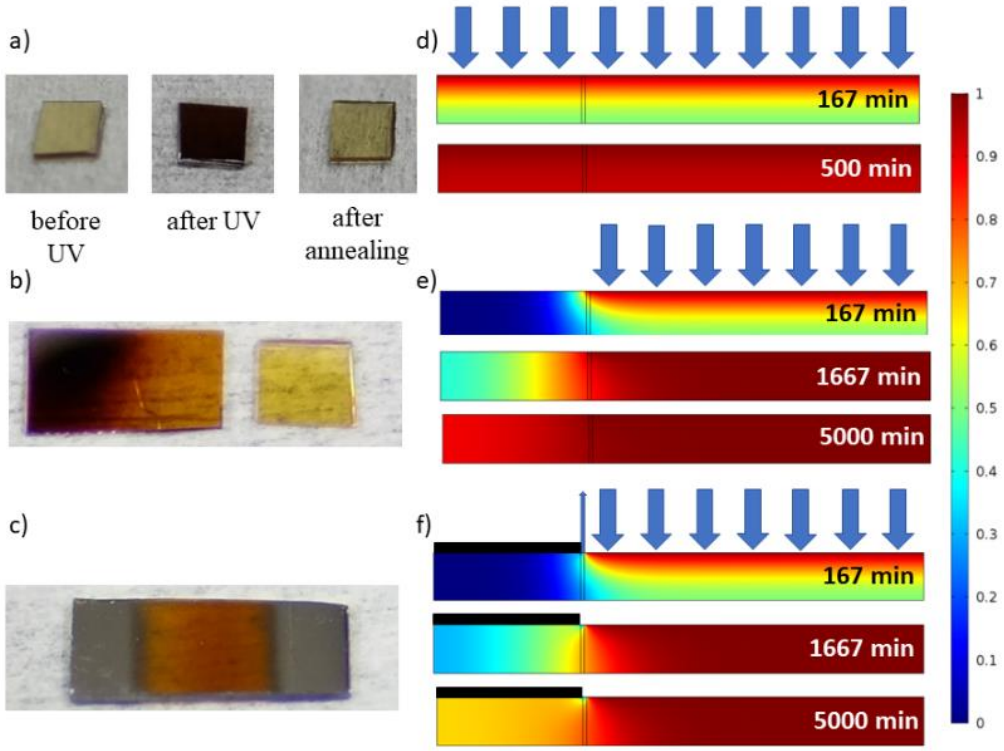

Figure 3: **a)** Photograph of a pristine Fe-doped $SrTiO_3$ with a transparent/brownish tint, blackened specimen after 1140 min under UV light at 440 °C and after annealing the blackened sample for 720 min at 700 °C – again transparent/brownish tint. **b)** After equilibration in air at 700 °C right half of the sample was illuminated for 1380 min at 440 °C. Brown color of the unexposed part and the in-plane color gradient indicates oxygen diffusion. For comparison also a sample without UV exposure is shown on the right. **c)** Fe-doped $SrTiO_3$ sample with two Pt electrodes (used for impedance studies) after UV illumination. A slight in-plane gradient suggests that incorporation took place exclusively between the electrodes and possibly oxygen was again released at the three-phase boundary. **d)** Two calculated oxygen diffusion profiles in a 0.5 mm thick sample, oxygen incorporation along the entire (illuminated) surface is assumed. The profiles are based on a diffusion coefficient of D_O^δ = 1×10^{-7} cm^2 s^{-1} and a surface exchange coefficient of k_O^δ = 1×10^{-4} cm s^{-1}; top profile after 167 min, lower after 500 min. **e)** Three calculated diffusion profiles, corresponding to sample b). Oxygen incorporation takes place only on the right side, indicated by the blue arrows (parameters as in d)). The slow in-plane diffusion is obvious. **f)** Diffusion profile calculated for the situation shown in c) after 167, 1667 and 5000 min with oxygen release at the three-phase boundary (k_O^δ = 1×10^{-4} cm s^{-1} with outer concentration at the initial state (i.e. at 0).

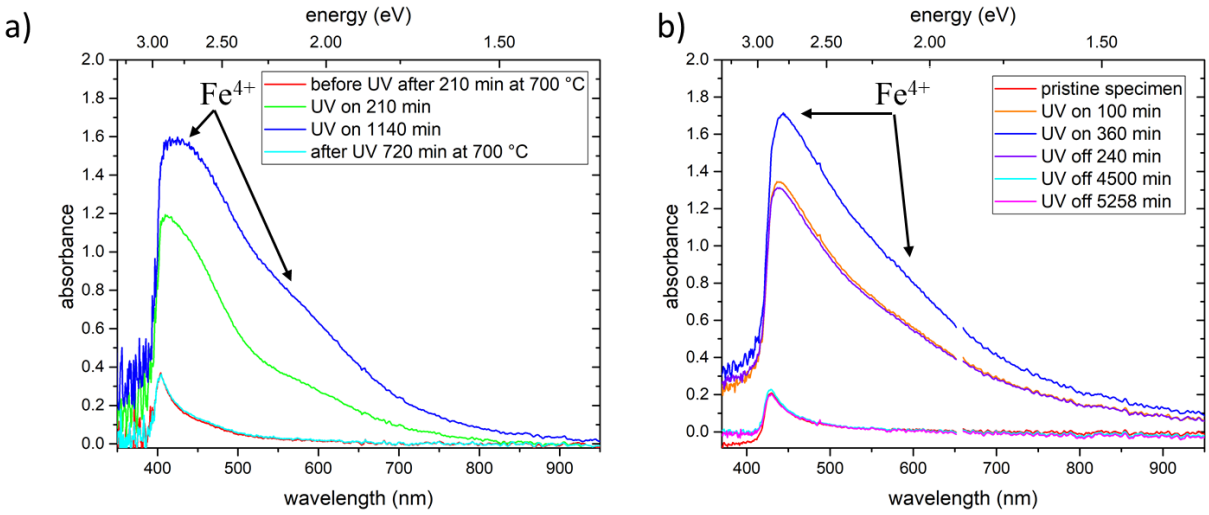

Figure 4: Absorption spectra of Fe-doped $SrTiO_3$ minus the absorption spectra of undoped $SrTiO_3$ measured **a)** ex-situ at 200 °C and **b)** in-situ at 440 °C. Several states are compared (UV blackening as well as post-annealing ("UV off") was done at 440 °C in both cases).

2.3.2 In-situ absorbance measurements

In a second approach, in-situ blackening was performed, i.e. quasi-simultaneous UV illumination and UV/Vis absorption measurement. More specific, a 360 min UV exposure at 440 °C was interrupted regularly for less than a minute to obtain absorption spectra. After this UV exposure the Fe-doped $SrTiO_3$ single crystal was equilibrated for more than 5200 min at 440 °C, accompanied by further spectroscopic measurements. As in the ex-situ experiment, an increase of the absorbance was observed under UV light (Figure 5a). The two Fe^{4+} bands, however, can no longer be distinguished at the temperature of 440 °C, even after subtracting the absorbance of a nominally undoped $SrTiO_3$ single crystal (Figure 4b). The increased absorbance vanished slowly, and almost completely, during the subsequent long re-equilibration at 440 °C (Figure 5b).

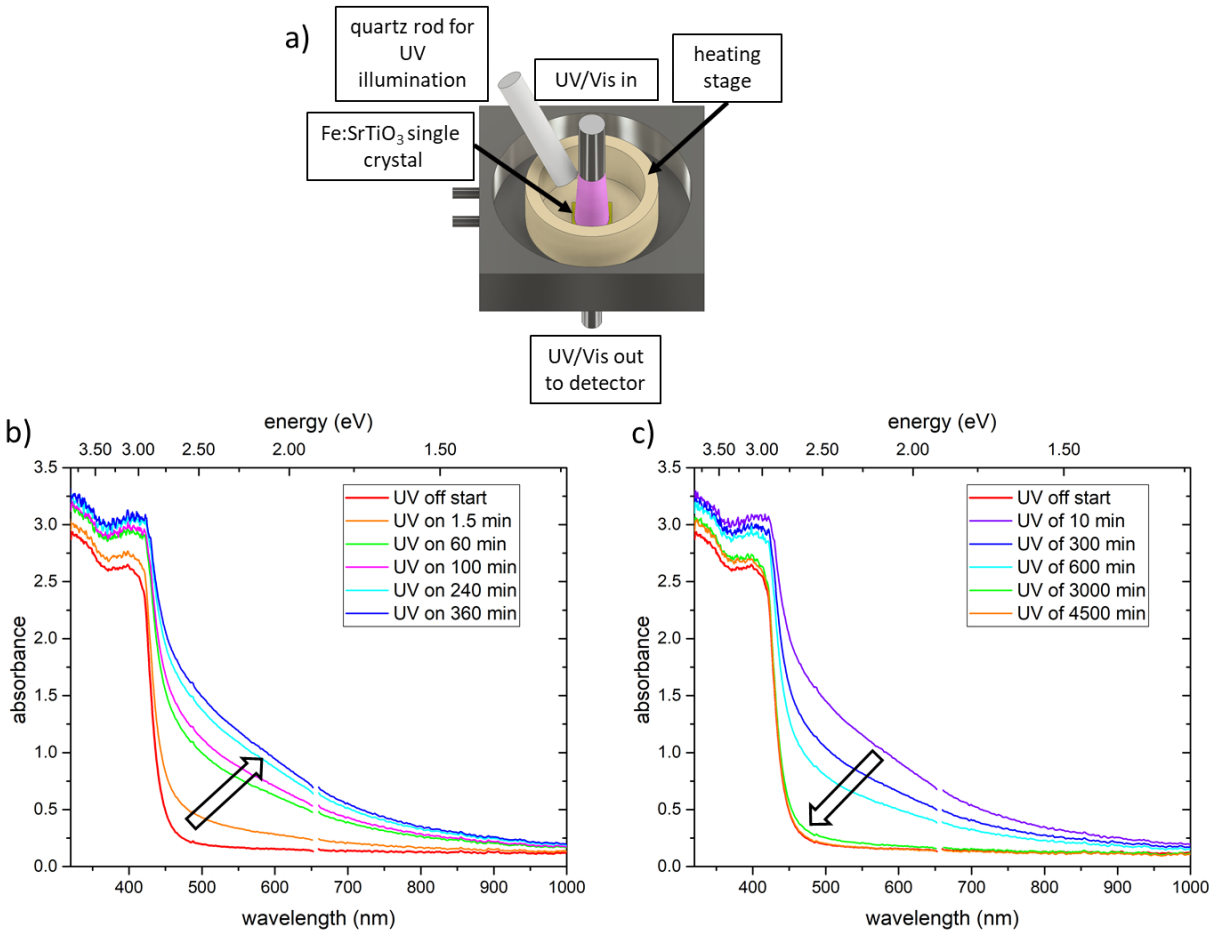

Figure 5: In-situ blackening/coloration was performed in the UV/Vis setup **(a)**. **b)** Absorption spectra at 440 °C before (red line) and during UV illumination (up to 360 min, violet line). The absorbance is increased over the whole spectral width. **c)** Absorbance of the pristine single crystal (red line) and bleaching of the blackened crystal at 440 °C, after the UV-LED was turned off. After 4500 min, the initial absorbance was nearly re-established (orange line) - further heating did not change the absorbance.

According to this interpretation, and in accordance with all obtained data, the Fe^{4+} concentration increase under UV light is caused by an oxygen uptake and the corresponding decrease of the oxygen vacancy concentration in the entire bulk of Fe-doped $SrTiO_3$. After turning the UV light off and remaining at the elevated temperature, oxygen is slowly released from the crystal, and the original optical absorption spectrum is nearly received after some time. However, this reduction step is much slower than the oxidation under UV-light. In the in-situ experiment, blackening was obtained after 360 min at 440 °C, while it took more than 4200 min at 440 °C to regain the spectrum of the pristine specimen. This is in line with earlier measurements by Merkle et al., who found that oxygen incorporation into Fe-doped $SrTiO_3$ is accelerated under UV. [45]

For oxygen equilibration of similar Fe-doped $SrTiO_3$ samples after p_{O_2} changes, surface exchange limitation is suggested below 400 °C and diffusion limitation above 500 °C.[48] However, as the oxygen uptake rate is strongly accelerated by UV, it is assumed that oxygen diffusion in the single crystal rather than oxygen incorporation determines the time dependence of establishing a new oxygen vacancy concentration and thus also of the new Fe^{4+} concentrations (c) in Fe-doped $SrTiO_3$. Accordingly, the following Equation 4 and Equation 5 for long time diffusion in a finite sample are applied to describe the obtained normalized absorbance A'. [84]

$$A' = \frac{A(t)-A(0)}{A(\infty)-A(0)} = \frac{c(t)-c(0)}{c(\infty)-c(0)} = 1 - B * exp\left(-\frac{1}{\tau^{\delta}} * t\right) \quad (4)$$

$$\tau^{\delta} = \frac{4L^2}{\pi^2 * D_O^{\delta}} \quad (5)$$

Herein B represents a prefactor, which ideally becomes $\frac{8}{\pi^2}$ for long time fits, τ^{δ} is the time constant, determined by the sample thickness (L = 0.05 cm) and the oxygen diffusion coefficient D_O^{δ}.

The normalized absorbance changes according to Equation 4 and the corresponding fits can be seen in Figure 6 for the energies related to the Fe^{4+} bands and for the point of inflexion of the entire absorption spectra. Reasonable fits are possible between 15 min and 360 min, though the B factor is between 0.57 and 0.67 instead of the ideal 0.81. This might be partly due to the fact that Equation 4 only describes the time dependence for small changes and here quite large changes take place.[84] It is still believed that an estimation of D_O^{δ} is possible from these fits. Oxygen diffusion coefficients of 1.4×10^{-7} cm^2 s^{-1} for the normalized absorbance change at 590 nm and 1.6×10^{-7} cm^2 s^{-1} at 440 nm were obtained at 440 °C. This is in the range of oxygen chemical diffusion coefficients reported for similar doped Fe-doped $SrTiO_3$ at 440 °C in 10^4 Pa p_{O_2} (about 10^{-7} cm^2 s^{-1}).[47, 85] Accordingly, this analysis further supports the interpretation of UV-induced oxygen incorporation and bulk diffusion as the origin of the observed photochromism. In Figure 3b a finite element calculation shows the oxygen diffusion profile for D_O^{δ} = 10^{-7} cm^2 s^{-1} and fast oxygen exchange after 167 min, i.e.

with about 50 % of the final concentration change already at the bottom side of the 0.5 mm thick crystal.

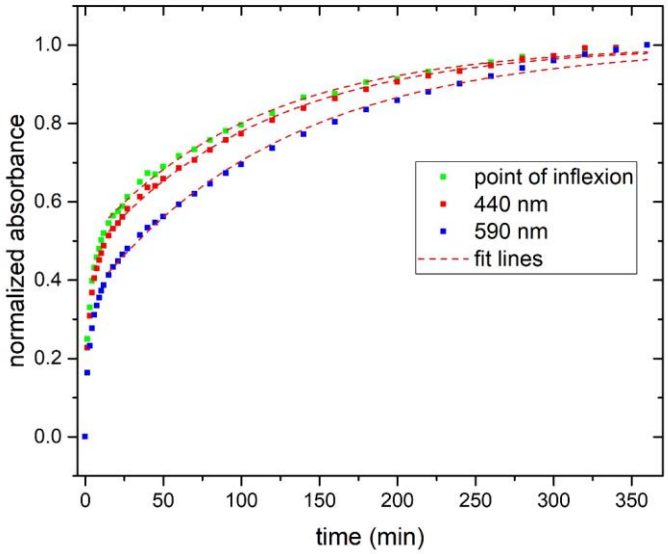

Figure 6: Evolution of the normalized absorbance A' with time under UV illumination at 440 °C; all three wavelengths (440, 590 nm and the point of inflexion at 432 nm) show a similar behavior. The long-time fits are marked with red dotted lines.

2.3.3 Analysis of the band gap energy

The photon energy (hυ) of the UV-LED used here (3.4 eV/365 nm) is larger than the indirect Fe-doped $SrTiO_3$ band gap (in the range of 3.1 eV at room temperature and below 3.0 eV at elevated temperatures, see Figure 7b). Electron excitation is thus possible from the valence band, mainly consisting of O(2p) states, to the conduction band Ti(3d) states.[8, 83] Indirect band gap energies can be estimated from Tauc plots of $(\alpha h\upsilon)^{1/2}$ against hυ; α = absorbance/L.[86] Two approaches can be found in literature: either the indirect band gap energy is referred to the intersection between a linear fit to the Tauc plot data in the band gap region and the hυ-axis[86, 87] or the band gap is deduced from the intersection between two linear fits, one to the data in the band gap region and one to the background data.[88] Both approaches are exemplified in Figure 7a for the absorption spectrum of a pristine sample at 100 °C measurement temperature. In Figure 7b the temperature dependent band gap obtained by the two methods is shown for a pristine Fe-doped $SrTiO_3$ single crystal. Bieger et al[47] described the band gap variation with temperature in 0.03-0.29 mol% Fe-doped $SrTiO_3$ by Equation 6:

$$E_g = E_g^0 - \beta * T \qquad (6)$$

Herein E_g^0 (3.3 eV) is the band gap at 0 K. The temperature coefficient β was determined to be 6×10^{-4} eV K^{-1}, the corresponding values are also shown in Figure 7b.[47] An E_g^0 of 3.31 eV (green data points in Figure 7b) or 3.37 eV (if the background was considered) and β of $8.7\pm0.29\times10^{-4}$ eV K^{-1} or $8.8\pm0.11\times10^{-4}$ eV K^{-1}, respectively were received. The background corrected band gap energies is considered as more reliable, see also below (i.e. $E_g = 3.37\ eV - 8.8 * 10^{-4}\ eV\ K^{-1} \times T$).

The same type of analysis can be applied to the spectra measured upon or after UV illumination and thus with strong Fe^{4+} bands. During UV irradiation at 440 °C, $(\alpha h\upsilon)^{1/2}$ as a function of hυ started to tilt. As a consequence, the slopes of the linear fits to the band gap region decreased, resulting in intersections with the hυ-axis at lower energies (Figure *8*). Hence, if only these fits were considered for band gap evaluation, the band gap seems to decline under UV irradiation (Figure 9). Keeping the temperature constant and turning the UV light off, these fits seem to indicate an increase of the band gap energy to the initial energy. However, if the intersection with a linear fit to the background was used for the band gap determination(cf. red and blue lines in Figure 8) the band gap did not change at all, neither under UV nor after UV. The evaluation leading to unchanged band gaps of 2.74 eV at 440 °C is considered superior. The reason is the rather small actual compositional change from filling of about 10^{18} cm^{-3} oxygen vacancies (counterbalancing the Fe^{3+} dopants), compared to the approx. 5×10^{22} cm^{-3} oxygen atoms in $SrTiO_3$. Therefore, it is expected that the relative energy of valence vs. conduction band - the band gap - to remain the same, even though the Fermi level or trapping states may vary strongly even due to such small compositional changes.

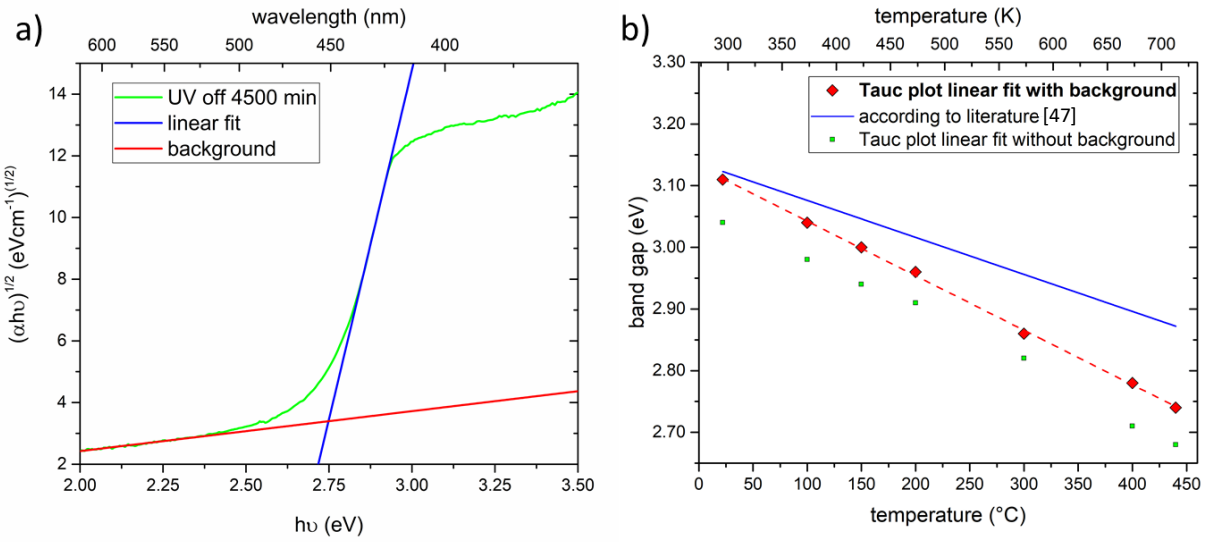

Figure 7: **a)** Tauc plot of pristine Fe-doped $SrTiO_3$ at 100 °C measurement temperature, with linear fits to the band gap region (blue line) and to the background (red line). **b)** Band gap evolution with temperature: The green squares refer to the intersection of a linear fit to Tauc plots in the band gap region and the hυ-axis and red diamonds represent the band gap energy resulting from the intersection between a linear fit to the band gap region and to the background. Blue line obtained from ref. [47].

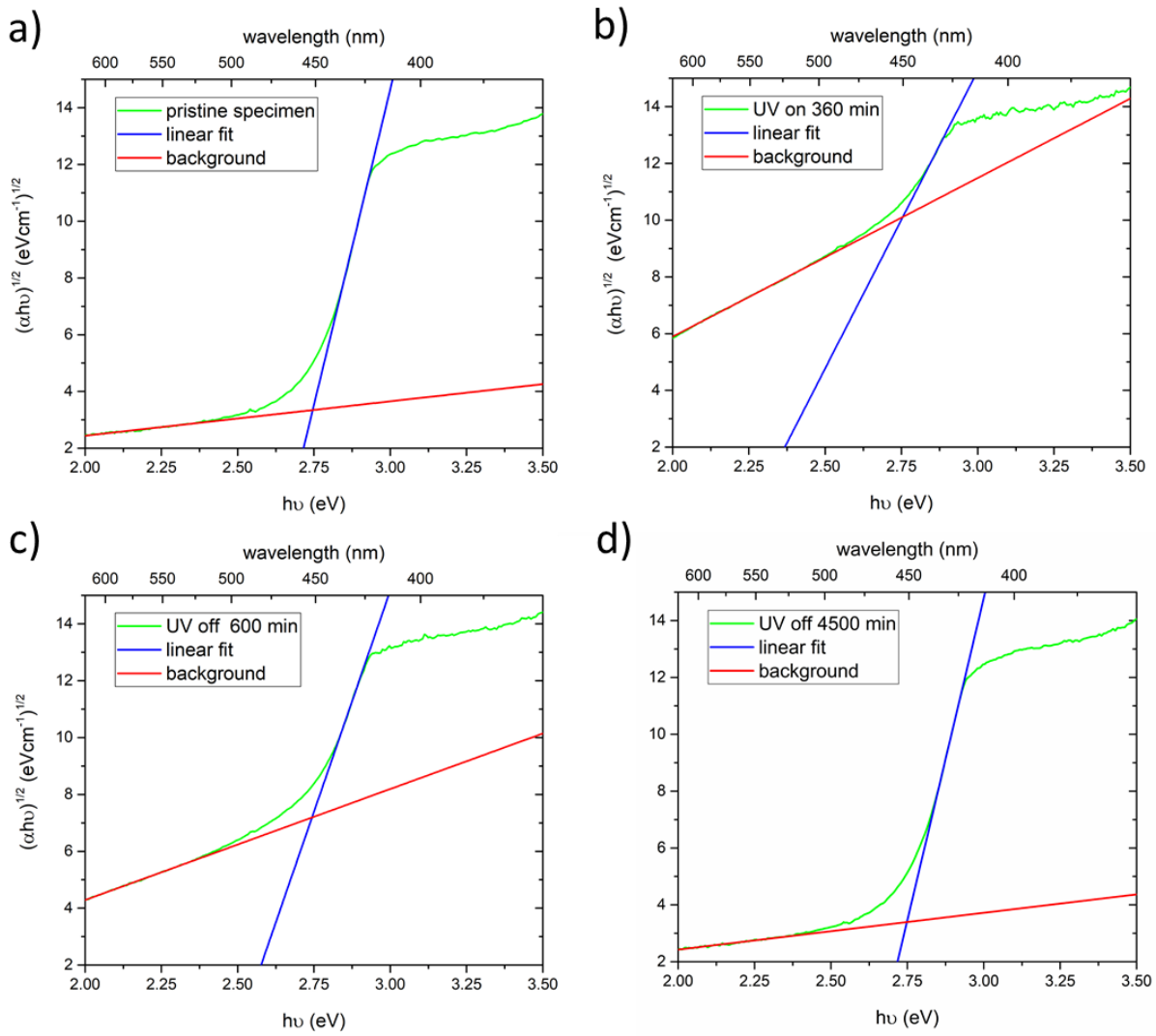

Figure 8: Tauc plots with linear fits to the band gap region (blue lines) and to the background (red lines) at 440 °C during in-situ blackening and bleaching. Spectra of the pristine Fe-doped $SrTiO_3$ crystal **(a)**, after 360 min of UV light illumination **(b)**, after the UV light was turned off for 600 min **(c)** and 4500 min **(d)**.

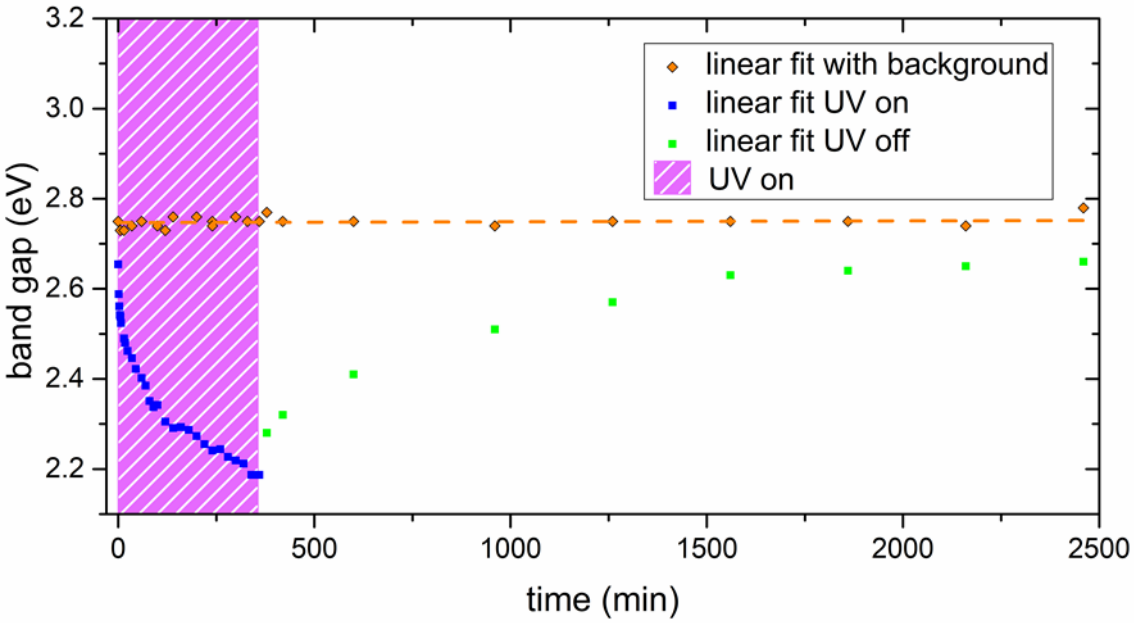

Figure 9: Band gap evolution with UV exposure at 440 °C. E_g was determined from intersections between a linear fit to the band gap region and the hυ-axis or a linear fit to the background.

2.4 Results and discussion of electrical measurements

2.4.1 *Van der Pauw* measurements – DC conductivity

According to the interpretation of the optical experiments, oxygen is incorporated under UV light. Hence, the ionic and electronic conductivity of Fe-doped $SrTiO_3$ should also strongly change. Conductivity changes were monitored either after UV exposure by DC conductivity *van der Pauw* measurements[89-92] or during illumination by in-plane electrochemical impedance spectroscopy. For *van der Pauw* measurements, pristine and blackened samples were investigated. Blackening was done under UV for 1140 min at 440 °C in ambient air. After UV irradiation four Pt electrodes were sputtered onto the corners of the crystals.

In Figure 10, an Arrhenius-type plot of the conductivity can be seen for pristine and blackened samples. Blackened Fe-doped $SrTiO_3$ exhibits a much higher DC conductivity than pristine Fe-doped $SrTiO_3$. This clearly indicates defect chemical changes upon UV irradiation. The first heating of the blackened Fe-doped $SrTiO_3$ lead to a slight decrease of the conductivity, probably due to some oxygen release. A second temperature cycle did not further modify the sample. Pristine Fe-doped $SrTiO_3$ exhibits an activation energy of 0.95 eV and the blackened specimen possesses activation energies of 0.87 eV during the first heating

period and 1.10 eV for further temperature cycles. According to the chemical defect model of Fe-doped $SrTiO_3$,[29] the hole conductivity of equilibrated Fe-doped $SrTiO_3$ should be 1.5×10^{-5} S cm^{-1} at 350 °C in air and this is very close to the values measured for the pristine sample. The activation energy of pristine and blackened Fe-doped $SrTiO_3$ largely reflects the temperature dependent hole concertation due to hole-trapping (Fe^{4+} formation) with an activation energy of 0.75-0.95 eV,[29, 47] in the investigated temperature range. a much smaller part comes from an increase of mobility of mobile holes with temperature, and therefore a total activation of approx. 1 eV is in accordance with literature. From the increased conductivity of the blackened specimen, an increased hole conductivity can be concluded. This enhanced mobile hole concentration also implies an increased trapped hole (i.e., Fe^{4+}) concentration in accordance with Equation 1 and all optical measurements. Moreover, it implies a reduced oxygen vacancy concentration and thus again supports the interpretation of, oxygen incorporation upon UV.

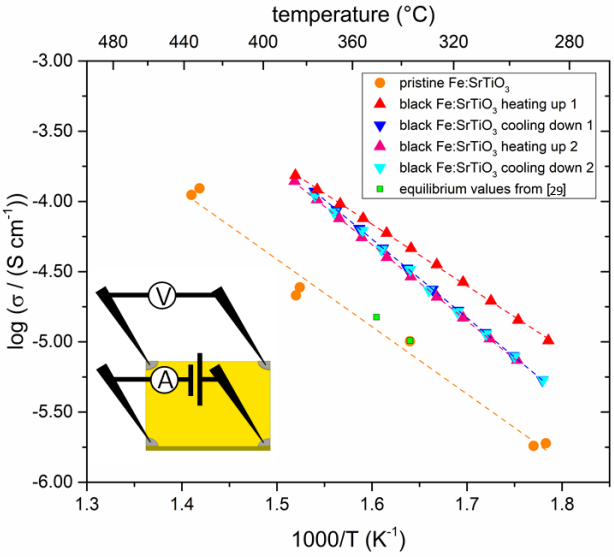

Figure 10: Arrhenius plot obtained by DC conductivity van der Pauw measurements (setup is sketched in the inset); the blackened specimen (triangles) exhibits an enhanced conductivity compared to pristine Fe-doped $SrTiO_3$ (orange dots) and the calculated values (green squares), obtained from equilibrium thermodynamic data.[29]

2.4.2 In-plane AC conductivity changes

Impedance spectra were recorded between two Pt-stripe electrodes on Fe-doped $SrTiO_3$ under UV illumination at 350 °C and 400 °C. At higher temperatures, the high frequency semicircle shifted towards even higher frequencies so that its capacitance could not be

evaluated. Spectra before and during UV exposure are shown in Figure 11. The largest arc of the spectra at high frequencies can be attributed to the bulk resistance of Fe-doped $SrTiO_3$ (in parallel to the geometric capacitance of the Fe-doped $SrTiO_3$ sample). The low frequency features were most probably caused by metal electrode related processes such as space charges. These features of the electric measurements are not further considered, as the bulk changes were predominant and sufficient to explain all optical and electric effects. Hence, a fit of the main high frequency arc using an RC element gives the total bulk resistance and this can be used to calculate the bulk conductivity. For the sake of simplicity, the two dimensionality of the current flow between the two stripe electrodes was neglected and the conductivity was calculated simply from the stripe distance and the sample thickness. The time dependence of this conductivity is analyzed in the following.

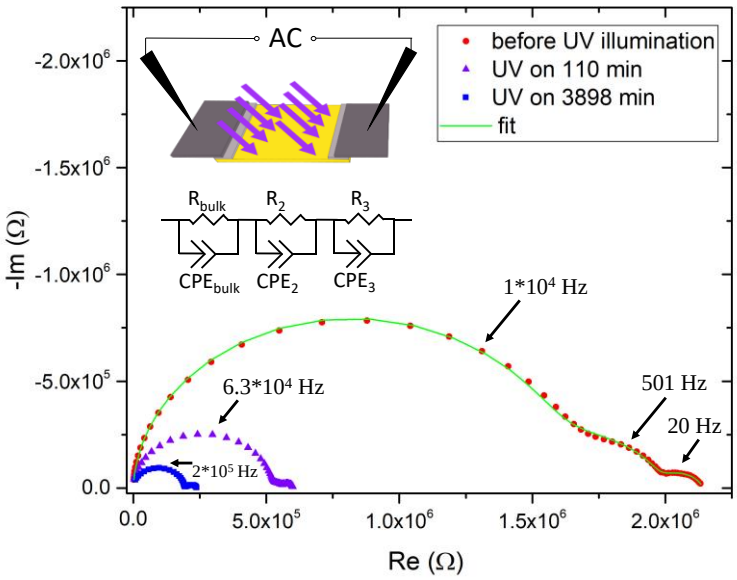

Figure 11: Impedance spectra before and during UV irradiation at 350 °C measured in the sketched manner, with a corresponding fit to the given equivalent circuit consisting of three R_{CPE} elements (CPE = constant phase element). The high frequenc arc with the largest individual resistance can be attributed to the bulk condutivity and permittivity of Fe-doped $SrTiO_3$. For higher temperatures under illumination, the first semicircle shifted to very high frequencies >10^6 Hz which were no longer accessable, and the resulting axis offset had to be used for determination of the resistivity.

The calculated in-plane conductivity of the pristine sample was about 7.4×10^{-6} S cm^{-1} at 350 °C. Upon UV light, the conductivity increased quickly by nearly a factor of four, followed by a further but much slower conductivity increase, reaching 6.2×10^{-5} S cm^{-1} after more than 4000 min. An end of this slow conductivity variation could not be observed over the experimental duration. By turning off the UV illumination, a quick and small conductivity

drop was obtained, followed by a slow decline in conductivity. It seems to level out at $1.9*10^{-5}$ S cm^{-1} but the initial value was not reached at 350 °C. A second UV irradiation cycle led to an even higher conductivity with a maximum at 8.4×10^{-5} S cm^{-1} before turning the light off, followed by a conductivity relaxation in dark. The measurement series in Figure 10a was followed by an equilibration step at 700 °C for 720 min to re-equilibrate the specimen. In a second experiment at 400 °C, the conductivity evolution showed the same trends as before. An initial conductivity of 5.6×10^{-5} S cm^{-1} and a maximum at 2.8×10^{-4} S cm^{-1} (upon UV) and 2.6×10^{-4} S cm^{-1} (after UV) were found.

The "step-like" initial conductivity changes in Figure 12 may include some photoconductivity due to the excitation of electrons from the valence to the conduction band by UV light. Moreover, some heating of the specimen by the UV irradiation contributed to the first conductivity increase. The upper limit of the temperature effect can be estimated from the first data point which was obtained from the initial impedance spectrum completed 6.5 min after switching the light on or off. From the Arrhenius-type conductivity measurements in Figure 10, the observed conductivity jump upon switching either on or off can be related to a temperature jump. The jump for turning the light off was considered to be more reliable for estimating the temperature change than the jump for switching on, as the conductivity change due to stoichiometry variation also contributed to the first data point. This change was significantly slower "off" than "on" and thus less overestimation of the temperature effect is expected when analyzing the "off" jump. Both "off" jumps in the measurement shown in Figure 12 are a factor 1.08 in conductivity or approx. 3 °C (calculating with E_a = 0.95 eV and T = 400 °C). Hence, the upper limit of UV induced temperature changes in this experiment was approx. 3 °C.

The changes following this quick jump are the true electrical counterpart to the absorbance changes upon UV irradiation. Those establish slowly under UV and relax even slower after UV exposure, i.e. on the time scale of many hours. These changes are again attributed to incorporation/release of oxygen into/out of Fe-doped $SrTiO_3$ under/after UV and thus to changes in defect concentrations and hole conductivity. One might expect that changes of the absorbance at 440 °C in Figure 5 and of conductivity at 400 °C in Figure 12b should take place on similar time scales. However, this was not the case; a steady state had not been reached in the impedance experiment. This continuing conductivity change on a long time scale was most probably simply a consequence of the stripe electrode geometry: In order to

reach the stripe electrodes the current had to flow also in Fe-doped $SrTiO_3$ beneath the stripes and thus in regions without UV illumination. Those bulk regions can also change their defect chemistry under UV due to in-plane diffusion of oxygen. However, this change takes place on a much longer time scale. This is illustrated by finite element calculations (Figure *3*e). While after 167 min the illuminated regions were already strongly filled with oxygen, the diffusion front had only slightly penetrated the region beneath the electrodes (only half a sample is shown in Figure 3d). This sample part thus still exhibited a low conductivity and contributed a substantial serial resistance. Even after 5000 min oxygen stoichiometry and thus conductivity changes were ongoing beneath the electrodes. This prolongs the conductivity changes upon UV drastically.

These effects were even aggravated by the tendency of Pt/Fe-doped $SrTiO_3$ three phase boundaries to equilibrate with the gas phase, i.e. to annihilate the UV effect. An exemplary calculated oxygen profiles can be found in Figure 3f. The concentration front reaches the region beneath the stripes even slower and this further increases the time constant. The importance of Pt/Fe-doped $SrTiO_3$ interfaces was also observed in a UV experiment with a porous Pt layer on the bottom side of a Fe-doped $SrTiO_3$ single crystal. In this case, strong blackening was not possible due to oxygen being pumped into Fe-doped $SrTiO_3$ on top and leaving the crystal again at the catalytically active, unilluminated bottom side. Accordingly, conductivity experiments with Pt electrodes on the non-illuminated sides showed qualitatively very similar results as in Figure 12 with long equilibration times for the conductivity increase alongside blackening and the decrease alongside bleaching.

Summarizing, the two retarding processes (in-plane diffusion and TPBs) strongly increased the time constant of the conductivity changes during UV illumination compared to the absorbance experiment. Owing to the same reasons also the re-equilibration after UV had to be much slower. This was further aggravated by the slower rate of oxygen release in dark compared to the oxygen incorporation upon UV. Therefore, a significant stoichiometry change was still present before the second UV illumination sets in (compare Figure 12). Only high temperature annealing would have brought the sample back to the original state. Accordingly, the initial conductivity value of the second UV exposure was higher than for the first UV exposure. The still existing “stoichiometry offset” from the first UV illumination also caused the higher final conductivities in Figure 12 reached during the second UV illumination.

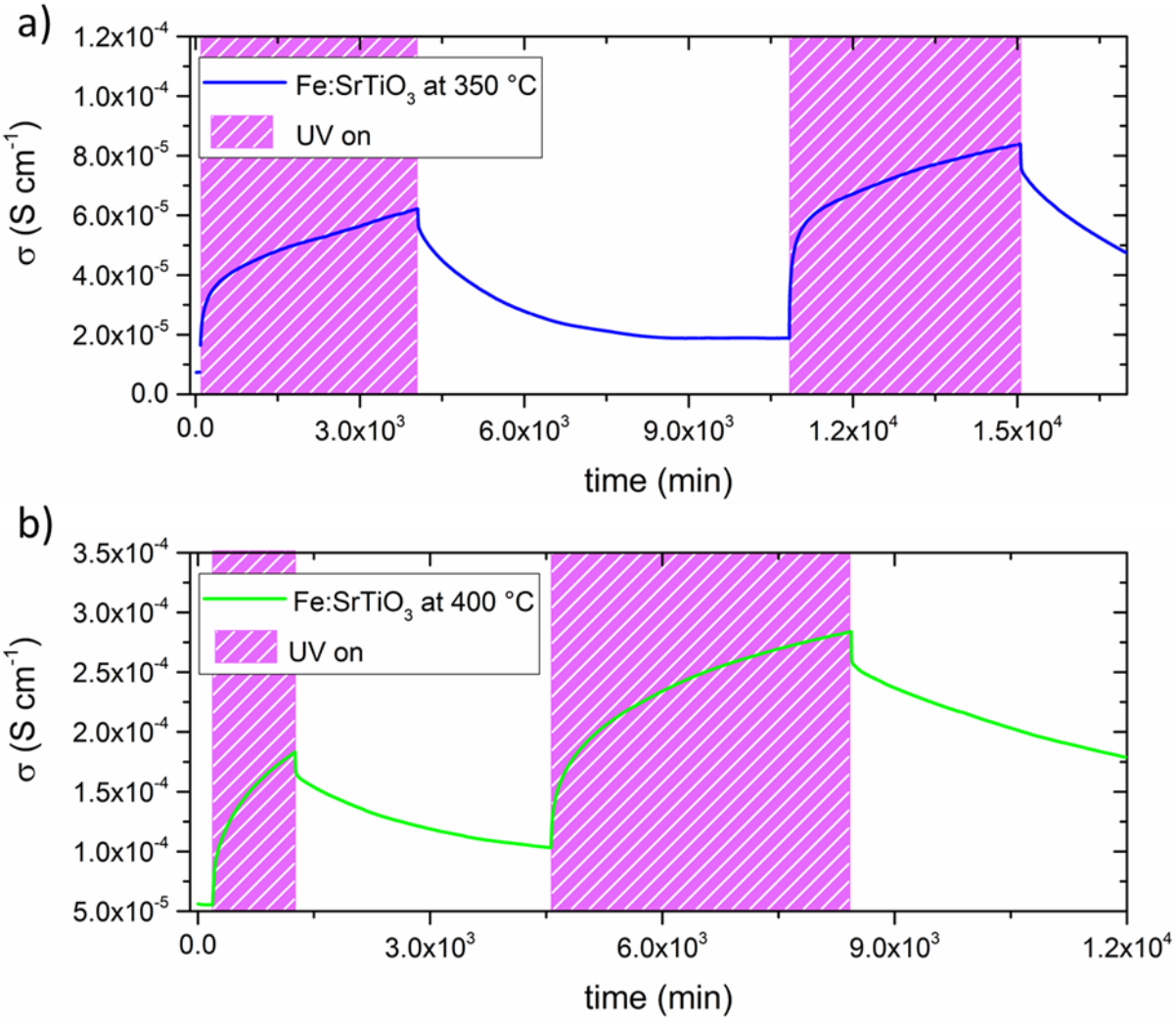

Figure 12: In-plane conductivity at **a)** 350 °C and **b)** 400 °C under UV on/off. Between these two experiments the sample was annealed at 700 °C for 12 h to bleach the blackened sample.

2.4.3 Estimating the chemical potential change caused by UV light

Finally, the defect chemical model of Fe-doped $SrTiO_3$[29] is used to get a quantitative idea of the oxygen chemical potential changes ($\Delta\mu_{O_2}$) resulting from UV light. This quantitative estimate is gained from the data of the conductivity measurements. First, the p_{O_2}, which is theoretically needed to obtain the measured in-plane conductivities of the bleached samples immediately after the conductivity drop when turning the UV light off (7.9×10^{-5} S cm^{-1} at 350 °C and 2.6×10^{-4} S cm^{-1} at 400 °C) was calculated. From the thermodynamic data of all defect equilibria and the charge carrier mobilities of ref. [29], it was found that the UV induced oxygen incorporation caused the oxygen potential (after UV illumination) to increase to a p_{O_2} of 4.3×10^{8} Pa respectively 8.4×10^{8} Pa, corresponding to a $\Delta\mu_{O_2}$ of 536 meV

at 350 °C and 618 meV at 400 °C, both compared to 2×10^4 Pa. These values are only lower estimates of the changes since obviously the steady state conductivity had not been reached in the experiments. Extrapolation of the ex-situ *van der Pauw* conductivity to 440 °C (i.e. the UV exposure condition) gives a conductivity in the 10^{-3} S cm^{-1} range and this would even indicate a p_{O_2} of 10^{11} Pa in Fe-doped $SrTiO_3$ after illumination, i.e. a $\Delta\mu_{O_2}$ of 948 meV. These chemical potential changes may translate to a cell voltage when using Fe-doped $SrTiO_3$ as a mixed conducting electrode in an electrochemical cell with an oxygen ion conducting electrolyte, cf. similar experiments with undoped $SrTiO_3$.[26]

2.5 Conclusion

UV irradiation at elevated temperatures in the range of 400 °C led to a blackening of Fe-doped $SrTiO_3$. This blackening permanently remained at room temperature and recovered only extremely slowly at about 400 °C, even at 700 °C in air it took 720 min to recover to the initial state. Characteristic changes in UV/Vis absorption spectra showed that this photochromic effect is caused by a change of the Fe^{4+} concentration and thus by an oxidation of the sample. Accordingly, an increase of the oxygen content took place in Fe-doped $SrTiO_3$ samples under UV, i.e. a decrease of the oxygen vacancy concentration. Impedance as well as *van der Pauw* measurements revealed that the (dark) hole conductivity was strongly increased after the UV exposure, in accordance with the optical studies and the suggested defect chemical changes (increase of Fe^{4+} and decrease of oxygen vacancy concentrations). The band gap energy (2.74 eV at 440 °C) did not change by UV irradiation. The time dependence of the absorbance under UV indicates a very reasonable oxygen chemical diffusion coefficient of about 10^{-7} cm^2 s^{-1} at 440 °C, which further supports the interpretation of the observed photochromism in terms of oxygen stoichiometry changes in the entire bulk of Fe-doped $SrTiO_3$. From the conductivity changes upon UV illumination an enhancement of the oxygen chemical potential by several hundred meV can be estimated. This corresponds to an (internal) p_{O_2} increase by several orders of magnitude (at least to 10^9 Pa). Altogether, it can be concluded that the observed photochromic effect can be consistently explained by oxygen stoichiometry changes under UV and thus it is very different from the common photochromic effects in oxides caused by the activation of color centers. Rather, it is the true counterpart of the known electrocoloration of Fe-doped $SrTiO_3$.

3 Mechanism of photo-ionic stoichiometry changes in $SrTiO_3$

The following chapter is part of the manuscript: “Mechanism of Photo-Ionic Stoichiometry Changes in $SrTiO_3$”, which is currently under review at Physical Chemistry Chemical Physics.[93]

3.1 Introduction

In a next step nominally undoped $SrTiO_3$ single crystals were investigated in air between 280 and 450 °C. Again in-plane conductivity measurements by impedance spectroscopy were used to monitor the time dependence of UV induced defect chemical changes. As an additional tool, X-ray absorption spectroscopy (XAS) was employed to measure the changes in the Ti-O chemical bonding[94-96] caused by UV light and gain information on the Ti valence state.[97] Based on these measurements a mechanistic model was developed which can serve as the basis for explaining UV-driven compositional bulk changes not only for the specific case shown here but also for the entire field of photo-ionics. In particular, a concept of quasi-chemical potentials of components (here oxygen) in accordance with the quasi-Fermi levels in illuminated semiconductors is introduced. It is shown how this concept can be used to understand the interaction of light and composition of semiconducting materials with a certain stoichiometric width.

3.2 Experimental section

3.2.1 Pre-treatment of $SrTiO_3$ single crystals and conductivity measurements

Undoped $SrTiO_3$ single crystals (100) (CrysTec GmbH, Germany; 5×5×0.5 mm^3) were used in this study. In earlier measurements based on ICP-MS and Positron Annihilation Lifetime Spectroscopy (PALS), Ti vacancies were identified as predominant acceptor-type dopants in these crystals (6-8 ppm, 1.0-1.3×10^{17} cm^{-3}, respectively).[98] Firstly, all investigated specimens were cleaned in an ultrasonic bath with ethanol for approx. 20 min. Subsequently, the samples were annealed at 900 °C for 12 h at ambient air in order to reduce surface defects. Thereafter the specimens were cleaned again with ethanol. Impedance spectroscopy was then employed to measure the impact of UV illumination on $SrTiO_3$. Sketches of the set-up

and the position of the electrodes are given in Figure 13. Pasted Pt stripes on back side of the samples were used for measuring the in-plane conductivity. Impedance spectra were recorded from 1 MHz to 1 Hz (with 10 points/decade) at an AC voltage of 0.1 V using Alpha-A High Performance Analyzers (Novocontrol Technologies, Germany). Subsequently, fitting was performed by means of Zview (Scribner Associates Inc., USA). A flame polished quartz rod pressed on the single crystals' front side acted as light guide. For illumination, high performance LEDs (LED Engin, USA) with wavelengths of 365 nm (UV), 523 nm (green), and 660 nm (red) LEDs were used. The radial outputs of the LEDs were in the range of 2.60-2.90 W, of which approx. 0.06 W reached the specimens, as measured by a FieldMaxII-TOPLaserTM Power/Energy Meter (Coherent Inc., USA). Measurements were performed at 280-450 °C in ambient air.

After any experimental series under UV, each sample was heated to 700 °C in air and kept at this temperature for a minimum of 6 h to re-establish a defined defect chemical state. Subsequently the single crystals were cooled to the temperature of the measurement. There the specimens were equilibrated for another 6-12 h.

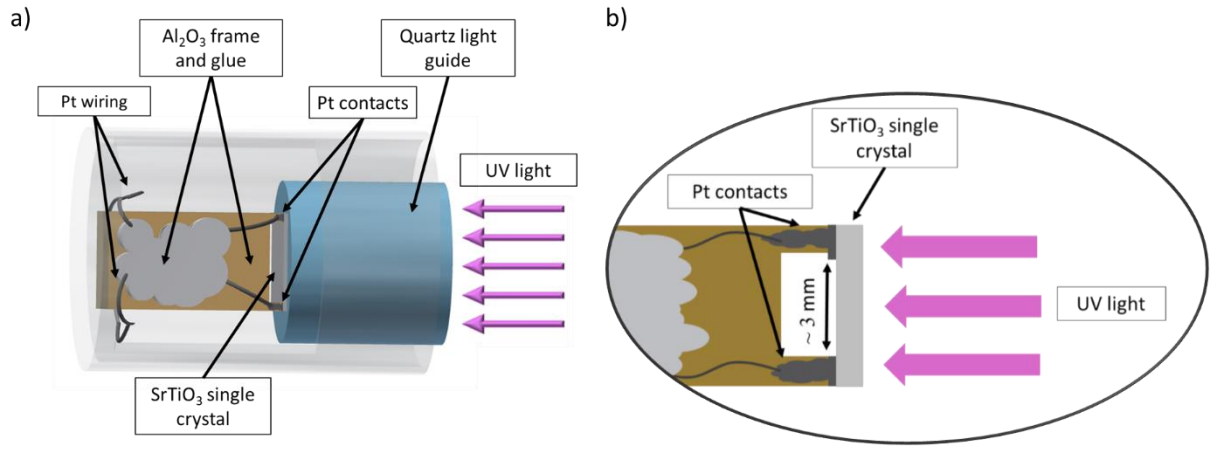

Figure 13: **a)** Sketch of the in-plane conductivity measurement set-up. The samples were attached to a corundum frame and contacted by Pt electrodes at their back sides. The irradition took place perpendicular to the direction of the impedance measurement and UV light was conducted by a quartz light guide in a quartz casing. **b)** Close-up view of the sample in the measurement set-up. Pt contacts were directly connected to the impedance analyzer via Pt wires.

3.2.2 X-ray absorption spectroscopy

In order to investigate the occurring redox processes, XAS was performed at the Surfaces/Interfaces: Microscopy (SIM) Beamline at the Swiss Light Source (SLS) (Paul Scherrer Institut, Switzerland). The Ti-$L_{2,3}$ edges (455 - 480 eV) and the O K-edge (525 - 585 eV) of two $SrTiO_3$ single crystals were measured in the total electron yield mode, using linearly polarized X-rays. The intensity of the incoming beam was normalized using a gold grid placed upstream to the samples. The nominal photon energy resolution is of the order of 100 meV, although typically one can resolve smaller changes in position energy of sharp spectral features. One specimen was equilibrated at 450 °C and subsequently illuminated with UV light for 19 h at 450 °C in ambient laboratory atmosphere. The sample was then rapidly cooled to room temperature still under illumination. The second sample was prepared in the same way, with the difference of not being illuminated. Subsequently, four different spots on each single crystal were measured. Spectra were analyzed using the Athena program.[99]

3.3 Results and discussion

3.3.1 In-plane conductivity measurements in air

The time dependent in-plane conductivity under and after UV illumination was deduced from the measured impedance spectra. Examples of in-plane impedance spectra before, during, and after UV exposure are presented in Figure 14. The dominating high frequency arc of the spectrum represents the bulk conductivity of the single crystal, in accordance with its bulk-like capacitance. The low frequency features are attributed to the $SrTiO_3$|electrode interface (porous Pt). A more detailed discussion of such spectra is given elsewhere.[100] Here, we focus entirely on the first feature, i.e. the (in-plane) $SrTiO_3$ bulk resistance in parallel to the geometrical capacitance of the sample. This was fitted to a resistor (R) in parallel with a constant phase element (CPE), an additional R|CPE element for the electrode features were also included, if required to model the data. A differentiation between bulk electronic and ionic conductivity was not feasible, because no ionic contribution could be extracted from the obtained impedance data. Defect chemical calculations suggest that between 280 and 450 °C in air hole conductivity is by a factor of 28 to 55 larger than the ionic conductivity before illumination and even more dominating under illumination and thus in our point of view the ionic contribution is negligible. The effective bulk conductivity was calculated from the

resistance by using the distance between the two stripe contacts on the back side of the sample (approx. 3 mm), the sample height (5 mm), and the sample thickness (0.5 mm). Deviations resulting from the two-dimensional current flow for the given electrode geometry were thus neglected.

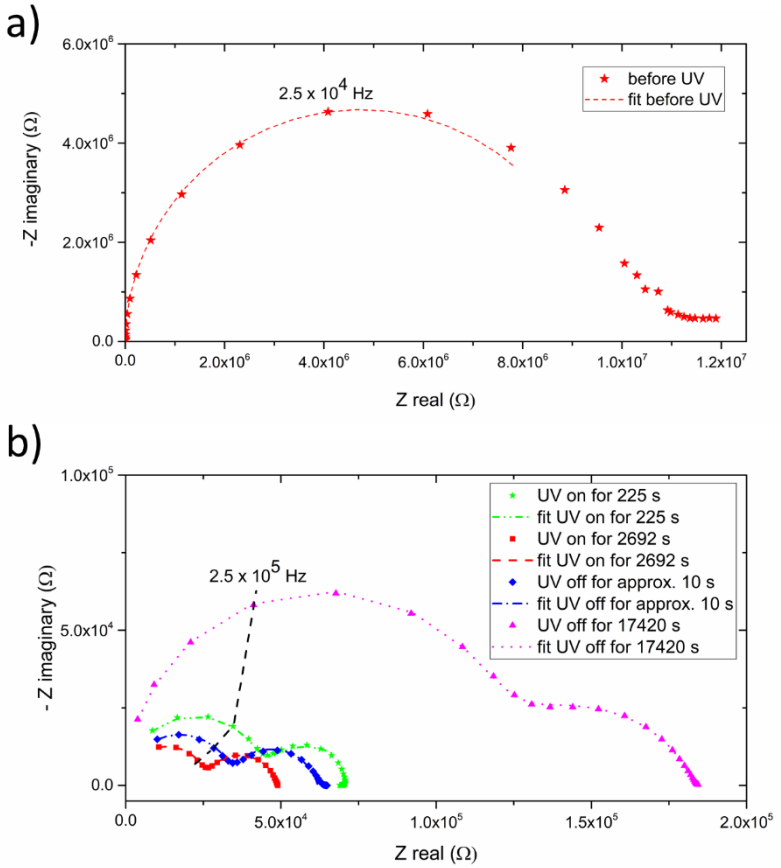

Figure 14: **a)** In-plane impedance spectra of an $SrTiO_3$ single crystal before UV irradiation at 350 °C and the obtained fitting curve. For the obtained fit one R/CPE element was used. A bulk resistance of more than 9.0×10^6 Ω is obtained. **b)** When UV light was turned on, the resistance decreased to below 2.6×10^4 Ω in approx. 45 min (red squares). After the UV light was turned off, the conductivity slowly relaxed back, but even after approx. 5 h it was still almost two orders of magnitude higher than before UV light irradiation.

The different scale of the spectra in Figure *14*a,b already indicates that huge resistance changes take place under UV illumination and after the light was switched off. The measured averaged bulk conductivities for a typical measurement series (UV on, UV off, temperature variation) are shown in Figure 15. Evidently, UV irradiation enhances the in-plane bulk conductivity of $SrTiO_3$ by more than three orders of magnitude at 280 °C and more than two orders of magnitude at 350 °C in air. Please note that for Figure 15 full impedance spectra

were measured, resulting in a very limited time resolution (ca. 3 min.). It is shown below that the initial increase was largely continuous rather than step-like. Immediately after switching off UV illumination, the conductivity remained high, and the following conductivity decrease was much slower than the increase under UV light, taking many hours to days to reach a constant conductivity.

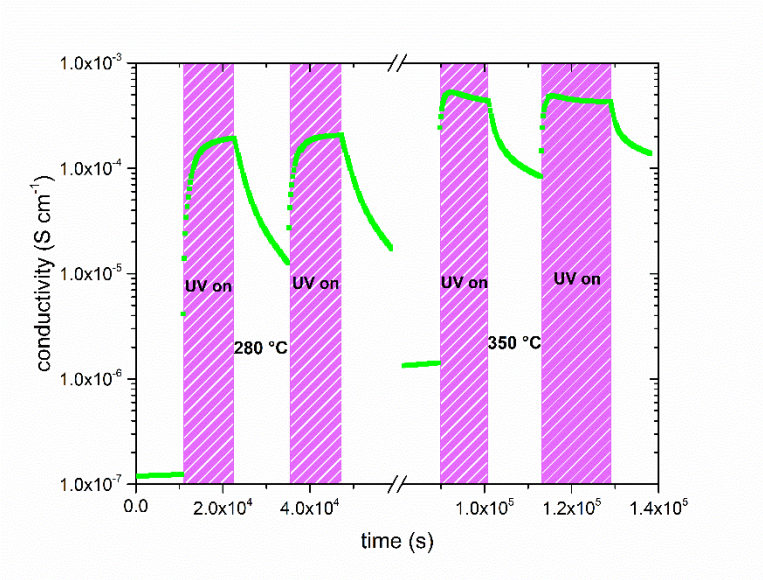

Figure 15: In-plane conductivity of $SrTiO_3$ before, under, and after UV illumination in air at 280 °C and 350 °C. The UV LED was turned on and off twice at each temperature. After the measurements at 280 °C the specimen was heated up to 700 °C in order to release most of the incorporated oxygen (broken time scale).

To show that UV light excitation rather than simple sample heating were responsible for the main effects, also illumination by red and green light was performed. This light was at least partially absorbed since 40 % of the back side was covered by Pt paste electrodes. For red and green light illumination only very minor effects were found, see Table 1. Possible heating effects were quantified by illuminating an YSZ single crystal with Pt paste top and bottom electrodes and measuring the change of the across-plane resistance in the same set-up under UV light. Here, a temperature increase of only 3 - 4 °C was found (see supporting information Figure 16) which cannot explain the large conductivity increase of $SrTiO_3$ under and after UV light irradiation.

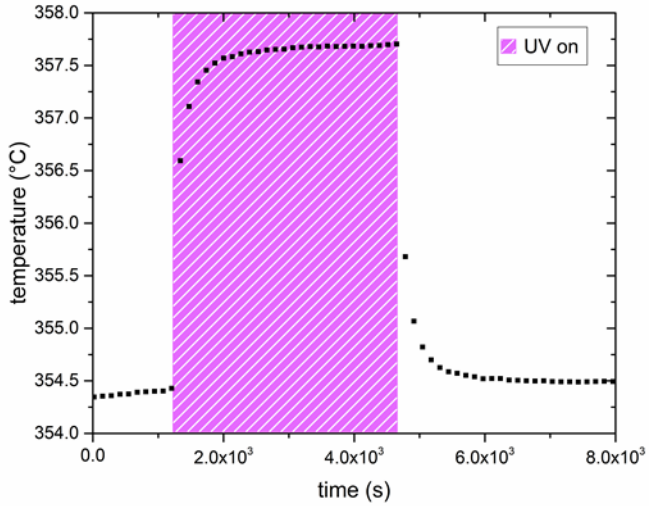

Figure 16: Temperature increase of a 5x5x0.5 mm^3 YSZ single crystal, caused by UV illumination at approx. 354 °C in air.

Table 1 provides a summary of the conductivity changes due to illumination with UV, red and green light in air at 280, 350, and 450 °C. Since conductivities before illumination are highest at 450 °C and the conductivity under UV irradiation is only moderately temperature dependent, relative changes induced by UV irradiation become smaller the higher the temperature. The time dependence of the conductivity during and after UV illumination with partly very long relaxation times indicates that we do not face a simple direct photoelectric effect (photo-conductance) which takes place typically in the µs range.[101] Rather, slow defect chemical diffusion processes in the bulk of $SrTiO_3$ are involved in these conductivity shifts, as already shown for Fe-doped $SrTiO_3$.[75] Photoconductivity due to the formation of electron-hole pairs near the surface cannot explain the huge observed changes.

Table 1: Summary of the obtained in-plane conductivity changes under UV, red, or green light at 280, 350, and 450 °C in air.

Temperature (°C)	Before UV (S cm^{-1})	Under UV [S cm^{-1}]	Under UV/before UV	Before red or green light (S cm^{-1})	Under red or green light (S cm^{-1})
280	1.2×10^{-7}	2.1×10^{-4}	1750	1.3×10^{-7}	1.7×10^{-7} (green LED)
350	$0.9\text{-}1.4\times10^{-6}$	5.3×10^{-4}	400-600	2.0×10^{-6}	2.2×10^{-6} (green LED)
450	4.9×10^{-5}	5.3×10^{-4}	11	3.0×10^{-5}	3.1×10^{-5} (red LED)

Since recording the full spectra (e.g. from 10^6 - 1 Hz with 10 points/decade) takes about three minutes, changes within the first minute(s) after the UV light was turned on/off are not properly resolved in Figure 15. This can be improved by measuring only three relevant frequencies within the high frequency semicircle, which takes 8 - 10 s. The bulk semicircle can be reconstructed using each of the three recorded data points and the origin of the Nyquist plot. The three resulting resistances were then averaged (standard deviations typically 0.2 - 2.0 %) and the conductivities were calculated. Data resulting from such experiments at 350 and 450 °C, respectively, are displayed in Figure 17.

It can be clearly seen that we largely face continuous long-time effects rather than step like changes (see Figure 17a for approx. 600 s illumination time). Moreover, conductivity changes upon UV illumination were much faster than those measured after the UV light was turned off. The velocity of the changes increased strongly with temperature. This supports the interpretation of ion diffusion-related defect chemical processes taking place upon UV irradiation. In Figure 17b, short illumination times of 150 s are displayed, followed by 1060 s relaxation time in dark. Owed to the very different time constants of changes for UV on and off we found that UV light subsequently pumped the conductivity up, again in accordance with diffusion related defect chemical phenomena in $SrTiO_3$. In these measurements a small decrease of the conductivity, immediately after the UV light was turned off, can be seen. This fast step might indeed come from either photoconductivity or heating/cooling effects,

while the long-time trend is caused by diffusion or oxygen exchange at the surface.

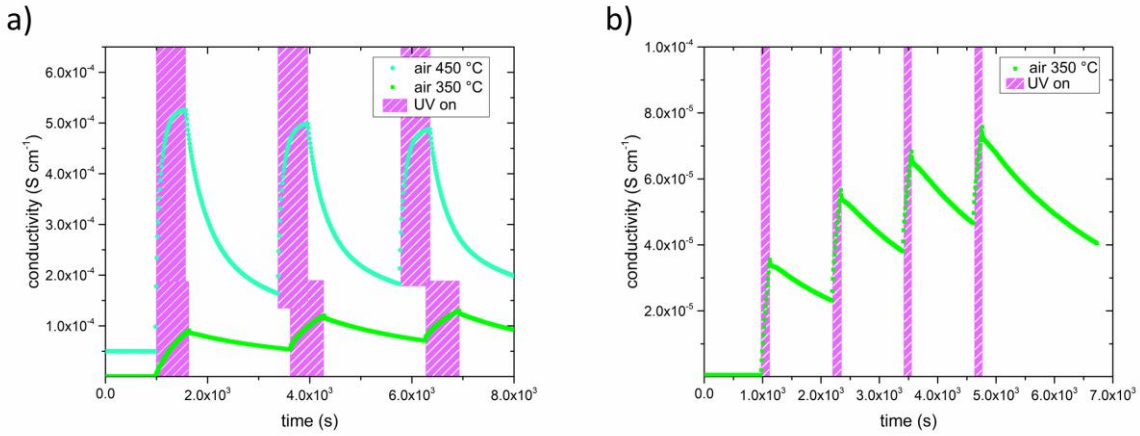

Figure 17: Impedance measurements with increased time resolution at only three frequencies to investigate the fast conductivity changes of $SrTiO_3$ shortly after the UV LED was turned on or off. **(a)** At 350 °C and 450 °C different time constants of the observed effect became visible. **(b)** Series with short illumination periods (150 s). Each illumination led to a further conductivity increase.

More specifically, in accordance with the explanation of similar experiments on Fe-doped $SrTiO_3$,[75] the conductivity changes are attributed to defect chemical changes triggered by UV-accelerated oxygen incorporation into the crystal. By means of bulk diffusion this additional oxygen incorporation reduces the oxygen vacancy concentration, not only in the illuminated part of the sample (a few µm at most) but in the entire bulk. Hence, the oxygen chemical potential of the crystal strongly increases. In air, nominally undoped $SrTiO_3$ is a slightly p-doped material due to metal vacancies, with predominant hole conduction in our temperature range. This hole conductivity increases with increasing oxygen chemical potential and thus UV driven oxygen incorporation ultimately leads to a hole conductivity increase as seen in our experiments. Formation of bulk oxygen vacancies instead of the suggested annihilation of vacancies can be ruled out, because a lowering of the effective p_{O_2} would reduce the (hole) conductivity. In the next section a more detailed model describing the phenomena taking place in $SrTiO_3$ upon UV illumination is introduced.

3.3.2 Quantitative analysis of the time dependent conductivities

Assuming the validity of this mechanistic explanation given above, one may use the time dependent conductivity to calculate the chemical diffusion coefficient of oxygen in these samples. This was done for measurements where almost constant conductivity values were reached under illumination, see Figure *18*. The solution of Fick's laws of diffusion[84, 102-104]

$$A = \frac{\sigma(t) - \sigma(0)}{\sigma(\infty) - \sigma(0)} = 1 - \frac{8}{\pi^2} \sum_{i=0}^{i=\infty} \frac{1}{(2i+1)^2} * \exp\left(\frac{-t}{\tau} * (2i+1)^2\right) \quad (7)$$

known from conductivity relaxation experiments after p_{O_2} changes was used for quantification. In Equation 7 σ(0) denotes the initial conductivity, σ(∞) the final conductivity, A is the normalized conductivity change, and t the time in seconds. The time constant τ is given by Equation 8:

$$\tau = \frac{4\,a^2}{\pi^2 * D_O^\delta} \quad (8)$$

where a is the sample thickness and D_O^δ the oxygen chemical diffusion coefficient. In this analysis several approximations were required: Firstly, oxygen exchange at the thin sides and the back side of the specimens was neglected. Secondly, a constant diffusion coefficient was assumed, which is an approximation given the gradual change of the oxygen chemical potential. And finally, any kinetic limitation by surface reactions was neglected.

The full-lines shown in Figure 18 are non-linear least square fits to the conductivity relaxation data. They describe the time dependence of the normalized in-plane conductivity changes under UV light illumination in air at 350 and 450 °C. From the fit, we obtained oxygen chemical diffusion coefficients of 6.3×10^{-7} cm^2 s^{-1} at 350 °C and 1.0×10^{-5} cm^2 s^{-1} at 450 °C, respectively. Assuming diffusion limitation this means that the oxygen incorporation coefficient under UV illumination $k_{O,in}^\delta$ is at least $10\times D_O^\delta/a$, i.e. larger than 2×10^{-3} cm s^{-1} at 450 °C.

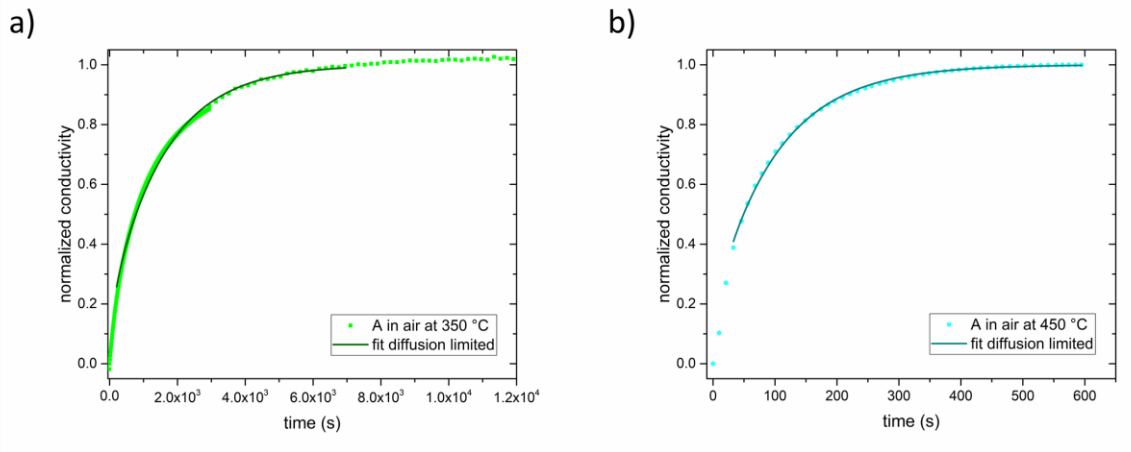

Figure 18: Normalized in-plane conductivity changes (A) under UV illumination at 350 °C **(a)** and 450 °C **(b)** in air. The fits (solid lines) were obtained using Equation 7 for diffusion limitation.

We can compare the measured conductivities and chemical diffusion coefficients with the values expected from the known defect chemical model of exactly this kind of undoped $SrTiO_3$ single crystals.[98] From the highest conductivity measured upon UV illumination and the defect chemical model the effective p_{O_2} present in the sample upon and immediately after UV irradiation can be estimated. Values of about 10^6 bar at 350 °C and 10^3 bar at 450 °C were obtained. This increase of the internal oxygen chemical potential by many orders of magnitude is in line with the 10^4 bar measured for Fe-doped $SrTiO_3$ at 440 °C under UV illumination. From the defect chemical model mentioned earlier a comparatively weakly p_{O_2}-dependent oxygen chemical diffusion coefficient with values at 350°C between 7.6×10^{-6} $cm^2\ s^{-1}$ at 0.21 bar and 2.7×10^{-6} $cm^2\ s^{-1}$ at 10^6 bar is estimated as well. At 450°C and 10^3 bar, an oxygen chemical diffusion coefficient of 8.5×10^{-6} $cm^2\ s^{-1}$ is predicted. This means we have an excellent agreement with the experiments at 450 °C and still a reasonable agreement at 350 °C, particularly when taking into account the approximations needed for the analysis.

The UV induced effects may also be compared with those reported in ref. [26] for the same kind of undoped $SrTiO_3$ single crystals but with a bottom layer of YSZ and measured across plane. There, a conductivity increase upon UV illumination at ca. 360 °C to a value of 2×10^{-5} S cm^{-1} is found. This is less than observed in this study, but also the light intensity was approx. 10 times lower in ref. [26], where parts of the surface were covered by an electrode. Owing to the YSZ bottom layer it was possible in ref. [26] to transpose the corresponding chemical potential change in the $SrTiO_3$ single crystal to a Nernstian voltage (electromotive force) and

the resulting value in the 100 mV range is well in line with the conductivity results, thus further supporting the interpretation of oxygen incorporation under UV irradiation.

Finally, we briefly discuss the much slower oxygen release after UV irradiation. Assuming a similar effective oxygen chemical diffusion coefficient for oxygen incorporation under UV light and oxygen release after UV exposure, it has to be concluded that the slower relaxation is due to a much slower surface reaction, i.e. much slower oxygen release in dark after UV irradiation than oxygen incorporation under UV illumination. Accordingly, release of oxygen is certainly surface limited in the conducted experiments. This is also in agreement with the measurements in ref. [45] where the UV dependence of the surface exchange kinetics of oxygen in Fe-doped $SrTiO_3$ was analyzed. There, it was shown that oxygen incorporation is strongly accelerated by UV light (due to the much higher electron concentration in the conduction band) while oxygen release is hardly affected. The slow kinetics of oxygen release reaction also justify the assumption that oxygen release on the dark back side of the sample plays a minor role and was neglected in the analysis of the changes under UV irradiation. A rough estimate of a surface release coefficient could be made from the conductivity relaxation at 450 °C after UV illumination using Equation 9. $\sigma(\infty)$ was fitted as well, since the equilibrium value could not be reached, after the UV light was turned off.

$$A = \frac{\sigma(t)-\sigma(0)}{\sigma(\infty)-\sigma(0)} = 1 - exp\left(\frac{-k^{\delta}_{O,out}}{\frac{a}{2}} * t\right) \quad (9)$$

with $k^{\delta}_{O,out}$ denoting the oxygen release coefficient. A value in the range of 5×10^{-5} cm s^{-1} was found, though the fit quality was moderate, it did not cover the long-term changes adequately (see Figure 19), possibly due to continuous and severe changes of $k^{\delta}_{O,out}$ during the measurement itself.

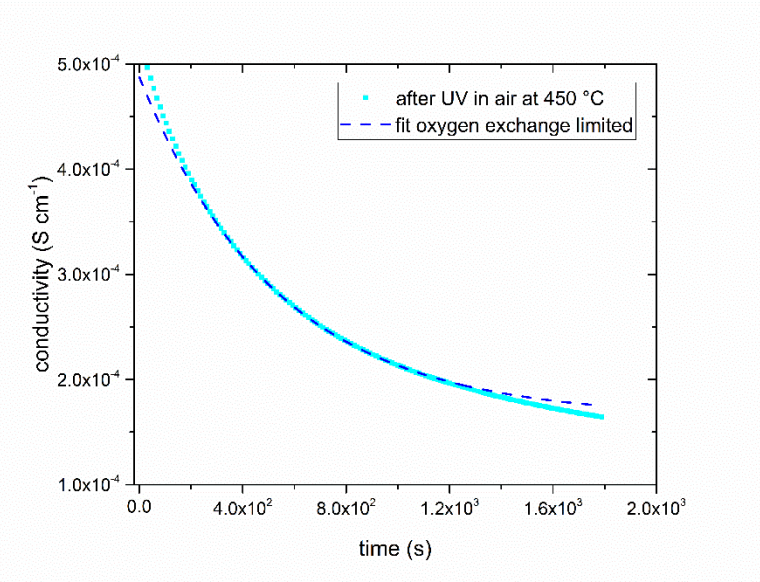

Figure 19: Conductivity decrease after UV irradiation was turned off at 450 °C in air. The shown fit is considering an oxygen surface exchange limitation and allows a rough estimation of the surface exchange coefficient.

3.3.3 X-ray absorption measurements of pristine and illuminated $SrTiO_3$ single crystals

In order to further investigate the processes taking place under UV irradiation in air, we carried out XAS measurements on two samples annealed at 450 °C for 19 h, one in darkness and the other under UV illumination. Here, we explore the fact that in $SrTiO_3$ the Ti-O bond is partly covalent, such that the free charge carriers associated to oxygen vacancies locally modify the Ti electronic state.[105, 106] Absorption spectra of the Ti $L_{2,3}$-edge are displayed in Figure 20a. In general, they correspond to electron transitions from the Ti(2p) to the Ti(3d) states and three regions can be distinguished (pre-edge (A, B), the transition from $2p_{1/2}$ (L_2) (E, F) and $2p_{3/2}$ (L_3) (C, D)) core levels.[97, 107, 108] The splitting of each edge into two peaks is caused by the energy difference in the t_{2g} and e_g orbitals. The peak C exhibits no splitting which indicates that the Ti ions are in a perfect octahedral environment.[96, 109] Moreover, the intensities reflect the density of unoccupied states, hence from the ratio of the t_{2g} (C, E) to the e_g (D,F) peaks the Ti occupancy and therefore the amount of oxygen vacancies and their change can be derived. Peaks were fitted using pseudo-Voigt functions (dashed green and pink lines in Figure 20a) and an arc tangent for the non-resonant background. When comparing the single crystal equilibrated in the dark to the one exposed to UV light, t_{2g} to e_g edge ratio changes from 0.41 to 0.46 for the Ti L_3-edge (higher value after UV) and from 0.52 to 0.53 at the Ti L_2-edge are found. This indicates an increase of the titanium valency caused

by the filling of oxygen vacancies[108] and thus the formation of electron holes. Moreover, an energy shift of roughly + 0.1 eV is found in the spectrum of the illuminated specimen compared to the pristine sample, which is another strong indication for oxidation.[97, 110] In Table 2**,** the peak positions, areas, and the area ratios obtained by fitting are given.

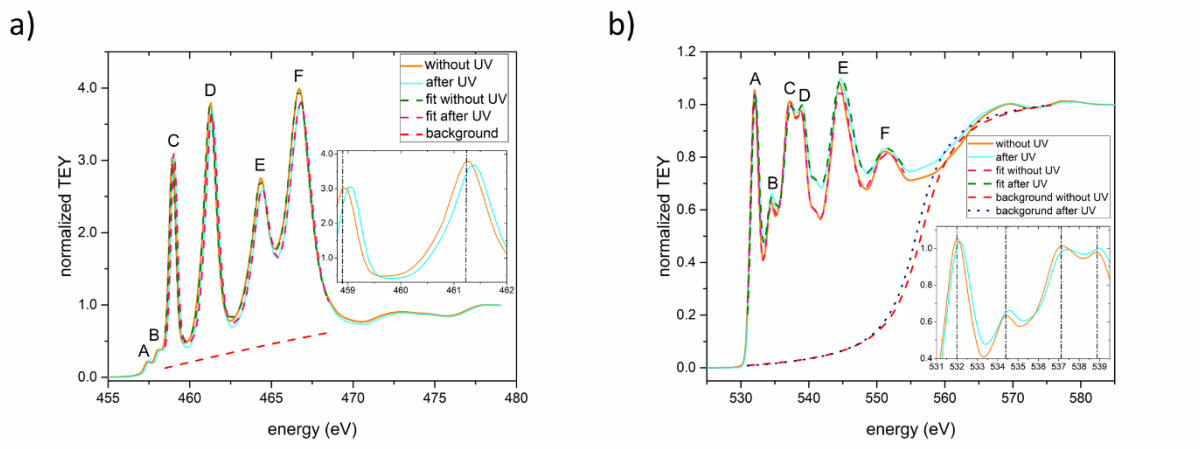

Figure 20: **a)** Ti $L_{2,3}$-edge without (solid orange line) and after (solid cyan line) UV irradiation for 19 h at 450 °C. A shift to a higher energy after UV illumination can be seen. Pre-edge features were excluded from the fits (dashed lines). **b)** XAS measurement of the O K-edge pristine (solid orange line) and UV illuminated (19 h at 450 °C) (cyan solid line) $SrTiO_3$ single crystals. Dashed lines represent the executed fits. Four different areas of the $SrTiO_3$ single crystals were measured and the TEY obtained.

Table 2: Summary of the fitted peak centers, areas, and calculated t_{2g}/e_g from the Ti $L_{2,3}$ edge of a pristine and an UV illuminated $SrTiO_3$ single crystal.

Peak	Peak center (eV)	Area	t_{2g}/e_g	
C	458.9	1.65 ± 0.04	0.41	non-illuminated
D	461.2	4.05 ± 0.07		
E	464.3	3.89 ±0.12	0.52	non-illuminated
F	466.7	7.46 ± 0.14		
C	459.0	1.74 ± 0.04	0.46	illuminated
D	461.3	3.81 ± 0.08		
E	464.4	3.63 ± 0.12	0.53	illuminated
F	466.8	6.90 ± 0.16		

In Figure 21b the O K-edge X-ray absorption spectra exhibit six main features, marked from A to F. These originate from O(1s) core electron transition into O(2p) orbitals hybridized with Ti(3d), Ti(4sp), Sr(4d), or Sr(5p) orbitals. A denotes the peak related to the O(2p)-Ti(3d) t_{2g} states and B the O(2p)-Ti(3d) e_g states. C and D represent the transition into the O(2p)-Sr(4d) orbital. Peak E is caused by an electron excitation into the O(2p)-Sr(5p) orbital and F by an electron excitation into the O(2p)-Ti(4sp) orbital. [36, 108, 111]

The O K-edge spectrum measured from the illuminated sample is shifted by approx. 0.1 eV to higher energies and the intensity is in general slightly increased compared to the spectrum of the non-illuminated specimen. Due to the partial covalent nature of the Ti-O bond, these changes are attributed to oxygen incorporation. On the other hand, the evaluation of the e_g/t_{2g} ratios is inconclusive.

3.4 Mechanistic model

As discussed above, only the formation of electron holes due to a decrease of the oxygen vacancy concentration under UV illumination can explain both the slow changes of the in-plane conductivity and the slight increase of the Ti valency suggested by the X-ray absorption measurements. Thus, our experimental results clearly indicate that oxygen is pumped into the crystal under UV irradiation, an interpretation that is also in accordance with several reports in literature.[26, 45, 75, 112] Interestingly, the corresponding chemical potential increase also affects all the dark parts of $SrTiO_3$, i.e. the region without significant exposure to UV light (due to strong UV absorption within the micrometer range).[113] In the following a more elaborate model explaining the obtained experimental results is suggested.

Our model assumes that oxygen exchange takes place by either involving electrons from the conduction band (CB) as discussed in ref. [24] and ref. [114].

$$\frac{1}{2}\, O_2 + 2e' + V_O^{\bullet\bullet} \rightleftharpoons O_O^x \qquad (10)$$

and/or holes from the valence band (VB) domination in concentration in the dark.

$$\frac{1}{2}\, O_2 + V_O^{\bullet\bullet} \rightleftharpoons O_O^x + 2h^{\bullet}\,. \qquad (11)$$

Both reactions are affected by the formation of additional electrons and holes under UV irradiation according to

$$nil + h\upsilon \rightarrow e' + h^{\bullet} \qquad (12)$$

Before illumination and in equilibrium the same amount of oxygen is incorporated and released into/out of $SrTiO_3$, and thus no net flux of oxygen results (Figure 21a). Please note that thermodynamic equilibrium requires individual equilibria for both Equation 10 and Equation 11, i.e., of oxygen exchange involving either the conduction band and/or the valence band. It is assumed that in air, the equilibrium oxygen exchange of the nominally undoped (i.e., effectively slightly acceptor doped) $SrTiO_3$ occurs mainly via the VB, Equation

11. Despite the charge transfer success probability could be much higher for the electrons in the conduction band (CB), those may play only a minor role in equilibrium oxygen exchange due to their extremely low concentration.

UV light leads to additional holes in the VB and a drastic increase of the electron concentration in the CB. This results in a splitting of the Fermi level into two quasi-Fermi levels, see Figure 21b. The change of the hole quasi-Fermi level is much less distinct due to the slight effective p-doping of $SrTiO_3$. The strongly increased electron concentration in the CB leads to a strongly enhanced electron transfer rate from the CB to adsorbed oxygen atoms. Consequently, oxygen incorporation via the CB is strongly accelerated whereas oxygen exchange kinetics via the VB do not change drastically. This was also suggested in ref. [45] for explaining an increased oxygen incorporation rate into Fe-doped $SrTiO_3$ under UV illumination. Thus, a net flux of oxygen from the gas phase into the $SrTiO_3$ crystal can be observed under UV irradiation, mostly occurring via CB electrons.

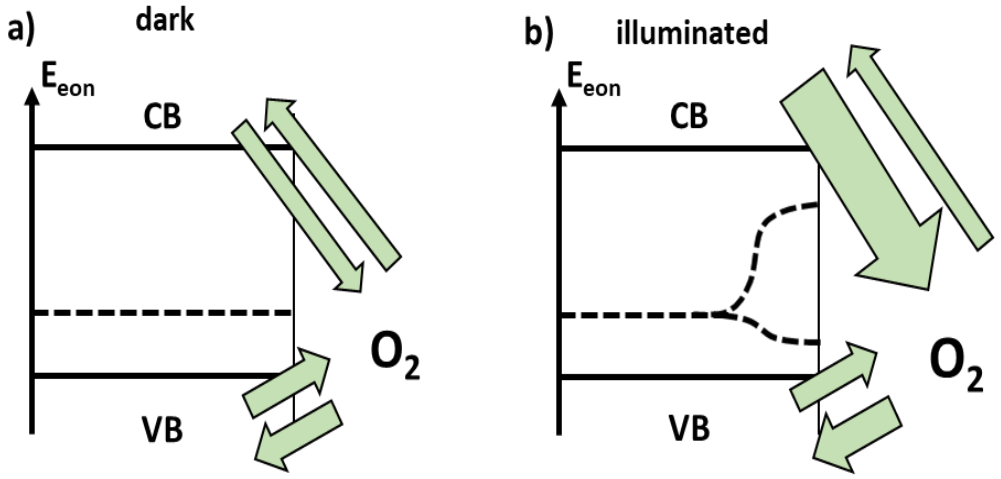

Figure 21: Schematic illustration of the impact of above band-gap energy illumination on electronic charge carriers and oxygen surface exchange: **a)** In the dark and in equilibrium, electron transfers for the oxygen exchange reaction occurs via the valence band (high concentration of electrons, but low probability) and via the conduction band (extremely low concentration, but higher probability). Impedance spectroscopy measurements indicate that despite the low transfer probability, valence band holes are more important. **b)** By generating electron-hole pairs, illumination leads to formation of quasi-Fermi levels for electrons and holes, respectively. Due to the strong increase of conduction band electron concentration, incorporation of oxygen is strongly enhanced, whereas changes in valence band related rates are minor. Please note that in reality band bending, and space charges are present at the surface of $SrTiO_3$. However, space charge effects are strongly reduced under UV irradiation and thus for simplicity such effect were not considered here.

For understanding the subsequently resulting oxygen diffusion effects, the changes in oxygen chemical potential have to be considered. Assuming that before illumination the oxygen chemical potential inside $SrTiO_3$ is in equilibrium with the gas phase, see Figure 22a. (For the sake of simplicity, we neglect that full equilibration may not be reached in the experiments due to the relatively low temperatures). The oxygen chemical potential μ_O can be described with the chemical potentials μ of charged defects according to

$$\mu_{O,e} = -\mu_{V_O^{\bullet\bullet}} - 2\mu_{e'} \quad (13)$$

or

$$\mu_{O,h} = -\mu_{V_O^{\bullet\bullet}} + 2\mu_{h^{\bullet}}, \quad (14)$$

respectively. In equilibrium, both definitions are equivalent, since electrons and holes are thermodynamically connected via equilibrium band-band excitation. This changes when illuminating $SrTiO_3$ with UV light. The two quasi-Fermi levels forming for electrons and holes also lead to two different oxygen quasi-chemical potentials (for neutral oxygen), one being CB-electron-related (μ_e) (Equation 13) and the other related to the VB-holes (μ_h) (Equation 14). Both oxygen quasi-chemical potentials of the illuminated region are no longer in equilibrium with the oxygen chemical potential in the dark bulk. These differences in the oxygen chemical potentials thus are the driving forces for oxygen diffusion, see Figure 22b. However, these driving forces are opposite with holes trying to pump oxygen into the dark zone and electrons trying to pull oxygen into the illuminated zone. This raises the question which of the two quasi-chemical potentials is the kinetically dominating one. The results indicate that, for the present experimental conditions, in the illuminated region, holes are still the majority electronic charge carriers and thus still dominate the chemical diffusion process.

Concerning the surface reaction, it has already been stated that the electron-related oxygen quasi-chemical potential step is decisive and leads to a finite net oxygen incorporation rate (Figure 22b). Thus, oxygen is pumped into the UV absorption region via the electron-related oxygen incorporation flux. This lowers the oxygen vacancy concentration near to the surface and thus increases both oxygen quasi-chemical potentials (Figure 22c). Moreover, electron and hole concentrations change accordingly. Thus, the hole related oxygen quasi-chemical

potential becomes strongly enhanced close to the surface and a further driving force for oxygen diffusion into $SrTiO_3$ is established, primarily into the illuminated region (Figure 22c) and subsequently into the dark bulk region (Figure 22d). Consequently, the entire dark bulk is pumped to a higher chemical potential of oxygen. This means that successively most oxygen vacancies are filled and hence a heavily increased hole concentration comes to be. The resulting strong hole conductivity enhancement is seen in the conductivity experiments upon UV light exposure and the oxygen chemical diffusion coefficient of $SrTiO_3$ describes the corresponding time dependence.

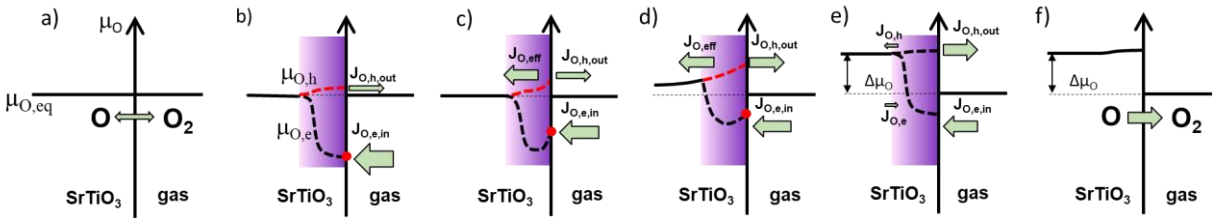

Figure 22: **a-e)** Series indicating the time dependent changes of the oxygen chemical potential μ_O and the hole and electron-related oxygen quasi-chemical potentials ($\mu_{O,h}$, $\mu_{O,e}$) under UV irradiation (violet indicates illuminated zone). The red broken line indicates the diffusion dominating quasi-chemical potential (hole related) and the red circle indicates the dominant surface process (electron related). After reaching the steady state **(e)**, in **(f)** the UV light is switched off and a chemical potential difference between bulk and gas phase remains.

As already mentioned, the UV light driven oxygen incorporation changes all defect concentrations in the near surface region and this reversely affects the oxygen release rate via the VB and the oxygen incorporation rate via the CB, see arrows $J_{O,h,out}$ and $J_{O,e,in}$ indicating the different oxygen fluxes out of and into the single crystal in Figure 22. Finally, a steady state (but not an equilibrium) is reached, in which net incorporation of oxygen via CB-electrons and net oxygen release via VB-holes balance each other out (Figure 22e) and the enhanced chemical potential of oxygen in $SrTiO_3$ is constant in the entire dark part of the crystal. A slight chemical potential step may still exist between dark and UV absorbing zone but now the two diffusion fluxes (electron related into the UV illuminated zone, and hole related in the opposite direction) balance each other (Figure 22e). When switching-off the UV light, the two different quasi-chemical potentials in the formerly illuminated region collapse to one value. The dark crystal now exhibits a strong driving force to release oxygen

back towards the equilibrium state (Figure 22f). However, since the oxygen chemical potential increase inside the $SrTiO_3$ is still present, the strongly enhanced in-plane conductivity of the sample is still measured. The crystal only slowly relaxes to equilibrium with the gas phase via slow oxygen release at the surfaces. This is visible as the slow surface limited conductivity decrease after UV light is turned off.

Please note, that the real situation may be further complicated by the space charge present at surfaces of mixed conductors. However, qualitatively, the model should remain valid even though concentrations of all charge carriers are modified by the space charge near to the surface. Quantitatively, the situation including the space charge is truly complex, since the ionically dominated space charge of $SrTiO_3$ (caused by vacancy depletion)[115, 116] may be severely modified by the numerous electrons-hole pairs created by light, it probably even largely diminishes.

Of course, many other kinetic situations are possible in different systems, e.g. oxygen exchange via the conduction band also in the dark, or predominant bulk diffusion due to the electron related oxygen quasi-chemical potential. Accordingly, the model has to be adapted to the specific case. The key is always the formation of oxygen quasi-chemical potentials in the absorption zone which causes driving forces for oxygen diffusion and oxygen exchange. The specific parameters such as hole-related oxygen chemical diffusion coefficient $D_{O,h}^{\delta}$, electron-related oxygen chemical diffusion coefficient $D_{O,e}^{\delta}$, hole-related oxygen incorporation and release coefficient $k_{O,h,out}^{\delta}$, $k_{O,h,in}^{\delta}$, and electron-related oxygen incorporation and release coefficient $k_{O,e,out}^{\delta}$, $k_{O,e,in}^{\delta}$ determine how this translates into stoichiometry changes Indeed, in literature, the generation of oxygen vacancies under UV illumination was reported during pulsed laser deposition.[59] However, the temperatures were much higher (800 °C) and p_{O_2} significant lower (10^{-8} bar),[59] causing different kinetic conditions for oxygen incorporation/release/diffusion compared to this study.

In general, most mixed conductors are doped and a similar behavior as in undoped $SrTiO_3$ can be expected. However due to possible trapping states and changes in the oxidation state of the dopants under UV illumination changes in the defect chemistry can become more complex. Nevertheless, the presented model is still valid in the presence of aliovalent dopants. In poly-crystalline samples the picture becomes even more complicated, since the defect chemistry at grain boundaries can substantially differ from the bulk defect chemistry. Moreover, grain boundaries may act as substantial barrier for oxygen or electronic transport

in $SrTiO_3$,[1] hence long-range photo-ionic effects may be largely impeded in poly-crystalline samples.

In a broader context, the same principle of photo-generated driving forces can be expected to hold true for all mixed ionic electronic materials with a similar band gap. These may be cation/electronic materials such as ion battery electrodes or alkali carbonitrides[117] or other anion/electronic systems such as halides, e.g. the archetypical perovskite solar cell material methylammonium lead iodide (MAPI).[118] For the latter two, studies on their photo-ionic properties exist. What is important to notice is that, despite the driving force being the same (i.e., the formation of two energetically different quasi-chemical potentials under illumination), the reactions for realizing the necessary ionic plus electronic transport may be very different and depend also on the adjacent phases. Important examples are: chemical diffusion ($SrTiO_3$ bulk) and surface reactions with the gas phase ($SrTiO_3$ surface) investigated in this paper, and also formation and incorporation of interstitials (potassium in K-poly (heptazine imide)),[117] iodine in MAPI.[118]

3.5 Conclusion

UV irradiation of undoped $SrTiO_3$ at elevated temperatures can increase its conductivity by two to three orders of magnitude. Photoconductivity in the illuminated region due to the formation of electron-hole pairs and temperature effects were ruled out as the main causes of this drastic enhancement. The conductivity changes under UV irradiation take place on time scales that correspond to oxygen chemical diffusion in the bulk of the material and can be explained by UV induced oxygen stoichiometry changes in the entire $SrTiO_3$ crystal, i.e., also in the dark regions without UV absorbance. After switching off the UV light, the very high conductivity remained and relaxed only very slowly, in accordance with the very slow oxygen exchange with the gas phase at the given temperatures. The sign of the conductivity changes (to higher conductivity) and energy shifts in the X-ray absorption spectra indicate that oxidation of $SrTiO_3$ takes place under UV illumination. Converting the measured p-type conductivity increase to the chemical potential changes in the material indicates effective oxygen pressures of up to 10^6 bar. Essentially, oxygen incorporation into $SrTiO_3$ is strongly accelerated by UV light, causing the oxidation of the entire material with annihilation of oxygen vacancies and formation of electron holes at elevated temperatures. A model is proposed explaining in detail the impact of UV irradiation on nominally pure $SrTiO_3$. This

model is based on the introduction of oxygen quasi-chemical potentials in analogy to the quasi-Fermi levels of electrons and holes in the illuminated region. The oxygen incorporation itself is strongly enhanced by the additional conduction band electrons. However, the oxygen diffusion in the illuminated $SrTiO_3$ bulk is still determined by the electron holes from the valence band and the corresponding quasi-chemical potential drives the incoming oxygen into the dark region, thus enhancing the effective oxygen pressure and hole conductivity. This model is equally applicable to UV effects in any other mobile component in a semiconductor e.g., metals in cation conductors or halides.

4 How can UV light lower the conductivity of $SrTiO_3$ by photochemical water splitting at elevated temperature?

The following chapter is part of the manuscript: “How UV Light Lowers the Conductivity of $SrTiO_3$ by Photochemical Water Splitting at Elevated Temperature ”, which is submitted to Material Advances.[119]

4.1 Introduction

In the last chapter a model was derived describing oxygen incorporation into $SrTiO_3$ due to UV illumination in air at elevated temperatures.[93] It is based on the formation of oxygen quasi-chemical potentials in the illuminated sample parts. However, despite enhanced oxygen incorporation, in literature also the formation of oxygen vacancies as a consequence of UV illumination is described.[59] Even though different UV-driven defect chemical consequences are not necessarily in contradiction with each other, questions about the factors determining the defect chemical situation under UV irradiation arises due to the mentioned findings. Hence, experiments in a large p_{O_2}range are of high interest and thus, also the effects of UV light on the conductivity of $SrTiO_3$ in N_2 with some residual oxygen and dry or humidified H_2 at 350 °C were investigated and are discussed in the following.

4.2 Experimental

Undoped $SrTiO_3$ single crystals (100) (5×5×0.5 mm^3, CrysTec GmbH, Germany) with Ti vacancies (6-8 ppm) as main charge active defects were used.[98] In order to prepare the specimens for the in-plane impedance measurements, they were cleaned with ethanol in an ultrasonic bath, subsequently they were annealed for 12 h at 900 °C in air to reduce surface defects and afterwards again cleaned as above. Then, the samples were equilibrated at 700 °C either in N_2 (containing approx. 70 ppm O_2), humidified H_2, or dry H_2, depending on the atmosphere in-plane conductivity measurements were conducted in. The strongly reducing atmospheres containing H_2 were established using commercially available gas mixtures of Ar and 2 % of H_2 (Messer, Germany). For humidification, the gas was passed through double-

distilled water at room temperature. After annealing, the temperature was lowered to the actual measurement temperature of 350 °C while keeping the atmosphere, and the single crystals were again equilibrated at least for 12 h. Owing to this comparatively low temperature some deviations from equilibrium defect concentrations at 350 °C might still be present. Then the actual electrical measurements were performed.

In-plane impedance measurements used Pt wires contacting Pt paste electrodes applied either only on the back side or on both the back and the front side of the samples (see Figure *23*). A flame polished quartz rod acted as light guide for the UV (365 nm), green (523 nm), and red (660 nm) light emitted by high performance LEDs (LED Engin, USA). A detailed description of the used set-up can be found in chapter 3.[93] The irradiation of $SrTiO_3$ with UV light causes the excitation of electrons from the valence band to the conduction band and consequently leads to the formation of electron-hole pairs. Green and red light are not absorbed by $SrTiO_3$ (compare absorption spectrum in Figure 24) at 350 °C. In-plane impedance spectra were recorded at 350 °C and between 1 MHz and 1 Hz using Alpha-A High Performance Analyzers (Novocontrol Technologies, Germany). Conductivity was then obtained by fitting the experimental data using Zview (Scribner Associates Inc., USA).

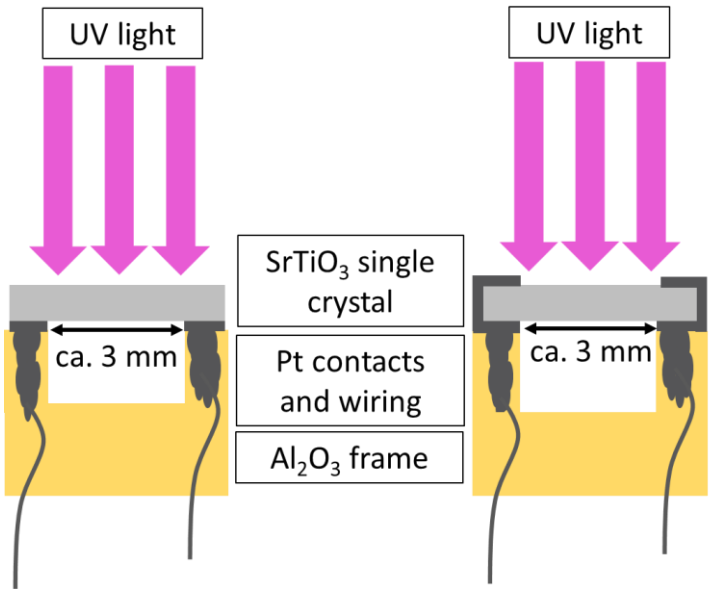

Figure 23: Sketches of the impedance spectroscopy set-up used; left: $SrTiO_3$ single crystal is only contacted on the back side; right: Pt contacts on both the front and back side. The specimens were connected directly to the impedance analyzer via Pt wires.

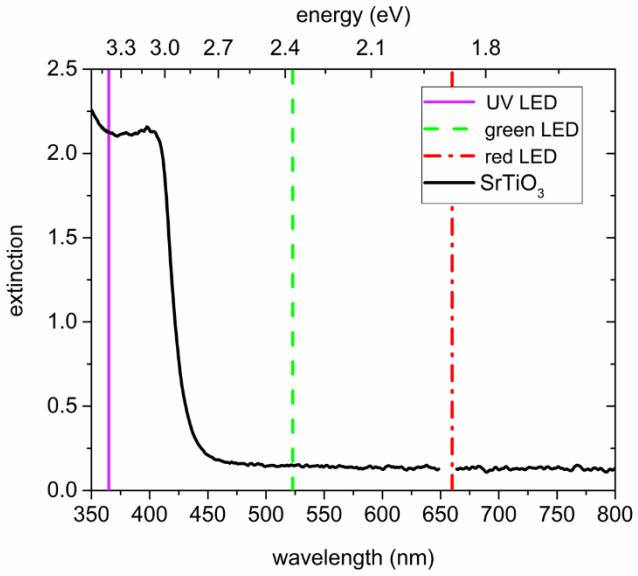

Figure 24: Extinction spectrum of a both side polished $SrTiO_3$ single crystal at 350 °C in air. Additionally, the emitted wavelengths of the used UV (365 nm), green (523 nm), and red (660 nm) LEDs are indicated.

4.3 Results

The in-plane conductivities of undoped $SrTiO_3$ were deduced from impedance spectra before, under, and after UV illumination. In air as well as in N_2 a dominating high frequency arc (representing the bulk resistance and geometrical capacitance) and some low frequency features due to the electrodes were found.[31, 34, 98, 120, 121] In dry and humidified H_2, only one almost ideal semicircle was obtained in the investigated frequency range. The bulk semicircles were fitted to a resistor in parallel to a constant phase element and in-plane sample conductivities were derived from the resistance assuming 1D current flow (length approx. 3 mm) and thus neglecting edge effects due to the exact electrode geometry.

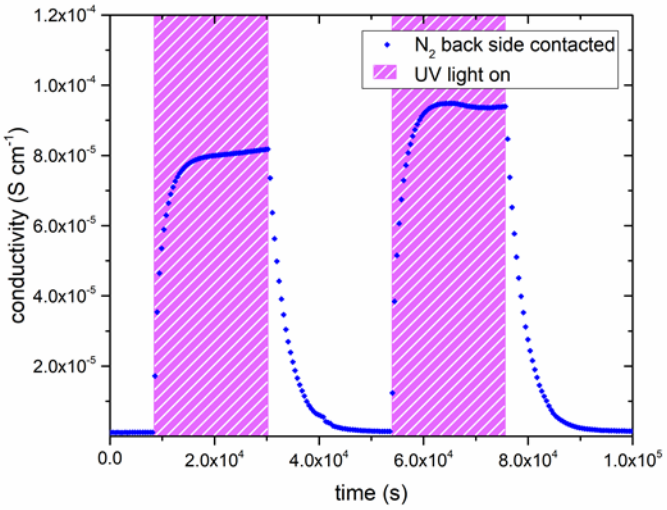

Figure 25: In-plane conductivities of back side contacted $SrTiO_3$ before, under, and after UV irradiation in N_2 at 350 °C. During UV illumination the conductivity increased by nearly two orders of magnitude. After the UV light was turned off, several hours were needed before the initial conductivity was restored.

Figure 25 displays results of impedance measurement cycles in N_2 during which the specimens were illuminated with UV light for several hours. The results are rather similar to those obtained in air, with drastic conductivity increases (up to more than two orders of magnitude) under UV irradiation on a time scale of about an hour. However, achieved maximum conductivities were lower in N_2 than in air. The conductivity remained very high after switching the UV light had been switched off and then slowly relaxed on the time scales of several hours. The relaxation was slower in air than in N_2. These extended relaxation time scales also led to the phenomenon that the conductivity could be driven up to higher values by subsequent short illumination periods (136 s) and longer dark times (832 s) as shown for N_2 in Figure 26. Before the UV irradiation an in-plane conductivity of 3.3×10^{-7} S cm^{-1} was measured and driven up to 2.6×10^{-6} S cm^{-1} during the first illumination period. This increase was followed by a minimal conductivity decrease to 2.1×10^{-6} S cm^{-1} after the UV source was turned off for the first time. Finally, after the fourth and last UV irradiation of $SrTiO_3$, its conductivity was driven up to 9.8×10^{-6} S cm^{-1}, this is in total a conductivity increase by a factor of nearly 30. Irradiation with red or green light lead only to a minor conductivity increase, probably due to a small temperature increase when the light was absorbed by the Pt paste and/or corundum frame. It is detailed in the previous chapters and also discussed below that all these long-time conductivity changes were caused by oxygen stoichiometry

changes in the bulk upon UV illumination. Photoconductivity (PC) due to additional electron-hole pairs plays a very minor role here, compared to the very strong photo-ionic (stoichiometry-driven) conductivity changes (PI).

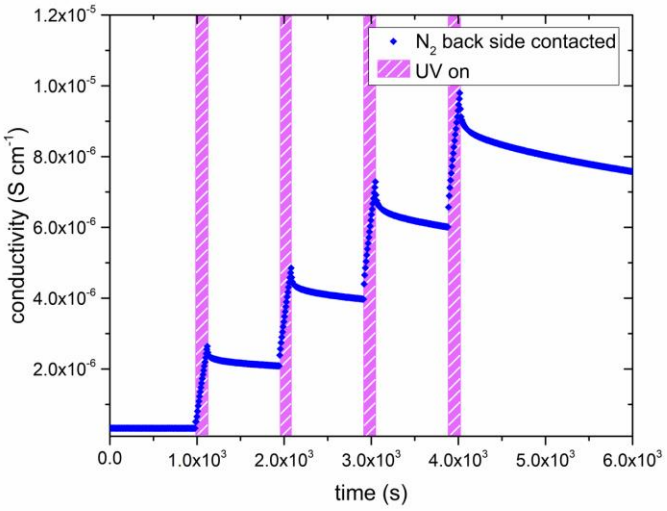

Figure 26: Due to the large time constant of the relaxation after the UV light was turned off, the in-plane conductivity increased more and more during each of the four short illumination periods (136 s each) at 350 °C in N_2. In total the in-plane conductivity was increased by a factor of 30.

In dry and humidified H_2 at 350 °C the $SrTiO_3$ sample is in the electron conducting regime.[98] UV induced effects still took place but there differences were found compared to the studies in O_2 containing gases: i) UV induced effects took place much faster. ii) They were much less pronounced (Figure 27). iii) UV may not only increase but also decrease the conductivity. More specific, the in-plane conductivity of a back side contacted $SrTiO_3$ single crystal instantly jumped from 1.3 × 10^{-6} S cm^{-1} to 1.8×10^{-6} S cm^{-1} in the first and 2.0×10^{-6} S cm^{-1} in the second cycle (cyan triangle Figure *27*a) after the UV light was turned on. It is discussed in more detail below that the instant effect was caused by additional photoconductivity due to electron-hole formation upon UV. This increase became counter-balanced by a moderately fast decrease of the conductivity within a few 100 s until a reproducible plateau at 1.1×10^{-6} S cm^{-1} was established, which was approx. 15 % below the original conductivity. After switching the UV light off, the conductivity dropped to 4.9×10^{-7} S cm^{-1} and to 5.6×10^{-7} S cm^{-1}, respectively, i.e. less than 50 % of the original value, due to the loss of photoconductivity. This immediate decline was followed by a conductivity increase within a few 100 s and finally nearly the initial value before illumination was again reached. Thus, two processes namely

the fast-evolving photoconductivity and a slower photo-ionic process determined the evolution of the sample conductivity.

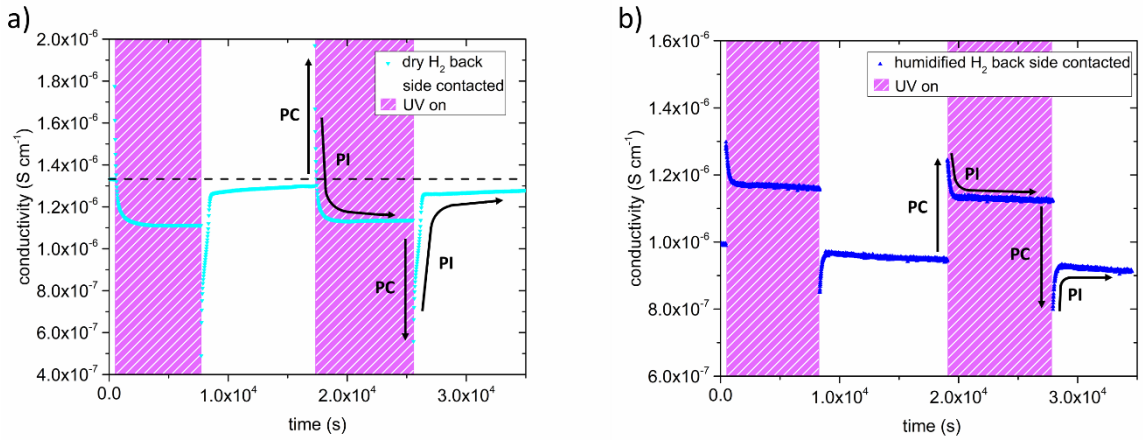

Figure 27: Results of impedance measurements performed in dry H_2 **(a)** and humidified H_2 **(b)** at 350 °C. The samples were contacted on the back side only. UV light was turned on twice leading to an abrupt conductivity increase due to photoconductivity (symbolized by black arrows marked with PC) followed by a steady decline of the conductivity (photo-ionic effect (PI)). In dry H_2 even a plateau below the initial value was found. After the UV light had been turned off, conductivity dropped promptly then increased and approached the initial values.

A very similar picture resulted for the experiments on back side contacted specimens conducted in humidified H_2 atmosphere (compare Figure 27b). Since the p_{O_2} was three to four orders of magnitude higher, the initial of the electron conducting $SrTiO_3$ was lower, and the changes were not as distinct. The measurements started at a conductivity of 9.9×10^{-7} S cm^{-1}, when UV light was turned on it peaks at 1.3×10^{-6} S cm^{-1} (1.2×10^{-6} S cm^{-1} respectively), and finally reached 1.2×10^{-6} S cm^{-1} (1.1×10^{-6} S cm^{-1}) under UV illumination. After switching the UV light off, the conductivity dropped to 8.5×10^{-7} S cm^{-1} (8.0×10^{-7} S cm^{-1}) and then relaxed to approximately the initial value.

In the following the differences between only back side and both-side contacted samples are shown. Here we consider the inverse resistance (1/R = conductance) of both measurement configurations and for the sake of comparability, the curves were normalized to the initial 1/R values before UV illumination. This eliminates differences in the electrode geometry, defect chemistry due to slow pre-equilibration or atmosphere and temperature.

Contacting the sample on both the front and the back side, led to a substantial change in the observed effect of UV exposure, compared to specimens contacted only on the back side,

see Figure 28. Due to photoconductivity, the inverse resistance of a both-side contacted $SrTiO_3$ single crystal immediately jumped up after UV light was turned on. The jump was much more pronounced for the both-side contacted sample (by a factor of 2.2) compared to the only back side contacted $SrTiO_3$ specimen (by a factor of 1.3). In contrast to the results shown in Figure 27a the inverse resistance remained far above the initial value for contacts on both sides, and only a small decline by approx. 11 % compared to the inverse resistance maximum was detectable. After the UV light was switched off, the inverse resistance of the both-side contacted specimen drastically dropped to approx. 40 % of the initial value (PC) and finally relaxed back to the amount obtained before UV irradiation (PI), in accordance with the only back side contacted sample. Also, both specimens seem to exhibit very similar time constants, since the conductivity plateau under UV irradiation as well as the relaxation to the initial value after UV illumination were established nearly after the same time. This suggest that the fast photoconductivity effects were different, while the slower photoionic effects were the same. This is not surprising since PC effects take place primarily in the absorption zone close to the surface.

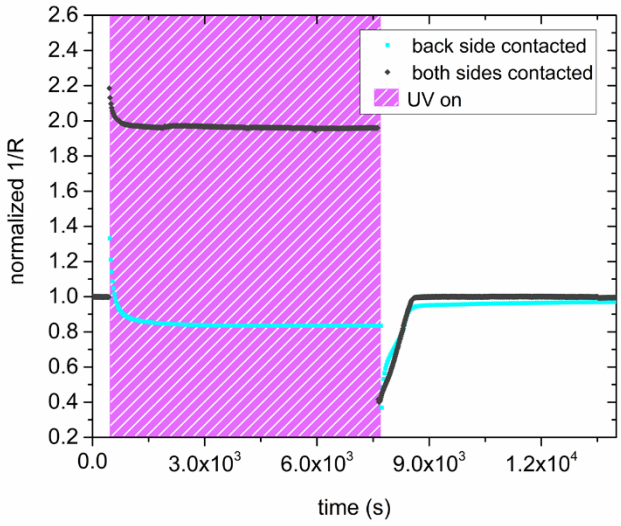

Figure 28: Inverse resistance (conductance) of a sample only contacted on the back side (cyan squares) and a specimen contacted on both the back and the front side (black diamonds). Both curves were normalized to the initial inverse resistance (before UV) for the sake of comparability. The initial photoconductivity related jump is more distinct in the both-side contacted sample. During irradiation both specimens showed a different behavior, due to the different emphasis of the illuminated surface region. After the UV light was turned off the inverse resistance dropped to 40 % of the initial (before UV irradiation) values in both cases. The data were obtained in dry H_2 at 350 °C.

4.4 Discussion

4.4.1 Quantitative comparison with the defect chemical model of undoped $SrTiO_3$

In the following, the shown UV light induced changes found in nominally undoped $SrTiO_3$ are discussed in more detail. To do so the underlying defect chemistry of the used $SrTiO_3$ specimens has to be determined and understood. Therefore, in Figure 29 several experimental results (black squares) of various in-plane conductivity measurements obtained in the four described atmospheres , namely air, N_2 with residual oxygen, dry H_2, and humidified H_2 at 350 °C before UV illumination are plotted.

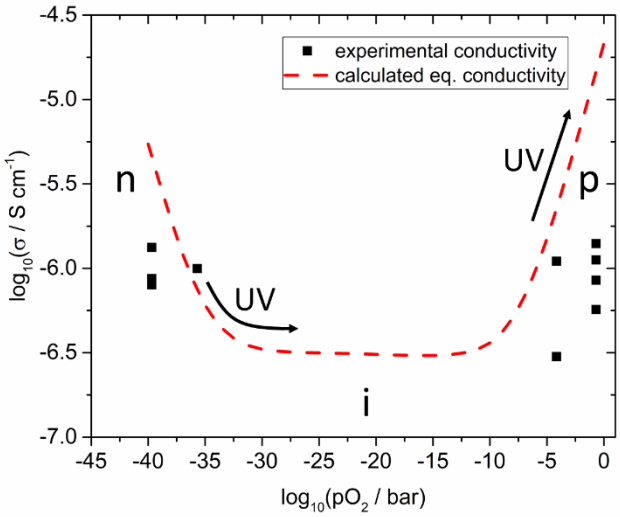

Figure 29: Measured in-plane conductivity (black squares) after heating the specimens to 700 °C and subsequently annealing at 350°C for several hours in dry H_2, humidified H_2, N_2, and air. Calculated conductivity assuming 6 ppm Ti vacancies as predominant dopant (red broken line) at 350 °C vs p_{O_2}, to give an impression of the change from p-type (p) conductivity at high oxygen partial pressures, to ionic (i), and finally to n-type (n) conductivity the lower p_{O_2} becomes. Arrows indicate stoichiometry changes in the bulk caused by UV.[98]

These data are compared with calculated conductivities derived from a detailed defect chemical model established by us for such undoped $SrTiO_3$ single crystals recently. For this, measurements in a wide p_{O_2} range and between 500 and 700 °C were performed.[98] Among others, the defect model is based on conductivity measurements in a wide p_{O_2} range between 500 and 700 °C. At these temperatures an equilibration with the gas phase takes place on a reasonable time scale and thus it was possible to extract equilibrium

conductivities and chemical capacitances, which both lay the foundation of an extended defect model. Essentially, it was shown that approx. 6 ppm Ti vacancies cause a slight p-type doping in the considered nominally undoped $SrTiO_3$ single crystals. From this data set, we can also predict the equilibrium conductivities for other p_{O_2} and temperatures. For 350 °C we find that hole conductivity dominates above a p_{O_2} of approx. 10^{-8} bar, electron conduction below 10^{-32} bar and in between there is a broad range with constant ionic conductivity due to the oxygen vacancies balancing the acceptor doping.[98]

While the values in humidified H_2 fits excellently to the prediction, measured values are somewhat too small in dry H_2, air, and N_2. Moreover, those values differ from experiment to experiment, i.e. they depend on the exact prehistory, indicating that equilibrium with the gas phase is hardly well-established, despite all specimens were annealed at 700 °C and subsequently equilibrated for at least hours at 350 °C in the respective atmosphere. This is in accordance with the statements that in $SrTiO_3$ oxygen surface exchange reactions are slow or even frozen-in at lower temperatures.[122, 123] Many days or even weeks might have been required for complete equilibration. Equilibrium values, however, seem to be reached in humidified H_2 at 350°C, suggesting that the corresponding gas exchange reaction

$$H_2O + V_O^{\bullet\bullet} + 2e' \rightleftharpoons H_2 + O_O^x \qquad (15)$$

is still in equilibrium here. These somewhat ill-defined defect chemical state of several samples, however, do not interfere with all the following interpretations and conclusions. As discussed in the last chapter the time scales on which the conductivity changed under UV irradiation in all four atmospheres was by far too large to be only caused by photoconductivity. In Cr doped $SrTiO_3$ recombination of electron-hole pairs take place mostly within 9.17 µs at room temperature.[101] Similar time constants in undoped $SrTiO_3$ are assumed. Furthermore, the used UV light is mostly absorbed in the first µm.[113] Thus the in-plane conductivity increases of back side contacted specimens by more (nearly) than two orders of magnitude in air (N_2) at 350 °C cannot be explained by photoconductivity solely. Rather, the whole bulk has to be affected by the UV illumination via changes of its defect

chemistry. However, in strongly reducing atmospheres these slow changes in the conductivities are still significantly faster than in air and N_2.

In accordance with the more detailed studies in air, it is concluded that indeed UV-induced oxygen stoichiometry changes in $SrTiO_3$ are the reasons for the large conductivity increase in N_2 as well. In the following the fact that the same effect is responsible for the conductivity decrease in dry H_2 is discussed. First, the question has to be addressed whether the chemical potential of oxygen is increased or decreased in $SrTiO_3$ under UV illumination. Here, Figure 29 gives a clear indication: In air and N_2 only an increase of the chemical potential can explain the huge increase of conductivity found. However, in this chapter the remarkable fact that UV irradiation of $SrTiO_3$ single crystals leads to a reduced in-plane conductivity in dry H_2 is discussed.

As already mentioned above, the instant the quick conductivity increase (decrease) (PC) observed in H_2 when the UV light was turned on (off) are largely due to photoconductivity. The slower change to lower values upon UV (PI), on the other hand, is the pendant to what can be seen in air and N_2, namely the change of the conductivity due to an oxygen stoichiometry changes in the bulk. From the conductivity vs p_{O_2}curve in Figure *29* it can thus be concluded whether oxygen incorporation or oxygen release takes place under UV irradiation. Since at such low p_{O_2} $SrTiO_3$ is a n-type semiconductor only the filling of oxygen vacancies and the formation of holes (i.e., annihilation of electrons) can explain the observed lowered conductivity. Hence, like in air and N_2, also in H_2 UV light pumps the crystal to a higher oxygen chemical potential. When the UV illumination stops, an instant drop of the conductivity occurs (PC) and only the decreased bulk conductivity determines the impedance of the specimen which then slowly relaxes by oxygen release. The decrease of the conductivity in H_2 due to UV-triggered oxygen incorporation is much less pronounced than the increase measured in air. This can be easily understood from Figure *29*: The conductivity cannot drop beneath the ionic conductivity plateau. Most probably this plateau was reached in the shown experiments, and thus the effective p_{O_2} change in $SrTiO_3$ cannot be estimated from the measured conductivity.

This interpretation is also supported by the second measurement mode, i.e., with single crystals being contacted on both the illuminated front and the dark back side. Here the fast increase of the inverse resistance right after the UV light was turned on was more pronounced and the slow decrease of the inverse resistance under UV illumination was by

far smaller than if the specimens were only contacted on the back side (see Figure *28*). However, shortly after the UV irradiation the inverse resistance reached approx. 40 % of the initial value in both experimental configurations. This is in perfect accordance with our interpretation of a thin top surface region where the UV light is absorbed, and where the conductivity is strongly enhanced due to the photogeneration of charge carriers. Below this zone the bulk conductivity is decreased due to a change in the oxygen content/chemical potential. Large parts of the bulk seem to be involved since otherwise an effective conductivity (or conductance) decrease of the entire sample can hardly be explained from the given conductivity p_{O_2} diagram. Thus, when electrodes are placed on the illuminated front side, the UV absorption zone becomes more decisive for the overall in-plane resistance (or conductance) of the investigated sample. In the following section we estimate the current density and the potential distribution in the two regions using finite element calculations.

The question remains, where the incorporated oxygen comes from when $SrTiO_3$ single crystals are under UV illumination in strongly reducing H_2 containing atmosphere. The oxygen stems from water, i.e. we face water splitting under UV light and thus hydrogen reduction rather than oxygen reduction. Accordingly, we suggest that UV illumination of $SrTiO_3$ in H_2 enhances the water splitting rate (including the corresponding oxygen incorporation into $SrTiO_3$) without enhancing the opposite reaction in the same manner. This UV effect is not surprising since $SrTiO_3$ is a well-known photocatalyst for water splitting.[124-127]

4.4.2 Conductivity analysis and current distribution

According to the model introduced in the last section, the conductivity of the bulk before UV illumination, the photoconductivity in the first µm of the illuminated specimen, and the decreased bulk conductivity under UV light for a $SrTiO_3$ single crystal contacted on both the front and the back side were estimated. To do so firstly a parallel circuit consisting of two resistors representing the bulk and the UV absorption region was assumed. Moreover, a second assumption had to be made, namely that the bulk does not change significantly during the first five to ten seconds of UV exposure. From the impedance of the first data point (R_{UV}) after the UV light was switched on and the in-plane resistance before UV irradiation ($R_{bulk,dark}$), the resistance of the thin UV region (R_{surf}) can be calculated. According to

$$\frac{1}{R_{UV}} = \frac{1}{R_{bulk,dark}} + \frac{1}{R_{surf}} \quad (16)$$

and assuming a thickness of 1 µm in which the UV light is mostly (approx. 80 %) absorbed,[128] the effective photoconductivity in this 1 µm layer is by a factor of approx. 600 higher than the bulk conductivity before UV irradiation. Shortly after the UV illumination the overall in-plane conductivity declined to 40 % of the initial value, indicating that R_{bulk} had increased upon UV by a factor of 2.5.

Subsequently these numbers were used to perform finite element simulations (Figure *30*). Assuming an applied voltage of 0.02 V between the two electrodes at the back side of the sample the potential distribution and current flow in the bulk before and during UV illumination can be calculated. Before illumination, the current density between the two electrodes is nearly uniformly distributed over the whole thickness of the sample. During UV irradiation the current density is decreased in the dark bulk and strongly increased (by more than three orders of magnitude) in the UV region (see Figure *31*).

These simulations graphically show the impact of the formation of a zone with an enhanced photoconductivity and the bulk region exhibiting a lower conductivity due to oxygen incorporation and diffusion. Additionally, it becomes more evident that the differing experimental results in Figure *28* were caused by the differences in the measurement configurations and support our interpretation.

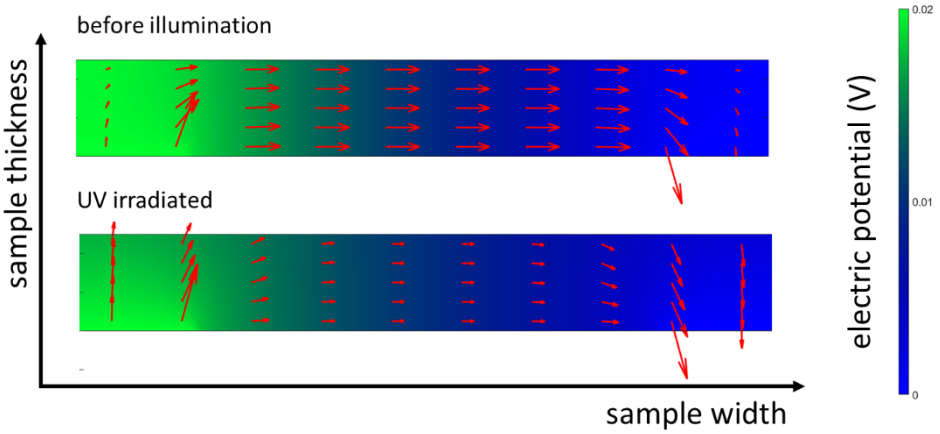

Figure 30: Finite element simulations of back side contacted $SrTiO_3$ before UV illumination (top) and under UV irradiation in the steady state case (bottom). The red arrows indicate the direction and amount of current flowing from the one electrode (left side) to the other (right side). The thin UV illuminated region is not visible in this sketch. Additionally, the voltage over the sample is indicated by the color bar on the right.

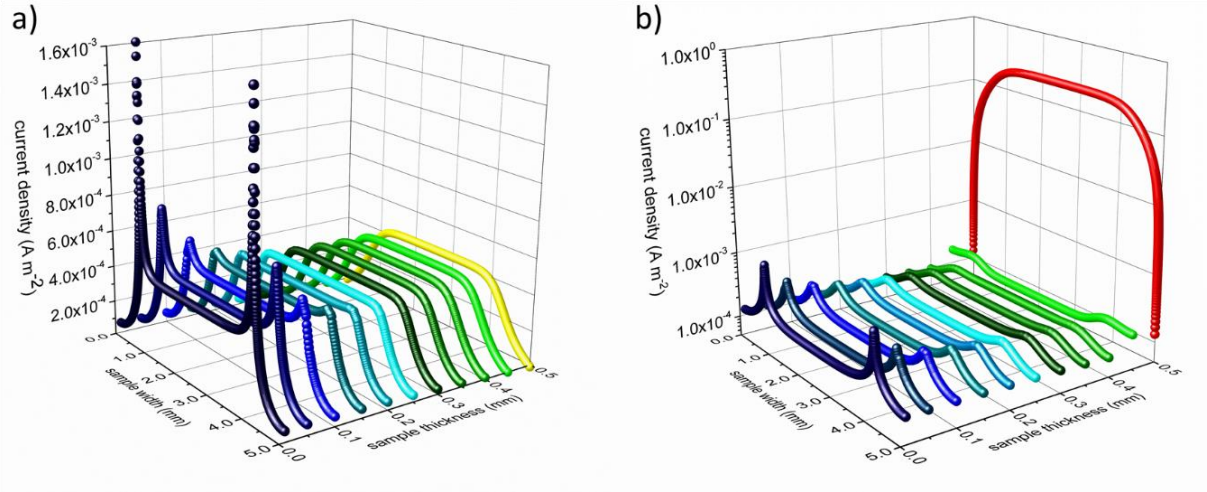

Figure 31: Current density before **(a)** and under UV illumination **(b)** of a back side contacted sample. The front side, illuminated by UV light, is at 0.5 mm sample thickness, the contacted back side at 0 mm. Current density is strongly enhanced in the UV absorption zone (red balls) which is assumed to be 1 µm thick in the displayed simulation. In the dark bulk the current density is slightly reduced under UV illumination compared to that in the bulk before UV light was turned on.

4.4.3 Quantitative analysis of the time dependency of the conductivity changes

In the previous chapter it was shown that oxygen composition change of $SrTiO_3$ upon UV is diffusion limited and a diffusion coefficient of $6.3\times10^{-7}cm^2\ s^{-1}$ was estimated at 350 °C in air. Whereas the oxygen release after UV is slower and surface limited.[93] The experiments shown in this chapter are in accordance with these this findings. On the other hand, when fitting the time dependent conductivity increase in N_2 under UV irradiation the diffusion limited model leads to less accurate fits than a model with surface limitation. Thus, the equation for surface limitation.

$$\frac{\sigma(t)-\sigma(0)}{\sigma(\infty)-\sigma(0)} = 1 - exp\left(\frac{-k_{chem}}{a} * t\right) \qquad (16)$$

Seems to be more appropriate to describe the experimental data.[49, 84, 104] In Equation 17 a constant oxygen chemical exchange coefficient k_{chem} is still used despite the large chemical potential changes considered here. The symbol σ(0) denotes the initial conductivity, σ(∞) the final conductivity, a is the sample thickness, and t the time of UV illumination.

Applying Equation 17 to our measurement data leads to a surface exchange coefficient of 2.7×10^{-5} cm s^{-1} for the oxygen incorporation under UV light in N_2 with some impurity O_2 at 350 °C. The normalized data and fit are displayed in Figure 32a. Without overinterpreting the fit (owing to the simplifications of the model), we can still say that such a transition from diffusion to surface limitation of oxygen incorporation during UV illumination would be in accordance with the fact of having much less oxygen available in the N_2 gas phase. A lower limit of the oxygen diffusion coefficient can also be estimated since for an oxygen surface exchange limitation the oxygen chemical diffusion coefficient has to exceed at least $k_{chem} \times a \times 10$, here approx. $D_O^\delta > 1.4\times10^{-5}$ cm^2 s^{-1}. The relaxation of the conductivity after UV irradiation in N_2 is again considerably slower than the conductivity enhancement under UV light, since the latter is based on oxygen incorporation which is accelerated by light. This is also in good agreement with the kinetic studies on Fe-doped $SrTiO_3$ upon UV illumination.[45]

In dry or humidified H_2 atmosphere, however, the conductivity relaxation after UV irradiation is on a similar time scale of approx. 900 s (dry H_2), or 600 s (humidified H_2) respectively, as the changes under UV. Thus, the oxygen incorporation under UV irradiation and the oxygen release after UV are both limited either by diffusion or by the surface exchange kinetics and much faster than in air.[49, 84, 102-104] At 350 °C in humidified H_2 the fits using Equation 16 match the experimental data (see Figure *32*b). Hence it is suggested that oxygen incorporation is limited by the surface reaction. A surface exchange coefficient of 2.2×10^{-4} cm s^{-1} was obtained, which is about one order of magnitude higher than in N_2. Using the same approximation as before D_O^δ thus has to be at least 1.1×10^{-4} cm^2 s^{-1}. This is higher than the equilibrium diffusion coefficient of 9.4×10^{-6} cm^2 s^{-1} predicted by our defect chemistry model of undoped $SrTiO_3$ in humidified H_2 and at 350 °C. This is only plausible, if UV irradiation leads to an increase of the oxygen chemical potential and the effective p_{O_2} respectively since this also enhances D_O^δ,[129] for example our defect chemical model suggests 1.5×10^{-4} at 10^{-25} bar p_{O_2}.

In order to describe the oxygen release after the UV light was turned off, Equation 16 had to be slightly modified, since now both the front and the back side had to be considered in the process. Therefore Equation 18 is introduced:

$$\frac{\sigma(t)-\sigma(0)}{\sigma(\infty)-\sigma(0)} = 1 - exp\left(\frac{-k_{chem}}{\frac{a}{2}} * t\right) \quad (18)$$

The fits (Figure 32c) resulted in k_{chem} of 1.7×10^{-4} and 1.8×10^{-4} cm s^{-1}. This indicate that UV illumination alters the oxygen incorporation in humidified H_2 only slightly.

Neither models describing diffusion limitation, exchange limitation, nor a mixed regime were able to describe the experimental data obtained from specimens contacted on both the front and back side properly. We suggest that the additional Pt coverage and the extended three phase boundary ($SrTiO_3$/Pt/H_2 atmosphere) may lead to changes in the oxygen exchange kinetics[75, 130] and also the diffusion itself.[75]

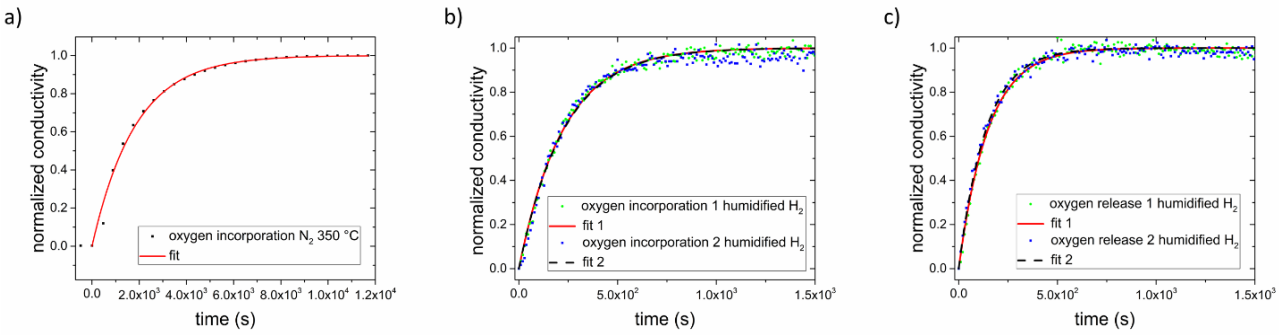

Figure 32: Normalized conductivity of $SrTiO_3$ in N_2 **(a)** and humidified H_2 **(b)** at 350 °C under UV illumination. Fits obtained applying Equation 17 are represented by either a solid red line or a dashed black line. **c)** Normalized conductivity of $SrTiO_3$ after UV light was turned off in humidified H_2 at 350 °C. Equation 18 was used for fitting the experimental data.

4.4.4 Model of the defect chemical processes under and after UV irradiation

Finally, all the consideration made to this point were utilized and a model describing the defect chemical changes in $SrTiO_3$ under and after UV illumination in a strongly reducing atmosphere (electrons are the major charge carriers) at elevated temperatures is introduced. The oxygen chemical potential can be defined by

$$\mu_{O,e} = -\mu_{V_O^{\bullet\bullet}} - 2\mu_{e'} \quad (19)$$

$$\mu_{O,h} = -\mu_{V_O^{\bullet\bullet}} + 2\mu_{h^{\bullet}}, \quad (20)$$

with either the CB electron chemical potential $\mu_{O,e}$ or the VB hole chemical potential $\mu_{O,h}$ respectively. In equilibrium oxygen incorporation and the oxygen release are balanced, the oxygen chemical potential is the same inside $SrTiO_3$ and in the gas phase. Additionally, $\mu_{O,e}$ equals $\mu_{O,h}$. Additionally, $\mu_{e'} = -\mu_{h^{\bullet}}$ and thus $\mu_{O,e}$ equals $\mu_{O,h}$.

When UV light is switched on, the oxygen chemical potential is split into two quasi chemical potentials $\mu_{O,e}$ and $\mu_{O,h}$ in the UV absorption zone. The oxygen chemical potential in the bulk is not affected yet (Figure 33b). The hole-related oxygen chemical potential is higher than in the bulk and drives oxygen from the absorption zone into the bulk, while the electron related $\mu_{O,e}$ does the opposite. Empirically, we find an increased chemical potential in the bulk after UV and thus we suppose that the hole-related chemical diffusion coefficient and driving force is predominant in this "competition" (Figure 33c). Since we assume slow surface kinetics and fast diffusion, this leads to a temporary oxygen depletion in the UV absorption zone.

However, also oxygen incorporation (via water splitting) and oxygen release (via water formation from H_2) are affected by UV due to the modified charge carrier concentrations. Oxygen incorporation rates due to water splitting are most probably enhanced by the additional photoelectrons in the conduction band and the same is true for oxygen evolution involving (photo)holes in the valence band. Empirically, we find a situation where under UV oxygen is continuously driven into the crystal. Hence, the electron related oxygen incorporation seems to be more accelerated by UV than the hole-related oxygen release (see Figure 33b and c). Therefore, we have a higher electron related net incorporation flux

($J_{O,e,in}$) than hole related oxygen release flux ($J_{O,h,out}$) upon UV. This warrants continuous oxygen supply to the UV zone and the bulk upon UV. Accordingly, the oxygen chemical potentials are successively pumped up. Finally, a steady state (not an equilibrium) is reached with equal diffusion fluxes into the bulk and into the UV zone due to hole/electron-related oxygen chemical diffusion (Figure 33d), and also equal oxygen incorporation and evolution rates. The oxygen chemical potential in the bulk is increased by $\Delta\mu_O$ compared to the chemical potential in the gas phase. After switching off UV the oxygen quasi-chemical potentials vanish (Figure 33f), and oxygen is slowly released back into the gas phase. $\Delta\mu_O$ declines until equilibrium ($\mu_{O,eq}$) is reached again. A very similar qualitative description results for bulk diffusion limitation. (Additional space charge effects may play only a minor role under UV but can also further complicate the picture).

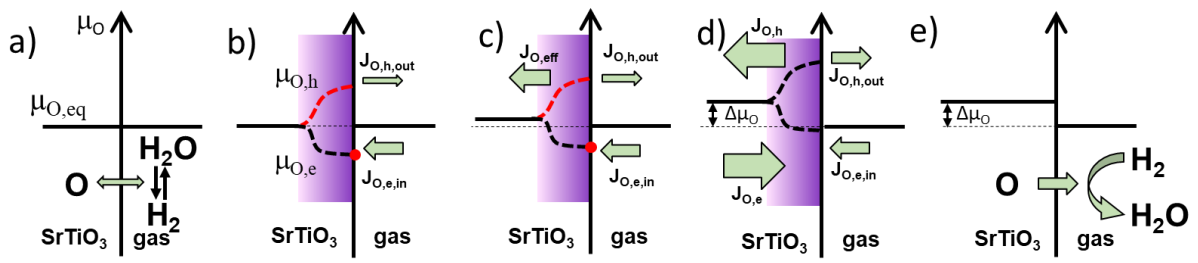

Figure 33: Model based on the formation of oxygen quasi-chemical potentials under UV illumination, explaining why oxygen is incorporated into and diffuses through an oxide-semiconductor, here $SrTiO_3$. **a)** Equilibrium oxygen chemical potential, oxygen incorporation into the semiconductor (by water splitting) equals the oxygen release into the gas phase (forming H_2O). **b)** As UV light is switched on, two oxygen quasi-chemical potentials are formed in the UV absorption zone due to the formation of electron-hole pairs. The dark bulk is not affected yet. The oxygen incorporation rate by conduction band electrons is enhanced. **c)** In the UV absorption zone valence band hole connected oxygen chemical diffusion drives oxygen into the bulk. Oxygen diffusion in the bulk increases the oxygen chemical potential throughout the whole specimen. **d)** A new steady state under UV illumination is finally established. Oxygen incorporation (via conduction band) is balanced by oxygen release (via valence band), the oxygen chemical potential in the dark bulk is increased by $\Delta\mu_O$. **e)** When the UV light is switched off, oxygen is released again out of the single crystal into the gas phase.

4.5 Conclusion

Under strongly reducing H_2-containing atmospheres UV irradiation of $SrTiO_3$ led to a decrease in the in-plane conductivity at 350 °C. At the illuminated surface, an approx. 1 µm thick zone was established in which photoconductivity was two to three orders of magnitude higher than the bulk conductivity before UV irradiation. Nevertheless, in the remaining bulk the conductivity decreased gradually upon UV illumination, due to water splitting, subsequent oxygen incorporation and oxygen diffusion. This effective p_{O_2} increase lowered the n-type conductivity of $SrTiO_3$. For back side contacted single crystals, the resulting effects of the bulk conductivity shift were simulated by finite element calculations. Oxygen incorporation under and oxygen release after UV illumination seem both limited by the surface exchange reactions in humidified H_2 and did not differ much. A change in the measurement configuration, where electrodes were placed at both the illuminated front side and the dark back side, led to a more pronounced photoconductivity effect which confirmed our interpretation, i.e., the formation of a highly conductive region near the surface and a decreased bulk conductivity. Finally, the changes in the defect chemistry were illustrated by a model based on oxygen quasi-chemical potential. On the other hand, in air/N_2 at 350 °C UV illumination led to a rise in the oxygen chemical potential due to an enlarged oxygen incorporation and a conductivity enhancement by more/nearly three orders of magnitude resulted. This is in accordance with the defect chemistry of $SrTiO_3$, since in the p-type conductive region an increased effective p_{O_2} means a higher conductivity.

5 Quantification of oxygen incorporation into polycrystalline Fe-doped $SrTiO_3$ thin films

The experiments shown in this chapter were carried out over the course of Emil Ellmeyer's diploma thesis[131] under Prof. Jürgen Fleig's and my supervision at the Institute of Chemical Technology and Analytics, TU Wien. My guidance included planning of the experiments and the discussion/evaluation of the results. Some small deviation between Ellmeyer's diploma thesis and my doctoral thesis are caused by the independent evaluation of the experimental data. Thus, calculations of the changes of the oxygen contents in the thin film and resonant frequency drift corrections slightly differ.

5.1 Introduction

To provide a direct proof of oxygen incorporation into Fe-doped $SrTiO_3$ thin films under UV irradiation and to quantitatively describe the processes behind, attempts were made to monitor the mass change caused by oxygen incorporation. However due to the small amount of material in thin films, standard approaches of weight measurements, e.g. known from TGA (thermogravimetric analysis) were not applicable. Thus, perovskite thin films were deposited on Y-11° cut gallium orthophosphate ($GaPO_4$) microbalances[70, 72, 132, 133] and the shifts in the resonant frequency occurring due to UV illumination or changes of the measurement atmosphere were monitored. Contrary to conventional AT-cut quartz crystals, $GaPO_4$ can also be used above 400 °C due to its much better high-temperature frequency stability.[133] Hence, $GaPO_4$ sensors are a possible tool to weigh the oxygen incorporated into perovskite thin films at elevated temperatures. Since these measurements were carried out using an in-house built measurement set-up, the system had to be evaluated at first. This was achieved by applying gas changes on microbalances with undoped $SrTiO_3$, $SrTi_{0.98}Fe_{0.02}O_3$, or $La_{0.6}Co_{0.4}SrTiO_{3-\delta}$ thin films on top. The defect chemistry of these three perovskites is very well known, thus the impact of p_{O_2} variations on the oxygen vacancy concentration can either be calculated using defect chemistry models (for $SrTiO_3$ and Fe-doped $SrTiO_3$)[29, 98] or is known from several studies.[134-136] Finally, the applicability of the measurement set-up was evaluated, using Fe-doped $SrTiO_3$ thin films upon UV light exposure.

5.2 Theory and background

5.2.1 $GaPO_4$ microbalances

In general, an oscillation of piezoelectric materials can be induced by applying an alternating field. Thereby a standing wave is generated when half the thickness of the resonator (including the applied electrodes) is equal to the acoustic wavelength of the material. Thus, the resonant frequency depends on the thickness, the shear modulus, the density of the used resonant crystal and the mass of the deposited material. It is important that the deposited electrodes are thin compared to the piezoelectric active material, since the velocity of sound has to be identical in the whole device. Considering the discussed relations Equation 21 can be derived.[137]

$$f_0 = \frac{\upsilon_{tr}}{2d_{tr}} \tag{21}$$

Where f_0 denotes the resonant frequency, υ_{tr} the velocity of sound, and d_{tr} the thickness of the system (crystal and electrodes).

In 1959 G. Sauerbrey first described the correlation between measured frequency change and elastic mass change. [138] With his Equation 22 he laid the foundation of commercial quartz crystal microbalances.[137]

$$-\Delta f = \frac{2Nf^2}{A\sqrt{\mu_q \rho_q}} \times \Delta m \tag{22}$$

Here the frequency change (Δf) depends on the number of the harmonic (in general N = 1), the resonant frequency (f), the piezoactive area (A), the shear modulus (μ_q = approx. 2.16×10^{11} g cm^{-1} s^{-2} at 400 °C),[71] elastic mass change(Δm), and the density of the used microbalance material (ρ_q = 3.539 g cm^{-3} at 400 °C)[139]. Equation 22 can be simplified to[137]

$$\Delta f = -C_m \times \Delta m \tag{23}$$

Thereby the sensitivity factor (C_m) of a Y-11° cut $GaPO_4$ crystal with a resonant frequency of 5.6 +/- 0.1 MHz and a piezoactive area of 28.27 mm^2 is in the range of 0.254 Hz ng^{-1}. Please note that these equations are only valid as long as the deposited thin films only exhibit 2 % of the thickness of the used piezoactive crystal. Additionally, surface roughness should be constant during the conducted experiments. The influence of the surrounding media is of great importance when mass changes are measured in fluids. When the measurements take place in gas atmospheres the influence of these can be neglected in a first approximation. [137] Nevertheless, gas convection should be minimized.

Under the assumption that the volume of the perovskite unit cell (deposited onto the front side of the microbalance) remains constant despite a change in the oxygen vacancy concentration, the change in its oxygen stoichiometry (Δδ) can be calculated using Equation 24:

$$\Delta\delta = \frac{\Delta m \times N_A}{M_{oxygen}} \times \frac{V_{unit\ cell}}{A \times d} \quad (17)$$

N_A is the Avogadro constant, d is the thin film thickness, $V_{unit\ cell}$ volume of the unit cell of the to investigate perovskite, and M_{oxygen} the molar mass of atomic oxygen.

5.2.2 Determination of the resonant frequency

In order to determine the resonant frequency an equivalent circuit can be constructed describing crystal oscillators. Such an equivalent circuit is displayed in Figure 34 below.[137]

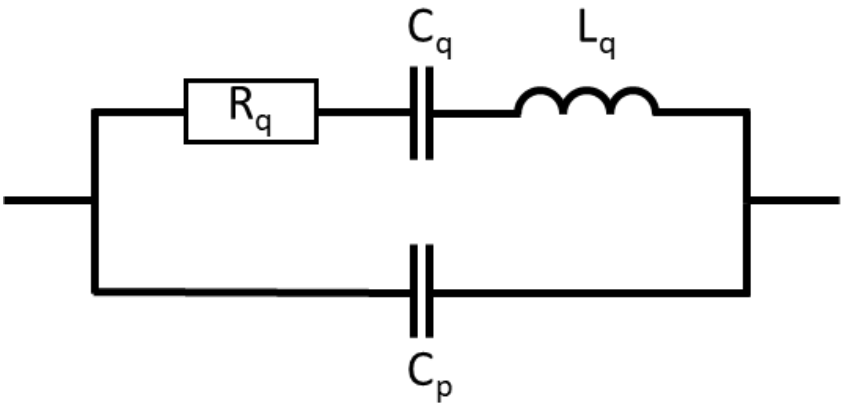

Figure 34: Equivalent circuit of a crystal oscillator.

The in circuit shown in Figure 34 exhibits two resonant frequencies, ω_S and ω_P. Thereby ω_S is the serial resonant frequency, which is equivalent to the mechanical resonant frequency ω_0 of the piezoelectric material.[138]

$$\omega_S = \frac{1}{\sqrt{L_q \times C_q}} = \omega_0 \tag{18}$$

If the losses at R_q are neglected, the parallel resonant frequency ω_p ($\omega_p > \omega_s$) can be calculated using Equation 26. The used commercial crystals exhibit by at least a factor of 1000 larger C_p than C_q. As a consequence, changes in the mechanical resonant ($\Delta\omega_0$) equal $\Delta\omega_S$ and $\Delta\omega_p$ (compare Equation 27).[138]

$$\omega_P = \frac{1}{\sqrt{L_q \frac{C_q \times C_p}{C_q + C_p}}} \approx \omega_0 \times \left(1 + \frac{C_q}{2C_p}\right) \tag{19}$$

$$\Delta\omega_0 = \Delta\omega_S = \Delta\omega_p \tag{20}$$

In Equation 26 and Equation 28 C_p represents the parallel (static) capacitance mainly caused by the applied electrodes. C_q is the motional capacitance and L_q the motional inductance. R_q represents the serial motional resistance.[138] Finally, a quality factor (Q) can be expressed as followed:[140]

$$Q = \frac{\omega_S L_q}{R_q} = \frac{1}{\omega_S C_q R_q} \tag{21}$$

5.2.3 Defect chemistry defining the oxygen vacancy concentration in Fe-doped $SrTiO_{3-\delta}$ and $La_{0.6}Sr_{0.4}CoO_{3-\delta}$

For the proper interpretation of the measured mass changes and the calculated changes in the oxygen stoichiometry, the following equations and reactions defining the perovskites defect chemistry have to be considered. Assuming Fe only to be present on the B-site of Fe-doped $SrTiO_3$ the total Fe concentration is the sum of Fe^{3+} (Fe'_{Ti}) and Fe^{4+} (Fe^{x}_{Ti}). Since Fe^{3+} on the B-site is mostly balanced by oxygen vacancies, the maximum oxygen vacancy concentration caused by iron doping is approx. half the doping concentration.[1, 29] However, Fe^{4+} lower the value: Assuming 2 % Fe on the B-site (3.3×10^{20} cm^{-3}), calculations using extended defect chemical models suggest an oxygen vacancy concentration between 8.4×10^{19} cm^{-3} at 380 °C and 9.8×10^{19} cm^{-3} at 410 °C in N_2 with 70 ppm residual oxygen.[98]

$$[Fe_{tot}] = [Fe'_{Ti}] + [Fe^{x}_{Ti}] \quad (22)^{[1]}$$

$$2\,[V_O^{\bullet\bullet}] + [h^{\bullet}] = [Fe'_{Ti}] + [e'] \quad (30)^{[1]}$$

$$Fe^{x}_{Ti} \rightleftharpoons Fe'_{Ti} + h^{\bullet} \quad (1)^{[1]}$$

In $La_xSr_{1-x}CoO_3$ doping with Sr^{2+} leads to a negative effective charge on the A-site (normally occupied by La^{3+}). This can be balanced either by the formation of oxygen vacancies or the formation Co^{4+} on the expense of Co^{3+}.[134, 135, 141] At doping concentrations of $x < 0.3$ mostly Co^{4+} is formed. Between $0.3 < x < 0.7$ the Co^{4+} concentration saturates and additionally oxygen vacancies are generated to maintain charge neutrality.[68] Moreover, the higher the temperature and the lower the applied p_{O_2} the more likely oxygen vacancies are formed. Finally ,the charge transfer between two adjacent Co^{x}_{Co} and the oxygen vacancy dependency from the surrounding p_{O_2} need to be considered.[141]

$$[Co^{\bullet}_{Co}] + 2\,[V_O^{\bullet\bullet}] = [Sr'_{La}] \quad (31)$$

$$2\,Co^{\bullet}_{Co} + O^{x}_{O} \rightleftharpoons 2\,Co^{x}_{Co} + V_O^{\bullet\bullet} + 1/2\,O_2(g) \quad (32)$$

$$2\,Co_{Co}^{x} \;\rightleftharpoons\; Co_{Co}' + Co_{Co}^{\bullet} \tag{23}$$

$$O_O^x + 2h^{\bullet} \;\rightleftharpoons\; 1/2\,O_2(g) + V_O^{\bullet\bullet} \tag{24}$$

5.3 Experimental

5.3.1 $GaPO_4$ microbalance and measurement set-up

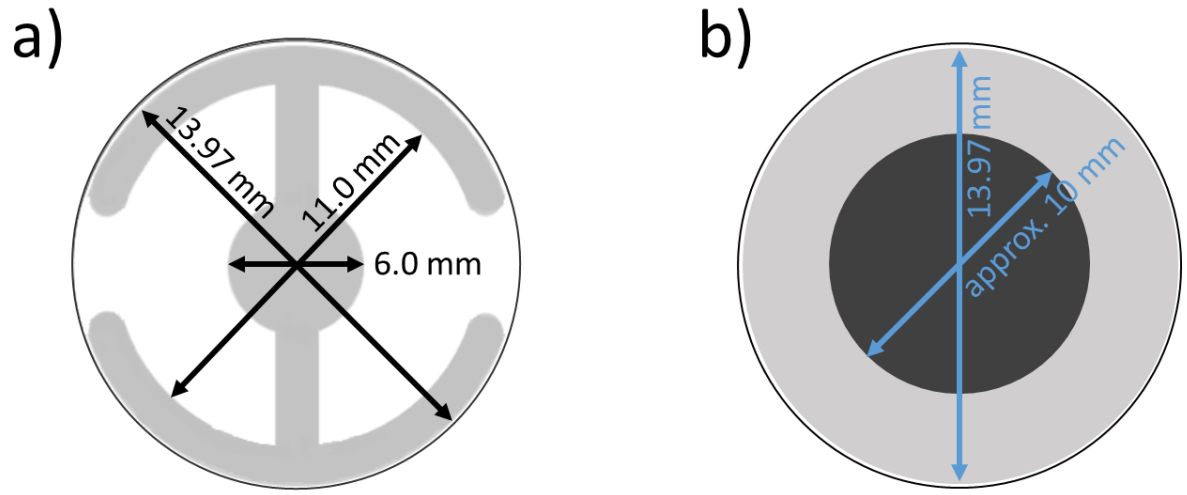

Figure 35: Sketches of $GaPO_4$ microbalances. Pt anchor on the back side **(a)** and Pt film and perovskite thin film on the (illuminated) front side **(b)**.

The experiments were carried out on commercially available $GaPO_4$ microbalances (Piezocryst, Austria). They exhibit a piezoactive area of 28.27 mm^2 and consist of an either 0.2 mm or 0.3 mm tick Y-11° cut $GaPO_4$ single crystal, a Pt anchor on the back side and a Pt layer and the thin film to investigate on top on the front side (compare Figure 35). The thicker single crystals are much easier to handle and exhibit less noise. However, they possess a lower resonant frequency (5.6 +/- 0.1 MHz, 4.1 +/- 0.1 MHz respectively) and therefore a poorer mass resolution (3.84×10^{-7} Hz cm^2 g^{-1}, 7.42×10^{-7} Hz cm^2 g^{-1}). Moreover, the thicker microbalances purchased had no Pt layer on the front side, hence 200 nm Pt was sputtered using a DC magnetron sputtering system (2×10^{-2} mbar Ar, 100 mA, BAL-TEC MED 020 Coating system, Baltec, Switzerland) onto the front side using a shadow mask to prevent Pt to cover the edges. The in-house built measurement set-up is displayed in Figure 36. It

consists of a Al_2O_3 frame, two Al_2O_3 disks, a Al_2O_3 rod, the $GaPO_4$ microbalance, Pt wiring and a quartz rod acting as UV light guide. The microbalance was placed in between of two Al_2O_3 disks. These are Pt coated on the sides facing the $GaPO_4$ single crystal and connected to a quartz crystal microbalance resonator (Gamry, USA) via Pt wires. For temperature monitoring a S-type thermocouple was placed beneath the Al_2O_3 near the sample. For experiments under UV irradiation, the flame-polished end of quartz rod (light guide) was mounted in a distance of approx. 2 cm from the microbalance. The entire set-up is housed by a borosilicate glass tube closed gas tight on one side. On the other side the gas inlet and outlet and sockets to connect the Pt wires are positioned. Temperature was controlled by a tube furnace (Carbolite Gero, Germany/United Kingdom) and a Eurotherm controller (Schneider Electric, France). All experiments were carried out in air, N_2 containing approx. 70 ppm O_2, synthetic air, or O_2. Gas flow rate was regulated using mass flow controllers (Brooks Instrument, Germany). Except for the temperature dependency measurements in N_2 (40 sccm) the flow rate was fixed to 10 sccm for all gases and gas mixtures, to reduce the drift of the resonant frequency over time.

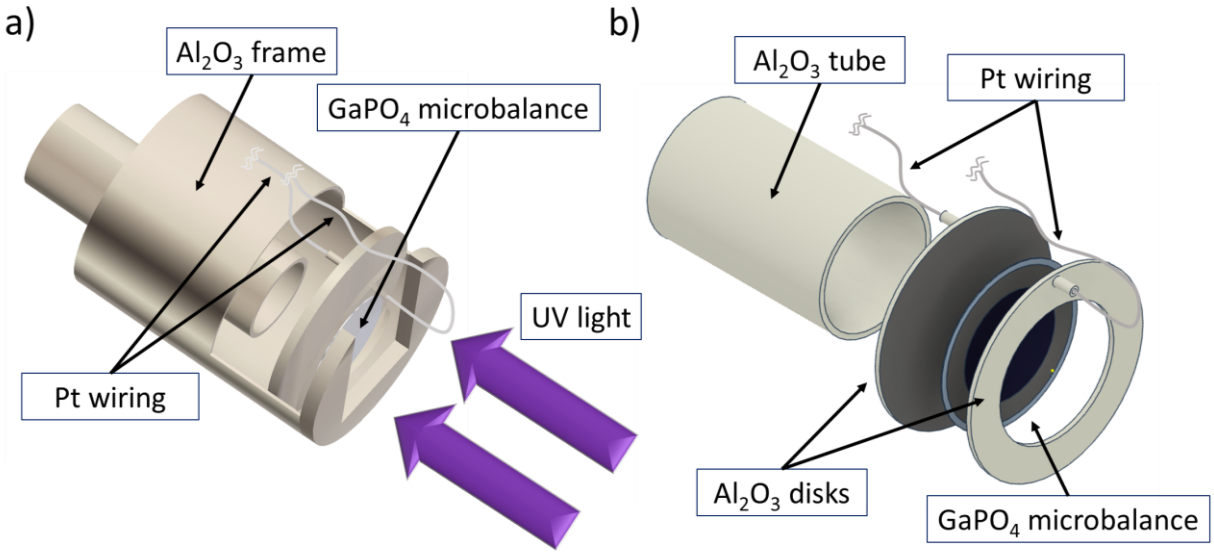

Figure 36: **a)** 3D sketch of the in house-built measurement set-up. It is made of a Al_2O_3 frame. An Al_2O_3 rod presses two Pt coated Al_2O_3 disks together. In between $GaPO_4$ microbalances are positioned. The frontside of the microbalance can be illuminated by UV light, a flame-polished quartz rod acts as light guide. Microbalances are conducted via the Pt films on the Al_2O_3 sheets and two Pt wires. **b)** Enlarged illustration of the Al_2O_3 tube and Al_2O_3 disks with a microbalance in between and Pt wiring.

5.3.2 Experimental parameters

All investigated thin films were produced using a pulsed laser deposition (PLD) system (Kr/F excimer laser (Lambda Compex Pro 205F, λ = 248, Coherent, USA). A more detailed description can be found elsewhere in this thesis. In the following, the deposition parameters for Fe-doped $SrTiO_3$ and $La_{0.6}Sr_{0.4}CoO_3$ are summarized.

Table 3: Deposition parameters of the investigated thin films

Thin film	Approx. thickness (nm)	Pressure (mbar)	Frequency (Hz)	Temperature (°C)	Target distance (cm)
$SrTiO_3$	220	$1.4*10^{-1}$	5	ca. 600 °C	6
$SrTi_{0.98}Fe_{0.02}O_3$	250	$1.4*10^{-1}$	5	ca. 600 °C	6
$La_{0.6}Sr_{0.4}Co_3$	415	$2.0*10^{-2}$	10	ca. 600 °C	5.7

All used thin films exhibited roughly a diameter of 10 mm and were positioned in the middle of the $GaPO_4$ single crystal with the help of a Al_2O_3 shadow mask. The performed experiments can be divided into three groups: determining the drift of the system and the ideal measurement temperature in air on a microbalance without thin film deposited, gas exchange experiments to verify the method and monitoring the impact of UV irradiation on the weight of a Fe-doped thin film. The parameters of the performed measurements are given in Table 4.

Table 4: Parameters of the weight measurements of thin films deposited onto $GaPO_4$ microbalances.

Measurements	$GaPO_4$ thickness (mm)	Thin film	Atmosphere	Temperature (°C)
Drift and temperature dependency	0.2	none	air, N_2	370-425
	0.2	$SrTiO_3$	N_2	400
Gas exchange	0.3	$La_{0.6}Sr_{0.4}CoO_3$	N_2 and O_2	380-410
	0.2	$SrTiO_3$	N_2, 1 % O_2, 20 % O_2, O_2	380, 400
	0.3	$SrTi_{0.98}Fe_{0.02}O_3$	N_2 and O_2	380-410
UV irradiation	0.3	$SrTi_{0.98}Fe_{0.02}O_3$	N_2, syn. air, O_2	ca. 360 - 400

5.4 Results and discussion

The measurements were performed either on 0.2 or 0.3 mm thick microbalances with a sputtered Pt layer and a $La_{0.6}Sr_{0.4}Co_3$, $SrTiO_3$ or $SrTi_{0.98}Fe_{0.02}O_3$ on top. Some of the used samples are pictured in Figure 37 below. Too rapid cooling after thin film deposition caused the cleavage of a 0.3 mm thick $GaPO_4$ single crystal (Figure 37d). Apart from that the thicker specimens were much easier to handle and therefore used for most of the experiments.

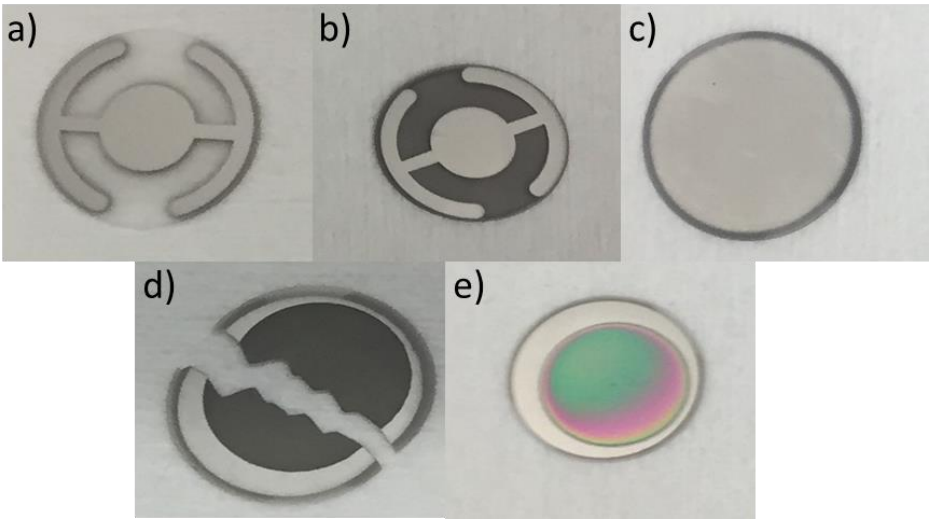

Figure 37: **a)** Purchased 0.3 mm thick $GaPO_4$ microbalance without Pt on the frontside. **b)** 0.2 thick microbalance before thin film deposition. Both sides exhibit Pt electrodes. **c)** 0.3 mm thick $GaPO_4$ single crystal after sputtering Pt on the front side, edges were not covered with Pt. **d)** Microbalances with $La_{0.6}Sr_{0.4}Co_3$ thin film on top (broken). **e)** Microbalance with $SrTi_{0.98}Fe_{0.02}O_3$.

5.4.1 Temperature dependency and drift of the resonant frequency

The resonant frequency of $GaPO_4$ microbalances is known to exhibit a much lower temperature dependency than the resonant frequency of quartz microbalance. Nevertheless, in air between 300 and 500 °C the resonant frequency of $GaPO_4$ can change by more than. 200 Hz. Additionally, the resonant frequency drifts and shifts over time. To find the optimal measurement parameters, the resonant frequency dependency of a 0.2 mm thick $GaPO_4$ microbalance was monitored without a thin film on top between 370 and 425 °C in air and approx. 370 and 390 °C in N_2 (steps of 10 °C set temperature for both atmospheres). In Figure 38 the results of these measurements are displayed.

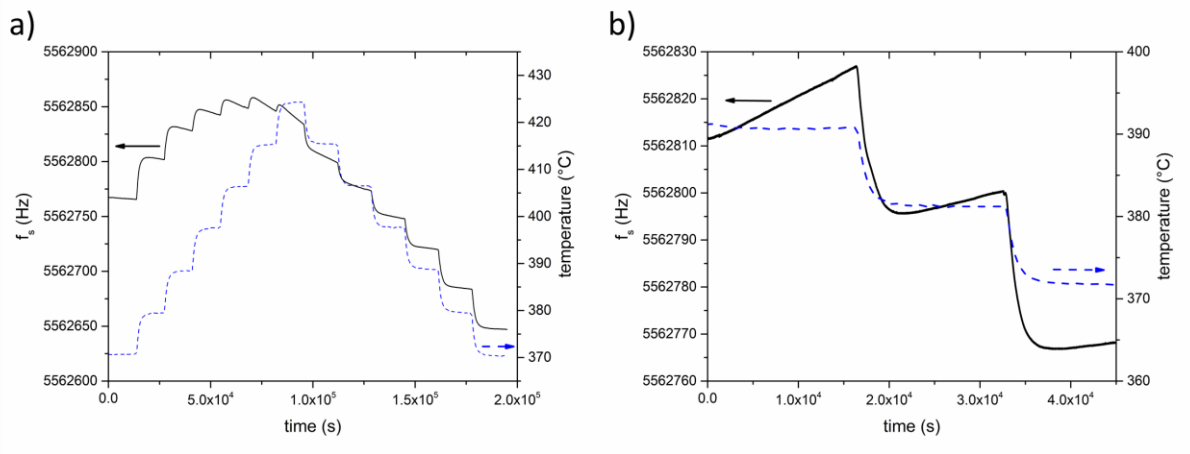

Figure 38: Temperature dependence of the resonant frequency measured in air **(a)** and N_2 **(b)**. Experiments were carried out on a 0.2 mm thick microbalance without a thin film on top. The higher the temperature the higher the resonant frequencies in both atmospheres. The slope of the drifts is negative in air and positive in N_2 (40 sccm flow).

In both atmospheres the resonant frequencies and the drifts increased with temperature. In air the drift amounted to -135.4 ppm Hz s^{-1} at 370 °C and at 425 °C to -1575 ppm Hz s^{-1}. On the other hand, the higher the temperature the smaller the frequency increases due to the temperature steps became. The temperature change from 370 to 380 °C resulted in a resonant frequency shift of +30 Hz, whereas an increase from 415 to 425 °C only caused the frequency to adjust by +5 Hz. Therefore at approx. 415 °C the frequency decline caused by the drift (approx. -25 Hz) was larger than the frequency increase (+5 Hz) due to heating the set-up by 10 °C (compare Figure 38a). The monitored frequency changes according to the temperature jumps were quite reproducible during cooling from 425 °C back to 370 °C. Consequently, the resonant frequency decease from 5562767 to 5562653 Hz over the course of the whole measurement occurred mostly due to the frequency drift. In N_2 the drift exhibited a positive slope and changes from 300 ppm Hz s^{-1} at 370 °C to 981 ppm Hz s^{-1} at 390 °C and a gas flow of 40 sccm. In a next step, a $SrTiO_3$ thin film was deposited on top of the microbalance and the temperature drifts were investigated in N_2. Reducing the flow from 40 sccm to 10 sccm the drift can be drastically reduced from 440 ppm Hz s^{-1} to -17 ppm Hz s^{-1} (Figure 39).

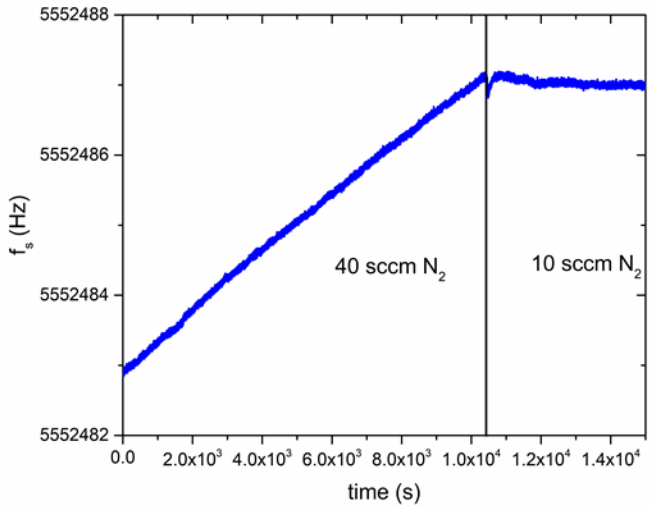

Figure 39: 0.2 mm thick $GaPO_4$ microbalance with a $SrTiO_3$ thin film on top. Reducing the flow rate from 40 sccm to 10 sccm reduced the drift to only -17 ppm Hz s^{-1} at 400 °C.

As a consequence of the described experiments the measurement parameters were optimized. The gas exchange experiments were subsequently conducted between 380 and 410 °C in a p_{O_2} range from 7.0×10^{-5} to 1.0 bar (N_2 to pure O_2) and the gas flow was fixed to 10 sccm.

5.4.2. Gas exchange experiments

According to thermogravimetric measurements an increase in the oxygen content of perovskites can be derived from weight gain during the change of the atmosphere from a low to a higher p_{O_2}.[141] We applied the same principle here, oxygen incorporation into $SrTiO_3$, Fe-doped $SrTiO_3$ and $La_{0.6}Sr_{0.4}CoO_3$ led to a drop in the resonant frequency and since we know the defect chemistry of these perovskites, the sensitivity of our microbalances and the thicknesses of the deposited thin films, we were able to verify our measurement set-up. The first gas exchange experiments were applied on 0.2 mm thick $GaPO_4$ single crystals with a 220 nm thick $SrTiO_3$ thin film on top. At 380 °C the atmosphere was changed from N_2 to O_2 (Figure 40a). The green line represents the actual experimental data. Particularly in O_2 they exhibit a considerable drift. Hence, the data were corrected by the slope of the observed drifts in N_2 and O_2. After this treatment the blue line was obtained, showing nearly no drift at all, neither before nor after the p_{O_2} change. A resonant frequency shift of -3.0 to -3.4 Hz Hz was monitored, which equals a mass gain of 12.0 to 13.6 ng. At 400 °C smaller p_{O_2} steps were realized, from N_2 to a mixture of N_2 and 1 % O_2, subsequently to 20 % O_2 and finally to

pure O_2 Figure 40b). The experimental data were corrected as in the first experiment and changes in the resonant frequency of -0.5 Hz, -2.3 Hz, and -0.9 Hz were obtained. In total the resonant frequency changed by -3.7 Hz (14.8 ng respectively) which is in a quite good accordance with the measurement at 380 °C, due to the fact that at a higher temperature more oxygen vacancies were present in N_2 and were filled when the p_{O_2} increased. The thin film is 220 nm thick and the piezoactive area is 28.27 mm^2. Thus, the weight increase was caused by oxygen incorporation into 6.219×10^{-3} mm^3 of $SrTiO_3$. Changes in the unit cell volume due to oxygen stoichiometry changes and thermal expansion were neglected. Please note that all produced thin films are polycrystalline and not epitaxially grown, the presented calculations are approximation and only serve as proof of concept. In the conducted gas exchange experiments the mass gain amounted to 12.0-13.6 ng or a Δδ of 0.004-0.005 at 380 °C and to 14.8 ng or a Δδ of 0.005 at 400 °C respectively. In undoped $SrTiO_3$ with 25 ppm Ti vacancies an oxygen vacancy concentration of approx. 8.4×10^{17} cm^{-3} (δ of 5.1×10^{-4}) was suggested by our defect chemical model[98] and the deuced changes were thus much larger than expected. However pulsed laser deposition can lead to major cationic deficiencies and therefore the true present oxygen vacancy concentration can be tremendously higher. An effective verification of the measurement set-up was not achievable with undoped $SrTiO_3$ thin films Furthermore, to this point the relatively large frequency decline of -2.3 Hz when the atmosphere was switched from 1 % O_2 to 20 % O_2 cannot be explained. Consequently, undoped $SrTiO_3$ thin films were not used for further microbalance experiments anymore.

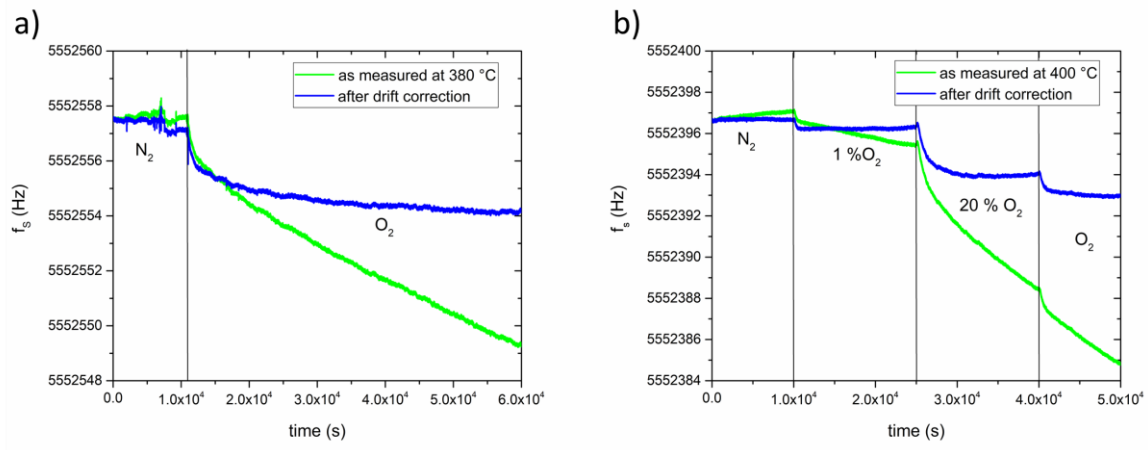

Figure 40: Gas exchange experiments of a $SrTiO_3$ thin film deposited at the frontside of a 0.2 mm thick $GaPO_4$ microbalance at 380 °C **(a)** and 400 °C **(b)**. Green lines represent the experimental data. After drift correction (blue lines) the frequency shifts due to p_{O_2} increase were measured and the mass gain calculated.

Instead, we investigated the mass gain of $La_{0.6}Sr_{0.4}Co_3$ thin films during an atmosphere change from N_2 to O_2 in a temperature range of 380 to 410 °C. Due to handling issues and a better signal to noise ratio 0.3 mm thick $GaPO_4$ microbalances were used from this point on. The reduced sensitivity compared to the 0.2 mm thick $GaPO_4$ single crystals did not impact the experiments dramatically. In N_2 the specimens exhibited hardly any drifts, in O_2 the frequency drifts were again corrected. The obtained experimental (green lines) and the corrected (blue lines) data are shown in Figure 41.

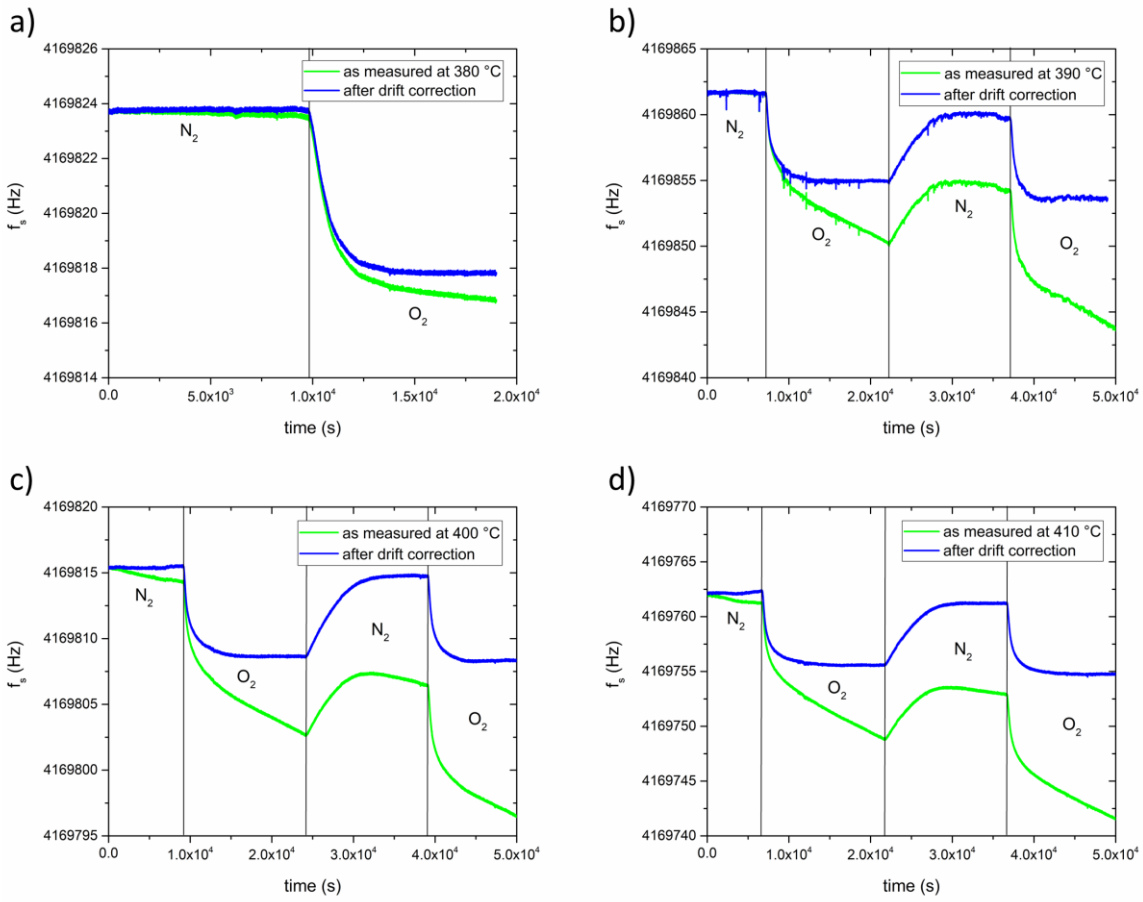

Figure 41: Gas exchange experiments of $La_{0.6}Sr_{0.4}CoO_3$ deposited on top of a 0.3 mm thick $GaPO_4$ microbalance. The measurements were carried out between 380 and 410 °C with temperature steps of 10 °C. and the atmospheres were changed from N_2 to O_2.

At each temperature (except at 380 °C) the atmosphere was changed three times, thus we measured two frequency shifts from N_2 to O_2. The temperature had only a minor impact on the measured shifts: At 380 °C the resonant frequency increased by -6.10 Hz, at 390 °C by -6.70 and -6.38 Hz, at 400 °C by -6.49 and -6.68 Hz, and at 410 °C by -6.57 and -6.45 Hz respectively. These changes are equal to a mass gain of 43.4 to 47.6 ng. All shifts were a little bit smaller when changing the atmosphere from O_2 to N_2. We did not consider these in the

further calculations since lowering the p_{O_2} took by far more time due to the low flow rate of 10 sccm and was more error prone. The film thickness was 415 nm and the piezoactive area 28.27 mm^2. Consequently the unit cell volume amounts to 57.42 $Å^3$ at 400 °C.[142] Using these values, the mass gain of 43.4 ng (47.6 ng) results in a Δδ of 0.008 (0.009). At approx. 420 °C a bulk composition of $La_{0.6}Sr_{0.4}CoO_{3-0.051}$ is expected in N_2 with 100 pm residual O_2 (p_{O_2} of 1.0×10^{-4} bar) and $La_{0.6}Sr_{0.4}CoO_{3-0.025}$ at 1.9×10^{-2} bar, leading to an expected Δδ in the range of 0.026.[135] These data from literature were obtained by thermogravimetric measurements of powders and consequently exhibit a different oxygen vacancy concentration as deposited thin films. Calculations based on impedance measurements, more precisely on the chemical capacitance of 1.5 µm thick $La_{0.4}Sr_{0.6}CoO_{3-\delta}$ dense thin films, suggest a composition of $La_{0.6}Sr_{0.4}CoO_{3-0.033}$ in N_2, and in O_2 δ is in the range of 1×10^{-3} at 600 °C.[136] Since we conducted our measurements in the range of 400 °C we assume an even slightly lower oxygen vacancy concentration. Nevertheless, our obtained results can be compared to these literature values to a certain extent. The mass gains measured by the $GaPO_4$ microbalances and the calculated changes in the stoichiometry seem to be plausible and in same range as those reported in literature.

Finally, oxygen composition changes of $SrTi_{0.98}Fe_{0.02}O_{3-\delta}$ were investigated by atmosphere changes from N_2 to O_2 in a temperature range of 380 to 410 °C (Figure 42). The experimental data were again corrected by the drift. At 410 °C the measured resonant frequencies scattered a lot, nevertheless a shift due to the p_{O_2} increase could be estimated. At 380 °C the changes of the resonant frequency amounted to -0.9 Hz, at 390 °C to -1.18 and -0.93 Hz, at 400 °C to -1.1 and -0.9 Hz, and at 410 °C -1.4 Hz. Overall, the results scatter a lot and differ by approx. 20 % at 390 and 400 °C. From the measured frequency declines mass gains of 6.6 ng (at 380 °C) to 10.3 ng (at 410 °C) were calculated and they are equal to a Δδ of 0.002 to 0.003. Our defect chemical model suggests a Δδ of 0.004 at 380°C and 0.003 at 410 °C. Please note that these represent bulk equilibrium values and most probably differ for polycrystalline thin films.[98] Nevertheless, our obtained changes are very similar to those expected from the calculations and thus we believe that our measurement set-up meets the standards to be used to prove whether oxygen is incorporated or released into/out of a Fe-doped thin films under UV irradiation in N_2 and O_2.

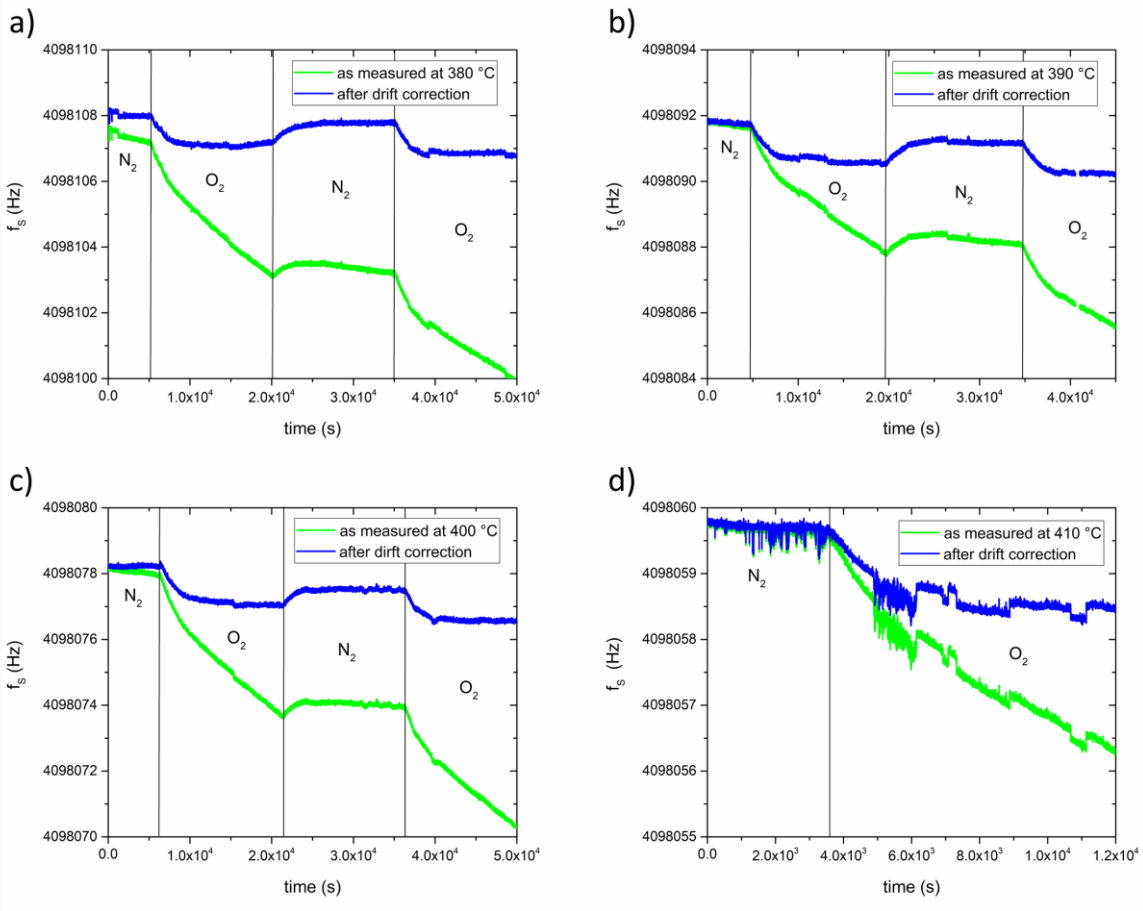

Figure 42: Resonant frequency shifts caused by atmosphere changes from N_2 to O_2 and vice versa between 380 and 410 °C. Oxygen stoichiometry and thus mass changes of a $SrTi_{0.98}Fe_{0.02}O_{3-\delta}$ thin film deposited onto the frontside of a 0.3 mm thick $GaPO_4$ microbalance. Experimental data (green line) were corrected by the drift (blue line data after correction) in order to obtain the frequency shifts.

5.4.3 UV irradiation

Subsequent to the gas change experiment the $GaPO_4$ microbalances were used to weigh the mass change of nominally 2 % Fe-doped thin films caused by UV irradiation due to a change in the oxygen stoichiometry. A Fe-doped $SrTiO_3$ thin film deposited on a 0.3 mm thick $GaPO_4$ single crystal was illuminated with UV light in N_2 and O_2 (Figure 43). Since the UV light itself heats the microbalance, the changes measured during UV illumination cannot be used for an analysis. However, the mass gain can be calculated by comparing the resonant frequency before and shortly after UV irradiation. Oxygen release is by far slower than the oxygen incorporation, hence the impact of UV heating on the resonant frequency can be separated from the shifts caused by mass gain. The resonant frequencies before UV illumination and 600 s after UV light was turned off are compared, since heating effects should be gone by

then. The sharp frequency spikes in the moment the UV light was turned on or off cannot be explained to this point. At 380 °C in O_2 the resonant frequency before and after UV illumination differ by -2.4 Hz and in N_2 by -1.4 Hz. The thin film mass gains amount to 17.7 ng in O_2 and 10.3 ng in N_2. These values correspond to a $\Delta\delta$ of 0.003 and 0.006 respectively. The measurements suggests that in N_2 less oxygen was incorporated into the Fe-doped $SrTiO_3$ thin film than in O_2 even though slightly more oxygen vacancies should be present before UV irradiation in N_2 (1.478×10^{20} cm^{-3}) than in the O_2 (8.4×10^{19} cm^{-3}) atmosphere. In N_2, twice the amount of oxygen was incorporated due to UV irradiation than during the gas exchange experiment. Calculations based on a defect chemical model suggest the presence of an oxygen vacancy concentration of 8.4×10^{19} cm^{-3} in O_2 and of 1.48×10^{20} cm^{-3} in N_2 at 380 °C.[98] This corresponds to an oxygen deficiency of 0.005 (0.009) in O_2 (N_2). Thus, the measurements suggest that more than half (two third) of the present oxygen vacancies were filled during the UV irradiation in O_2 (N_2).

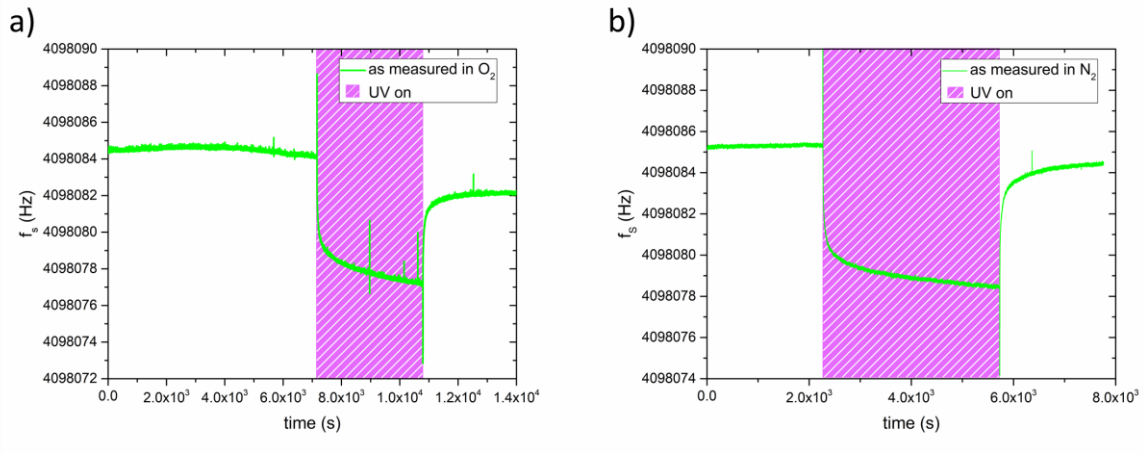

Figure 43: Resonant frequency shifts due oxygen stoichiometry changes of a Fe-doped $SrTiO_3$ thin film under UV irradiation at 380 °C in O_2 **(a)** and N_2 **(b)**. The green line resembles the experimental data, no drift correction was applied.

In Figure 44 UV irradiation measurements of a Fe-doped $SrTiO_3$ thin film between approx. 360 and 405 °C in an atmosphere consisting of 80 % N_2 and 20 % O_2 are displayed. Heating the sample from approx. 363 °C to 393 °C caused an increase of the resonant frequency before illumination. However nearly no change was detected during the temperature increase from 383 to 393 °C. Above 393 °C the resonant frequency started to drop during further heating. During UV irradiation itself, the resonant frequency sharply increased below and quickly declined above 383 °C. At each temperature, the experimental data were

corrected by the drift before UV, since under UV drift and frequency shift due to mass gain cannot be separated from each other. When the resonant frequencies before and after UV illumination are compared, shifts between -2.5 Hz (at 363 °C) and -3.0 (at 393 °C) are measured. A mass gain of 18.4 to 22.1 ng and a Δδ of 0.006 to 0.007 is suggested. Compared to the results from our defect chemical model, these changes suggest that nearly all oxygen vacancies present before UV irradiation were filled after the illumination.

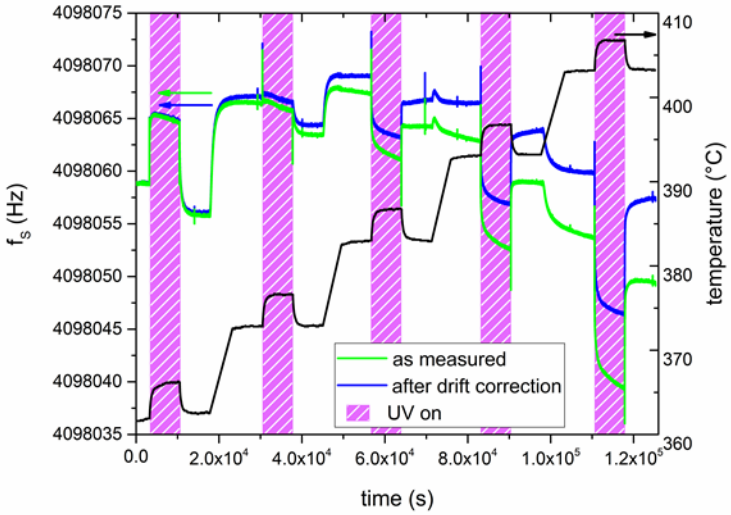

Figure 44: UV irradiation of a $GaPO_4$ microbalance with a Fe-doped thin film on top at approx. 363 to 403 °C in an atmosphere of 80 %N_2 and 20 %O_2. Heating the specimen from 393 to 403 °C led to a decline of the resonant frequency. Depending on the temperature under UV irradiation the resonant can either be reduced or increased.

Further investigations are needed to gain a better understanding if/how the $GaPO_4$ single crystal itself interacts with UV light. Thus, in our understanding the measurements under UV illumination provide only an estimation of the amount of oxygen which is incorporated into the Fe-doped $SrTiO_3$. To this point it is not possible to perform kinetic studies on $GaPO_4$ microbalances, there are still too many uncertainties (e.g. drift, temperature impact) present. Nevertheless, the experiments clearly show that oxygen is incorporated into the thin film and alters its mass.

5.5 Conclusion

An in-house build measurement set-up was used to determine mass changes of perovskite thin films in the range of ng. For this purpose, purchased 0.2 and 0.3 mm thick $GaPO_4$ microbalances were positioned between two Pt coated Al_2O_3 disks and resonant frequency shifts caused either by varying the p_{O_2} or UV irradiation were monitored. Three different perovskites namely undoped $SrTiO_3$, $SrTi_{0.98}Fe_{0.02}O_3$, and $La_{0.6}Sr_{0.4}CoTiO_{3-\delta}$ were investigated. First the measurement parameters were optimized, and subsequently mass gains obtained by changing the atmosphere from N_2 to O_2 are discussed. Using these data Δδ of the oxygen contents were calculated. The results are plausible and are in the range of calculated or literature data, respectively, for Fe-doped $SrTiO_3$ and $La_{0.6}Sr_{0.4}CoTiO_{3-\delta}$. Finally, the first direct proof of oxygen incorporation into a polycrystalline $SrTi_{0.98}Fe_{0.02}O_3$ thin film by UV irradiation was found. However, the impact of UV light on the $GaPO_4$ single crystals is not clear yet. Also, the occurrence of spikes in the moment when UV light was turned on or off cannot be explained, for a deeper understanding of this phenomenon further investigations are needed. Kinetic studies on the oxygen incorporation or release were not possible since the observed changes in the resonant frequency were caused at least by three overlapping processes: the change in the oxygen content, heating effects of the UV light, and drifts in the frequency.

6 Ultra-low conductivity in doped $SrTiO_3$ thin films

The data shown in the following chapter were obtained while working on the manuscript "Unravelling the Origin of Ultra-Low Conductivity in Doped $SrTiO_3$ Thin Films: Sr Vacancies as the Key Driver for Fermi level Pinning".[143] The manuscript is currently close to submission and the authors Maximilian Morgenbesser and myself contributed equally to this work. Besides discussion I focused on the performing the sample preparation, X-ray diffraction, X-ray absorption, and X-ray standing wave measurements and writing the respective parts of the manuscript. Thus, parts of the text e.g., the experimental section of the X-ray diffraction, X-ray absorption, and X-ray standing wave measurements and the results of X-ray absorption and X-ray standing wave measurements are directly taken from the abovementioned manuscript. Also, the focus of this following chapter lies on these X-ray based measurements. Nonetheless, to provide a conclusive discussion and interpretation of the findings, additional measurements (e.g., impedance spectroscopy, RBS, ICP-OES, etc.), and calculations of other contributors are displayed as well. These are undoubtedly marked, and the respective main contributor(s) is(are) stated.

6.1 Introduction

After the investigation of undoped and Fe-doped $SrTiO_3$ single crystals, epitaxially grown $SrTiO_3$ thin films were investigated in terms of their conductivity and defect chemistry. This is of high interest, since the understanding of their properties is essential for the development of $SrTiO_3$ based high temperature thin film photovoltaic cell and also for applications in the field of resistive switching.[19, 21, 32] Recently, pseudo-intrinsic conductivities were found in doped $SrTiO_3$ thin films at 300-700 °C by Morgenbesser et al..[74] Consequently, in the following $SrTiO_3$ thin films with a broad range of dopants were investigated and a model was deduced, explaining the observed very low conductivity. In general, differences between single/polycrystalline $SrTiO_3$ and thin films can be caused by structural differences, the nature of present space charge zones, nonstoichiometry accommodation trap states in the band gap. A correlation between pseudo-intrinsic behavior and Sr deficiency was already

found and discussed in a previous study of Morgenbesser et al..[74] This indicates that the pseudo-intrinsic conductivities of doped $SrTiO_3$ thin films requires a deep knowledge of their defect chemistry and the effects of doping.

Dopants affect the properties of $SrTiO_3$ differently depending on its charge, position in the crystal lattice (A or B side) and concentration. In the following, Fe is used as a model dopant and the essential defect chemical reactions in Fe-doped $SrTiO_3$ are discussed.

$$Sr_{Sr}^{x} + O_{O}^{x} \rightleftharpoons V_{Sr}'' + V_{O}^{\bullet\bullet} + SrO \quad (25)$$

$$V_{Sr}' \rightleftharpoons V_{Sr}'' + h^{\bullet} \quad (26)$$

$$V_{Sr}^{x} \rightleftharpoons V_{Sr}' + h^{\bullet} \quad (27)$$

$$Ti_{Sr}^{\bullet} \rightleftharpoons Ti_{Sr}^{\bullet\bullet} + e' \quad (28)$$

$$Fe_{Sr}^{\bullet} \rightleftharpoons Fe_{Sr}^{x} + h^{\bullet} \quad (29)$$

$$Fe_{Ti}^{X} \rightleftharpoons Fe_{Ti}' + h^{\bullet} \quad (1)$$

$$O_{O}^{x} \rightleftharpoons \frac{1}{2}O_2 + V_{O}^{\bullet\bullet} + 2e' \quad (40)$$

$$nil \rightleftharpoons h^{\bullet} + e' \quad (3)$$

The formation of cation vacancies (partial Schottky reaction, Equation 35)[115] are only relevant during sample preparation, due to their low mobility at the measurement conditions.[29] Additionally, thin films produced by pulsed laser deposition tend to exhibit a lower Sr/Ti ratio than the used target material.[144-148] Consequently, Sr vacancies are assumed to be the dominant cation vacancy in the investigated thin films. In general, they act as acceptor dopants and affect the activation barrier of oxygen ion diffusion.[149, 150] The formation of antistites defects, due to a change in site occupation of Ti^{4+} (from B to A-site) generates donor states.[151-153] A reduction of Ti^{4+} to Ti^{3+} on the A-site is plausible and thus has to be considered as well (Equation 38). Fe can either occupy the Sr or the Ti lattice site. When positioned on the A-site the valency is 2+ or 3+ (Equation 39), either being defect chemically neutral or acting as a donor. On the B-site, on the other hand, Fe exhibits the

valency of 3+ or 4+. Here, Fe is an acceptor or again neutral.[154] As discussed before, conductivity is also a function of the p_{O_2} and $SrTiO_3$ can change from a n-type semiconductor to a p-type semiconductor in dependence of the surrounding atmosphere (Equation 40). Finally, the generation of electron and holes due to thermal excitation has to be considered (Equation 3).[115] In the following the conductivity elemental composition, structure, and defect chemistry of metal doped $SrTiO_3$ thin films were investigated by impedance spectroscopy, inductively-coupled plasma optical emission spectroscopy (ICP-OES), Rutherford backscattering spectrometry (RBS), X-ray diffraction (XRD), X-ray standing wave measurements (XSW), X-ray absorption spectroscopy (XAS), time-of-flight heavy ion elastic recoil detection analysis (ToF-ERDA), and positron annihilation lifetime spectroscopy (PALS).

6.2 Experimental

6.2.1 Sample preparation

For pulsed laser deposition target preparation $SrCO_3$, TiO_2, and in case of doping either Fe_2O_3, NiO, or Al_2O_3 were mixed in an agate mortar and subsequently isostatically pressed. Finally, the pellets were calcinated at 1000 °C for 2h in air, milled again and sintered at 1500 °C for 5h in air. Phase purity was confirmed by X-ray diffraction. Thin films were deposited either on undoped $SrTiO_3$, on Nb-doped $SrTiO_3$ (0.5 wt% Nb), or on yttria doped zirconia substrates (all purchased from Crysrec GmbH, Germany). Films on undoped $SrTiO_3$ substrates were used for reciprocal space mapping, X-ray absorption, XSW, PALS, and RBS measurements. Impedance spectroscopy was performed on films deposited on Nb-doped $SrTiO_3$ and YSZ substrates were used for ICP-OES measurements. Thin films were prepared using a KrF excimer laser (λ = 248 nm, COMPex Pro 201F, Coherent, Netherlands) with a pulse duration of 25 ns. The target to substrate distance was set to 55 mm, the laser fluence to 1.1 J cm^{-2}, the p_{O_2} to 0.15 mbar, the substrate temperature to approx. 650 °C, and the pulse frequency to 5 Hz. The thickness was determined using a ZrO_2 slurry, shielding parts of the substrate during the deposition process. Afterwards the height of the formed step was determined by stylus profilometry using a Dektak measurement set-up (Brucker, USA). Films with a thickness of 80-350 nm were produced.

6.2.2 Determination of the composition and defect chemistry

The composition was analyzed by ICP-OES, RBS and ToF-ERDA measurements. ICP-OES was performed by Christopher Herzig at TU Wien, details of the performed measurements can be

found elsewhere.[143] RBS and ToF-ERDA measurements were performed at PSI, Switzerland by Max Döbeli. Additional information on the defect chemistry was determined by PALS, carried out at ELBE at the Helmholtz-Zentrum Dresden - Rossendorf e. V., a member of the Helmholtz Association by Oskar Liedke and others.

6.2.3 Impedance spectroscopy

Electrochemical impedance spectroscopy was performed using an Alpha-A High Resolution Analyzer (Novocontrol, Germany). The impedance was measured from 0.9 MHz to 1 Hz (10 points per decade) and a temperature range of 280-740 °C. Temperatures were measured by K- or S-type thermocouples. Homogeneous heating was assured by a tube furnace (Gero, CARBOLITE GERO, Germany). On the thin films Pt microelectrodes (as working electrodes) with thicknesses of approx. 100 nm and diameters of 300 µm were applied by lift off photolithography and sputtering (BAL-TEC MED 020 Coating system, Baltec, Switzerland). On the backside of the Nb-doped $SrTiO_3$ substrates, porous Pt paste formed the counter electrodes. In order to obtain the conductivity from the experimental data, fitting was performed using Zview (Scribner Associates Inc., USA) and an adaption of the transition line model consisting of an ionic and an electronic rail.[155-157] Fitting and the analysis of the impedance data was done by Maximilian Morgenbesser (TU Wien) only.

6.2.4 X-ray diffraction

Reciprocal space maps of the (002), (103), and (113) reflections of undoped $SrTiO_3$ and Al, Nb, Ni and Fe-doped $SrTiO_3$ were recorded to investigate the lattice mismatch between deposited thin films and $SrTiO_3$ single crystals. The measurements were conducted on an Empyrean multipurpose diffractometer (Malvern Panalytical Ltd, UK) with a Cu-anode operating at 45 kV and 40 mA, which yields a wavelength of λ=1.5406 Å (Cu $K_{\alpha1}$ radiation) and λ=1.5444 Å (Cu $K_{\alpha2}$ radiation). A hybrid monochromator (2xGe(220)) with a 1/32 ° divergence slit and a 4 mm mask was placed in the incident X-ray beam, while on the detector side a GaliPIX 3D detector in the frame based mode was used. This allows the measurement of 6.8672 ° of 2θ without moving the GaliPIX detector (resolution 0.01434 °). Therefore, only ω was scanned with a step size of 0.00716 °. Thus, the required time for data acquisition was tremendously reduced. Reciprocal space maps were measured for the (002) (ω = 23.2376 °, 2θ = 46.4752 °), the (103) (ω = 20.1378 °, 2θ = 46.4752 °), and the (113) (ω =

15.6000 °, 2θ = 46.4752 °) reflections. φ had to be adjusted before each measurement of the (103) and (113) reflections (rotation along the axis perpendicular to the sample's surfaces) to optimize the signal strength. In total four different thin films (from nominally undoped, 0.4 % Ni-doped, 0.3 % Al-doped, and 1 % Fe-doped $SrTiO_3$ targets) deposited on undoped (001) oriented $SrTiO_3$ single crystals were measured at ambient conditions.

6.2.5 X-ray standing wave measurements

The X-ray standing wave (XSW) technique is a method allowing direct structure determination, with pm resolution.[158] XSW measurements were conducted at the chemical crystallography beamline P24 at the PETRA III storage ring at Deutsches Elektronen-Synchroton (DESY) in Hamburg, Germany. The standing wave field was generated by interference of the incoming beam and the Bragg reflected beam from two Fe-doped $SrTiO_3$ thin films (each deposited on a $SrTiO_3$ single crystal). Photo-absorption and, as a result, also emission of fluorescence from the probed atoms are proportional (within electric-dipole approximation) to the intensity of the interference field at the respective atoms. Atoms located at the maxima of the standing wave emit more fluorescence radiation whereas atoms at positions of the destructive interference emit less. By changing incidence angle or the photon energy, the positions of the nodes and antinodes of the interference field can be varied, resulting in changes in the fluorescence yield. For different atom positions (e.g. interstitial, A-, and/or B-site) different dependencies from the deviation of the Bragg angle can be observed.[158] Here, the angular dependency of the Fe K-fluorescence yield was measured. Probing the (002) reflection allows to determine whether Fe is located on an interstitial site or at a lattice site (A-site or B-site). To distinguish between A- and B-site occupancy of Fe, the (001) or (003) reflection can be used. At the (003) reflection, the probed sample volume is smaller, thus minimizing the potential influence of spatial variation of the substrate (e.g. due to substrate imperfections). Therefore, rocking scans of the (002) and (003) reflections were carried out at 220 nm thick thin films deposited from PLD targets with a stoichiometric composition of $Sr_{1.00}Ti_{0.98}Fe_{0.02}O_3$ and of $Sr_{1.05}Ti_{0.98}Fe_{0.02}O_3$ (Sr overstoichiometry to compensate Sr loss in the preparation process).[74] A fluorescence spectrum was recorded at each angular step of each scan. Subsequently, the fluorescence spectra from several scans were summed up to improve the counting statistics. All XSW experiments were carried out at ambient conditions and the incident beam energy was fixed to 8.500 keV, (λ = 1.459 Å).

Finally, the Fe K-edge emission line was fitted with a Gaussian function and linear background, and the yield calculated as an integral of the Gaussian. The obtained results were compared to simulations for different Fe occupancies (A-site, B-site, mixed, interstitial). The simulations were based on the dynamical theory of diffraction[159] and a finite crystal thickness was assumed to consider the influence of the wavefields related to both branches of the dispersion surface. Fitting procedure and the simulation software was developed by Michał Kamiński, DESY.

6.2.6 X-ray absorption spectroscopy

X-ray absorption spectroscopy was performed at the Surfaces/Interfaces: Microscopy (SIM) Beamline at Swiss Light Source (SLS) at Paul Scherrer Institut (PSI), Switzerland. The absorption of linear polarized X-rays in energy ranges of 521.0 - 589.0 eV (O K-edge), 441.0 - 479.0 eV (Ti $L_{2,3}$-edge), and 691.1 - 749.0 eV (Fe $L_{2,3}$-edge) was measured. Thereby a 220 nm thick thin film deposited from a stoichiometric target with 2 % Fe was investigated after deposition and after subsequent annealing for 12 h at 700 °C in air. The total electron yield as well as the fluorescence yield were obtained. The experimental spectra were normalized to the incident beam intensity using a gold mesh positioned upstream to the samples. The experimental data were processed using the Athena program.[99] Interpretation of the XAS spectra is supported by linear combinations of simulated Fe^{2+} and Fe^{3+} spectra. Therefore, the TM4XAS program[160] was used and a perfect octahedral environment of the Fe ions was assumed.

6.3 Results

6.3.1 Impedance spectroscopy

Fe-doped $SrTiO_3$ thin films exhibit a very low conductivity compared to the grain conductivity of polycrystalline bulk specimens (compare Figure 45a). Even doping with different metals does not lead to an enhancement (Figure 46). Calculations suggest that the conductivity is fixed to the intrinsic conductivity (c_e=c_h). This corresponds to a Fermi level positioned in the middle of the band gap. Increasing for example the Fe concentration up to 10 % seems to have hardly any effect. Additionally, conductivity of 0.4 % Fe-doped $SrTiO_3$ is independent of the oxygen partial pressure at 555, 603, and 650 °C and matches the respective calculated pseudo-intrinsic conductivities. A more detailed discussion of the shown impedance data and defect chemistry calculations can be found elsewhere, while this thesis focuses primarily

on the X-ray based analytical methods applied to these films.[143] These are crucial in order to gain further information about the mechanism behind the pseudo-intrinsic conductivity.

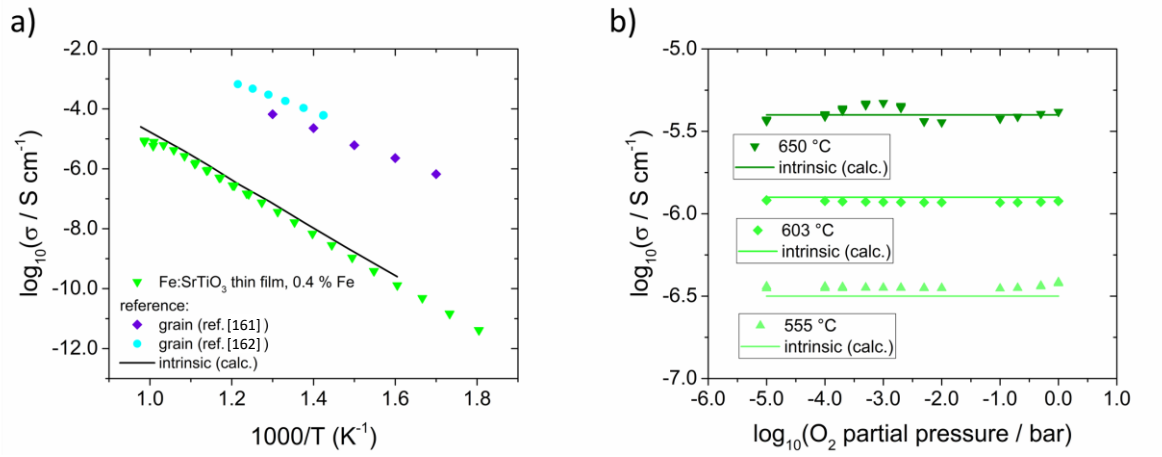

Figure 45: **a)** DC conductivity of Fe-doped $SrTiO_3$ thin films deposited from a $SrTi_{0.96}Fe_{0.004}O_3$ target in air. Additionally, data obtained from polycrystalline bulk samples (cyan circles and violet diamonds)[161, 162] and calculated conductivity of intrinsic electronic conductivity (c_h = c_e) (black line)[29] are shown. Despite doping experimental data match the intrinsic conductivity of $SrTiO_3$. **b)** Conductivity at 555, 603, and 650 °C in dependency of p_{O_2}; conductivity seems to be independent from partial pressure changes between a p_{O_2} of 10^{-5} and 1 bar oxygen. Again, the experimental data match the intrinsic conductivity nearly perfectly.

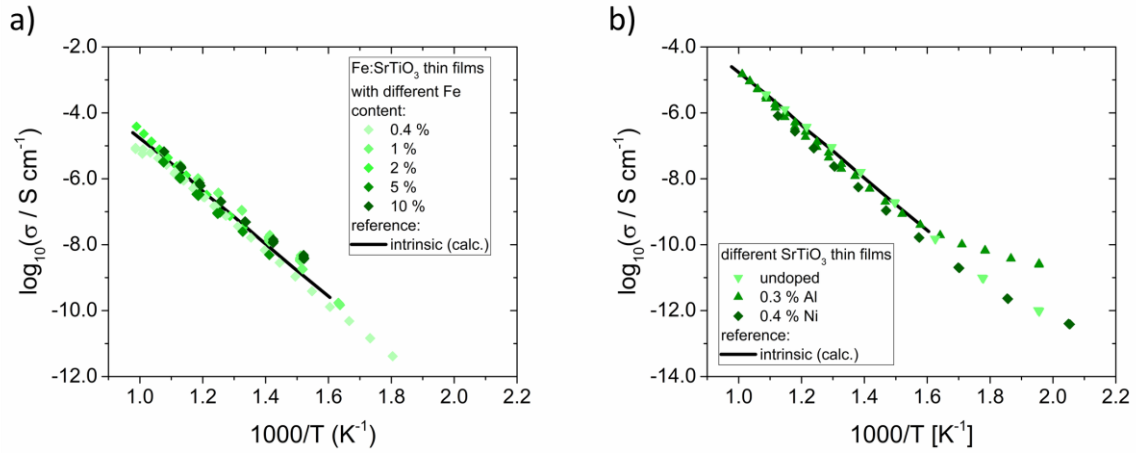

Figure 46: **a)** Increasing the Fe dopant concentration does not enhance the DC conductivity of Fe-doped $SrTiO_3$ thin films in air. All thin films deposited from targets containing 0.4 to 10 % Fe on the B-site exhibit pseudo-intrinsic conductivity (black line symbolize the calculated values from defect chemical data in ref. [29]). **b)** Ni- and Al-doped $SrTiO_3$ thin films possess the same DC conductivity as undoped thin films above 350 °C in air. All films were deposited from targets listed in Table 5.

6.3.2 Thin film compositions

The composition of the used specimens is displayed in Table 5 below. Pulsed laser deposition led to a reduced Sr content compared to the target pellets. The dopant concentration deviates as well. Variations can be caused by preferential scattering and incongruent ablation during the deposition process.[163] The error of the analysis is < 1 % for Sr and Ti and approx. 5 % for the dopants. Additionally, thin films on undoped $SrTiO_3$ substrates deposited from $SrTi_{0.95}Fe_{0.05}O_3$ targets were analyzed using RBS and ToF-ERDA. RBS indicates Sr deficiency as well and ToF-ERDA a Fe/Ti ratio of 0.047 (expected value 0.052). Thus, in order to cope with the found Sr deficiency either Sr vacancies, Ti rich secondary phases, or antisite defects (e.g. $Ti_{Sr}^{\bullet\bullet}$) were formed.

Table 5: Results of the compositional analysis of $SrTiO_3$ thin films deposited from stoichiometric targets. The sum of all metals is fixed to two formula units.

Target material	Thin film composition			Method
	Sr	Ti	Dopant	
$SrTi_{0.99}Fe_{0.01}O_3$	0.950	1.041	0.009	ICP-OES
$SrTi_{0.98}Fe_{0.02}O_3$	0.945	1.020	0.035	ICP-OES
$SrTi_{0.95}Fe_{0.05}O_3$	0.937	1.015	0.048	RBS (Sr, Ti), ToF-ERDA (Fe)
$SrTi_{0.9}Fe_{0.1}O_3$	0.960	0.953	0.087	ICP-OES
$SrTi_{0.996}Ni_{0.004}O_3$	0.944	1.046	0.010	ICP-OES
$SrTi_{0.997}Al_{0.003}O_3$	0.988	1.007	0.005	ICP-OES
$Sr_{1.05}Ti_{0.98}Fe_{0.02}O_{3+\delta}$	0.98	0.98	0.04	ICP-OES (from ref. [74])
$SrTiO_3$	0.957	1.043	-	ICP-OES

6.3.3 X-ray diffraction

X-ray diffraction confirmed epitaxial growth of all deposited thin films on undoped oriented (001) $SrTiO_3$ single crystals. Additionally, RSM measurements were performed in order investigate differences in the unit cell parameters of the substrates and deposited thin films. The reciprocal space maps of the (002) reflections are shown in Figure 47. The unit cells of all investigated thin films except the Al-doped layer, are elongated in the direction of the c axis. As a consequence of the elongation two separated diffraction peaks were found. The upper ones correspond to the substrate and the lower ones to the thin films. To confirm these measurements reciprocal space maps were recorded in the (103) and (113) directions as well (see Figure 48 and Figure 49). The maps of all thin films except the Al-doped ones exhibit two separated peaks in these directions as well. Shifts only occurred in the $q_{\perp}$ direction and not in the q_{II} direction. Hence, the in-plane cell parameters of the substrate and the deposited thin films are equal. Accordingly, the symmetry of the thin films is reduced compared to the substrate, since in the thin films (except Al-doped $SrTiO_3$) possess a tetragonal lattice. In literature cation vacancies (e.g. Sr/Ti or Sr/(Ti+dopant) ≠ 1) are known to cause such elongations. [145, 164-166] Thus, we assume that the measured Sr deficiency in the thin films is at least partially manifested by the formation of Sr vacancies. This would also explain the missing second peaks in the reciprocal space maps of Al-doped thin films, since in these the Sr deficiency is the lowest of all produced samples. On the other hand, $SrTi_{0.996}Ni_{0.004}O_3$ exhibits the lowest Sr/(Ti+dopant) ratio and the most pronounced elongation of the c axis.

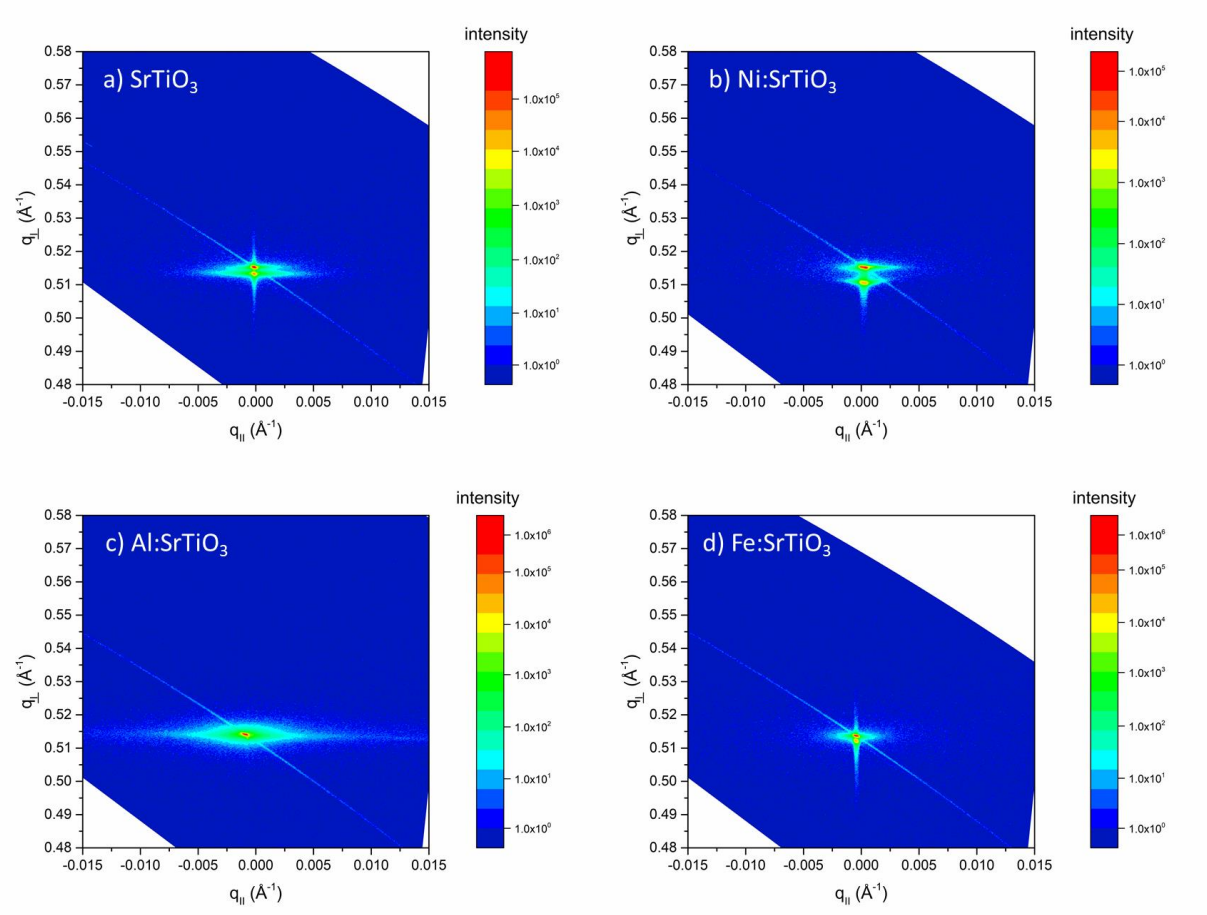

Figure 47: Reciprocal space maps of epitaxially grown doped an undoped $SrTiO_3$ thin films on top of undoped (001) oriented $SrTiO_3$ substrates. Deposition of the thin films from nominally undoped **(a)**, 0.4 % Ni-doped **(b)**, 0.3 % Al-doped **(c)**, and 1 % Fe-doped **(d)** $SrTiO_3$ targets (compare Table 5). Here the (002) reflections were measured. Two separated reflections were found for all thin films except for the Al-doped layer, revealing an elongation of the c axis (out of plane) of the thin films compared to the $SrTiO_3$ substrates. The deviations between films and substrates originate from the presence of Sr deficiency, causing a high Sr vacancy concentration.

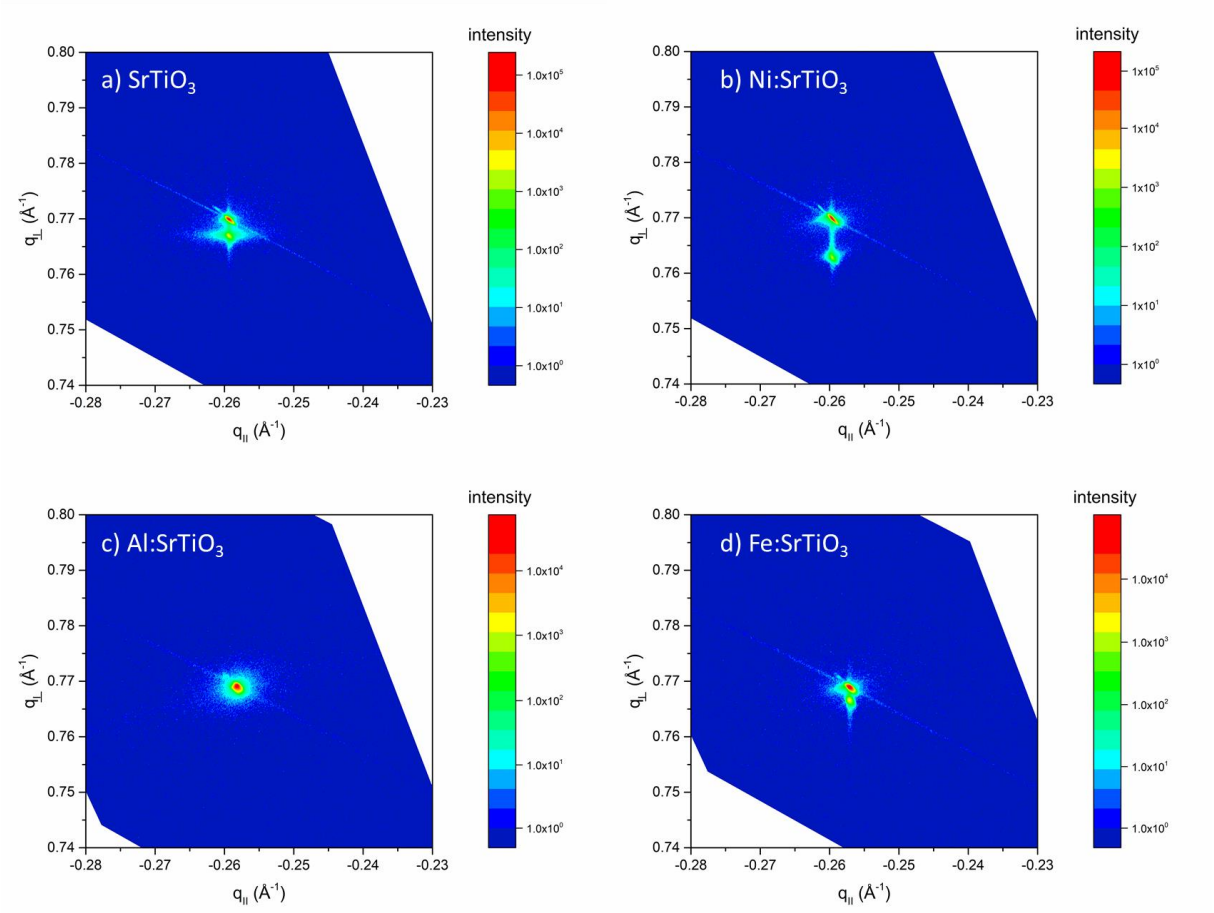

Figure 48: Reciprocal space maps of the (103) reflections of undoped **(a)**, 0.4 % Ni-doped **(b)**, 0.3 % Al-doped **(c)**, and 1 % Fe-doped **(d)** $SrTiO_3$ targets (compare Table 5). Thin films were deposited on undoped (001) oriented $STiO_3$ substrates. All thin films exhibit a smaller $q_\perp$ (except Al-doped layers) than the substrate.

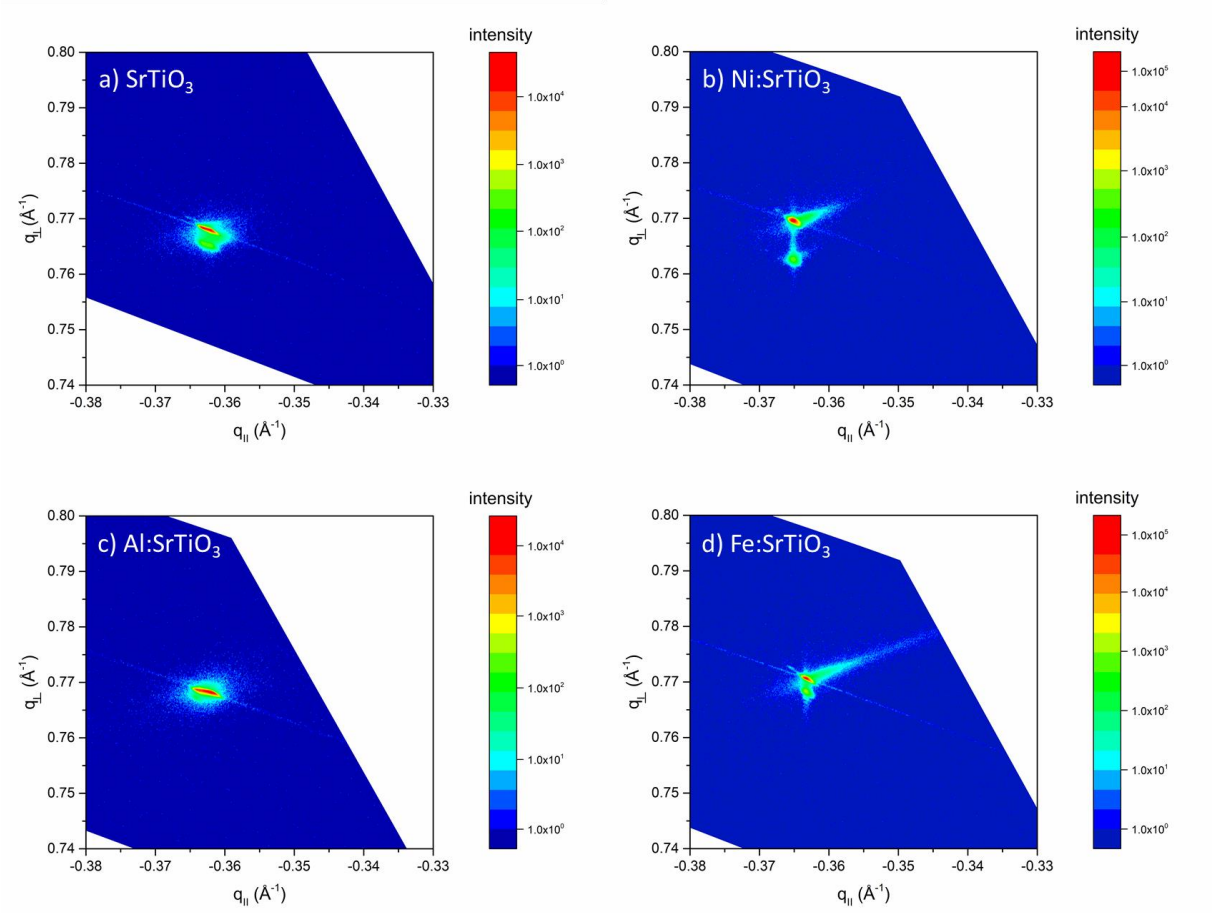

Figure 49: Reciprocal space maps of the (113) reflections of undoped **(a)**, 0.4 % Ni-doped **(b)**, 0.3 % Al-doped **(c)**, and 1 % Fe-doped **(d)** $SrTiO_3$ targets (compare Table 5). Only differences can be found in the $q_\perp$ (except Al-doped layers) directions, thus the in-plane cell parameters are equal in the thin films and substrates. Only elongations (except for Al-doped layers) in the out of plane direction (c axis) were found.

6.3.4 Positron annihilation lifetime spectroscopy

The PALS measurements and the interpretation of the experimental data were carried out by Maciej Oskar Liedke, Max Doebeli, Federico Baiutti, Juan de Dios Sirvent, Maik Butterling and Eric Hirschmann at the Helmholtz-Zentrum Dresden-Rossendorf, Dresden, Germany.

Probing the positron lifetime and its energy in dependency of the positron implantation energy suggest Sr vacancies with a positron lifetime of approx. 280 ns to be the dominant defects in undoped and Fe-doped $SrTiO_3$ thin films (deposited from a stochiometric target containing 2 % (atm. % of the B-site cations) Fe). On the other hand, undoped and Fe-doped $SrTiO_3$ (0.15 atm.% Fe) single crystals exhibit Ti vacancies as main cation defects (positron lifetime approx. 180 ns). Due to the close to 100 % relative intensity I_{defect}, a large defect concentration and positron saturation trapping is suggested for both thin films. More details can be found in ref. [143]. These findings are in excellent accordance with the interpretation of the reciprocal space maps.

6.3.5 X-ray standing wave measurements

The defect chemistry for Fe-doped $SrTiO_3$ apart of undoped $SrTiO_3$ is well described in literature, thus further measurements were only carried out on Fe-doped thin films. Fe acts as model dopant for further considerations. In order to determine, whether Fe is located at an interstitial, A- or the B-site X-ray standing wave measurements were performed on thin films deposited from a $Sr_{1.05}Ti_{0.98}Fe_{0.02}O_{3+\delta}$ and a $Sr_{1.00}Ti_{0.98}Fe_{0.02}O_3$ target. In dependency of Θ the K-fluorescence of the (002) and (003) Bragg reflections were recorded, and the normalized fluorescence yield obtained. The results of the measurement of the (002) reflection of a sample deposited from the $Sr_{1.05}Ti_{0.98}Fe_{0.02}O_{3+\delta}$ target is displayed in Figure 50a. The (002) reflection does not contain any information if Fe is present on the A- or B-site, only a differentiation between interstitial and lattice site is possible. A minimum is followed by a maximum, indicating that Fe is positioned on the A- and/or B-site and not on an interstitial site. The maximum at $(\Theta - \Theta_B)$ of 0.01 ° is caused by the X-ray beam reflected from the substrate and overlays at this angle the fluorescence yield caused by the thin film. In Figure 50a the green solid line is the expected fluorescence yield when Fe is present only at the Ti site and the black solid line when Fe is located only at an interstitial site. Thus our interpretation is confirmed by these simulations and we conclude that Fe occupies exclusively the A- or/and B-sites.

In order to differentiate between A- and B-site, a X-ray standing wave measurement of the (003) reflection was conducted. As mentioned above, thereby, two thin films were compared, one deposited from a stoichiometric target with 2 % Fe and one from an target with 5 % Sr excess and 2 % Fe. This was done to investigate the impact of the Sr vacancy concentration/deficiency on the distribution of Fe between the A and the B-site. In Figure 50b simulations of the normalized fluorescence yield are shown in dependency on the Fe occupancy. The ratio of A/B occupation determines the shape of the displayed curve. If Fe is primary present on the B-site ($\xi < 0.5$) a maximum is followed by a minimum. If the ratio A/B becomes > 1 ($\xi > 0.5$) the fluorescence yield reaches first a minimum and subsequently a maximum. In thin films deposited from a target with a composition of $Sr_{1.00}Ti_{0.98}Fe_{0.02}O_3$ and consequently exhibiting Sr deficiency and a high Sr vacancy concentration, 30-40 % of Fe is located at the A-site (see Figure 50c). In samples deposited from targets with 5 % Sr excess, Fe can only be found on the B-site. In these the Sr-loss during the deposition process is compensated by the Sr excess of the target and as a consequence the Sr vacancy concentration is reduced in those thin films.[74] Even though the experimental data scatter and differences in the Fe distribution causes only small changes they match the simulations. Additionally, in one measurement of Figure 50c the reflex related to the substrate can be found as well and therefore this part of the diagram is not considered in the interpretation of these experimental data. Please note that Fe at the A-site changes the defect chemistry significantly since it acts as a donor.

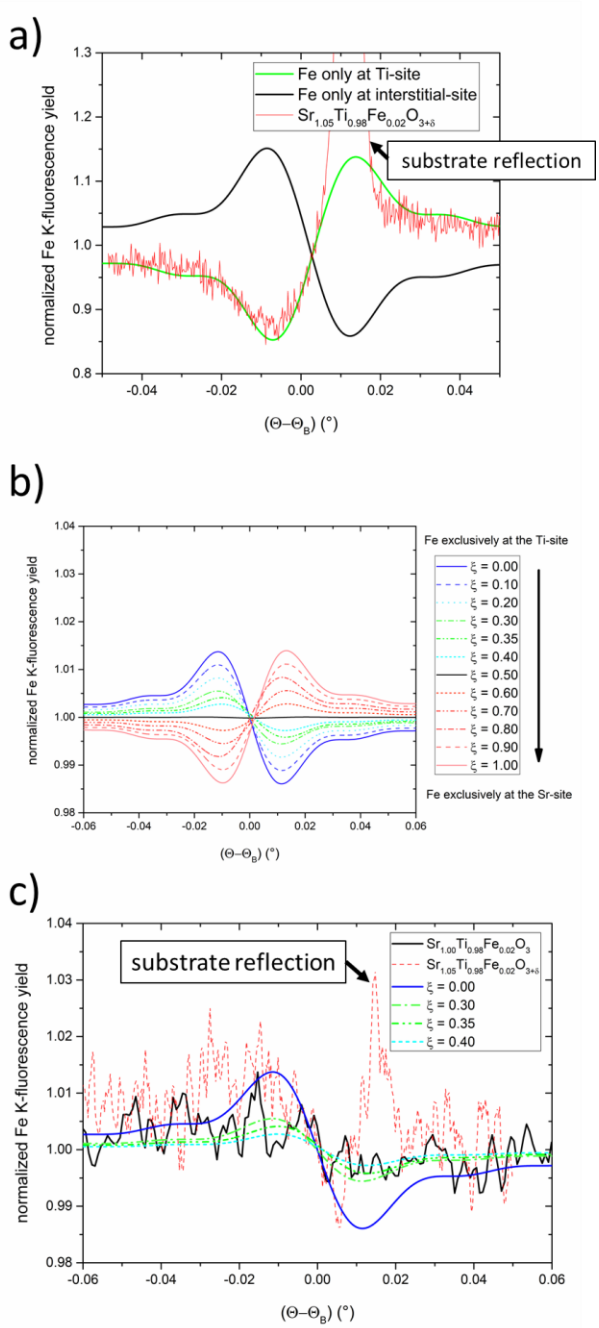

Figure 50: **a)** X-ray standing wave measurement of the (002) reflection of a Fe-doped thin film deposited from a $Sr_{1.05}Ti_{0.98}Fe_{0.02}O_{3+\delta}$ target. Normalized Fe K-fluorescence yield (red line) and simulations (green and black solid lines). Fe seems to be exclusively present on the A and/or the B-site and not on an interstitial position. **b)** Simulations of the fluorescence yield of the (003) reflection in dependency of the Fe distribution between A and B lattice site. At ξ = 1 Fe is only present on the Sr (A) site, whereas at ξ = 0 Fe is positioned exclusively on the Ti (B)-site. **c)** X-ray standing wave measurements of the (003) reflections of thin films deposited either from a $Sr_{1.05}Ti_{0.98}Fe_{0.02}O_{3+\delta}$ or a $Sr_{1.00}Ti_{0.98}Fe_{0.02}O_3$ target. Results suggest that in the thin film produced form the stochiometric target 30-40 % of the Fe is located on the A site. On the other hand, the 5 % Sr excess in the target seems to prevent Fe A-site occupancy. Moreover, substrate related reflections can be found in the measurements of thin films from the $Sr_{1.05}Ti_{0.98}Fe_{0.02}O_{3+\delta}$ target. However, these do not affect the interpretation.

6.3.6 X-ray absorption spectroscopy

Fe can change its valency between 2+ and 4+ in Fe-doped $SrTiO_3$ thin films, which has a tremendous effect on the defect chemistry of the perovskite. Thus, X-ray absorption spectra of Fe-doped thin films deposited from a target with a composition of $Sr_{1.00}Ti_{0.98}Fe_{0.02}O_3$, were recorded in the total electron yield mode and the fluorescence yield mode. The fluorescence yield mode is more bulk sensitive, whereas the total electron yield mode is a surface sensitive method, and its information depth is approx. 5 nm. In total, the Fe $L_{2,3}$-edge, Ti $L_{2,3}$-edge, and O K-edge of Fe-doped thin films were investigated after the deposition and after 12 h at 700 °C in air. Additionally, the $L_{2,3}$-edge of Fe^{2+} and Fe^{3+} were simulated and the obtained data fitted to the experimental results by linear combination. Fe^{4+} was excluded, since like in literature the simulated Fe^{4+} $L_{2,3}$-edge did not fit the measured spectra at all.[36] For the simulations, the Slater integral reduction was 80 % and the core spin orbital coupling was reduced by 1.0 % for Fe^{3+} and 1.1 % for Fe^{2+}. The valence spin orbital coupling amounted to 3.70 % and 3.25 % for Fe^{2+} and Fe^{3+}, respectively. The crystal field parameters were fixed to 10 Dq = 1.5 eV and the charge transfer parameters to Δ = 2 eV. Lorentzian broadening was set to 0.2 eV and Gaussian broadening to 0.3 eV. The best match between simulation and the experimental data in the fluorescence yield mode was achieved for the linear combination of 10 % Fe^{2+} and 90 % Fe^{3+}. The spectra were not corrected to compensate self-absorption or saturation effects; thus, the results are only first estimates. Furthermore, effects of Fe site occupation, oxygen vacancies, cation vacancies and Fe'_{Ti}-$V_O^{\bullet\bullet}$ complexes were not considered as well. Deviation between the measured spectra and the simulations above 715 eV cannot be explained at this point. The impact of the substrate on the measurements conducted in the fluorescence yield mode can be neglected since ICP-OES measurements showed no significant Fe impurities in undoped $SrTiO_3$ single crystals[98] and information depth of the fluorescence yield mode can be as deep as approx. 100 nm[167] (thin film thickness approx. 220 nm). Interestingly no significant difference was found between spectra recorded in the total fluorescence yield mode directly after the PLD process (p_{O_2} of 0.15 mbar and 650 °C) and after the annealing step (200 mbar O_2 at 700 °C). Consequently, in the bulk of the thin film the Fe^{2+} to Fe^{3+} ratio did not change and was independent of the oxygen partial pressure in the range of 0.15 mbar to 200 mbar (compare Figure 51a). This is in accordance with the impedance measurements, since conductivity is also independent from the p_{O_2} between 555 and 650 °C.

In Figure 51b and Figure 51c the O K-edge and the Ti $L_{2,3}$-edge spectra respectively, are displayed. They are in accordance with literature[97, 111, 168] and show no p_{O_2} dependency as well. The annealing step did not cause a substantial change of these spectra. Electron transition from the O(1s) core level into O(2p) orbitals hybridized either with Ti(3d) orbitals (at 532.2 and 534.6 eV), Sr(4d) orbitals (at 537.2 and 538.9 eV), or Sr(5p) orbitals (at 544.7 eV) lead to the shown O K-edge spectra. The peaks in the Ti $L_{2,3}$ spectra can be divided into the two pre peaks[169] the L_3 edge (at 459.0 and 461.3 eV) and the L_2 edge (at 464.4 and 466.8 eV), both exhibiting two peaks due to the splitting into the t_{2g} and e_g levels.[168, 169] Ti is in a perfect octahedral environment, since in each spectrum only one peak at 461.3 eV is visible.[170]

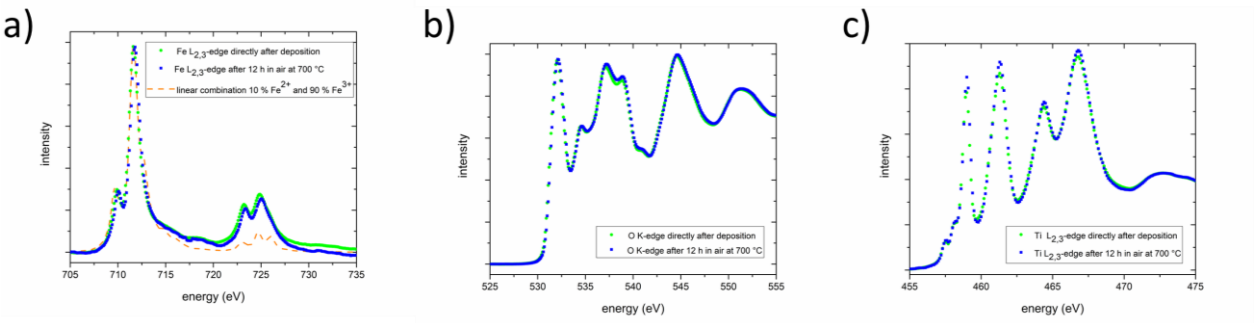

Figure 51: X-ray absorption spectra of the Fe $L_{2,3}$-edge **(a)**, O K-edge **(b)**, and the Ti $L_{2,3}$-edge **(c)** recorded in the fluorescence yield mode. Specimens were deposited from a stoichiometric Fe-doped $SrTiO_3$ target with 2 % Fe and the measurements were conducted directly after the deposition (green dots) and after an additional annealing step at 700 °C in air for 12 h (blue squares). Simulations with subsequent linear combination of 10 % Fe^{2+} and 90 % Fe^{3+} (dashed orange line) matches the experimental data best.

In Figure 52a the simulated spectra of Fe^{2+} (cyan dashed line) and Fe^{3+} (red solid line) are shown. The peak at 710 eV originates mainly from Fe^{2+} whereas the peak at 712 eV is caused by the presence of Fe^{3+}. In the total electron yield mode Fe is probed only near the surface (information depth approx. 5 nm). The Fe $L_{2,3}$-edge spectra recorded in this mode is displayed in Figure 52b. According to the conducted simulations, near the surface a higher Fe^{2+} concentration (strongly increased peak at 710 eV) can be found compared to the bulk. Furthermore, the spectrum is shifted due to the annealing step by nearly 0.2 eV to higher energies, and the first peak is lowered. Directly after deposition a calculated spectrum containing 58 % Fe^{2+} and 42 % Fe^{3+} fits best the experimental data. During the annealing

step, Fe^{3+} is formed on the expense of Fe^{2+}, consequently after the annealing the presence of 36 % Fe^{2+} and 64 % Fe^{3+} is suggested.

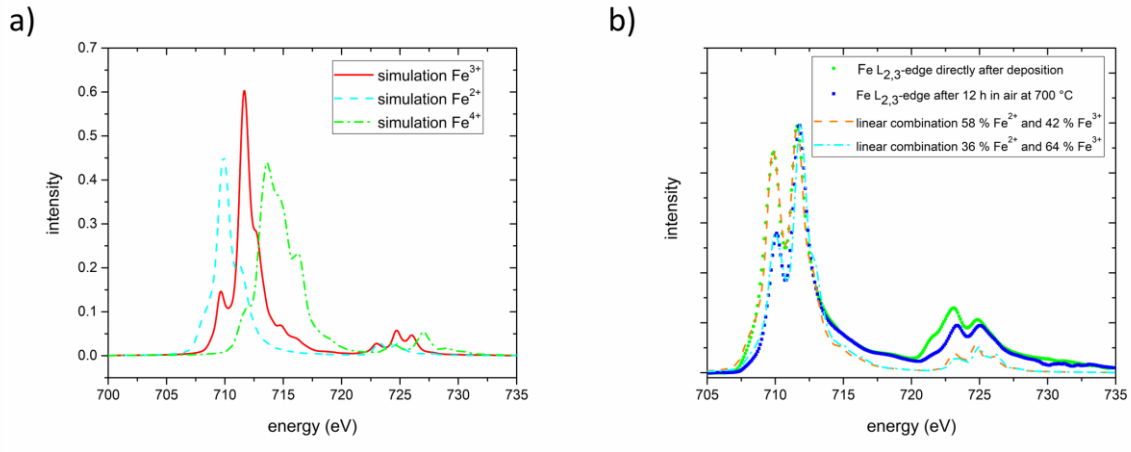

Figure 52: **a)** Simulated spectra of Fe^{2+}(cyan broken line), Fe^{3+} (red solid line), and Fe^{4+} (green broken line).**b)** XAS measurements of the Fe $L_{2,3}$-edge of a 2 % Fe-doped $SrTiO_3$ thin film directly after the pulsed laser deposition (green dots) and after an additional annealing step at 700 °C in air for 12 h (blue squares). The spectra were recorded in the total electron yield mode. Near the surface, a significant amount of Fe^{2+} is present. Annealing in air leads to the oxidation of some of the Fe^{2+} to Fe^{3+}, increasing the Fe^{3+} to Fe^{2+} ratio. This can be seen in the decrease in the peak at approx. 710 eV and a shift of the whole spectra by +0.2 eV.

6.4 Discussion

In general, it is expected that only $SrTiO_3$ films exhibiting impurities in the sub ppb range can exhibit an intrinsic electronic conductivity. The specimens investigated here were deposited from highly doped targets and chemical analysis confirm high dopant concentration in the thin films. Moreover, the mechanism behind pseudo-intrinsic conductivities needs to be very robust since different acceptor dopants in a wide range of concentration show such a behavior. Thus, it is also not realistic that the acceptor dopants are simply counterbalanced by donor dopants, since only a very specific combination of these would lead to a mid-band gap Fermi level. Rather, we suggest that the pseudo-intrinsic conductivity of all investigated thin films is caused by a pinning of the Fermi level to the mid band gap energy.

In order to establish a Fermi level pinning a three-level model is suggested for semi-insulating GaAs with Cr impurities in literature.[171] However, even a mid-gap acceptor state and a donor state would be sufficient to pin the Fermi level. In accordance with the elemental analysis, reciprocal space mapping, and the PALS measurements, Sr vacancies are

believed to act as the required mid-gap acceptors. In literature these were already discussed, however without any experimental evidence.[30] Thus, in our model the pinning of the Fermi level would be caused by hole trapping of V_{Sr}'', and consequently due to the formation of V_{Sr}'. The energy of the trapping process is assumed to be mid-band gap. The trapping of a second hole is energetically rather shallow.[172]

Possible donor states are generated by a site change of the metal dopant itself from the A to the B site. According to the conducted X-ray standing wave measurements 30-40 % of Fe is located at the A-site. Additionally, X-ray absorption spectroscopy indicates, that roughly 10 % of the Fe in the bulk exhibits an oxidation state of 2+. It is assumed that Fe^{2+} is only located on the A site, thus a mixture of Fe^{2+} and Fe^{3+} on the A-site with a ratio of 1/3 to 1/4 (Fe^{2+}/Fe^{3+} on the A-site) is received. Consequently, corresponding Fe donor states are just slightly above the Fermi level (which must be mid-gap according to the conductivity measurements). A Fe_{Sr}^{X} level far above the Fermi level can be ruled out, since according to the measurements also Fe^{2+} is still present on the A-site.

However, the intrinsic conductivity of thin films deposited from a nominally undoped $SrTiO_3$ target has to be explained, as well, since the impurity concentrations in these layers are by far above the sub ppb range. Thus, additional donor states must be present to explain the generality of the Fermi level pinning. Also, for Al and Ni as dopants the same effect was found.

According to Equation 35 Ti on the A-site acts as donor and such a redistribution of Ti was even discussed in literature.[151, 152, 173] We suppose that these donor states are located above the mid-band gap, even close to the conduction band (compare Figure 53). A combination of Sr vacancies and Ti on the A-site is able to explain the ultra-low conductivity of undoped and metal doped $SrTiO_3$ thin films deposited from stochiometric targets.

However, to this point the presence of oxygen vacancies was not considered. Their formation is electronically balanced by 2e' (compare Equation 40), thus they also may serve as donor dopants. Nevertheless, due to the extremely low hole concentration in the pseudo-intrinsic thin films only comparably few oxygen vacancies can be found as well, according to bulk defect chemical model, i.e. Equation 40 and Equation 3.[29] Consequently, they can be neglected, without any substantial impact on the described basic model.

Consequently, the Fermi level pinning leading to the extremely low conductivity in metal doped $SrTiO_3$ thin films is caused by the interplay of mid-gap acceptor states V_{Sr}''/V_{Sr}' and

donor states ($Ti_{Sr}^{\bullet\bullet}/Ti_{Sr}^{\bullet}$). Dopants such as Fe add either donor or acceptor states depending on their position (A- or B-site), however, these do not have substantial impact on the energy of the Fermi level. Thus, the model is independent from the dopant and applicable to thin films deposited from a nominally undoped $SrTiO_3$ target as well as Al- and Ni-doped $SrTiO_3$.

In order to validate the introduced model, defect chemical calculations were performed by Alexander Schmid, TU Wien. They confirmed the plausibility of the model. Additionally, they indicate that to obtain intrinsic conductivity in Fe-doped $SrTiO_3$ it is not necessary that the concentrations of donors (e.g. Ti on A-site) and acceptors are present in a fixed ratio in order to receive a pseudo-intrinsic conductivity. A shift in the Sr vacancy ionization between V_{Sr}'' and V_{Sr}' is to a certain extend able to balance deviations from the ideal ratio and thus this pins the Fermi level to the middle of the band gap over a wide range of dopant concentrations (compare Figure 46). Nevertheless, calculations suggest that the ideal ratio between singly charged donors and Sr vacancies plus (in the case of Fe doping) Fe dopant on the B-site is 1.5. A more detailed discussion and more information about the calculations itself can be found in the prepared manuscript.[143]

The model is also in accordance with literature, since thin films deposited from Fe-doped $SrTiO_3$ targets with Sr excess (approx. 7 %) were reported to be stoichiometric and to exhibit $V_{Ti}V_O$ clusters as predominant point defects. Sr vacancies were not found and therefore, the Fermi level was not pinned to the middle of the band gap. Hole conductivity as expected from the acceptor dopant concentration were thus obtained.[74]

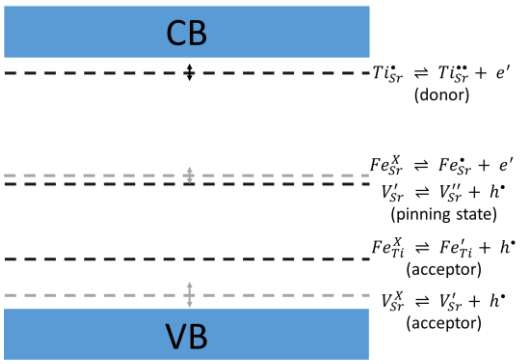

Figure 53: Fermi level pinning to the mid-band gap region is caused by the interplay of a donor state ($Ti_{Sr}^{\bullet\bullet}/Ti_{Sr}^{\bullet}$) and the mid band gap V_{Sr}'/V_{Sr}'' state. The V_{Sr}''/V_{Sr}' mid-band gap state "buffers" the pinning of the Fermi level. Additionally, acceptor states are formed by Fe at the B site (Fe_{Ti}'/Fe_{Ti}^{x}) and V_{Sr}'/V_{Sr}^{x}. Slightly above mid-band gap donor states originating from Fe at the A site ($Fe_{Sr}^{x}/Fe_{Sr}^{\bullet}$) are established. Please note that the positions of the displayed states are only rough estimations, but a deviation from the displayed positions would not change our model significantly.

6.5 Conclusion

Ultra-low bulk conductivity of undoped and metal doped $SrTiO_3$ thin films deposited from stoichiometric targets was investigated. As reason a very robust pinning of the Fermi level to the middle of the band gap is suggested. Thin film characterization revealed Sr vacancies to be the main active defect in the investigated specimens. Moreover, in Fe-doped $SrTiO_3$, XAS and subsequent simulations suggest that Fe is present at the A-site as Fe^{2+} and Fe^{3+} and on the B-site as Fe^{3+}, while no Fe^{4+} was found. Finally, a model is derived, suggesting that Sr vacancies act as acceptor-type mid-gap states, and together with a donor dopant (here Ti at the A-site), those are responsible for the Fermi level pinning.

7 Review on the photocatalytic activity of $SrTiO_3$

Since photocatalytic H_2O splitting is essential for the oxygen incorporation in humidified and dry H_2 atmosphere, in the following the photocatalytic capability of $SrTiO_3$ is reviewed. The following chapter largely corresponds to the manuscript: "Photo-Induced Electronic and Ionic Effects in Strontium Titanate", which is under review at Journal of Materials Chemistry A.[174]

7.1 Introduction

In 1972, Fujishima and Honda discovered the ability of TiO_2 and Pt as photoanode and cathode to facilitate water splitting under UV light.[175] Since their groundbreaking experiments, related semiconductors such as ZnO,[176-179] SnO_2,[180-184] Fe_2O_3,[185-188] and $SrTiO_3$ attracted a lot of interest and were studied extensively throughout the last decades. Among others, $SrTiO_3$ became one of the best investigated compounds and applications in the field of photocatalytic overall water splitting,[189-197] H_2 evolution,[198-209] CO_2 conversion,[210-212] inorganic/organic pollutant, NO_x, SO_x and dye degradation,[205, 213-224] N_2 fixation,[225] and bacteria inactivation[226] were reported.

Operation at ambient conditions is most important for technological processes and therefore also preferred in research. Regardless of operation conditions, electrons have to be excited from the valence band to the conduction band by illumination in order to utilize solar energy for photocatalytic processes. Subsequently, the photogenerated electrons and holes need to be separated, and the charge carriers have to be transferred to active sites (either the surface of $SrTiO_3$ or of loaded cocatalysts), where oxidation or reduction processes take place. Hence, to understand the photocatalytic properties of $SrTiO_3$, detailed knowledge of the band structure of $SrTiO_3$ is necessary. Compared to TiO_2, undoped $SrTiO_3$ exhibits a conduction band closer to the vacuum level and a higher electron mobility. It is capable of photocatalytic water splitting, since its electrons/holes in the conduction/valence band are able to reduce/oxidize water, respectively. The valence band consists mainly of O(2p) orbitals and its upper edge is positioned at 2.59 eV vs. NHE.[124] The lower edge of the

conduction band is located at -0.61 eV vs NHE[124] consisting predominantly of Ti(3d) states.[8] Since only a small part of the solar radiation at the earth's surface has a wavelength below approx. 390 nm[227] and therefore is capable to excite electrons from the valence to the conduction band in $SrTiO_3$, it is desired to expand the range of usable wavelengths. For improving the overall photocatalytic activity of $SrTiO_3$, the photogenerated charge carrier separation, charge transport and finally the reduction/oxidation reactions also have to be optimized. For these complex tasks, various approaches and techniques have been developed and described in the last decades. Several review articles provide an overview of these aspects for $SrTiO_3$ or related materials.[124, 228-231] In the following chapter, existing $SrTiO_3$-based photocatalytic systems will be described and the most important strategies will be summarized to improve catalytic activity either by doping, the formation of heterojunctions, or further techniques (e.g. introducing semipermeable protective layers or carboxyl groups at the surface).

7.2 Doping

The intentional introduction of impurity atoms changes the electronic structure of the host material and consequently doping is regularly used to tailor the band structure with the aim of enhancing certain properties such as conductivity and photocatalytic activity. To enhance the photocatalytic properties of $SrTiO_3$, various dopants e.g. Na,[230, 231] Li,[230, 231] K,[230, 231] Rb,[230, 231] Cs,[230, 231] Mg,[230, 231] In,[230, 231] Ga,[230, 231] Ir,[232] Nb,[233-235] Rb,[231] Fe,[213, 236] Cr,[198, 208, 237-239] Sc,[240] Ni,[233, 241, 242] La,[208, 231, 241-244] Rh,[244-246] Al,[127, 212, 230, 231, 247] Sb,[191, 248] Ta,[198, 233, 237] Co,[127] Cu,[127] Mn,[249] B,[250] N,[250-255] S,[250, 255, 256] C,[234, 250, 254, 256] P,[250] or F[250] were reported. Since doping with only one element may lead to the formation of very active recombination centers, and other disadvantages, codoping with either two cations, two anions or one cation and one anion became popular.[208, 233, 234, 242, 243, 254, 256]

7.2.1 Cationic monodoping

In $SrTiO_3$, doping with Al (Al: $SrTiO_3$) leads to the incorporation of Al^{3+} on the Ti^{4+} site and to a shift of the absorption edge to approx. 390 nm. In combination with Ag loading on the surface, a highly selective CO_2 conversion towards CO was achieved. The best results were achieved with 4 mol% Al doping.[212] Other systems consisting of Al:$SrTiO_3$ and cocatalysts forming a heterojunction are used for hydrogen evolution reactions[257] or overall water splitting[247, 258] with external quantum efficiencies of up to astonishing 96 % at 350 and 360

nm.[258] Cr doped $SrTiO_3$ nanoparticles can be used for NOx degradation and photocatalytic activity could be found under red light irradiation. Thereby a charge transfer from Cr^{3+} to the Ti^{4+} 3d orbital in the conduction band is responsible for the generation of $^{\bullet}O^{2-}$ and subsequently the formation of $^{\bullet}OOH$. Due to the reaction of $^{\bullet}OOH$, molecular oxygen, water and NO, HNO_2 and HNO_3 are formed.[239] In the degradation of gaseous isopropyl alcohol, Cr doping is also used to expand the absorption to the visible range and consequently improves the photoactivity of the Ag_3PO_4/Cr:$SrTiO_3$[259] and g-C_3N_4/Cr:$SrTiO_3$[260] heterojunctions. Even though Cr^{3+} enhances the efficiency of water splitting tremendously, in monodoped Cr:$SrTiO_3$ also Cr^{6+} is formed which is known to be a recombination center for photogenerated electrons and holes.[208] Fe: $SrTiO_3$ may be used for organic pollutant degradation.[213, 236] For Rhodamin B (RhB) degradation it is suggested that Fe-doped $SrTiO_3$ shows high visible light photocatalytic activity, due to Ti^{4+}-O^{2-}-Fe^{2+} linkages at and nearest to the surface. However, Fe energy states in the band gap can also act as electronic traps. Further, Mn doped $SrTiO_3$ can be used for water purification, where Mn^{4+} and Mn^{3+} coexist on the Ti^{4+} site and expand the photocatalytic activity to the visible light range,[249] an effect that was also shown for Ru, Rh and Ir doped $SrTiO_3$ loaded with Pt as cocatalyst.[261] In recent years, Rh doped $SrTiO_3$ became the basis of Z-scheme photocatalytic systems for water splitting under visible light.[189, 262, 263] Another application for Rh doped $SrTiO_3$ is the purification of wastewater e.g. by effectively killing E. coli bacteria under visible light. In this process, Rh^{3+} is present in the bulk as the photoactive substance and Rh^{4+} can be found at the surface.[226]In the presence of only Rh^{4+} in $SrTiO_3$, phages can be selectively inactivated by not harming E. coli bacteria at the same time.[264]

7.2.2 Cationic codoping

As mentioned above, single element doping can lead to the formation of recombination centers for photogenerated electron-hole pairs. Codoping is one way to overcome this problem. Ni doping of $SrTiO_3$ results in the formation of Ni^{2+} and Ni^{3+} states. Ni^{2+} introduces electron donor levels and consequently is a photoactive dopant for hydrogen evolution in the visible light range. Ni^{3+} on the other hand is believed to trap photogenerated electrons.[233] The introduction of La^{3+}[241, 242, 265, 266] on the Sr^{2+} site or Ta^{5+} or Nb^{5+}[233] on the Ti^{4+} site reduces the concentration of Ni^{3+} in favor of Ni^{2+} due to charge balance reasons.[233, 265] The same principle is utilized in the case of Cr doping. Cr^{3+} is desired and Cr^{6+} a well-known recombination center, whose formation can be prevented by codoping with La,[267]

Nb,[237] Sb[268] or Ta.[198, 237, 269, 270] Rh doping is more complex, since for some applications Rh^{3+} is favorable and for others Rh^{4+}. For example, codoping with La[243, 244] or Sb[191] leads to the formation of mainly Rh^{3+} and highly effective surfaces for hydrogen evolution.[244]

7.2.3 Anionic monodoping

For replacing oxygen in the lattice, fewer elements are available than for cationic doping. Since S, N, P and C exhibit higher p-orbital energies than oxygen, doping with these elements should shift the top of the valence band upwards and as a consequence, narrow the band gap.[271] However, all 2p states of the listed dopants except those of S show no strong interactions with the O(2p) orbitals and therefore cannot influence the valence band substantially. The band gap narrowing is either very small for N[250, 254, 271] or in the case of P doping quasi non-existent[250] and only localized states above the top of the valence band are introduced [294, 297, 314].[250, 254, 272] N(2p) states are quite close to the top of the $SrTiO_3$ valence band, while the impurity states introduced by C and P are located unfavorably mid-band gap.[250] On the other hand, S(2p) states mix with the O(2p) states, shifting the top edge of the valence band and effectively narrowing the band gap.[250, 272] In Figure *54*, calculated band positions and impurity states, introduced by anionic doping, are displayed.

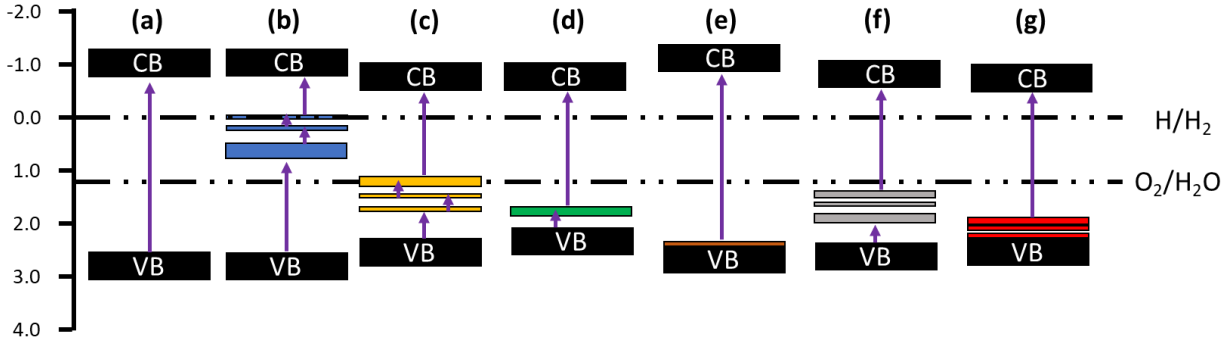

Figure 54: Calculated valence band and conduction band positions of non-doped **(a)** and no-metal doped **(b-g)** $SrTiO_3$. Additionally, the from the anionic doping introduced states are displayed. Doping accounts always to 4.167 atm% for the **(b)** B, **(c)** C, **(d)** N, **(e)** F, **(f)** P, and **(g)** S dopants. Position of the VB,CB and additional energy states from ref. [250]

7.2.4 Anionic codoping

Often, anionic codoping leads to more stable compounds than monodoping.[271] DFT calculations suggest that codoping of N and S causes synergistic effects and a strong band gap narrowing, which induces a good visible light absorption and may facilitate the

separation of photogenerated electrons and holes.[255] Codoping with C and S results in a mixture of O(2p), C(2s) and S(3s) orbitals as top of the valence band. The conduction band is composed of Ti(3d), C(2p) and S(3p) orbitals.[273] Thiourea (CH_4N_2S) is claimed to not only be a good codoping source for C,S:$SrTiO_3$ but also for N,S:$SrTiO_3$ photocatalysts.[253, 256] In order to determine the true sample composition, a careful interpretation of XRD and XPS data or additional analytic techniques are necessary.

7.2.5 Cationic anionic codoped systems

N and La codoping is expected to reduce the formation of oxygen vacancies[274, 275] and impurity states in the band gap[276] due to charge balance, furthermore it enhances the absorption ability and the photocatalytic activity of $SrTiO_3$ in visible light range.[274, 275] N,La:$SrTiO_3$ possesses one additional absorption band between 400 and 500 nm and features broad light absorption above 500 nm. Because of the codoping the oxidation of 2-propanol to CO_2 is photocatalyzed above 410 nm and the catalytic activity in the UV range is not decreased compared to pristine $SrTiO_3$.[275] Other examples for mixed cationic and anionic codoping are C,Nb:$SrTiO_3$[234] and Cr,B:$SrTiO_3$.[268] First principle studies suggest that strong Coulomb interaction between donors and acceptors results in an enhanced stability of codoped systems.[277]

7.3 Heterojunctions

Three types of heterojunctions can be distinguished, when two semiconductors (A and B) are brought into contact, compare Figure *55*. Depending on the respective band energies and doping levels, band alignment may lead to several different energetic situations for each type with ohmic junctions or either charge carrier depletion or accumulation zones. Establishing a driving force for charge carrier separation is decisive for a junction's suitability for photocatalytic applications. Alternatives are metal/semiconductor heterojunctions, surface heterojunctions, and Z-scheme heterojunctions that mimic the natural photosynthesis based on two photon excitation processes. In the following, a few out of the various $SrTiO_3$ based heterojunction photocatalysts are explained.

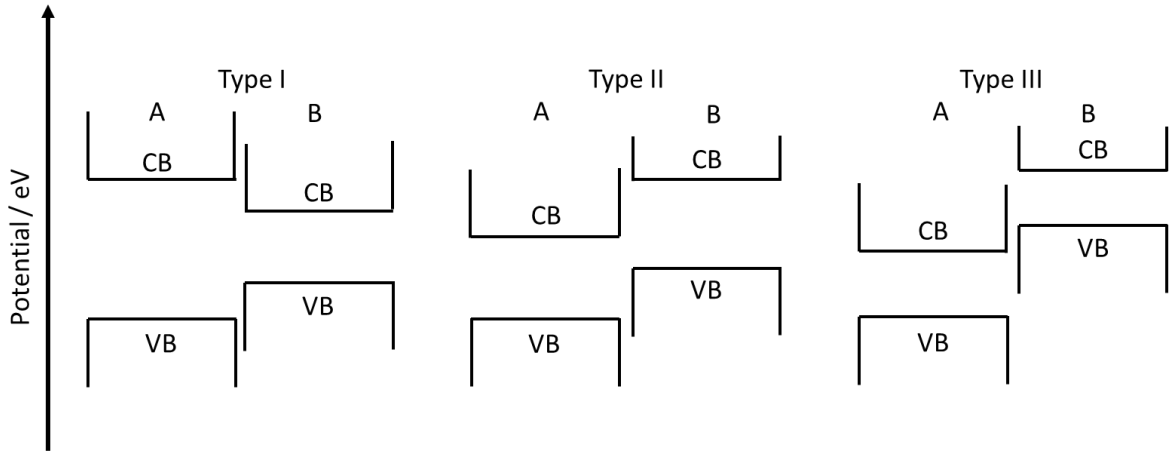

Figure 55: Schematic of the band position of type I, type II, and type III hetero junctions.

A widely used combination to form a type II heterojunction is $SrTiO_3/TiO_2$ with $SrTiO_3$ exhibiting higher CB and VB energies .[192, 204, 214, 216, 276, 278-283] Holes are transferred from the TiO_2 valence band to the valence band of $SrTiO_3$. On the other hand, electrons move from the $SrTiO_3$ conduction band to the conduction band of TiO_2 (see Figure *56*).[192] A pure $SrTiO_3/TiO_2$ system only absorbs light in the UV range, since TiO_2 and $SrTiO_3$ exhibit very similar band gaps of approximately 3.2 eV at room temperature. In order to facilitate/enable photocatalytic activity in the visible light range, $SrTiO_3$ and TiO_2 can both be doped to modify the electronic structure, or their surface can be loaded with metal nanoparticles such as Pt, Rh, or Ru.[283]

An advantage of loading semiconductors with metals may be the formation of a Schottky barrier, further suppressing recombination. However, if too many particles are present on the surface, they can also become recombination centers themselves,[283] resulting in an optimal loading, e.g. in the case of Rh on $SrTiO_3$, 0.05 wt%.[283] Another way to enable visible light photocatalytic activity is to engineer a ternary system consisting out of $TiO_2/SrTiO_3/g\text{-}C_3N_4$ (A) or $SrTiO_3/TiO_2/g\text{-}C_3N_4$ (B) nano compounds.[284, 285] In A, cascade charge transfer under UV illumination takes place, since the $g\text{-}C_3N_4$ valence and conduction bands are above the $SrTiO_3$ and the TiO_2 valence/conduction bands. Excited electrons are transported to the TiO_2 conduction band, whereas holes are transferred to the $g\text{-}C_3N_4$ conduction band.[285] In B, electrons are still only moved to the TiO_2 conduction band, but holes from the TiO_2 valence band can now be transported either into the valence band of $g\text{-}C_3N_4$ or $SrTiO_3$. Visible light can only excite electrons in $g\text{-}C_3N_4$, which exhibits a band gap of approx. 2.7 eV.[286]

Moreover, it is a cheap,[287] polymeric and metal-free material[286] and is chemically stable. $TiO_2/SrTiO_3$ heterojunctions can be used as photocatalyst in organic pollutant degradation [244, 317, 323],[214, 276, 283] for hydrogen production[276, 285] or N_2 fixation.[285] The described ternary $TiO_2/SrTiO_3/g\text{-}C_3N_4$ has similar applications, and the system can also be simplified to $SrTiO_3/g\text{-}C_3N_4$.[218, 260, 287] In such a two-component system it is easier to modify the electronic structure of $SrTiO_3$, since in a composition with only one heterojunction, the position of the band gaps can be chosen more freely. To enable visible light absorption in both $g\text{-}C_3N_4$ and $SrTiO_3$, doping of $SrTiO_3$ with Cr is common.[218]

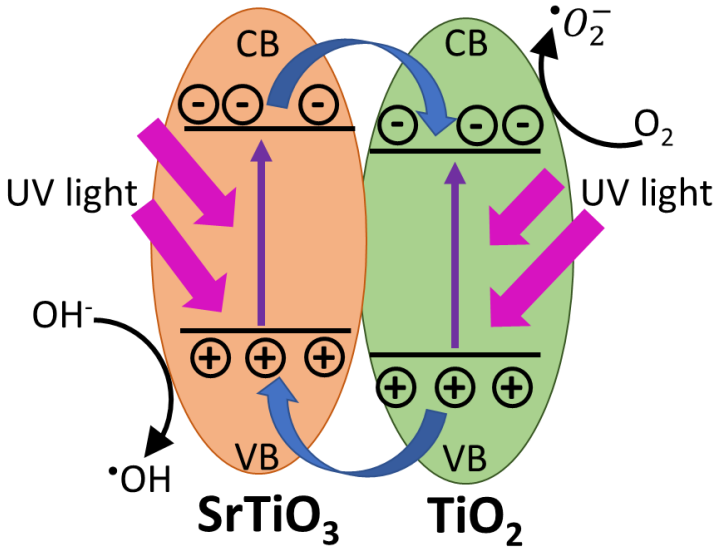

Figure 56: $SrTiO_3$ and TiO_2 based type II hetero junction for the illustration of the band positions and mechanisms behind the photocatalytic activity of such systems.[214]

Another example for a type II heterojunction for water splitting is $NiO/SrTiO_3$.[196, 288-291] Under irradiation with a 450 W high pressure mercury lamp its water splitting ability is tremendously enhanced compared to pure $SrTiO_3$. Moreover, it facilitates the evolution of H_2 and O_2 from pure water without the need of additional cocatalysts like Pt.[288] A more recent study suggests that $NiO_x/SrTiO_3$ compounds are in reality $Ni/SrTiO_3/NiO$ systems.[288] On these, Ni^0 acts as electron trap and as reduction site and lowers the proton reduction overpotential. NiO serves as water oxidation site and limits the performance of this system.[288] Methyl orange photo-degradation can be achieved with the combination of La doped WO_3 and $SrTiO_3$. La:WO_3 is nontoxic and exhibits a band gap of 2.8 eV, hence shows

photocatalytic activity under visible light. $SrTiO_3$ serves as co-catalyst and increases the photocatalytic activity of La doped WO_3. The degradation itself is caused by $^{\bullet}OH$ and $^{\bullet}O_2^-$ radicals, holes, and hydrogen peroxide.[292] In the last decades, many other $SrTiO_3$/metal oxide type II heterojunctions such as $SrTiO_3$/ZnO[293] and $SrTiO_3$/Ag_3PO_4[259] were described in literature.

Metal sulfides such as CdS[193, 215, 294] and MoS_2[295] can also form appropriate heterojunctions with $SrTiO_3$. With the help of chemical bath deposition, CdS nanodots can be applied on $SrTiO_3$ nanocubes at room temperature. CdS/$SrTiO_3$ is able to facilitate the hydrogen evolution under simulated sunlight irradiation. It exhibits an apparent quantum yield of 0.03 % at 375 nm, which means an improvement by a factor of 12.2 compared to pure $SrTiO_3$.[294] The ideal loading of CdS on $SrTiO_3$ is reported to be approx. 23.6 wt%. CdS has a band gap of 2.38 eV and its conduction band is slightly lower than the $SrTiO_3$ conduction band. Consequently, electrons are transferred to CdS and the recombination of photogenerated charge carriers is suppressed.[294] MoS_2/$SrTiO_3$ can be used for organic dye degradation, since electrons from the $SrTiO_3$ conduction band can move to the lower conduction band of MoS_2. Loadings of 0.05 wt% exhibited the best performance, higher amounts of MoS_2 on the $SrTiO_3$ surface block the active sites.[295] The absorption of $SrTiO_3$ does not change significantly due to MoS_2 loading, hence dye degradation is only enhanced under UV illumination.[295] An additional way to increase H_2 production of $SrTiO_3$ based catalysts under UV light is the coating with a conducting hydrophilic organic compound. A heterojunction is formed and the absorption of H_2O on the surface is improved. Consequently, charge recombination in the bulk and at the surface is reduced, furthermore the charge transfer from catalyst to the water molecule is alleviated.[296]

P-n junctions are a special of type II heterojunctions as the additional internal field formed by the contact helps to further improve the photogenerated charge carrier separation. In the following, some examples of such systems are given and explained. CuO and Cu_2O are p-type semiconductors and therefore form a p-n junction with n-type $SrTiO_3$ (compare Figure *57*). Thereby the Cu_xO bands are shifted upwards. This leads to a synergistic effect and a photocatalytic activity in the UV and visible light range. Both the valence and the conduction bands of the copper oxides are above the corresponding bands of $SrTiO_3$, consequently electrons are transferred to $SrTiO_3$ and holes to the copper oxides.[209, 297-299] Such composites can be used for CO_2 conversion, H_2 generation,[209, 298] or degradation of dyes.[297,

[298] BiOI is a p-type semiconductor with a band gap of 1.94 eV.[217] It is catalytically active under visible light and stable but exhibits a fast recombination rate.[217] In contact with $SrTiO_3$, the Fermi levels align and the bands of the BiOI nanoparticles on $SrTiO_3$ are shifted upwards, causing an electric field, enhancing charge carrier separation and suppressing recombination.[217] $SrTiO_3$/BiOI is able to catalyze the degradation of organic pollutants such as bisphenol A or methyl orange. The involved reactive species in this process are mainly $h^\bullet$ and $^\bullet O_2^-$.[217]

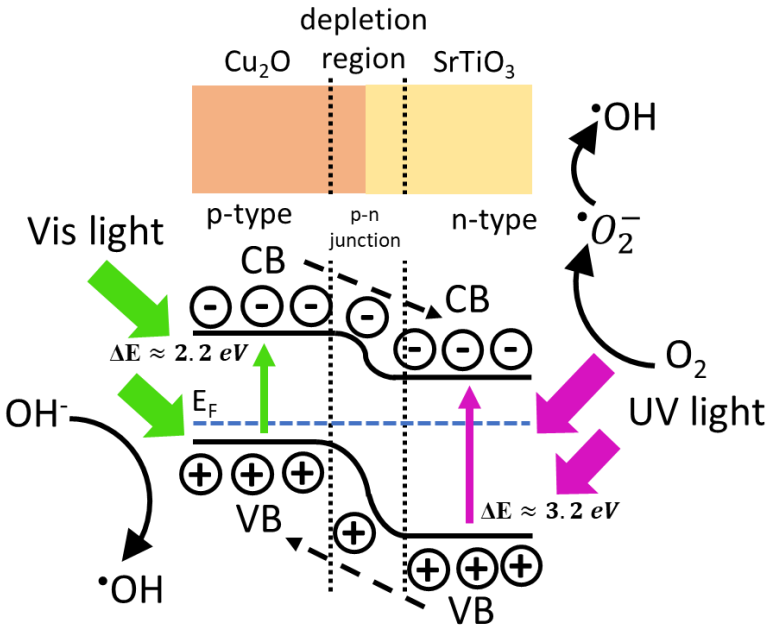

Figure 57: Schematic illustration of the n-$SrTiO_3$/p-Cu_2O p-n junction, with an in-build internal electric field, helping to separate charge carriers, thus suppressing recombination.[297]

7.4 Metal loading on the $SrTiO_3$ surface

Metal surface loadings of Cu,[207, 300] Ir ,[301] Pt,[189, 269, 283, 302] Rh,[193] Ru[193] Au,[193, 303] and Ag[212, 221, 304, 305] on $SrTiO_3$ and their influence on the photocatalytic activity have been investigated. The metals typically act as electron sink and as active reaction sites, thereby enhancing the separation of photogenerated electrons and holes. Too high loading amounts lead to overlapping agglomerations and possibly to electron accumulations, which induce an electric field which attracts electron holes.[193, 212] Pt is the most commonly used loading

material for photocatalytic water splitting and organic pollutant degradation. Pt nanoclusters form a Schottky barrier with $SrTiO_3$, facilitate the reduction process and absorb visible light due to localized energy levels in the band gap of $SrTiO_3$. However, studies suggest that under optimum conditions Cu can be a cheaper replacement for Pt. $SrTiO_3$ loaded with 0.5 wt% Cu shows a similar performance as $SrTiO_3$ loaded with 0.5 wt% Pt in the H_2 evolution from aqueous methanol solution under UV irradiation.[207] Apart from metal loadings, graphene can act as electron sink as well and enhance the charge separation.[306]

Additionally, Au,[307-310] Ag,[304, 305, 310, 311] and Pd[312] nanoparticles are known to exhibit surface plasmon resonance (SPR), which can be capitalized in photocatalytic processes. Free charge carries collectively oscillate and when light with the oscillation frequency shines on the nanoparticles, strong absorption can be observed. Thereby the resonance frequency can be easily tuned by variation of material, surrounding, shape, and size of the metal clusters. The smaller the nanoparticles, the lower the resonance frequency becomes; hence Ag clusters can be tuned to absorb light in the visible range and gold clusters even in the near infrared. Light below the resonance frequency is reflected and light with a wavelength too short for absorption is transmitted.[310, 313]

Three mechanisms are discussed to improve the photocatalytic activity of metal semiconductor heterojunctions, based on surface plasmon resonance.[314] Firstly, electrons are easily excited in Au or Ag by plasmon resonance and subsequently transferred by tunneling to the conduction band of the nearby semiconductor. For this electron injection, the metal and the semiconductor have to be in direct contact. Secondly, huge and strongly localized electric fields are generated by the light absorption. In areas very close to these hot spots the photogeneration of electron hole pairs is strongly accelerated in the semiconductor. Moreover, the field intensity is spatially inhomogeneous, the closer to the metal surface, the stronger the electric field becomes. This has two main impacts, (i) the photogenerated electrons holes are separated (suppressed recombination) and (ii) most of the charge carries are formed close to the semiconductor's surface (short migration length). Thirdly, photons are scattered by the metal clusters. This causes an increased electron hole pair formation since the mean photon path is increased.[314] Since the resonance frequencies are in the range of visible light and undoped $SrTiO_3$ exhibits a band gap of approx. 3.2 eV at room temperature, Au or Ag loading alone would not lead to an optimal enhancement, since the incoming photons need to induce the surface plasmon resonance effects and excite

electrons in the semiconductor. Consequently, to utilize the surface plasmon resonance effect of Au or Ag in the photocatalytic degradation of organic pollutants, water splitting, or CO_2 conversion, the metal nanostructures have to be carefully designed and the metal loading needs to be combined with doping of $SrTiO_3$.[310]

7.5 Z-scheme Systems

In contrast to other approaches, Z-Scheme systems are based on a two-photon process and two photocatalysts are combined. One is specially designed for the oxygen evolution reaction and the other for the hydrogen evolution reaction in an overall water splitting system. Between the two, usually a redox system (redox mediator) is responsible for the uptake of photogenerated electrons from the conduction bands of the oxygen evolution photocatalyst (OEP) and the photogenerated holes from the valence band of the hydrogen evolution photocatalyst (HEP), thus enabling an electric current. The valence band of the OEP is more positive than the H_2O/O_2 potential whereas the conduction band of the HEP is so negative that it facilitates the proton reduction. Optionally each catalyst surface may be loaded with co-catalysts such as Ru, Mo, or Pt.[195, 262]

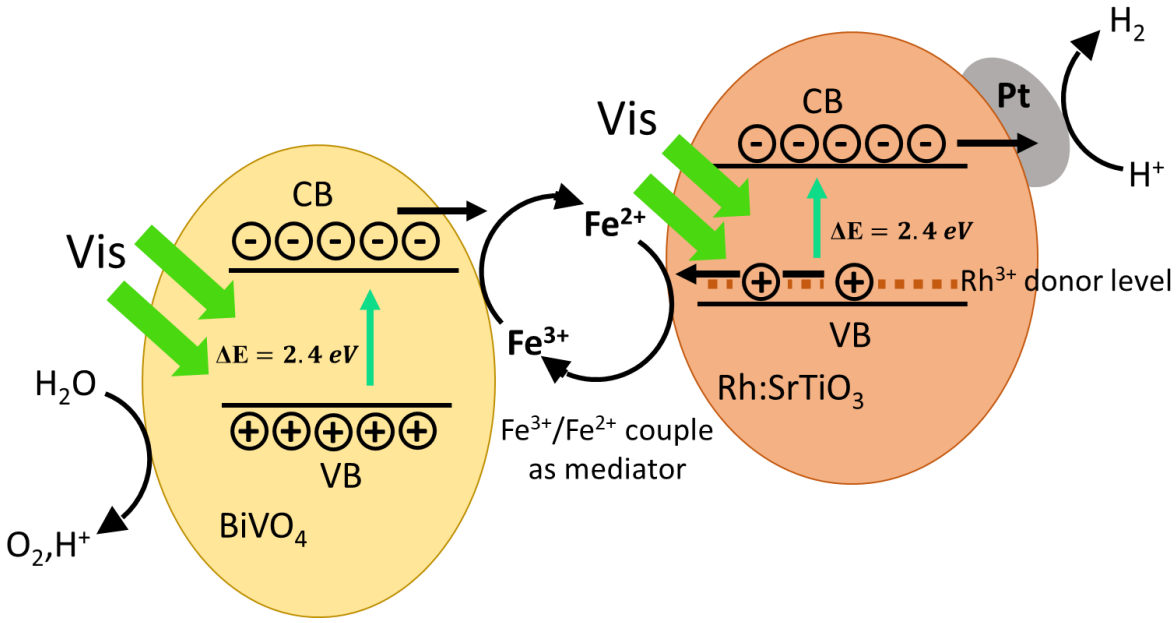

Figure 58: Band position and schematic of the mechanism behind a Z-scheme photocatalyst based on Pt loaded Rh-doped $SrTiO_3$, $BiVO_4$, and $Fe^{2+/3+}$ couple as mediator. The energy gap between Rh^{3+} donor levels and the conduction band of $SrTiO_3$ amounts to 2.4 eV, thus visible light is able to excite e^- from the valence band to the conduction band. Rh:$SrTiO_3$ acts as HEP and $BiVO_4$ as OEP.[302]

Such Z-scheme photocatalyst systems can be rather complicated (compare Figure 58), and $SrTiO_3$ based systems still exhibit moderate solar to hydrogen energy conversion efficiencies, the best in the range of 1.2 % at 420 nm, 331 K, and under 10 kPa.[262] However, they have some undeniable advantages such as: the catalysts can be individually optimized for the oxidation and reduction reactions, the oxygen and hydrogen evolution can be spatially separated, and visible light is sufficient to excite electrons from the conduction bands to the valence bands.[262, 315]

In the last years, the most promising HEPs have been La,Cr: $SrTiO_3$,[316] La,Rh: $SrTiO_3$,[195] Cr,Ta: $SrTiO_3$,[270] or Rh: $SrTiO_3$.[302, 317-319] All of these can be loaded with cocatalysts, for example Ru[194, 315, 317-319] or Pt.[263, 270, 302] The loading takes care of the electron transfer to reduce H^+ and can enhance the charge separation. Rh doping leads to the formation of Rh^{3+} and Rh^{4+} and enables $SrTiO_3$ to absorb visible light, due to the introducing Rh^{3+} electron donor levels.[194, 263, 315] As redox mediator between the HEPs and OEPs, various systems were developed and have their specific advantages and disadvantages. In general, they need to meet certain criteria to be suitable: their redox potential must be between the reduction and oxidation potential of water, they have to be transparent, and the change of their oxidation state has to reversible under the predominant conditions. Used mediator systems are IO^{3-}/I^-,[270, 320] Fe^{2+}/Fe^{3+},[263, 302, 317, 320] $[Co(bpy)_3]^{3+}/[Co(bpy)_3]^{2+}$,[194, 315] $[Co(phen)_3]^{3+}/[Co(phen)_3]^{2+}$ [315] and VO_2^+/VO^{2+}.[321] All of these operate in aqueous solutions with pH ranging from 2.1 to 11. Co-complexes exhibit a high turnover rate, bind well to the catalysts' surfaces, are very selective to the forward reaction and have their optimum at pH 7. In acidic reaction solutions, the oxygen evolution is hindered and instead Co^{2+} is oxidized. IO^{3-}/I^- and Fe^{2+}/Fe^{3+} systems are widely used and Fe^{2+} can also act as a catalyst for the H_2 production. On the other hand, Fe^{3+}/Fe^{2+} systems can only be used up to approx. 550 nm. In a Rh: $SrTiO_3$ based and Fe^{2+}/Fe^{3+} mediated system, Ru loading leads to a higher photocatalytic activity than Pt loading, since the suppression of the backward reaction is improved by Ru.[262]

Additionally, to the listed redox mediators, also solids such as Au,[322] Ag,[221] Ir,[243] indium tin oxide (ITO)[195] and reduced graphene oxide[319] can act as mediators, however the synthesis of such systems is challenging. Some studies went even further and abandoned the mediator

completely. In these, for example reversible $Rh^{3+/4+}$ species on the surface of Rh doped $SrTiO_3$ act as charge carrier/transporter.[318]

As OEPs $BiVO_4$,[263, 317, 318] $BiVO_4$ loaded with RuO_2, Mo[322] or CdS,[323] WO_3,[316] WO_3 with PtO_x[324] or Pt loading,[324] $AgNbO_3$,[262] Cr,Sb:TiO_2,[262] Ta_3N_5 loaded with CoO_x,[243] Bi_2MoO_6,[189, 262] $Bi_6NbWO_{14}Cl$,[262, 325] Ag_3PO_4[221] and others[219] can be found in literature. WO_3 and $BiVO_4$ do not need any co-catalyst in combination with an Fe^{3+}/Fe^{2+} mediator for the oxygen evolution. Moreover, these two are the most common OEPs in $SrTiO_3$ based Z-Scheme photocatalysts.[262]

7.6 Further techniques

7.6.1 Surface anisotropy

As described above, charge separation is one of the main challenges during photocatalytic processes and many strategies were developed to suppress charge recombination. In most approaches, metal loadings were used as electron sinks and/or enhance the charge separation by forming a Schottky barrier. However, also the surface anisotropy between the {001} and {110} facets of $SrTiO_3$ can be capitalized to increase the photocatalytic activity. The {001} surface is charge neutral, due to its SrO or TiO_2 termination. The {110} facets are formed either by positively charged $SrTiO_3$ or negatively charged oxygen layers. Furthermore, under illumination with wavelengths near the absorption edge, the electronic band structure of $SrTiO_3$ facilitates the formation of electrons and holes with a momentum in the {001} direction. This may be the reason that the {001} facet exhibits a higher photocatalytic activity than the {111} or {110} facets.[326] In general, the existence of catalytic anisotropy as well as oxidizing and reducing facets is known not only for $SrTiO_3$,[126, 327] but also for $BiVO_4$,[328, 329] TiO_2,[330] and Cu_2O.[331]

18-facet $SrTiO_3$ microcrystals were produced and a cocatalyst was selectively simultaneously photo-deposited either on the {100} or the {110} facets. On the {100} surfaces, Pt nanoparticles facilitate the hydrogen evolution and on the {110} surface, Co_3O_4 facilitates the oxygen evolution in overall water splitting. Such systems with two spatially separated cocatalysts show a five-time better quantum efficiency than $SrTiO_3$ with randomly distributed cocatalysts on its surfaces (in the case of cubic $SrTiO_3$, with only six {100} facets present).[126] Another study showed that charge and cocatalyst separation is even possible on one surface of an $SrTiO_3$ cube. The authors suggest that the upwards surface band

bending depends on illumination and is stronger at the edges and corners under no or under weak irradiation. This leads to a hole movement towards the edges and corners and to the ability to deposit Pt selectively in the center and Co_3O_4 on the edges of $SrTiO_3$ cubes.[332]

7.6.2 Surface manipulation

Carboxyl groups from oleic acids bond to Ti^{4+} on $SrTiO_3$ and by forming a dipole layer, visible light absorption for photocatalytic NO degradation becomes possible.[333] Surface-alkalization of $SrTiO_3$ in a NaOH/methanol/water solution with pH>13 shifts the surface energy bands upwards. Thus, reduction power is enhanced, and the decreased oxidation potential is balanced by the fact that the absorbed hydroxide ions promote the methanol oxidation.[334] Sc doped $SrTiO_3$ with Rh_2O_3 as cocatalyst suffers from a fast back reaction of H_2 and O_2 acting as a chemical short circuit.

Here, semipermeable protective layers consisting of Cr_2O_3 or Ta_2O_3 covering the cocatalysts and the $SrTiO_3$ surface block oxygen and organic molecules (e.g. ethanol) from active sides, whereas H_2O and H_2O_2 can reach the surface of the catalyst. Consequently, the total photocatalytic activity of overall water splitting is increased.[240]

Oxygen vacancies near the $SrTiO_3$ surface can act as electron traps and adsorption sites for N_2, hence enhancing photocatalytic activity for N_2 fixation.[225] A different thermal expansion coefficient of $SrTiO_3$ and Au when combining the materials, can be used to introduce tensile strain in $SrTiO_3$ and thus promote the formation of oxygen vacancies and Ti^{3+}, altering the electronic band structure and thus enhancing the photocatalytic activity of $SrTiO_3$.[335] Further, also liquid nitrogen treatment may introduce compressive strain, causing a narrowed band gap and consequently a shifted light absorption edge to lower energies.[225] Solid state reaction of $SrTiO_3$ with $NaBH_4$ leads to a disordered shell while retaining a crystalline bulk. Again, oxygen vacancies are introduced and the oxygen vacancy concentration for optimal efficiency was found to be in the range of 3.3 atom%.[336] Treating $SrTiO_3$ with $NaBH_4$ was further beneficial by increasing light absorption in the visible light range.[336]

7.7 Future perspectives

For nearly all of the described $SrTiO_3$ based photocatalysts, further improvements are desirable to be competitive in industrial processes. Current research efforts are improving the efficiency, durability, production costs, and/or safety, before the photocatalytic systems can be scaled up to pilot- or industrial-scale. To reduce production costs, new Z-scheme based printable particulate catalyst sheets are being developed. Rh-doped $SrTiO_3$ (HER) was mixed with indium tin oxide (as conductive solid mediator), Mo-doped $BiVO_4$ (OER), and an organic solvent. Subsequently, the mixture was printed on a glass substrate and calcinated at 573 K for 30 min. This method can be scaled up easily and cost effective mass production.[193] In another approach a 1 m^2 sized photocatalytic water splitting panel was fabricated of Al:$SrTiO_3$ decorated with $RhCrO_x$. The system was tested under natural sunlight on the rooftop of the University of Tokyo and according to Y. Goto et al.: “could be the basis for a self-running large-scale solar hydrogen plant in the future”.[247] A decrease in the photocatalytic activity was witnessed and minimized with the co-loading of CoO_x. However, degradation and safety issues remained. In large scale plants an efficient gas separation of H_2 and O_2 is essential and can for example be done by ceramic membranes.[247] A further possible way to tackle this safety issue is the use of a twin reactor in which O_2 and H_2 formation is completely spatially separated. Under visible light irradiation H_2 evolves from a Rh-doped and Pt loaded $SrTiO_3$ catalyst in one reactor and O_2 is formed over WO_3 in the second one. The reaction chambers are separated by a Nafion membrane which allows the exchange of protons and an aqueous Fe^{2+}/Fe^{3+} redox system acts as mediator between the reduction and the oxidation site.[190] Even though attempts were made to develop large-scale plants, several technological issues remain to be solved. A mix of fundamental research towards a better understanding of the photocatalytic charge transfer or reaction mechanisms as well as improvements in application of photocatalysts will advance the technology towards industrial environmental-friendly processes.

8 Conclusion / Final remarks

It was shown that UV irradiation causes oxygen to be incorporated into undoped and Fe-doped $SrTiO_3$ at elevated temperatures. Consequently, oxygen vacancies were filled, and holes were created due to charge neutrality. This affected the whole bulk rather than merely the thin layer near the surface where the UV light was absorbed. In air at 400 °C a blackening of Fe-doped $SrTiO_3$ single crystals was observed. Using UV/Vis spectroscopy the continuous darkening of specimens under UV irradiation was monitored and a chemical diffusion coefficient determined. Additionally, van der Pauw and impedance measurements showed on Fe-doped $SrTiO_3$ that in-plane bulk conductivity was strongly enhanced during and after UV irradiation. After UV exposure the conductivity decreased extremely slowly. Even at a temperature as high as 700 °C nearly 12 h were needed to reestablish the initial defect state and conductivity. This further shows that in contrast to low temperature photochromism the effects witnessed over the course of this work were the result of oxygen stoichiometry changes and not due to the activation of color centers by UV illumination. Under UV irradiation an oxygen chemical potential increase by several hundred meV was observed.

In undoped $SrTiO_3$ single crystals with Pt electrodes on the dark back side the conductivity even increased by several orders upon UV irradiation between 280 and 400 °C in air. After the UV light was turned off the enhanced conductivity again relaxed only slowly. Oxygen chemical diffusion coefficients were obtained from time dependent conductivity measurements. Shifts of X-ray absorption spectra of the Ti $L_{2,3}$-edge to higher energies and the in-plane conductivity increase indicate that also undoped $SrTiO_3$ single crystals were oxidized under UV illumination in air at elevated temperatures. Finally, a model explaining the impact of UV illumination was derived, based on oxygen quasi-chemical potentials. According to this model, conduction band electrons strongly accelerate the oxygen incorporation and oxygen diffusion from the illuminated zone into the dark bulk is determined by electron holes.

Under UV light exposure and strongly reducing atmospheres, namely dry and humidified H_2, the conductance of an undoped $SrTiO_3$ single crystal increased shortly upon UV irradation, but then started to decline and in dry H_2 conductivity dropped even below the initial (dark) value. This can again be explained by oxygen incorporation into the entire $SrTiO_3$ single crystal, since at this low oxygen partial pressures $SrTiO_3$ became a n-type semiconductor and

the consumption of electrons due to the filling of oxygen vacancies decreased the bulk conductivity. Here oxygen incorporation required light induced water splitting at the $SrTiO_3$ surface. Consequently, the photocatalytic activity of $SrTiO_3$ played a crucial role in this process.

To this point oxygen incorporation in air and N_2 at elevated temperatures was only detected indirectly, thus in a next step the weight gain due to an oxygen content increase was measured by $GaPO_4$ microbalances. A measurement set-up was built and tested by gas exchange experiments applied on undoped $SrTiO_3$, Fe-doped $SrTiO_3$ and $La_{0.6}Sr_{0.4}CoO_3$ polycrystalline thin films. Mass gain of Fe-doped $SrTiO_3$ samples by UV illumination was confirmed. However, further investigations are needed since the interaction between the $GaPO_4$ single crystals and UV light is not yet understood. Moreover, the shifts in the resonant frequency due to UV irradiation were caused by three different processes, namely the change in the oxygen content, heating effects of the UV light, and drifts in the frequency. Thus, the mass gain by UV illumination was determined only after the UV light was turned off.

Finally pseudo-intrinsic (ultra-low) bulk conductivities of epitaxially grown undoped and acceptor doped $SrTiO_3$ thin films deposited from stochiometric targets were investigated. As electronically active main defect, Sr vacancies were confirmed by different analysis tools such as PALS, ICMP-OES, and RBS. In a Fe-doped $SrTiO_3$ thin film the Fe distribution between the A- and B-site was determined by X-ray standing wave measurements. They revealed that 30-40 % of Fe is present at the A site and the rest at the B-site. No Fe was found on an interstitial site. Additionally, X-ray absorption spectroscopy with subsequent simulations suggest that approx. 10 % of the Fe present in the bulk exhibits the valency of 2+. Thus, Fe acts as acceptor as well as donor in the investigated thin films. However, the pseudo-intrinsic behavior attributed to a pinning of the Fermi level to the middle of the band gap could not be explained by an unexpected Fe distribution. A model was derived and confirmed by calculations based on mass action laws. The observed robust Fermi level pinning is explained by the interplay of acceptor-type mid-gap states and a donor dopant, here Sr vacancies and Ti at the A-site.

Acknowledgement

First of all, special thanks to my supervisor Prof. Jürgen Fleig, who made this work possible in the first place. Our fruitful discussions were inspiring and allowed me to see many of the obtained results from another point of view. Without the input and ideas from my office colleague Markus I would not have been able to write these lines, thank you very much for all your support throughout the last years. Max, it was always fun and productive to work together with you and I will not forget the nights spent at the beamlines in Hamburg and at the Paul Scherrer Institut. Many thanks to Matthäus & Alex for all the defect chemical calculations and discussions. Tobi lunch times were always a welcome change in the day, thank you for building all the great measurement set-ups. I would like to express my gratitude to the whole working group for creating such an amazing working atmosphere. Great thanks to Werner, who taught me how to operate the X-ray diffractometer and Christopher for the ICP-OES measurements.

Furthermore, I would like to acknowledge facility and staff, special thanks to Gesara and Carlos, from the Paul Scherrer Institut for making the X-ray absorption measurements, the Rutherford backscattering spectroscopic measurements, and the elastic recoil detection analysis possible and for helping to interpret the experimental data. Of course, also many thanks to facility and staff of DESY, where Max and I conducted the X-ray standing wave measurements. Michał thank you for writing the software allowing us to fit the data and to simulate various Fe site occupations.

The Austrian Science Fund (FWF) (projects: F4509-N16 and P31654-N37) and the European Union's Horizon 2020 research and innovation program under grant agreement No. 824072 are acknowledged for their financial support.

To all my friends of pre-kindergarten times and from later on in life, thank you for all the fun time during our holidays, adventures, frisbee tournaments, barbeque evenings, etc. Finally, I would like to thank my family for all the support and Marlies for your love.

References

[1] R. Merkle, and J. Maier, How is Oxygen Incorporated into Oxides? A Comprehensive Kinetic Study of a Simple Solid-State Reaction with $SrTiO_3$ as a Model Material, Angew. Chem. Int. Ed. 47 (2008) 3874-3894.

[2] S.A. Hayward, and E.K.H. Salje, Cubic-Tetragonal Phase Transition in $SrTiO_3$ Revisited: Landau Theory and Transition Mechanism, Phase Transit. 68 (2006) 501-522.

[3] R. Loetzsch, A. Lübcke, I. Uschmann, E. Förster, V. Große, M. Thuerk, T. Koettig, F. Schmidl, and P. Seidel, The Cubic to Tetragonal Phase Transition in $SrTiO_3$ Single Crystals Near its Surface under Internal and External Strains, Appl. Phys. Lett. 96 (2010) 071901.

[4] U. Aschauer, and N.A. Spaldin, Competition and Cooperation between Antiferrodistortive and Ferroelectric Instabilities in the Model Perovskite $SrTiO_3$, J. Phys. Condens. Matter 26 (2014) 122203.

[5] R.A. De Souza, J. Fleig, R. Merkle, and J. Maier, $SrTiO_3$: A Model Electroceramic, Z. Metallkd. 69 (2003) 218-225.

[6] P.K. Gogoi, and D. Schmidt, Temperature-Dependent Dielectric Function of Bulk $SrTiO_3$: Urbach Tail, Band Edges, and Excitonic Effects, Phys. Rev. B 93 (2016) 075204.

[7] D.J. Kok, K. Irmscher, M. Naumann, C. Guguschev, Z. Galazka, and R. Uecker, Temperature-Dependent Optical Absorption of $SrTiO_3$, Phys. Status Solidi A 212 (2015) 1880-1887.

[8] K. van Benthem, C. Elsässer, and R.H. French, Bulk Electronic Structure of $SrTiO_3$: Experiment and Theory, J. Appl. Phys. 90 (2001) 6156-6164.

[9] R. Astala, and P.D. Bristowe, A Computational Study of Twist Boundary Structures in Strontium Titanate, J. Phys. Condens. Matter 14 (2002) 13635-13641.

[10] H. Shen, Y. Song, P. Wang, and Y. Xi, A High-Permittivity $SrTiO_3$-Based Grain Boundary Barrier Layer Capacitor Material Single-Fired under Low Temperature, Mater. Lett. 56 (2002) 802–805.

[11] J.W. Fergus, Perovskite Oxides for Semiconductor-Based Gas Sensors, Sens. Actuators B 123 (2007) 1169-1179.

[12] W. Menesklou, H.-J. Schreiner, K.H. Härdtl, and E. Ivers-Tiffee, High Temperature Oxygen Sensors Based on Doped $SrTiO_3$, Sens. Actuators B 59 (1999) 184-189.

[13] D.M. Hill, H.M. Meyer, and J.H. Weaver, Y, Ba, Cu, and Ti Interface Reactions with $SrTiO_3$ (100) Surfaces, J. Appl. Phys. 65 (1989) 4943-4950.

[14] A. Ohtomo, and H.Y. Hwang, A High-Mobility Electron Gas at the $LaAlO_3/SrTiO_3$ Heterointerface, Nature 427 (2004) 423-426.

[15] A. Kalabukhov, R. Gunnarsson, J. Börjesson, E. Olsson, T. Claeson, and D. Winkler, Effect of Oxygen Vacancies in the $SrTiO_3$ Substrate on the Electrical Properties of the $LaAlO_3/SrTiO_3$ interface, Phys. Rev. B 75 (2007) 121404.

[16] G. Herranz, F. Sánchez, N. Dix, M. Scigaj, and J. Fontcuberta, High mobility conduction at (110) and (111) $LaAlO_3/SrTiO_3$ interfaces, Scientific Reports 2 (2012).

[17] A. Tebano, E. Fabbri, D. Pergolesi, G. Balestrino, and E. Traversa, Room-Temperature Giant Persistent Photoconductivity in $SrTiO_3/LaAlO_3$ Heterostructures, ACS Nano 6 (2012) 1278-1283.

[18] M.C. Ni, S.M. Guo, H.F. Tian, Y.G. Zhao, and J.Q. Li, Resistive Switching Effect in $SrTiO_{3-\delta}$/Nb-Doped $SrTiO_3$ Heterojunction, Appl. Phys. Lett. 91 (2007) 183502.

[19] R. Waser, R. Dittmann, G. Staikov, and K. Szot, Redox-Based Resistive Switching Memories - Nanoionic Mechanisms, Prospects, and Challenges, Adv. Mater. 21 (2009) 2632-2663.
[20] H. Nili, S. Walia, S. Balendhran, D.B. Strukov, M. Bhaskaran, and S. Sriram, Nanoscale Resistive Switching in Amorphous Perovskite Oxide (a-$SrTiO_3$) Memristors, Adv. Funct. Mater. 24 (2014) 6741-6750.
[21] M. Kubicek, R. Schmitt, F. Messerschmitt, and J.L.M. Rupp, Uncovering Two Competing Switching Mechanisms for Epitaxial and Ultrathin Strontium Titanate-Based Resistive Switching Bits, ACS Nano 9 (2015) 10734-10748.
[22] C. Lenser, A. Koehl, I. Slipukhina, H. Du, M. Patt, V. Feyer, C.M. Schneider, M. Lezaic, R. Waser, and R. Dittmann, Formation and Movement of Cationic Defects During Forming and Resistive Switching in $SrTiO_3$ Thin Film Devices, Adv. Funct. Mater. 25 (2015) 6360-6368.
[23] C.H. Kim, Y. Ahn, J.Y. Son, and J.A. Varela, SrTiO3-Based Resistive Switching Memory Device with Graphene Nanoribbon Electrodes, Journal of the American Ceramic Society 99 (2016) 9-11.
[24] W. Jung, and H.L. Tuller, A New Model Describing Solid Oxide Fuel Cell Cathode Kinetics: Model Thin Film $SrTi_{1-x}Fe_xO_{3-\delta}$ Mixed Conducting Oxides-a Case Study, Adv. Energy Mater. 1 (2011) 1184-1191.
[25] D.C. Johnson, and A.L. Prieto, Use of Strontium Titanate ($SrTiO_3$) as an Anode Material for Lithium-Ion Batteries, J. Power Sources 196 (2011) 7736-7741.
[26] G. Walch, B. Rotter, G.C. Brunauer, E. Esmaeili, A.K. Opitz, M. Kubicek, J. Summhammer, K. Ponweiser, and J. Fleig, A Solid Oxide Photoelectrochemical Cell with UV Light-Driven Oxygen Storage in Mixed Conducting Electrodes, J. Mater. Chem. A 5 (2017) 1637-1649.
[27] A. Rothschild, W. Menesklou, H. Tuller, and E. Ivers-Tiffe´e, Electronic Structure, Defect Chemistry, and Transport Properties of $SrTi_{1-x}Fe_xO_{3-y}$ Solid Solutions, Chem. Mater. 18 (2006) 3651-3659.
[28] C. Rodenbücher, C. Korte, T. Schmitz-Kempen, S. Bette, and K. Szot, A Physical Method for Investigating Defect Chemistry in Solid Metal Oxides, APL Mater. 9 (2021) 011106.
[29] I. Denk, W. Münch, and J. Maier, Partial Conductivities in $SrTiO_3$: Bulk Polarization Experiments, Oxygen Concetration Cell Measurments, and Defect-Chemical Modeling, J. Am. Ceram. Soc. 78 (1995) 3265-3272.
[30] R. Moos, and K.H. Härdtl, Defect Chemistry of Donor-Doped and Undoped Strontium Titanate Ceramics between 1000° and 1400°C, J. Am. Ceram. Soc. 80 (1997) 2549–2562.
[31] S. Rodewald, J. Fleig, and J. Maier, Measurement of Conductivity Profiles in Acceptor-Doped Strontium Titanate, J. Eur. Ceram. Soc. 19 (1999) 797-801.
[32] F. Messerschmitt, M. Kubicek, S. Schweiger, and J.L.M. Rupp, Memristor Kinetics and Diffusion Characteristics for Mixed Anionic-Electronic $SrTiO_{3-\delta}$ Bits: The Memristor-Based Cottrell Analysis Connecting Material to Device Performance, Adv. Funct. Mater. 24 (2014) 7448-7460.
[33] R. Waser, DC Electrical Degradation of Perovskite-Type Titanates: II, Single Crystals, J. Am. Ceram. Soc. 73 (1990) 1654-1662.
[34] S. Rodewald, J. Fleig, and J. Maier, Resistance Degradation of Iron-Doped Strontium Titanate Investigated by Spatially Resolved Conductivity Measurements, J. Am. Ceram. Soc. 83 (2000) 1969-1976.
[35] E.M. Rockkar, and R.A. Forman, Fe^{4+} ($3d^4$) Optical Absorption in Oxidized $SrTiO_3$, Phys. Status Solidi A 33 (1976) K91-K95.

[36] A. Koehl, D. Kajewski, J. Kubacki, C. Lenser, R. Dittmann, P. Meuffels, K. Szot, R. Waser, and J. Szade, Detection of Fe^{2+} Valence States in Fe Doped $SrTiO_3$ Epitaxial Thin Films Grown by Pulsed Laser Deposition, Phys. Chem. Chem. Phys. 15 (2013) 8311-8317.
[37] K.A. Müller, T. von Waldkirch, and W. Berlinger, Photochromic Fe^{5+} ($3d^3$) in $SrTiO_3$ Evidence From Paramagnetic Resonance, Solid State Commun. 9 (1971) 1097-1101.
[38] K.W. Blazey, O.F. Schirmer, W. Berlinger, and K.A. Müller, Identifcation of Fe^{4+} and Fe^{5+} Charge-Transfer Photochromic Absorption Bands in $SrTiO_3$, Solid State Commun. 16 (1975) 589-592.
[39] K.W. Blazey, Optical Absorption of $SrTiO_3$:Fe^{4+}, Phys. Status Solidi A 38 (1976) K97-K99.
[40] T.W. Kool, and M. Glasbeek, Photchromic Fe^{5+} in Non-Cubic Local Fields in $SrTiO_3$, Solid State Commun. 22 (1977) 193-197.
[41] J. Szade, K. Szot, M. Kulpa, J. Kubacki, C. Lenser, R. Dittmann, and R. Waser, Electronic Structure of Epitaxial Fe-Doped $SrTiO_3$ Thin Films, Phase Transitions 84 (2011) 489-500.
[42] J. Kubacki, D. Kajewski, J. Goraus, K. Szot, A. Koehl, C. Lenser, R. Dittmann, and J. Szade, Impact of Fe Doping on the Electronic Structure of $SrTiO_3$ Thin Films Determined by Resonant Photoemission, J. Chem. Phys. 148 (2018) 154702.
[43] R. Merkle, and J. Maier, Defect Association in Acceptor-Doped $SrTiO_3$: Case Study for $Fe'_{Ti}V^{\cdot\cdot}_O$ and $Mn''_{Ti}V^{\cdot\cdot}_O$, Phys. Chem. Chem. Phys. 5 (2003) 2297-2303.
[44] R. Waser, T. Bieger, and J. Maier, Determination of Accceptor Concentrations and Energie Levels in Oxides using an Optoelectrochemical Technique, Solid State Commun. 76 (1990) 1077-1081.
[45] R. Merkle, R.A. De Souza, and J. Maier, Optically Tuning the Rate of Stoichimetry Changes: Surface-Controlled Oxygen Incorporation into Oxides under UV Irradiation, Angew. Chem. Int. Ed. 40 (2001) 2126-2129.
[46] B.W. Faughnan, Photochromism in Transition-Metal-Doped $SrTiO_3$, Phys. Rev. B 4 (1971) 3623-3636.
[47] T. Bieger, J. Maier, and R. Waser, Optical Investigation of Oxygen Incorporation in $SrTiO_3$, Solid State Ion. 53-56 (1992) 578-582.
[48] T. Bieger, J. Maier, and R. Waser, Kinetics of Oxygen Incorporation in $SrTiO_3$ (Fe-Doped): An Optical Investigation, Sens. and Actuator. B 7 (1992) 763-768.
[49] C.B. Gopal, and S.M. Haile, An Electrical Conductivity Relaxation Study of Oxygen Transport in Samarium Doped Ceria, J. Mater. Chem. A 2 (2014) 2405-2417.
[50] J.A. Lane, and J. Kilner, Measuring Oxygen Diffusion and Oxygen Surface Exchange by Conductivity Relaxation, Solid State Ion. 136-137 (2000) 997-1001.
[51] C. Shin, and H. Yoo, Al-Doped $SrTiO_3$: Part II, unusual Thermodynamic Factor and Chemical Diffusivity, Solid State Ion. 178 (2007) 1089-1094.
[52] M. Wojtyniak, K. Szot, R. Wrzalik, C. Rodenbücher, G. Roth, and R. Waser, Electro-Degradation and Resistive Switching of Fe-Doped $SrTiO_3$ Single Crystal, J. Appl. Phys. 113 (2013) 083713.
[53] J.-J. Wang, H.-B. Huang, T.J.M. Bayer, A. Moballegh, Y. Cao, A. Klein, E.C. Dickey, D.L. Irving, C.A. Randall, and L.-Q. Chen, Defect Chemistry and Resistance Degradation in Fe-Doped $SrTiO_3$ Single Crystal, Acta Mater. 108 (2016) 229-240.
[54] T.-F. Zhang, X.-G. Tang, Q.-X. Liu, and Y.-P. Jiang, Electrode Effect Regulated Resistance Switching and Selector Characteristics in Nb Doped $SrTiO_3$ Single Crystal for Potential Cross-Point Memory Applications, J. Alloys Compd. 730 (2018) 516-520.
[55] R. Waser, and M. Aono, Nanoionic-Based Resisitve Switching Memories, Nature Mater. 6 (2007) 833-840.

[56] J. Blanc, and D.L. Staebler, Electrocoloration in $SrTiO_3$: Vacancy Drift and Oxidation-Reduction of Transition Metals, Phys. Rev. B 4 (1971) 3548-3557.
[57] J. Janek, and C. Korte, Electrochemical Blackening of Yttria-Stabilized Zirconia – Morphological Instability of the Moving Reaction Front, Solid State Ion. 116 (1999) 181-195.
[58] R.E.W. Casselton, Blackening in Yttria Stabilized Zirconia due to Cathodic Processes at Solid Platinum Electrodes, J. Appl. Electrochem. 4 (1974) 25-48.
[59] F.V.E. Hensling, D.J. Keeble, J. Zhu, S. Brose, C. Xu, F. Gunkel, S. Danylyuk, S.S. Nonnenmann, W. Egger, and R. Dittmann, UV Radiation Enhanced Oxygen Vacancy Formation Caused by the PLD Plasma Plume, Sci. Rep. 8 (2018) 8846.
[60] M. Akiyama, Blue-Green Light Photochromism in Europium doped $BaMgSiO_4$, Appl. Phys. Lett. (2010) 181905.
[61] M. Akiyama, H. Yamada, and K. Sakai, Photochromism Enhancement in Reduced Tridymite $BaMgSiO_4$ by Fe-Doping, J. Ceram. Soc. Jpn. 119 (2011) 338-341.
[62] S. Kamimura, H. Yamada, and C.-N. Xu, Purple Photochromism in $Sr_2SnO_4:Eu^{3+}$ with Layered Perovskite-Related Structure, Appl. Phys. Lett. 102 (2013) 031110.
[63] Y. Jin, Y. Hun, Y. Fu, Z. Mu, and G. Ju, Reversible White and Light Gray Photochromism in Europium doped Zn_2GeO_4, Mater. Lett. 134 (2014) 187-189.
[64] Y.J. Bai, W.Z. Liu, A. Chen, L. Shi, X.H. Liu, and Z. Zi, Fast Photo-Induced Color Changes of Ag Particles Deposited on Single-Crystalline TiO_2 Surface, Appl. Phys. Lett. 112 (2018) 211101.
[65] D.M. Tobaldi, M.J. Hortiguela Gallo, G. Otero-Irurueta, M.K. Singh, R.C. Pullar, M.P. Seabra, and J.A. Labrincha, Purely Visible-Light-Induced Photochromism in Ag-TiO_2 Nanoheterostructures, Langmuir 33 (2017) 4890-4902.
[66] D. Cibrev, M. Jankulovska, T. Lana-Villarreal, and R. Gomez, Potentiostatic Reversible Photoelectrochromism: An Effect Appearing in Nanoporous $TiO_2/Ni(OH)_2$ Thin Films, ACS Appl. Mater. Interfaces 6 (2014) 10304-12.
[67] V.N. Kuznetsov, N.I. Glazkova, R.V. Mikhaylov, and N. Serpone, In Situ Sstudy of Photo- and Thermo-Induced Color Centers in Photochromic Rutile TiO_2 in the Temperature Range 90-720 K, Photochem. Photobiol. Sci. 15 (2016) 1289-1298.
[68] J. Mizusaki, Y. Mima, S. Yamauchi, K. Fueki, and H. Tagawa, Nonstoichiometry of the Perovskite-Type Oxides $La_{1-x}Sr_xCoO_3$, J. Solid State Chem. 80 (1989) 102-111.
[69] M. Kuhn, S. Hashimoto, K. Sato, K. Yashiro, and J. Mizusaki, Oxygen Nonstoichiometry and Thermo-Chemical Stability of $La_{0.6}Sr_{0.4}CoO_{3-\delta}$, J. Solid State Chem. 197 (2013) 38-45.
[70] P.W. Krempl, W. Schleinzer, and W. Wallnöfer, Gallium Phosphate, $GaPO_4$: A New Piezoelectric Crystal Material for High-Temperature Sensorics, Sens. Actuators B Chem. 61 (1997) 361-363.
[71] C. Reiter, P.W. Krempl, H. Thanner, W. Wallnöfer, and P.M. Worsch, Material Properites of GaPO4 and their Relvance for Applications, Ann. Chim. Sci. Mat. 26 (2001) 91-94.
[72] H. Thanner, P.W. Krempl, F. Krispel, C. Reiter, and R. Selic, High Temperture Microbalances Based on $GaPO_4$, Ann. Chim. Sci. Mat. 26 (2001) 161-164.
[73] H. Thanner, P.W. Krempl, R. Selic, W. Wallnöfer, and P.M. Worsch, $GaPO_4$ High Temperature Crystal Microbalance Demonstration up to 720 °C, J. Therm. Anal. Calorim. 71 (2003) 53-59.
[74] M. Morgenbesser, S. Taibl, M. Kubicek, A. Schmid, A. Viernstein, C. Herzig, F. Baiutti, J. de Dios Sirvent, M.O. Liedke, M. Butterling, A. Wagner, W. Artner, A. Limbeck, A. Tarancon, and J. Fleig, Cation Non-Stoichiometry in Fe:$SrTiO_3$ Thin Films and its Effect on the Electrical Conductivity, under review (2021).

[75] A. Viernstein, M. Kubicek, M. Morgenbesser, G. Walch, G.C. Brunauer, and J. Fleig, High-Temperature Photochromism of Fe-Doped $SrTiO_3$ Caused by UV-Induced Bulk Stoichiometry Changes, Adv. Funct. Mater. 29 (2019) 1900196.
[76] J. Fleig, and M. Kubicek, Ligth May Harm or Help, Nat. Mater. 17 (2018) 389-391.
[77] F.A. Orellana, C.G. Gálvez, F.A. Orellana, C.G. Gálvez, M.T. Roldán, C. García-Ruiz, M.T. Roldán, and C. García-Ruiz, Applications of Laser-Ablation-Inductively-Coupled Plasma-Mass Spectrometry in Chemical Analysis of Forensic Evidence, Trends Anal. Chem. 42 (2013) 1-34.
[78] G. Bauer, and A. Limbeck, Quantitative Analysis of Trace Elements in Environmental Powders with Laser Ablation Inductively Coupled Mass Spectrometry using Non-Sample-Corresponding Reference Materials for Signal Evaluation, Spectrochim. Acta B 113 (2015) 63-69.
[79] K. Szot, W. Speier, U. Breuer, R. Meyer , J. Szade, and R. Waser, Formation of Micro-Crystals on the (100) Surface of $SrTiO_3$ at Elevated Temperatures, Surf. Sci. 460 (2000) 112-128.
[80] R.A. De Souza, Transport Properties of Dislocations in $SrTiO_3$ and other Perovskites, Curr. Opin. Solid State Mater. Sci. 25 (2021) 100923.
[81] K. Szot, W. Speier, R. Carius, U. Zastrow, and W. Beyer, Localized Metallic Conductivity and Self-Healing During Thermal Reduction of $SrTiO_3$, Phys. Rev. Lett. 88 (2002) 075508.
[82] K.K. Adepalli, J. Yang, J. Maier, H.L. Tuller, and B. Yildiz, Tunable Oxygen Diffusion and Electronic Conduction in $SrTiO_3$ by Dislocation-Induced Space Charge Fields, Adv. Funct. Mater. 27 (2017) 1700243.
[83] J.N. Baker, P.C. Bowes, D.M. Long, A. Moballegh, J.S. Harris, E.C. Dickey, and D.L. Irving, Defect Mechanisms of Coloration in Fe-Doped $SrTiO_3$ from First Principles, Appl. Phys. Lett. 110 (2017) 122903.
[84] J. Maier, Physical Chemistry of Ionic Materials Ions and Electrons in Solids, John Wiley & Sons Ltd., Chichester, England, 2004.
[85] T. Bieger, H. Yugami, N. Nicoloso, J. Maier, and R. Waser, Optical Absorption Relaxation Applied to $SrTiO_3$ and ZrO_2: An In-Situ Method to Study Trapping Effects on Chemical Diffusion, Solid State Ion. 72 (1994) 41-46.
[86] S. Kiran, S. Naveen Kumar, K.C. Yogananda, and D. Rangappa, Optimization of TiO_2/MWCNT Composites for Efficient Dye Sensitized Solar Cells, J. Mater. Sci.: Mater. Electron. 29 (2018) 12681–12689.
[87] S.K. O'Learyur, and P.K. Lim, On Determining the Optical Gap Associated with an Amorphous Semiconductor: A Generalization of the Tauc Model, Solid State Commun. 104 (1997) 17-21.
[88] P.S. Shinde, G.H. Go, and W.J. Lee, Supplementary Information: Facile Growth of Hierarchical Hematite (a-Fe_2O_3) Nanopetals on FTO by Pulse Reverse Electrodeposition for Photoelectrochemical Water Splitting, J. Mater. Chem. 22 (2012) 10469.
[89] A.A. Ramadan, R.D. Gould, and A. Ashour, On the Van der Pauw Method of Resistivity Measurements, Thin Solid Films 239 (1994) 272-275.
[90] W.L.V. Price, Extension of Van der Pauw's Theorem for Measuring Specific Resistivity in Discs of Arbitrary Shape to Anisotropic Media, Appl. Phys. 5 (1972) 1127-1132.
[91] L.J. van der Pauw, A Method of Measuring Specific resisitivity and Hall Effet of Discs of Arbitrary Shape, Philips Res. Rep. 13 (1958) 1-9.
[92] L.J. van der Pauw, A Method of Masuring the Restivity and Hall Coefficient on Lamellae of Arbitrary Shape, Philips Techn. Rev. 20 (1958/59) 220-224.

[93] A. Viernstein, G. Bimashofer, M. Kubicek, M. Morgenbesser, T. Huber, E. Ellmeyer, M. Siebenhofer, C.A.F. Vaz, J. Stahn, and J. Fleig, Mechanism of Photo-Ionic Stoichiometry Changes in $SrTiO_3$ under review (2021).
[94] F. Frati, M. Hunault, and F.M.F. de Groot, Oxygen K-edge X-Ray Absorption Spectra, Chem. Rev. 120 (2020) 4056-4110.
[95] J.P. Crocombette, and F. Jollet, Ti 2p X-ray Absorption in Titanium Dioxides (TiO_2): The Influence of the Cation Site Environment, J. Phys. Condens. Matter 6 (1994).
[96] G.S. Henderson, X. Liu, and M.E. Fleet, A Ti L-Edge X-Ray Absorption Study of Ti-Silicate Glasses, Phys. Chem. Minerals 29 (2002) 32-42.
[97] Q. Zhao, and X.L. Cheng, Study on the Ti K, $L_{2,3}$, and M Edges of $SrTiO_3$ and $PbTiO_3$, J. Phys. Chem. A 124 (2020) 322-327.
[98] M. Siebenhofer, F. Baiutti, J. Sirvent, T.M. Huber, A. Viernstein, S. Smetaczek, C. Herzig, M.O. Liedke, M. Butterling, A. Wagner, E. Hirschmann, A. Limbeck, A. Tarancon, J. Fleig, and M. Kubicek, Exploring Point Defects and Trap States in Undoped $SrTiO_3$ - under review, (2021).
[99] B. Ravel, and M. Newville, Athena, Artemis, Hephaestus: Data Analysis for X-Ray Absorption Spectroscopy using IFEFFIT, J. Synchrotron Rad. 12 (2005) 537-541.
[100] J. Jamnik, Electrochemistry of CrystallineMixed Conductors: Concepts and Examples with $SrTiO_3$, Chem. Biochem. Eng. Q. 21 (2007) 15-19.
[101] S. Shen, Y. Jia, F. Fan, Z. Feng, and C. Li, Time-Resolved Infrared Spectroscopic Investigation of Roles of Valence States of Cr in (La,Cr)-Doped $SrTiO_3$ Photocatalysts, Chin. J. Catal. 34 (2013) 2036-2040.
[102] J. Maier, Mass Transport in the Presence of Internal Defect Reactions-Concept of Conservative Ensembles: I, Chemical Diffusion in Pure Compounds, J. Am. Ceram. Soc. 76 (1993) 1212-1217.
[103] J. Maier, Mass Transport in the Presence of Internal Defect Reactions-Concept of Conservative Ensembles: III, Trapping Effect of Dopants on Chemical Diffusion, J. Am. Ceram. Soc. 76 (1993) 1223-1227.
[104] J. Crank, The Mathematics of Diffusion, 2 ed., Oxford University Press, Great Britain, 1956.
[105] C. Ricca, I. Timrov, M. Cococcioni, N. Marzari, and U. Aschauer, Self-Consistent DFT+U+V Study of Oxygen Vacancies in $SrTiO_3$, Phys. Rev. Res. 2 (2020).
[106] Y. Li, Q. Wang, M. An, K. Li, N. Wehbe, Q. Zhang, S. Dong, and T. Wu, Nanoscale Chemical and Valence Evolution at the Metal/Oxide Interface: A Case Study of Ti/$SrTiO_3$, Adv. Mater. Interfaces 3 (2016) 1600201.
[107] M. Wu, H.L. Xin, J.O. Wang, X.J. Li, X.B. Yuan, H. Zeng, J.C. Zheng, and H.Q. Wang, Investigation of the Multiplet Features of $SrTiO_3$ in X-Ray Absorption Spectra Based on Configuration Interaction Calculations, J. Synchrotron Radiat. 25 (2018) 777-784.
[108] V. Kumar, S. Choudhary, V. Malik, R. Nagarajan, A. Kandasami, and A. Subramanian, Enhancement in Photocatalytic Activity of $SrTiO_3$ by Tailoring Particle Size and Defects, Phys. Status Solidi A 216 (2019) 1900294.
[109] R. Brydson, Electron Energy-Loss Spectroscopy (EELS) and the Electronic Structure of Titanium Dioxide, Solid State Commun. 64 (1987) 609-612.
[110] W. Ra, M. Nakayama, W. Cho, M. Wakihara, and Y. Uchimoto, Electronic and Local Structural Changes in $Li_{(2+x)}Ti_3O_7$ Ramsdellite Compounds upon Electrochemical Li-Ion Insertion Reactions by X-Ray Absorption Spectroscopy, Phys. Chem. Chem. Phys. 8 (2006) 882-889.

[111] F.M. de Groot, J. Faber, J.J. Michiels, M.T. Czyzyk, M. Abbate, and J.C. Fuggle, Oxygen 1s X-Ray Absorption of Tetravalent Titanium Oxides: A Comparison with Single-Particle Calculations, Phys. Rev. B 48 (1993) 2074-2080.
[112] G.C. Brunauer, B. Rotter, G. Walch, E. Esmaeili, A.K. Opitz, K. Ponweiser, J. Summhammer, and J. Fleig, UV-Light-Driven Oxygen Pumping in a High-Temperature Solid Oxide Photoelectrochemical Cell, Adv. Funct. Mater. 26 (2016) 120-128.
[113] S. Zoller, A.A. Demkov, R. Liu, P.L. Fejes, R.B. Gregory, P. Alluri, J.A. Curless, Z. Yu, J. Ramdani, R. Droopad, T.E. Tiwald, J.N. Hilfiker, and J.A. Woodlam, Optical Properties of Bulk and Thin-Film $SrTiO_3$ on Si and Pt, J. Vac. Sci. Technol. B 18 (2000) 2242-2254.
[114] V. Metlenko, W. Jung, S.R. Bishop, H.L. Tuller, and R.A. De Souza, Oxygen Diffusion and Surface Exchange in the Mixed Conducting Oxides $SrTi_{1-y}Fe_yO_{3-d}$, Phys. Chem. Chem. Phys. 18 (2016) 29495-29505.
[115] R.A. De Souza, V. Metlenko, D. Park, and T.E. Weirich, Behavior of Oxygen Vacancies in Single-crystal $SrTiO_3$: Equilibrium Distribution and Diffusion Kinetics, Phys. Rev. B 85 (2012) 174109.
[116] R.A. De Souza, and M. Martin, Using $^{18}O/^{16}O$ Exchange to Probe an Equilibrium Space-Charge Layer at the Surface of a Crystalline Oxide: Method and Application, Phys Chem Chem Phys 10 (2008) 2356-2367.
[117] F. Podjaski, and B.V. Lotsch, Optoelectronics Meets Optoionics: Light Storing Carbon Nitrides and Beyond, Adv. Energy Mater. 11 (2021) 2003049.
[118] G.Y. Kim, A. Senocrate, T.Y. Yang, G. Gregori, M. Grätzel, and J. Maier, Large Tunable Photoeffect on Ion Conduction in Halide Perovskites and Implications for Photodecomposition, Nat. Mater. 17 (2018) 445-449.
[119] A. Viernstein, M. Kubicek, M. Morgenbesser, T. Huber, M. Siebenhofer, and J. Fleig, How UV Light Lowers the Conductivity of $SrTiO_3$ by Photochemical Water Splitting at Elevated Temperature under review (2021).
[120] X. Guo, Z. Zhang, W. Sigle, E. Wachsman, and R. Waser, Schottky Barrier Formed by Network of Screw Ddislocations in $SrTiO_3$, Appl. Phys. Lett. 87 (2005) 162105.
[121] F. Noll, W. Münch, I. Denk, and J. Maier, $SrTiO_3$ as a Prototype of a Mixed Conductor Conductivities, Oxygen Diffusion and Boundary Effects, Solid State Ion. 86-88 (1996) 711-717.
[122] M. Stöber, C. Cherkouk, T. Leisegang, M. Schelter, J. Zosel, J. Walter, J. Hanzig, M. Zschornak, S. Prucnal, R. Böttger, and D.C. Meyer, Oxygen Exchange Kinetics of $SrTiO_3$ Single Crystals: A Non-Destructive, Quantitative Method, Cryst. Res. Technol. 53 (2018) 1800004.
[123] D. Hertkorn, M. Benkler, U. Gleißner, F. Büker, C. Megnin, C. Müller, T. Hanemann, and H. Reinecke, Morphology and Oxygen Vacancy Investigation of Strontium Titanate-based Photo Electrochemical Cells, J. Mater. Sci. 50 (2014) 40-48.
[124] B.L. Phoon, C.W. Lai, J.C. Juan, P.-L. Show, and G.-T. Pan, Recent Developments of Strontium Titanate for Photocatalytic Water Splitting Application, Int. J. Hydrog. Energy 44 (2019) 14316-14340.
[125] S. Patial, V. Hasija, P. Raizada, P. Singh, A.A.P. Khan Singh, and A.M. Asiri, Tunable Photocatalytic Activity of $SrTiO_3$ for Water Splitting: Strategies and Future Scenario, J. Environ. Eng. 8 (2020) 103791.
[126] L. Mu, Y. Zhao, A. Li, S. Wang, Z. Wang, J. Yang, Y. Wang, T. Liu, R. Chen, J. Zhu, F. Fan, R. Li, and C. Li, Enhancing Charge Separation on High Symmetry $SrTiO_3$ Exposed with Anisotropic Facets for Photocatalytic Water Splitting, Energy Environ. Sci. 9 (2016) 2463-2469.

[127] S. Carlotto, The Role of the Dopant and Structural Defects on the Water Absorption and on the H_2 Formation in the Al, Co and Cu Doped $SrTiO_3$ Perovskite Steps, Appl. Surf. Sci. 527 (2020) 146850.
[128] M. Morgenbesser, A. Schmid, A. Viernstein, J.d.D. Srivent, F. Chiabrera, N. Bodenmüller, S. Taibl, M. Kubicek, F. Baiutti, A. Tarancon, and J. Fleig, $SrTiO_3$ Based High Temperature Solid Oxide Solar Cells: Photovoltages, Photocurrents and Mechanistic Insight, Solid State Ion. 368 (2021) 115700.
[129] R. Merkle, J. Maier, K.-D. Becker, and M. Kreye, Chemical Diffusion With Non-Constant D^{δ} and the Aappearance of a Parabolic Rate Law: Model Study on $SrTiO_3$, Phys. Chem. Chem. Phys. 6 (2004) 3633-3638.
[130] J. Maier, Interaction of Oxygen with Oxides: How to Interpret Measured Effective Rate Constants?, Solid State Ion. 135 (2000) 575-588.
[131] E. Ellmeyer, Oxygen Nonstoichiometry in Undoped and Iron-Doped Strontium Titanate, Institute of Chemical Technologies and Analytics, TU Wien, Vienna, 2020.
[132] H. Thanner, P.W. Krempl, W. Wallnöfer, and P.M. Worsch, GaPO4 high Temperature Crystal Microbalance with Zero Temperature Coefficient, Vacuum 67 (2002) 687-691.
[133] J.W. Elam, and M.J. Pellin, $GaPO_4$ Sensors for Gravimetric Monitoring during Atomic Layer Deposition at High Temperatures, Anal. Chem. 77 (2005) 3531-3535.
[134] W. Sitte, E. Bucher, A. Benisek, and W. Preis, Oxygen Nonstoichiometry and Ionic Transport Properties of $La_{0.4}Sr_{0.6}CoO_{3-d}$, Spectrochim. Acta A 57 (2001) 2071-2076.
[135] W. Sitte, E. Bucher, and W. Preis, Nonstoichiometry and Transport Properties of Strontium-Substituted Lanthanum Cobaltites, Solid State Ion. 154-155 (2002) 517-522.
[136] T. Kawada, J. Suzuki, M. Sase, A. Kaimai, K. Yashiro, Y. Nigara, J. Mizusaki, K. Kawamura, and H. Yugami, Determination of Oxygen Vacancy Concentration in a Thin Film of $La_{0.6}Sr_{0.4}CoO_{3-\delta}$ by an Electrochemical Method, J. Electrochem. Soc. 149 (2002) E252.
[137] N. Eliaz, and E. Gileadi, Physical Electrochemistry Fundamentals, Techniques, and Applications 2nd ed., Wiley-VCH Verlaf GmbH & Co KGaA, Weinheim, Germany, 2019.
[138] G. Sauerbrey, Verwendung von Schwingquarzen zur Wägung dünner Schichten und zur Mikrowägung, Z. Phys. 55 (1959) 206-222.
[139] P. Armand, M. Beaurain, B. Ruffle, B. Menaert, and P. Papet, Temperature Dependence of Single-Crystal Elastic Constants of Flux-Grown a-$GaPO_4$, Inorg. Chem. 48 (2009) 4988-96.
[140] F. Krispel, H. Thanner, P.W. Krempl, C. Reiter, P.M. Worsch, and W. Wallnöfer, $GaPO_4$ Resonators with Q Factors of some Millions in the Fundamental Mode, in IEEE International Frequency Control Symposium and PDA Exhibition, 2002.
[141] A.Y. Zuev, A.N. Petrov, A.I. Vylkov, and D.S. Tsvetkov, Oxygen Nonstoichiometry and Defect Structure of Undoped and Doped Lanthanum Cobaltites, J. Mater. Sci. 42 (2007) 1901-1908.
[142] J. Mastin, M.-A. Einarsud, and T. Grande, Structural and Thermal Properties of $La_{1-x}Sr_xCoO_{3-d}$, Chem. Mater. 18 (2006) 6047-6053.
[143] M. Morgenbesser, A. Viernstein, A. Schmid, C. Herzig, N. Bodenmüller, M. Kubicek, S. Taibl, G. Bimashofer, J. Stahn, C.A.F. Vaz, M. Döbeli, F. Baiutti, J.d.D. Sirvent, M.O. Liedke, M. Butterling, E. Hirschmann, M. Kaminski, M. Tolkiehn, V. Vonk, A. Stierle, A. Wagner, A. Tarancon, A. Limbeck, and J. Fleig, Unravelling the Origin of Ultra-Low Conductivity in Doped $SrTiO_3$ Thin Films: Sr Vacancies as the Key Driver for Fermi Level Pinning, in preperation (2021).
[144] T. Ohnishi, M. Lippmaa, T. Yamamoto, S. Meguro, and H. Koinuma, Improved Stoichiometry and Misfit Control in Perovskite Thin Film Formation at a Critical Fluence by Pulsed Laser Deposition, Appl. Phys. Lett. 87 (2005) 241919.

[145] D.J. Keeble, S. Wicklein, L. Jin, C.L. Jia, W. Egger, and R. Dittmann, Nonstoichiometry Accommodation in $SrTiO_3$ Thin Films Studied by Positron Annihilation and Electron Microscopy, Phys. Rev. B 87 (2013) 195409.
[146] E. Breckenfeld, R. Wilson, J. Karthik, A.R. Damodaran, D.G. Cahill, and L.W. Martin, Effect of Growth Induced (Non)Stoichiometry on the Structure, Dielectric Response, and Thermal Conductivity of $SrTiO_3$ Thin Films, Chem. Mater. 24 (2012) 331-337.
[147] B. Dam, J.H. Rector, J. Johansson, J. Huijbregtse, and D.G. De Groot, Mechanism of Incongruent Ablation of $SrTiO_3$, J. Appl. Phys. 83 (1998) 3386-3389.
[148] T. Ohnishi, K. Shibuya, T. Yamamoto, and M. Lippmaa, Defects and Transport in Complex Oxide Thin Films, J. Appl. Phys. 103 (2008) 103703.
[149] U.N. Gries, M. Kessel, F.V.E. Hensling, R. Dittmann, M. Martin, and R.A. De Souza, Behavior of Cation Vacancies in Single-Crystal and in Thin-Film $SrTiO_3$: The Importance of Strontium Vacancies and their Defect Associates, Phys. Rev. Mater. 4 (2020) 123404.
[150] A. Walsh, C.R.A. Catlow, A.G.H. Smith, A.A. Sokol, and S.M. Woodley, Strontium Migration Assisted by Oxygen Vacancies in $SrTiO_3$ from Classical and Quantum Mechanical Simulations, Phys. Rev. B 83 (2011) 220301.
[151] M. Choi, F. Oba, and I. Tanaka, Role of Ti Antisitelike Defects in $SrTiO_3$, Phys. Rev. Lett. 103 (2009) 185502.
[152] A. Karjalainen, V. Prozheeva, I. Makkonen, C. Guguschev, T. Markurt, M. Bickermann, and F. Tuomisto, Ti_{Sr} Antisite: An Abundant Point Defect in $SrTiO_3$, J. Appl. Phys. 127 (2020) 245702.
[153] B. Liu, V.R. Cooper, H. Xu, H. Xiao, Y. Zhang, and W.J. Weber, Composition Dependent Intrinsic Defect Structures in $SrTiO_3$, Phys. Chem. Chem. Phys. 16 (2014) 15590-15596.
[154] J. Claus, M. Leonhardt, and J. Maier, Tracer Diffusion and Chemical Diffusion of Oxygen in Acceptor Soped $SrTiO_3$, Journal of Physics and Chemistry of Solids 61 (2000) 1199-1207.
[155] J. Jamnik, and J. Maier, Generalised Equivalent Circuits for Mass and Charge Transport: Chemical Capacitance and its Implications, Phys. Chem. Chem. Phys. 3 (2001) 1668-1678.
[156] J. Jamnik, J. Maier, and S. Pejovnik, A Powerful Electrical Network Model for the Impedance of Mixed Conductors, Electrochim. Acta 44 (1999) 4139-4145.
[157] J. Jamnik, and J. Maier, Treatment of the Impedance of Mixed Conductors Equivalent Circuit Model and Explicit Approximate Solutions, J. Electrochem. Soc. 146 (1999) 4183.
[158] J. Zegenhagen, and A. Kazimirov, X-Ray Standing Wave Technique, The: Principles and Applications, World Scientific, Singapore, 2013.
[159] A. Authier, Dynamical Theory of X-Ray Diffraction, International Tables of Crystallography2006, pp. 534-551.
[160] E. Stavitski, and F.M. de Groot, The CTM4XAS Program for EELS and XAS Spectral Shape Analysis of Transition Metal L Edges, Micron 41 (2010) 687-94.
[161] M. Kubicek, S. Taibl, E. Navickas, H. Hutter, G. Fafilek, and J. Fleig, Resistive States in Strontium Titanate Thin Films: Bias Effects and Mechanisms at High and Low Temperature, J. Electroceram. 39 (2017) 197-209.
[162] S. Rodewald, J. Fleig, and J. Maier, The Distribution of Grain Boundary Resistivities in $SrTiO_3$ Polycrystals: A Comparison between Spatially Resolved and Macroscopic Measurments, J. Eur. Ceram. Soc. 21 (2001) 1749-1752.
[163] S. Wicklein, A. Sambri, S. Amoruso, X. Wang, R. Bruzzese, A. Koehl, and R. Dittmann, Pulsed Laser ablation of Complex Oxides: The Role of Congruent Ablation and Preferential Scattering for the Film Stoichiometry, Appl. Phys. Lett. 101 (2012) 131601.
[164] Q.Y. Lei, G.Z. Liu, and X.X. Xi, Structural Characterization of Homoepitaxial $SrTiO_3$ Films Grown by Pulsed Laser Deposition, Integr. Ferroelectr. 141 (2013) 128-133.

[165] C.M. Brooks, L.F. Kourkoutis, T. Heeg, J. Schubert, D.A. Muller, and D.G. Schlom, Growth of Homoepitaxial $SrTiO_3$ Thin Films by Molecular-Beam Epitaxy, Appl. Phys. Lett. 94 (2009) 162905.
[166] M. Markovich, J. Roqueta, J. Santiso, E. Lakin, E. Zolotoyabko, and A. Rothschild, Epitaxial Growth of Nb-Doped $SrTiO_3$ Films by Pulsed Laser Deposition, Appl. Surf. Sci. 258 (2012) 9496-9500.
[167] D. Asakura, E. Hosono, Y. Nanba, H. Zhou, J. Okabayashi, C. Ban, P.-A. Glans, J. Guo, T. Mizokawa, G. Chen, A.J. Achkar, D.G. Hawthron, T.Z. Regier, and H. Wadati, Material/Element-Dependent Fluorescence-Yield Modes on Soft X-Xay Absorption Spectroscopy of Cathode Materials for Li-Ion Batteries, AIP Adv. 88 (2016) 035105.
[168] J. Kubacki, D. Kajewski, A. Koehl, M. Wojtyniak, R. Dittmann, and J. Szade, X-Ray Absorption and Resonant Photoemission Studies of Mn Doped $SrTiO_3$ Epitaxial Films, Radiat. Phys. Chem. 93 (2013) 123-128.
[169] J. Schlappa, C.F. Chang, Z. Hu, E. Schierle, H. Ott, E. Weschke, G. Kaindl, M. Huijben, G. Rijnders, D.H. Blank, L.H. Tjeng, and C. Schussler-Langeheine, Resonant Soft X-Ray Scattering from Stepped Surfaces of $SrTiO_3$, J. Phys. Condens. Matter 24 (2012) 035501.
[170] R. Laskowski, and P. Blaha, Understanding the $L_{2,3}$ X-Ray Absorption Spectra of Early 3d Transition Elements, Phys. Rev. B 82 (2010) 205104.
[171] R. Zucca, Electrical Compensation in Semi-Insulating GaAs, J. Appl. Phys. 48 (1977) 1987-1994.
[172] N. Osawa, R. Takahashi, and M. Lippmaa, Hole Trap State Analysis in $SrTiO_3$, Appl. Phys. Lett. 110 (2017) 263902.
[173] K. Klyukin, and V. Alexandrov, Effect of Intrinsic Point Defects on Ferroelectric Polarization Behavior of $SrTiO_3$, Phys. Rev. B 95 (2017).
[174] M. Siebenhofer, A. Viernstein, M. Morgenbesser, J. Fleig, and M. Kubicek, Photo-Induced Electronic and Ionc Effect in Srontium Titanate, under review (2021).
[175] A. Fujishima, and K. Honda, Electrochemical Photolysis of Water at a Semiconductor Electrode, Nature 238 (1972) 37-38.
[176] M. Ismael, The Photocatalytic Performance of the ZnO/g-C_3N_4 Composite Photocatalyst Toward Degradation of Organic Pollutants and its Inactivity Toward Hydrogen Evolution: The Influence of Light Irradiation and Charge Transfer, Chem. Phys. Lett. 739 (2020) 136992.
[177] N. Roy, and S. Chakraborty, ZnO as Photocatalyst: An Approach to Waste Water Treatment, Mater. Today: Proceedings (2020).
[178] A. Serrà, P. Pip, E. Gómez, and L. Philippe, Efficient Magnetic Hybrid ZnO-Based Photocatalysts for Visible-Light-Driven Removal of Toxic Cyanobacteria Blooms and Cyanotoxins, Appl. Catal. B 268 (2020) 118745.
[179] T. Senasu, T. Chankhanittha, K. Hemavibool, and S. Nanan, Visible-Light-Responsive Photocatalyst based on ZnO/CdS Nanocomposite for Photodegradation of Reactive Red Azo Dye and Ofloxacin Antibiotic, Mater. Sci. Semicond. Process. 123 (2021) 105558.
[180] T. Kimijima, K. Kanie, M. Nakaya, and A. Muramatsu, Solvothermal Synthesis of $SrTiO_3$ Nanoparticles Precisely Controlled in Surface Crystal Planes and their Photocatalytic Activity, Appl. Catal. B 144 (2014) 462-467.
[181] K. Prakash, P. Senthil Kumar, S. Pandiaraj, K. Saravanakumar, and S. Karuthapandian, Controllable Synthesis of SnO_2 Photocatalyst with Superior Photocatalytic Activity for the Degradation of Methylene Blue Dye Solution, J. Exp. Nanosci. 11 (2016) 1138-1155.
[182] M. Aslam, M.T. Qamar, S. Ali, A.U. Rehman, M.T. Soomro, I. Ahmed, I.M.I. Ismail, and A. Hameed, Evaluation of SnO_2 for Sunlight Photocatalytic Decontamination of Water, J. Environ. Manage. 217 (2018) 805-814.

[183] H. Zhan, C. Deng, X.-L. Shi, C. Wu, X. Li, Z. Xie, C. Wang, and Z.-G. Chen, Correlation between the Photocatalysis and Growth Mechanism of SnO_2 Nanocrystals, J. Phys. D Appl. Phys. 53 (2020) 154005.
[184] X. Chen, Z. Wu, D. Liu, and Z. Gao, Preparation of ZnO Photocatalyst for the Efficient and Rapid Photocatalytic Degradation of Azo Dyes, Nanoscale Res. Lett. 12 (2017) 143.
[185] K.L. Hardee, and A.J. Bard, Semiconductor Electrodes: V . The Application of Chemically Vapor Deposited Iron Oxide Films to Photosensitized Electrolysis, J. Electrochem. Soc. 123 (1976) 1024-1026.
[186] H. Liang, X. Jiang, W. Chen, S. Wang, B. Xu, and Z. Wang, α-Fe_2O_3/Pt Hybrid Nanorings and their Enhanced Photocatalytic Activities, Ceram. Int. 40 (2014) 5653-5658.
[187] M. Mishra, and D.-M. Chun, α-Fe_2O_3 as a Photocatalytic Material: A Review, Appl. Catal. A-Gen. 498 (2015) 126-141.
[188] Z. Lin, C. Du, B. Yan, and G. Yang, Amorphous Fe_2O_3 for Photocatalytic Hydrogen Evolution, Catal. Sci. Technol. 9 (2019) 5582-5592.
[189] H. Kato, M. Hori, R. Konta, Y. Shimodaira, and A. Kudo, Construction of Z-scheme Type Heterogeneous Photocatalysis Systems for Water Splitting into H_2 and O_2 under Visible Light Irradiation, Chem. Lett. 33 (2004) 1348-1349.
[190] C.-C. Lo, C.-W. Huang, C.-H. Liao, and J.C.S. Wu, Novel Twin Reactor for Separate Evolution of Hydrogen and Oxygen in Photocatalytic Water Splitting, Int. J. Hydrog. Energy 35 (2010) 1523-1529.
[191] R. Niishiro, S. Tanaka, and A. Kudo, Hydrothermal-Synthesized $SrTiO_3$ Photocatalyst Codoped with Rhodium and Antimony with Visible-Light Response for Sacrificial H_2 and O_2 Evolution and Application to Overall Water Splitting, Appl. Catal. B 150-151 (2014) 187-196.
[192] M.N. Ha, F. Zhu, Z. Liu, L. Wang, L. Liu, G. Lu, and Z. Zhao, Morphology-Controlled Synthesis of $SrTiO_3$/TiO_2 Heterostructures and their Photocatalytic Performance for Water Splitting, RSC Adv. 6 (2016) 21111-21118.
[193] Y. Chang, K. Yu, C. Zhang, Z. Yang, Y. Feng, H. Hao, Y. Jiang, L.-L. Lou, W. Zhou, and S. Liu, Ternary CdS/Au/3DOM-$SrTiO_3$ Composites with Synergistic Enhancement for Hydrogen Production from Visible-Light Photocatalytic Water Splitting, Appl. Catal. B 215 (2017) 74-84.
[194] H.-y. Lin, and L.-T. Cian, Microwave-Assisted Hydrothermal Synthesis of $SrTiO_3$:Rh for Photocatalytic Z-scheme Overall Water Splitting, Appl. Sci. 9 (2018) 55.
[195] Q. Wang, S. Okunaka, H. Tokudome, T. Hisatomi, M. Nakabayashi, N. Shibata, T. Yamada, and K. Domen, Printable Photocatalyst Sheets Incorporating a Transparent Conductive Mediator for Z-Scheme Water Splitting, Joule 2 (2018) 2667-2680.
[196] K. Domen, A. Kudo, and O. Takaharu, Mechanism of Photocatalytic Decomposition of Water into H_2 and O_2 over NiO-$SrTiO_3$, J. Catal. 102 (1986) 92-98.
[197] M. Matsumura, M. Hiramoto, and H. Tsubomura, Photoelectrolysis of Water under Visible Light with Doped $SrTiO_3$ Electrodes, J. Electrochem. Soc. 130 (1983) 326-330.
[198] H.W. Kang, and S.B. Park, H_2 Evolution under Visible Light Irradiation from Aqueous Methanol Solution on $SrTiO_3$:Cr/Ta prepared by Spray Pyrolysis from Polymeric Precursor, Int. J. Hydrog. Energy 36 (2011) 9496-9504.
[199] J. Liu, Y. Sun, Z. Li, S. Li, and J. Zhao, Photocatalytic Hydrogen Production from Water/Methanol Solutions over Highly ordered Ag–$SrTiO_3$ Nanotube Arrays, Int. J. Hydrog. Energy 36 (2011) 5811-5816.
[200] T. Puangpetch, S. Chavadej, and T. Sreethawong, Hydrogen Production over Au-Loaded Mesoporous-Assembled $SrTiO_3$ Nanocrystal Photocatalyst: Effects of Molecular Structure and Cemical Properties of Hole Scavengers, Energy Convers. Manag. 52 (2011) 2256-2261.

[201] F.T. Wagner, and G.A. Somorjai, Photocatalytic Hydrogen Porduction from Water on Pt-free $SrTiO_3$ in Alkali Hydroxide Solutions, Nature 285 (1980) 559-560.
[202] J.S. Jang, S.H. Choi, H.G. Kim, and J.S. Lee, Location and State of Pt in Platinized CdS/TiO2 Photocatalysts for Hydrogen Production from Water under Visible Light, J. Phys. Chem. C 112 (2008) 17200-17205.
[203] X. Wang, K. Maeda, A. Thomas, K. Takanabe, G. Xin, J.M. Carlsson, K. Domen, and M. Antonietti, A Metal-Free Polymeric Photocatalyst for Hydrogen Production from Water under Visible Light, Nat. Mater. 8 (2009) 76-80.
[204] J.-H. Yan, Y.-R. Zhu, Y.-G. Tang, and S.-Q. Zheng, Nitrogen-Doped $SrTiO_3/TiO_2$ Composite Photocatalysts for Hydrogen Production under Visible Light Irradiation, J. Alloys Compd. 472 (2009) 429-433.
[205] V.M. Daskalaki, M. Antoniadou, G.L. Puma, D.I. Kondarides, and P. Lianos, Solar Light-Responsive $Pt/CdS/TiO_2$ Photocatalysts for Hydrogen Production and Simultaneous Degradation of Inorganic or Organic Sacrificial Agents in Wastewater, Environ. Sci. Technol. 44 (2010) 7200-7205.
[206] M. de Oliveira Melo, and L.A. Silva, Visible Light-Induced Hydrogen Production from Glycerol Aqueous Solution on Hybrid $Pt–CdS–TiO_2$ Photocatalysts, J. Photochem. Photobiol. A 226 (2011) 36-41.
[207] D.-N. Bui, J. Mu, L. Wang, S.-Z. Kang, and X. Li, Preparation of Cu-loaded $SrTiO_3$ Nanoparticles and their Photocatalytic Activity for Hydrogen Evolution from Methanol Aqueous Solution, Appl. Surf. Sci. 274 (2013) 328-333.
[208] Y. Jia, S. Shen, D. Wang, X. Wang, J. Shi, F. Zhang, H. Han, and C. Li, Composite $Sr_2TiO_4/SrTiO_3$(La,Cr) Heterojunction Based Photocatalyst for Hydrogen Production under Visible Light Irradiation, J. Mater. Chem. A 1 (2013) 7905.
[209] D. Sharma, A. Verma, V.R. Satsangi, R. Shrivastav, and S. Dass, Nanostructured $SrTiO_3$ Thin Films Sensitized by Cu_2O for Photoelectrochemical Hydrogen Generation, Int. J. Hydrog. Energy 39 (2014) 4189-4197.
[210] C. Luo, J. Zhao, Y. Li, W. Zhao, Y. Zeng, and C. Wang, Photocatalytic CO_2 Reduction over $SrTiO_3$: Correlation between Surface Structure and Activity, Appl. Surf. Sci. 447 (2018) 627-635.
[211] J. Shan, F. Raziq, M. Humayun, W. Zhou, Y. Qu, G. Wang, and Y. Li, Improved Charge Separation and Surface Activation via Boron-Doped Layered Polyhedron $SrTiO_3$ for Co-Catalyst free Photocatalytic CO_2 Conversion, Appl. Catal. B 219 (2017) 10-17.
[212] S. Wang, K. Teramura, T. Hisatomi, K. Domen, H. Asakura, S. Hosokawa, and T. Tanaka, Effective Driving of Ag-Loaded and Al-Doped $SrTiO_3$ under Irradiation at $\lambda > 300$ nm for the Photocatalytic Conversion of CO_2 by H_2O, ACS Appl. Energy Mater. 3 (2020) 1468-1475.
[213] P. Li, C. Liu, G. Wu, Y. Heng, S. Lin, A. Ren, K. Lv, L. Xiao, and W. Shi, Solvothermal Synthesis and Visible Light-Driven Photocatalytic Degradation for Tetracycline of Fe-Doped $SrTiO_3$, RSC Adv. 4 (2014) 47615-47624.
[214] X. Yue, J. Zhang, F. Yan, X. Wang, and F. Huang, A Situ Hydrothermal Synthesis of $SrTiO_3/TiO_2$ Heterostructure Nanosheets with Exposed (001) Facets for Enhancing Photocatalytic Degradation Activity, Appl. Surf. Sci. 319 (2014) 68-74.
[215] G. Wu, L. Xiao, W. Gu, W. Shi, D. Jiang, and C. Liu, Fabrication and Excellent Visible-Light-Driven Photodegradation Activity for Antibiotics of $SrTiO_3$ Nanocube Coated CdS Microsphere Heterojunctions, RSC Adv. 6 (2016) 19878-19886.
[216] O. Ruzimuradov, M. Hojamberdiev, C. Fasel, and R. Riedel, Fabrication of Lanthanum and Nitrogen – Co-Doped $SrTiO_3 – TiO_2$ Heterostructured Macroporous Monolithic Materials

for Photocatalytic Degradation of Organic Dyes under Visible Light, J. Alloys Compd. 699 (2017) 144-150.
[217] X.-J. Wen, C.-G. Niu, L. Zhang, C. Liang, and G.-M. Zeng, An in Depth Mechanism Insight of the Degradation of Multiple Refractory Pollutants via a Novel $SrTiO_3$/BiOI Heterojunction Photocatalysts, J. Catal. 356 (2017) 283-299.
[218] P.-S. Konstas, I. Konstantinou, D. Petrakis, and T. Albanis, Synthesis, Characterization of g-C_3N_4/$SrTiO_3$ Heterojunctions and Photocatalytic Activity for Organic Pollutants Degradation, Catalysts 8 (2018) 554.
[219] J. Qiao, H. Zhang, G. Li, S. Li, Z. Qu, M. Zhang, J. Wang, and Y. Song, Fabrication of a Novel Z-scheme $SrTiO_3$/Ag_2S/$CoWO_4$ Composite and its Application in Sonocatalytic Degradation of Tetracyclines, Sep. Purif. Technol. 211 (2019) 843-856.
[220] Y. Chen, Z. Peng, Y. Li, Y. Liu, Y. Chen, Y. Wu, R. Xu, S. Wang, and Z. Zeng, Photocatalytic Performance of Z-scheme $SrCO_3$-$SrTiO_3$/Ag_3PO_4 Heterojunction for Tetracycline Hydrochloride Degradation, J. Mater. Sci. 56 (2020) 4356-4365.
[221] X. Yu, J. Wang, X. Fu, H. Meng, Y. Zhu, and Y. Zhang, Construction of Z-scheme $SrTiO_3$/Ag/Ag_3PO_4 Photocatalyst with Oxygen Vacancies for Highly Efficient Degradation Activity towards Tetracycline, Sep. Purif. Technol. 241 (2020) 116718.
[222] J. Wang, S. Yin, Q. Zhang, F. Saito, and T. Sato, Mechanochemical Synthesis of $SrTiO_{3-x}F_x$ with High Visible Light Photocatalytic Activities for Nitrogen Monoxide Destruction, J. Mater. Chem. 13 (2003) 2348-2352.
[223] I.M. Arabatzis, T. Stergiopoulos, M.C. Bernard, D. Labou, S.G. Neophytides, and P. Falaras, Silver-Modified Titanium Dioxide Thin Films for Efficient Photodegradation of Methyl Orange, Appl. Catal. B 42 (2003) 187-201.
[224] X. Wei, G. Xu, Z. Ren, C. Xu, G. Shen, and G. Han, PVA-Assisted Hydrothermal Synthesis of $SrTiO_3$ Nanoparticles with Enhanced Photocatalytic Activity for Degradation of RhB, J. Am. Ceram. Soc. 91 (2008) 3795-3799.
[225] B. Huang, Y. Liu, Q. Pang, X. Zhang, H. Wang, and P.K. Shen, Boosting the Photocatalytic Activity of Mesoporous $SrTiO_3$ for Nitrogen Fixation through Multiple Defects and Strain Engineering, J. Mater. Chem. A 8 (2020) 22251-22256.
[226] B. Kiss, T.D. Manning, D. Hesp, C. Didier, A. Taylor, D.M. Pickup, A.V. Chadwick, H.E. Allison, V.R. Dhanak, J.B. Claridge, J.R. Darwent, and M.J. Rosseinsky, Nano-Structured Rhodium Doped $SrTiO_3$–Visible Light Activated Photocatalyst for Water Decontamination, Appl. Catal. B 206 (2017) 547-555.
[227] D.Y. Goswami, Principles of Solar Engineering, 3rd ed., Taylor and Francis Group, New York, 2014.
[228] P. Kanhere, and Z. Chen, A Review on Visible Light Active Perovskite-based Photocatalysts, Molecules 19 (2014) 19995-20022.
[229] E. Grabowska, Selected Perovskite Oxides: Characterization, Preparation and Photocatalytic Properties—A Review, Appl. Catal. B 186 (2016) 97-126.
[230] Y. Sakata, Y. Miyoshi, T. Maeda, K. Ishikiriyama, Y. Yamazaki, H. Imamura, Y. Ham, T. Hisatomi, J. Kubota, A. Yamakata, and K. Domen, Photocatalytic Property of Metal Ion added $SrTiO_3$ to Overall H_2O Splitting, Appl. Catal. A-Gen. 521 (2016) 227-232.
[231] Q. Wang, and K. Domen, Particulate Photocatalysts for Light-Driven Water Splitting: Mechanisms, Challenges, and Design Strategies, Chem. Rev. 120 (2020) 919-985.
[232] C.V. Nguyen, T.N.Q. Trang, H.Q. Pham, V.T.H. Thu, and V.T.T. Ho, One-step Heating Hydrothermal of Iridium-Doped Cubic Perovskite Strontium Titanate Towards Hydrogen Evolution, Mater. Lett. 282 (2021) 128686.

[233] R. Niishiro, H. Kato, and A. Kudo, Nickel and Either Tantalum or Niobium-Codoped TiO_2 and $SrTiO_3$ Photocatalysts with Vsible-Light Response for H_2 or O_2 Evolution from Equeous Solutions, Phys. Chem. Chem. Phys. 7 (2005) 2241-2245.
[234] W.-J. Shi, and S.-J. Xiong, Ab Initiostudy on Band-Gap Nrrowing in $SrTiO_3$ with Nb-C-Nb Codoping, Phys. Rev. B 84 (2011) 205210.
[235] J.-Q. Zheng, Y.-J. Zhu, J.-S. Xu, B.-Q. Lu, C. Qi, F. Chen, and J. Wu, Microwave-Assisted Rapid Synthesis and Photocatalytic Activity of Mesoporous Nd-Doped $SrTiO_3$ Nanospheres and Nanoplates, Materials Letters 100 (2013) 62-65.
[236] T.-H. Xie, X. Sun, and J. Lin, Enhanced Photocatalytic Degradation of RhB Driven by Visible Light-Induced MMCT of Ti(IV)-O-Fe(II) Formed in Fe-Doped $SrTiO_3$, J. Phys. Chem. C 112 (2008) 9753-9759.
[237] T. Ishii, H. Kato, and A. Kudo, H_2 Evolution From an Aqueous Methanol Solution on $SrTiO_3$ Photocatalysts Codoped with Chromium and Tantalum Ions under Visible Light Irradiation, J. Photochem. Photobiol. C 163 (2004) 181-186.
[238] D. Wang, Y. J., T. Kako, and T. Kimura, Photophysical and Photocatalytic Properties of $SrTiO_3$ J. Phys. Chem. B 110 (2006) 15824-15830.
[239] U. Sulaeman, S. Yin, and T. Sato, Solvothermal Synthesis and Photocatalytic Properties of Chromium-Doped $SrTiO_3$ Nanoparticles, Appl. Catal. B 105 (2011) 206-210.
[240] T. Takata, C. Pan, M. Nakabayashi, N. Shibata, and K. Domen, Fabrication of a Core-Shell-Type Photocatalyst via Photodeposition of Group IV and V Transition Metal Oxyhydroxides: An Effective Surface Modification Method for Overall Water Splitting, J. Am. Chem. Soc. 137 (2015) 9627-9634.
[241] A. Jia, X. Liang, Z. Su, T. Zhu, and S. Liu, Synthesis and the Effect of Calcination Temperature on the Physical-Chemical Properties and Photocatalytic Activities of Ni,La Codoped $SrTiO_3$, J. Hazard. Mater. 178 (2010) 233-242.
[242] F. Li, K. Yu, L.-L. Lou, Z. Su, and S. Liu, Theoretical and Experimental Study of La/Ni Co-Doped $SrTiO_3$ Photocatalyst, Mater. Sci. Eng. B 172 (2010) 136-141.
[243] Q. Wang, T. Hisatomi, S.S.K. Ma, Y. Li, and K. Domen, Core/Shell Structured La- and Rh-Codoped $SrTiO_3$ as a Hydrogen Evolution Photocatalyst in Z-Scheme Overall Water Splitting under Visible Light Irradiation, Chem. Mater. 26 (2014) 4144-4150.
[244] D.H.K. Murthy, H. Matsuzaki, Q. Wang, Y. Suzuki, K. Seki, T. Hisatomi, T. Yamada, A. Kudo, K. Domen, and A. Furube, Revealing the Role of the Rh Valence State, La Doping Level and Ru Cocatalyst in Determining the H_2 Evolution Efficiency in Doped $SrTiO_3$ Photocatalysts, Sustain. Energy Fuels 3 (2019) 208-218.
[245] H.W. Kang, S.N. Lim, D. Song, and S.B. Park, Organic-Inorganic Composite of g-C3N4–$SrTiO_3$:Rh Photocatalyst for Improved H_2 Evolution under Visible Light Irradiation, Int. J. Hydrog. Energy 37 (2012) 11602-11610.
[246] M. Antuch, P. Millet, A. Iwase, A. Kudo, S.A. Grigoriev, and Y.Z. Voloshin, Characterization of Rh:$SrTiO_3$ Photoelectrodes Surface-Modified with a Cobalt Clathrochelate and their Application to the Hydrogen Evolution Reaction, Electrochim. Acta 258 (2017) 255-265.
[247] Y. Goto, T. Hisatomi, Q. Wang, T. Higashi, K. Ishikiriyama, T. Maeda, Y. Sakata, S. Okunaka, H. Tokudome, M. Katayama, S. Akiyama, H. Nishiyama, Y. Inoue, T. Takewaki, T. Setoyama, T. Minegishi, T. Takata, T. Yamada, and K. Domen, A Particulate Photocatalyst Water-Splitting Panel for Large-Scale Solar Hydrogen Generation, Joule 2 (2018) 509-520.
[248] H. Kato, and A. Kudo, Visible-Light-Response and Photocatalytic Activities of TiO_2 and $SrTiO_3$ Photocatalysts Codoped with Antimony and Chromium, J. Phys. Chem. B 106 (2002) 5029-5034.

[249] X. Sun, and J. Lin, Synergetic Effects of Thermal and Photo-Catalysis in Purification of Dye Water over $SrTi_{1-x}Mn_xO_3$ Solid Solutions, J. Phys. Chem. C 113 (2009) 4970-4975.
[250] C. Zhang, Y. Jia, Y. Jing, Y. Yao, J. Ma, and J. Sun, Effect of Non-Metal Elements (B, C, N, F, P, S) Mono-Doping as Anions on Electronic Structure of $SrTiO_3$, Comput. Mater. Sci. 79 (2013) 69-74.
[251] J. Wang, S. Yin, M. Komatsu, Q. Zhang, F. Saito, and T. Sato, Preparation and Characterization of Nitrogen Doped $SrTiO_3$ Photocatalyst, J. Photochem. Photobiol. A 165 (2004) 149-156.
[252] J. Wang, S. Yin, Q. Zhang, F. Saito, and T. Sato, Mechanochemical Synthesis and Photocatalytic Activity of Nitrogen Doped $SrTiO_3$, J. Ceram. Soc. Jpn. 112 (2004) S1408-S1410.
[253] J. Wang, H. Li, H. Li, S. Yin, and T. Sato, Preparation and Photocatalytic Activity of Visible Light-Active Sulfur and Nitrogen Co-Doped $SrTiO_3$, Solid State Sci. 11 (2009) 182-188.
[254] H.F. Liu, Effect of Nitrogen and Carbon Doping on Electronic Properties of $SrTiO_3$, Solid State Commun. 152 (2012) 2063-2065.
[255] C. Zhang, Y. Jia, Y. Jing, Y. Yao, J. Ma, and J. Sun, DFT Study on Electronic Structure and Optical Properties of N-Doped, S-Doped, and N/S Co-Doped $SrTiO_3$, Physica B 407 (2012) 4649-4654.
[256] T. Ohno, T. Tsubota, Y. Nakamura, and K. Sayama, Preparation of S, C Cation-Codoped $SrTiO_3$ and its Photocatalytic Activity under Visible Light, Appl. Catal. A-Gen. 288 (2005) 74-79.
[257] T.H. Chiang, H. Lyu, T. Hisatomi, Y. Goto, T. Takata, M. Katayama, T. Minegishi, and K. Domen, Efficient Photocatalytic Water Splitting Using Al-Doped $SrTiO_3$ Coloaded with Molybdenum Oxide and Rhodium–Chromium Oxide, ACS Catal. 8 (2018) 2782-2788.
[258] T. Takata, J. Jiang, Y. Sakata, M. Nakabayashi, N. Shibata, V. Nandal, K. Seki, T. Hisatomi, and K. Domen, Photocatalytic Water Splitting with a Quantum Efficiency of Almost Unity, Nature 581 (2020) 411-414.
[259] J. Guo, S. Ouyang, P. Li, Y. Zhang, T. Kako, and J. Ye, A new Heterojunction Ag_3PO_4/Cr-$SrTiO_3$ Photocatalyst towards Efficient Elimination of Gaseous Organic Pollutants under Visible Light Irradiation, Appl. Catal. B 134-135 (2013) 286-292.
[260] X. Chen, P. Tan, B. Zhou, H. Dong, J. Pan, and X. Xiong, A Green and Facile Strategy for Preparation of Novel and Stable Cr-Doped $SrTiO_3$/g-C_3N_4 Hybrid Nanocomposites with Enhanced Visible Light Photocatalytic Activity, J. Alloys Compd. 647 (2015) 456-462.
[261] R. Konta, T. Ishii, H. Kato, and A. Kudo, Photocatalytic Activities of Noble Metal Ion Doped $SrTiO_3$ under Visible Light Irradiation, J. Phys. Chem. B 108 (2004) 8992-8995.
[262] Y. Wang, H. Suzuki, J. Xie, O. Tomita, D.J. Martin, M. Higashi, D. Kong, R. Abe, and J. Tang, Mimicking Natural Photosynthesis: Solar to Renewable H_2 Fuel Synthesis by Z-Scheme Water Splitting Systems, Chem. Rev. 118 (2018) 5201-5241.
[263] H. Kato, Y. Sasaki, N. Shirakura, and A. Kudo, Synthesis of Highly Active Rhodium-Doped $SrTiO_3$ Powders in Z-scheme Systems for Visible-Light-Driven Photocatalytic Overall Water Splitting, J. Mater. Chem. A 1 (2013) 12327.
[264] Y. Yamaguchi, S. Usuki, Y. Kanai, K. Yamatoya, N. Suzuki, K.I. Katsumata, C. Terashima, T. Suzuki, A. Fujishima, H. Sakai, A. Kudo, and K. Nakata, Selective Inactivation of Bacteriophage in the Presence of Bacteria by Use of Ground Rh-Doped $SrTiO_3$ Photocatalyst and Visible Light, ACS Appl. Mater. Interfaces 9 (2017) 31393-31400.
[265] H.W. Kang, S.N. Lim, and S.B. Park, Co-Doping Schemes to enhance H_2 Evolution under Visible Light Irradiation over $SrTiO_3$:Ni/M (M = La or Ta) Prepared by Spray Pyrolysis, Int. J. Hydrog. Energy 37 (2012) 5540-5549.

[266] A. Jia, Z. Su, L.-L. Lou, and S. Liu, Synthesis and Characterization of Highly-Active Nickel and Lanthanum Co-Doped $SrTiO_3$, Solid State Sci. 12 (2010) 1140-1145.
[267] P. Reunchan, S. Ouyang, N. Umezawa, H. Xu, Y. Zhang, and J. Ye, Theoretical Design of Highly Active $SrTiO_3$-Based Photocatalysts by a Codoping Scheme towards Solar Energy Utilization for Hydrogen Production, J. Mater. Chem. A 1 (2013) 4221.
[268] H. Yu, J. Wang, S. Yan, T. Yu, and Z. Zou, Elements Doping to Expand the Light Response of $SrTiO_3$, J. Photochem. Photobiol. A 275 (2014) 65-71.
[269] R. Abe, K. Sayama, and H. Sugihara, Development of New Photocatalytic Water Splitting into H_2 and O_2 using Two Different Semiconductor Photocatalysts and a Shuttle Redox Mediator IO_3^-/I^-, J. Phys. Chem. B 109 (2005) 16052-16061.
[270] K. Sayama, K. Mukasa, R. Abe, Y. Abe, and H. Arakawa, A new Photocatalytic Water Splitting System under Visible Light Irradiation Mimicking a Z-scheme Mechanism in Photosynthesis, J. Photochem. Photobiol. A 148 (2002) 71-77.
[271] P. Liu, J. Nisar, B. Pathak, and R. Ahuja, Hybrid Density Functional Study on $SrTiO_3$ for Visible Light Photocatalysis, Int. J. Hydrog. Energy 37 (2012) 11611-11617.
[272] Y.Y. Mi, S.J. Wang, J.W. Chai, J.S. Pan, C.H.A. Huan, Y.P. Feng, and C.K. Ong, Effect of Nitrogen Doping on Optical Properties and Electronic Structures of $SrTiO_3$ Films, Appl. Phys. Lett. 89 (2006) 231922.
[273] J. Liu, L. Wang, J. Liu, T. Wang, W. Qu, and Z. Li, DFT Study on Electronic Structures and Optical Absorption Properties of C, S Cation- Doped $SrTiO_3$, Open Phys. 7 (2009).
[274] J. Wang, S. Yin, M. Komatsu, and T. Sato, Lanthanum and Nitrogen Co-Doped $SrTiO_3$ powders as Visible Light Sensitive Photocatalyst, J. Eur. Ceram. Soc. 25 (2005) 3207-3212.
[275] M. Miyauchi, M. Takashio, and H. Tobimatsu, Photocatalytic Activity of $SrTiO_3$ Codoped with Nitrogen and Lanthanum under Visible Light Illumination, Langmuir 20 (2004) 232-236.
[276] J. Zhang, J.H. Bang, C. Tang, and P.V. Kamat, Tailored TiO_2-$SrTiO_3$ Heterostructure Nanotube Arrays for Improved Photoelectrochemical Performance, ACS Nano 4 (2010) 387-395.
[277] C. Wang, H. Qiu, T. Inoue, and Q. Yao, Highly Active $SrTiO_3$ for Visible Light Photocatalysis: A First-Principles Prediction, Solid State Commun. 181 (2014) 5-8.
[278] T. Cao, Y. Li, C. Wang, C. Shao, and Y. Liu, A Facile in situ Hydrothermal Method to $SrTiO_3/TiO_2$ Nanofiber Heterostructures with High Photocatalytic Activity, Langmuir 27 (2011) 2946-2952.
[279] H. Bai, J. Juay, Z. Liu, X. Song, S.S. Lee, and D.D. Sun, Hierarchical $SrTiO_3/TiO_2$ Nanofibers Heterostructures with high Efficiency in Photocatalytic H_2 Generation, Appl. Catal. B 125 (2012) 367-374.
[280] Y. Yang, K. Lee, Y. Kado, and P. Schmuki, Nb-Doping of $TiO_2/SrTiO_3$ Nanotubular Heterostructures for enhanced Photocatalytic Water Splitting, Electrochem. Commun. 17 (2012) 56-59.
[281] L. Wang, Z. Wang, D. Wang, X. Shi, H. Song, and X. Gao, The Photocatalysis and Mechanism of new $SrTiO_3/TiO_2$, Solid State Sci. 31 (2014) 85-90.
[282] H. Wang, W. Zhao, Y. Zhang, S. Zhang, Z. Wang, and D. Zhao, A Facile in-situ Hydrothermal Synthesis of $SrTiO_3/TiO_2$ Microsphere Composite, Solid State Commun. 236 (2016) 27-31.
[283] E. Grabowska, M. Marchelek, T. Klimczuk, W. Lisowski, and A. Zaleska-Medynska, $TiO_2/SrTiO_3$ and $SrTiO_3$ Microspheres Decorated with Rh, Ru or Pt Nanoparticles: Highly UV–vis Responsible Photoactivity and Mechanism, J. Catal. 350 (2017) 159-173.

[284] R. Bashiri, N.M. Mohamed, N.A. Suhaimi, M.U. Shahid, C.F. Kait, S. Sufian, M. Khatani, and A. Mumtaz, Photoelectrochemical Water Splitting with Tailored $TiO_2/SrTiO_3$ @g-C_3N_4 Heterostructure Nanorod in Photoelectrochemical Cell, Diam. Relat. Mater. 85 (2018) 5-12.
[285] R. Tao, X. Li, X. Li, C. Shao, and Y. Liu, $TiO_2/SrTiO_3$/g-C_3N_4 Ternary Heterojunction Nanofibers: Gradient Energy Band, Cascade Charge Transfer, Enhanced Photocatalytic Hydrogen Evolution, and Nitrogen Fixation, Nanoscale 12 (2020) 8320-8329.
[286] J. Zhu, P. Xiao, H. Li, and S.A. Carabineiro, Graphitic Carbon Nitride: Synthesis, Properties, and Applications in Catalysis, ACS Appl. Mater. Interfaces 6 (2014) 16449-16465.
[287] X. Xu, G. Liu, C. Randorn, and J.T.S. Irvine, g-C_3N_4 Coated $SrTiO_3$ as an Efficient Photocatalyst for H_2 Production in Aqueous Solution under Visible Light Irradiation, Int. J. Hydrog. Energy 36 (2011) 13501-13507.
[288] T.K. Townsend, N.D. Browning, and F.E. Osterloh, Overall Photocatalytic Water Splitting with NiO_x–$SrTiO_3$ – a Revised Mechanism, Energy Environ. Sci. 5 (2012) 9543.
[289] K. Domen, A. Kudo, and T. Onishi, Photocatalytic Decomposition of Water into H_2 and O_2 over NiO-$SrTiO_3$ Power. 1. Structure of the Catalyst, J. Phys. Chem. 90 (1986) 292-295.
[290] K. Domen, S. Naito, T. Onishi, K. Tamaru, and M. Soma, Study of the Photocatalytic Decomposition of Water vapor over a NiO-$SrTiO_3$ Catalyst, J. Phys. Chem. 86 (1982) 3657-3661.
[291] Y. Fo, M. Wang, Y. Ma, H. Dong, and X. Zhou, Origin of Highly Efficient Photocatalyst NiO/$SrTiO_3$ for Overall Water Splitting: Insights from Density Functional Theory Calculations, J. Solid State Chem. 292 (2020) 121683.
[292] Y. Wu, Y. Wei, Q. Guo, H. Xu, L. Gu, F. Huang, D. Luo, Y. Huang, L. Fan, and J. Wu, Solvothermal Fabrication of La-$WO_3/SrTiO_3$ Heterojunction with High Photocatalytic Performance under Visible Light Irradiation, Sol. Energy Mater. Sol. Cells 176 (2018) 230-238.
[293] Y. Wu, B. Dong, J. Zhang, H. Song, and C. Yan, The Synthesis of ZnO/$SrTiO_3$ Composite for High-Efficiency Photocatalytic Hydrogen and Eelectricity Conversion, Int. J. Hydrog. Energy 43 (2018) 12627-12636.
[294] X.L. Yin, L.L. Li, D.C. Li, D.H. Wei, C.C. Hu, and J.M. Dou, Room Temperature Synthesis of CdS/$SrTiO_3$ Nanodots-on-Nanocubes for Efficient Photocatalytic H_2 Evolution from Water, J. Colloid Interface Sci. 536 (2019) 694-700.
[295] J. Liu, L. Zhang, N. Li, Q. Tian, J. Zhou, and Y. Sun, Synthesis of $MoS_2/SrTiO_3$ Composite Materials for Enhanced Photocatalytic Activity under UV Irradiation, J. Mater. Chem. A 3 (2015) 706-712.
[296] L. Zhu, W. Gu, H. Li, W. Zou, H. Liu, Y. Zhang, Q. Wu, Z. Fu, and Y. Lu, Enhancing the Photocatalytic Hydrogen Production Performance of $SrTiO_3$ by Coating with a Hydrophilic Poloxamer, Appl. Surf. Sci. 528 (2020) 146837.
[297] Y. Xia, Z. He, K. Hu, B. Tang, J. Su, Y. Liu, and X. Li, Fabrication of n-$SrTiO_3$/p-Cu_2O Heterojunction Composites with Enhanced Photocatalytic Performance, J. Alloys Compd. 753 (2018) 356-363.
[298] S. Choudhary, A. Solanki, S. Upadhyay, N. Singh, V.R. Satsangi, R. Shrivastav, and S. Dass, Nanostructured CuO/$SrTiO_3$ Bilayered Thin Films for Photoelectrochemical Water Splitting, J. Solid State Electrochem. 17 (2013) 2531-2538.
[299] M. Ahmadi, M.S. Seyed Dorraji, I. Hajimiri, and M.H. Rasoulifard, The Main Role of CuO Loading against Electron-Hole Recombination of $SrTiO_3$: Improvement and Investigation of Photocatalytic Activity, Modeling and Optimization by Response Surface Methodology, J. Photochem. Photobiol. A 404 (2021) 112886.
[300] L. Ren, X. Yi, L. Tong, W. Zhou, D. Wang, L. Liu, and J. Ye, Nitrogen-Doped Ultrathin Graphene Encapsulated Cu Nanoparticles Decorated on $SrTiO_3$ as an Efficient Water

Oxidation Photocatalyst with Activity Comparable to $BiVO_4$ under Visible-Light Irradiation, Appl. Catal. B 279 (2020) 119352.
[301] S. Suzuki, H. Matsumoto, A. Iwase, and A. Kudo, Enhanced H_2 Evolution over an Ir-Doped $SrTiO_3$ Photocatalyst by Loading of an Ir Cocatalyst using Visible Light up to 800 nm, Chem. Commun. 54 (2018) 10606-10609.
[302] H. Kato, Y. Sasaki, A. Iwase, and A. Kudo, Role of Iron Ion Electron Mediator on Photocatalytic Overall Water Splitting under Visible Light Irradiation Using Z-Scheme Systems, Bull. Chem. Soc. Jpn. 80 (2007) 2457-2464.
[303] L. Liu, P. Li, B. Adisak, S. Ouyang, N. Umezawa, J. Ye, R. Kodiyath, T. Tanabe, G.V. Ramesh, S. Ueda, and H. Abe, Gold Photosensitized $SrTiO_3$ for Visible-Light Water Oxidation Induced by Au Interband Transitions, J. Mater. Chem. A 2 (2014) 9875.
[304] L. Ma, T. Sun, H. Cai, Z.Q. Zhou, J. Sun, and M. Lu, Enhancing Photocatalysis in $SrTiO_3$ by using Ag Nanoparticles: A Two-Step Excitation Model for Surface Plasmon-Enhanced Photocatalysis, J. Chem. Phys. 143 (2015) 084706.
[305] H. Shen, H. Wei, Z. Pan, Y. Lu, and Y. Wang, Preparation and Characterization of $SrTiO_3$-Ag/AgCl Hybrid Composite with Promoted Plasmonic Visible Light Excited Photocatalysis, Appl. Surf. Sci. 423 (2017) 403-416.
[306] T. Xian, H. Yang, L. Di, J. Ma, H. Zhang, and J. Dai, Photocatalytic Reduction Synthesis of $SrTiO_3$-Graphene Nanocomposites and their Enhanced Photocatalytic Activity, Nanoscale Res. Lett. 9 (2014) 327.
[307] Y. Tian, and T. Tatsuma, Mechanisms and Applications of Plasmon-Induced Charge Separation at TiO_2 Films Loaded with Gold Nanoparticles, J. Am. Chem. Soc. 127 (2005) 7632-7637.
[308] S.T. Kochuveedu, D.-P. Kim, and D.H. Kim, Surface-Plasmon-Induced Visible Light Photocatalytic Activity of TiO_2 Nanospheres Decorated by Au Nanoparticles with Controlled Configuration, J. Phys. Chem. C 116 (2012) 2500-2506.
[309] Z. Zhang, L. Zhang, M.N. Hedhili, H. Zhang, and P. Wang, Plasmonic Gold Nanocrystals Coupled with Photonic Crystal Seamlessly on TiO_2 Nanotube Photoelectrodes for Efficient Visible Light Photoelectrochemical Water Splitting, Nano Lett. 13 (2012) 14-20.
[310] W. Hou, and S.B. Cronin, A Review of Surface Plasmon Resonance-Enhanced Photocatalysis, Adv. Funct. Mater. 23 (2013) 1612-1619.
[311] K. Awazu, M. Fujimaki, C. Rockstuhl, J. Tominaga, H. Murakami, Y. Ohki, N. Yoshida, and T. Watanabe, A Plasmonic Photocatalyst Consisting of Silver Nanoparticles Embedded in Titanium Dioxide, J. Am. Chem. Soc. 130 (2008) 1676-1680.
[312] P.F. Lim, K.H. Leong, L.C. Sim, W.-D. Oh, Y.H. Chin, P. Saravanan, and C. Dai, Mechanism Insight of Dual Synergistic Effects of Plasmonic Pd-$SrTiO_3$ for Enhanced Solar Energy Photocatalysis, Appl. Phys. A 126 (2020) 550.
[313] X.C. Ma, Y. Dai, L. Yu, and B.B. Huang, Energy Transfer in Plasmonic Photocatalytic Composites, Light Sci. Appl. 5 (2016) e16017.
[314] S. Linic, P. Christopher, and D.B. Ingram, Plasmonic-Metal Nanostructures for Efficient Conversion of Solar to Chemical Energy, Nat. Mater. 10 (2011) 911-921.
[315] Y. Sasaki, H. Kato, and A. Kudo, $[Co(bpy)_3]^{3+/2+}$ and $[Co(phen)_3]^{3+/2+}$ Electron Mediators for Overall Water Splitting under Sunlight Irradiation using Z-Scheme Photocatalyst System, J. Am. Chem. Soc. 135 (2013) 5441-5449.
[316] X. Liu, J. Jiang, Y. Jia, J. Qiu, T. Xia, Y. Zhang, Y. Li, and X. Chen, Insight into Synergistically Enhanced Adsorption and Visible Light Photocatalytic Performance of Z-Scheme Heterojunction of $SrTiO_3$(La,Cr)-Decorated WO_3 Nanosheets, Appl. Surf. Sci. 412 (2017) 279-289.

[317] Y. Sasaki, A. Iwase, H. Kato, and A. Kudo, The Effect of Co-Catalyst for Z-Scheme Photocatalysis Systems with an Fe^{3+}/Fe^{2+} Electron Mediator on Overall Water Splitting under Visible Light Irradiation, J. Catal. 259 (2008) 133-137.
[318] Y. Sasaki, H. Nemoto, K. Saito, and A. Kudo, Solar Water Splitting Using Powdered Photocatalysts Driven by Z-Schematic Interparticle Electron Transfer without an Electron Mediator, J. Phys. Chem. C 113 (2009) 17536-17542.
[319] A. Iwase, Y.H. Ng, Y. Ishiguro, A. Kudo, and R. Amal, Reduced Graphene Oxide as a Solid-Etate electron Mediator in Z-Scheme Photocatalytic Water Splitting under Visible Light, J. Am. Chem. Soc. 133 (2011) 11054-11057.
[320] A. Kudo, Z-Scheme Photocatalyst Systems for Water Splitting under Visible Light Irradiation, MRS Bulletin 36 (2011) 32-38.
[321] Y. Miseki, S. Fujiyoshi, T. Gunji, and K. Sayama, Photocatalytic Z-Scheme Water Splitting for Independent H_2/O_2 Production via a Stepwise Operation Employing a Vanadate Redox Mediator under Visible Light, J. Phys. Chem. C 121 (2017) 9691-9697.
[322] S. Okunaka, H. Kameshige, T. Ikeda, H. Tokudome, T. Hisatomi, T. Yamada, and K. Domen, Z-Scheme Water Splitting under Near-Ambient Pressure using a Zirconium Oxide Coating on Printable Photocatalyst Sheets, ChemSusChem 13 (2020) 4906-4910.
[323] F.Q. Zhou, J.C. Fan, Q.J. Xu, and Y.L. Min, $BiVO_4$ Nanowires Decorated with CdS Nanoparticles as Z-Scheme Photocatalyst with Enhanced H_2 Generation, Appl. Catal. B 201 (2017) 77-83.
[324] K. Maeda, Z-Scheme Water Splitting Using Two Different Semiconductor Photocatalysts, ACS Catal. 3 (2013) 1486-1503.
[325] H. Kunioku, M. Higashi, C. Tassel, D. Kato, O. Tomita, H. Kageyama, and R. Abe, Sillén–Aurivillius-related Oxychloride $Bi_6NbWO_{14}Cl$ as a Stable O_2-evolving Photocatalyst in Z-scheme Water Splitting under Visible Light, Chem. Lett. 46 (2017) 583-586.
[326] J.L. Giocondi, P.A. Salvador, and G.S. Rohrer, The Origin of Photochemical Anisotropy in $SrTiO_3$, Top. Catal. 44 (2007) 529-533.
[327] B. Wang, S. Shen, and L. Guo, $SrTiO_3$ Single Crystals Enclosed with High-Indexed {023} Facets and {001} Facets for Photocatalytic Hydrogen and Oxygen Evolution, Appl. Catal. B 166-167 (2015) 320-326.
[328] R. Li, F. Zhang, D. Wang, J. Yang, M. Li, J. Zhu, X. Zhou, H. Han, and C. Li, Spatial Separation of Photogenerated Electrons and Holes Among {010} and {110} Crystal Facets of $BiVO_4$, Nat. Commun. 4 (2013) 1432.
[329] D. Wang, H. Jiang, X. Zong, Q. Xu, Y. Ma, G. Li, and C. Li, Crystal Facet Dependence of Water Oxidation on BiVO4 Sheets under Visible Light Irradiation, Chem. Eur. J. 17 (2011) 1275-1282.
[330] T. Tachikawa, S. Yamashita, and T. Majima, Evidence for Crystal-Face-Dependent TiO_2 Photocatalysis from Single-Molecule Imaging and Kinetic Analysis, J. Am. Chem. Soc. 133 (2011) 7197-7204.
[331] R. Li, X. Tao, R. Chen, F. Fan, and C. Li, Synergetic Effect of Dual Co-Catalysts on the Activity of p-Type Cu_2O Crystals with Anisotropic Facets, Chemistry 21 (2015) 14337-41.
[332] L. Mu, B. Zeng, X. Tao, Y. Zhao, and C. Li, Unusual Charge Distribution on the Facet of a $SrTiO_3$ Nanocube under Light Irradiation, J. Phys. Chem. Lett. 10 (2019) 1212-1216.
[333] U. Sulaeman, S. Yin, and T. Sato, Visible Light Photocatalytic Activity Induced by the Carboxyl Group Chemically Bonded on the Surface of $SrTiO_3$, Appl. Catal. B 102 (2011) 286-290.

[334] S. Ouyang, H. Tong, N. Umezawa, J. Cao, P. Li, Y. Bi, Y. Zhang, and J. Ye, Surface-Alkalinization-Induced Enhancement of Photocatalytic H_2 Evolution over $SrTiO_3$-based Photocatalysts, J. Am. Chem. Soc. 134 (2012) 1974-1977.
[335] Y. Kim, M. Watanabe, J. Matsuda, J.T. Song, A. Takagaki, A. Staykov, and T. Ishihara, Tensile Strain for Band Engineering of $SrTiO_3$ for Increasing Photocatalytic Activity to Water Splitting, Appl. Catal. B 278 (2020) 119292.
[336] H. Tan, Z. Zhao, W.B. Zhu, E.N. Coker, B. Li, M. Zheng, W. Yu, H. Fan, and Z. Sun, Oxygen Vacancy Enhanced Photocatalytic Activity of Pervoskite $SrTiO_3$, ACS Appl. Mater. Interfaces 6 (2014) 19184-19190.